



Aristotle University of Thessaloniki

Faculty of Engineering

School of Mechanical Engineering

Development of algorithms for estimation of particle emissions using soot sensor for on-board diagnostic systems

Dimitrios Kontses

Dipl. Mechanical Engineer

PhD Thesis

“This research is co-financed by Greece and the European Union (European Social Fund- ESF) through the Operational Programme «Human Resources Development, Education and Lifelong Learning» in the context of the project “Scholarships programme for post-graduate studies - 2nd Study Cycle” (MIS-5003404), implemented by the State Scholarships Foundation (IKY).”



Thessaloniki, September 2019

Aristotle University of Thessaloniki

Faculty of Engineering

School of Mechanical Engineering

Development of algorithms for estimation of particle emissions using soot sensor for on-board
diagnostic systems

Dimitrios Kontses

Dipl. Mechanical Engineer

PhD Thesis

Submitted in partial fulfilment of the requirements for the degree of Doctor of Philosophy in
Department of Mechanical Engineering of the Aristotle University of Thessaloniki

Examination Committee	
Supervisor	Prof. Zissis Samaras
Advisors	Assoc. Prof. Leonidas Ntziachristos
	Assist. Prof. Savas Geivanidis
Examiners	Prof. Grigorios Koltsakis
	Prof. Ananias Tompoulidis
	Prof. Nikolaos Mousiopoulos
	Prof. Dimitrios Vlachos

To my family and Eleftheria, for supporting my dreams

Executive Summary

Particulate matter emissions have been the subject of intense research due to their adverse effect to air quality, the environment and human health. The transportation sector significantly contributes to the anthropogenic particulate matter emissions, and nowadays, diesel particulate filter (DPF) is the standard equipment for particulate matter reduction in all diesel light and heavy-duty vehicles. The DPF though is prone to failures such as melting or cracking during uncontrolled regenerations, while the intentional removal of DPF for by tampering is another serious concern. To ensure the functionality of the DPF, emission regulations require on-board diagnostic (OBD) systems to monitor its performance. Until recently, a sensor system measuring the pressure drop induced by the soot accumulation in the DPF was used for diagnosing the status of the DPF. However, this approach is not accurate enough to detect a malfunctioning DPF under all conditions. The resistive soot sensor is therefore the current state-of-the-art by the automotive industry because of its low cost and effectiveness in DPF diagnosis. This sensor correlates soot mass concentration in the exhaust with the electrical resistance between two sensing electrodes, which decreases as soot accumulates on the sensor surface. The actual metric of the sensor of DPF condition is the response time, which is the time needed for the sensor to go from the clean to the fully loaded state.

The current thesis developed and optimised an OBD system for DPF diagnosis using a resistive soot sensor and proposed solutions for advanced on-board DPF diagnosis. The methodology followed to achieve the targets of the thesis included extensive testing and simulation for the model and the sensor, which is the key component of the application. The Simulink® environment was used for the development of the overall OBD model. The testing campaigns were mainly performed on engines and vehicles available in the Laboratory of Applied Thermodynamics. Also, a pre-production vehicle with the soot sensor installed as factory equipment was used for preliminary calibration.

Following the introduction in chapter 1, the study is structured around the chapters below:

- Chapter 2: methodology for DPF diagnosis
- Chapter 3: development and calibration of the OBD model
- Chapter 4: optimisation of the sensor and the sensor model
- Chapter 5: future requirements and solutions for advanced particle number and particulate mass (PN/PM) OBD

The study concludes with the summary and the future steps in chapter 6.

Chapter 2 describes the methodology that was followed for the diagnosis of a DPF using a resistive soot sensor. The first part analyses the operating principle of the resistive sensor and the various generations of the sensors that have been used for this study. It continues with the architecture of the developed OBD model, the definition of the threshold emissions level and the conditions to start the diagnosis. The second part of the methodology describes the experimental set-ups. Two engine dynamometers and three test vehicles were used to perform the steady-state and the transient measurements for this study. To control and adjust soot emissions, various artificially failed DPFs were created by partially unplugging the outlet channels. The Micro Soot Sensor (MSS) and the Pegasor Particle Sensor (PPS) were the reference equipment for the measurement of soot mass concentration. Finally, surface and elemental analysis were utilised to verify the effect of contaminants on the response time of the sensors.

Chapter 3 presents the development of the OBD model. The model is based on the comparison between the measured response time of a resistive soot sensor and the modelled sensor response time for a DPF failed at the OBD limit (12 mg/km on the NEDC). The modelled response time was predicted using:

- the soot model to estimate engine-out emissions
- the DPF model to calculate the filtration efficiency of the threshold DPF and
- the sensor model to convert the calculated emissions to sensor response time

As a next step, a simple approach and an advanced solution were selected and developed for each sub-model, and their accuracy was assessed for different driving conditions. The overall model was evaluated for its accuracy in terms of relative error on the estimated final OBD index over the new European driving cycle (NEDC) based on the current legislation. Finally, the OBD model was validated in various driving cycles, and the effectiveness of rejection criteria was examined.

The results show that the error associated with the soot model for the estimation of the engine-out soot emissions compared to the measured emission by the reference equipment (Micro Soot Sensor, MSS) was calculated to be 25% and 2% for the base and the advanced model, respectively. The improved performance is attributed to the transient correction applied in the advanced solution. The accuracy of the DPF model was 9% for the non-optimal scenario of constant filtration efficiency. The corresponding error for the advanced filtration efficiency, which accounts for the DPF loading and the exhaust volume flow was significantly lower (5%). The sensor model, which implements the empirical function and estimates the sensor response time, was found to be associated with a 7% error attributed to measurement inaccuracies effects on the sensor model. The advanced physical model provides similar accuracy, but it can be additionally utilised for sensitivity analyses of the effect of the different deposition mechanisms on the sensor response. The sensor inaccuracy was estimated to be about 18% and is attributed to the stochastic construction of soot dendrites which leads to variability of the response

time for a specific particle flux. This variability is more profound during transient operation. The overall OBD index error based on a propagation analysis of the above errors was estimated to be 28% and 19% for the base and the advanced approaches, respectively.

The calculated error is expected to be higher over more transient operation during on-road driving conditions. Nevertheless, improvements in every sub-model and sensor accuracy in its final production version will compensate for the effect of dynamic driving conditions. The performed sensitivity analysis indicates that the sensor accuracy improvement, along with a more accurate soot model, can sufficiently improve the performance of the OBD model. Finally, a fast sensor allows for ECU debouncing and rejection criteria for adverse transient periods, and thus the successful diagnosis of a failed DPF under real driving conditions is possible. This is verified by the ability of the OBD model to distinguish the emissions of two DPFs failed at different levels using the advanced models and the rejection criteria for the final implementation.

The challenges and the limitations related to the sensor model and the resistive soot sensor that came up during the realisation of the OBD model on a vehicle application are analysed in Chapter 4. The application of the sensor model in extreme conditions is challenging for the accuracy of the sensor model and is analysed in the first section of that chapter. The extension of the operating conditions to higher exhaust speed and temperature levels during the development of the transfer function (TF) improves the performance over a wider operation range and can result in a sufficient accuracy of diagnosis.

Continuing with the challenges related with the resistive sensor, the supply voltage was found to affect the regeneration effectiveness of the sensor. For 9V, the sensor needs a second regeneration event to clean the accumulated soot. This issue was resolved by increasing the regeneration temperature by 5% over the previous default value. The sensor mounting orientation increased the response time up to 17% for Gen1 sensors (single-tip) based on experimental data. A new tip design was evaluated using both CFD analysis and engine measurements. The orientation effect in response time was insignificant (<4%) and thus, the orientation mark was no longer needed. A significant drawback of the first sensor design was the inadequate protection from water droplets, which resulted in bias during cold operation and cracks due to thermal stress. The new tip design, along with an improved dew point strategy significantly diminishes the risk of element failures and artefacts during cold operation.

Cross sensitivities are a serious concern for resistive sensors. The direct effect during sensor exposure and/or the remaining effect after the end of the exposure was evaluated for 8 contaminants. Experiments for sulphur, methane, carbon monoxide, hydrogen and sodium showed no significant effect (either direct or remaining) on sensor behaviour (<10% effect on response time). Urea solution can increase the response time of the sensor by 35%, creating a remaining effect possibly due to deposition of salts. The main concern was about the regeneration time-out error reported by one sensor which

advises us that following the need of very low NO_x emissions in a modern vehicle, significant effort should be put to ensure low urea excess on the resistive sensor area to avoid issues with sensor and model robustness. NH_3 , as the main product of urea decomposition, can reach up to 700 ppm in the investigated application. The direct effect of such a high concentration is a reduction in response time by 15% attributed mainly to the different construction of dendrites. Despite the temporary effect of excessive NH_3 slip in an SCR system, the remaining effect after 300h of operation over NH_3 excess was insignificant. Finally, ash accumulation significantly increased the response time of the resistive sensors (up to 250% for the single tip sensor at the end of the useful life of the vehicle). The evaluation of the effect of ash showed that the latest tip design and the use of a repelling voltage (software solution) could retain the increase in response time at approximately 43%. To further improve this behaviour, additional protection measures are currently investigated.

Chapter 5 presents the requirements and the methods for PN/PM estimation for advanced on-board applications. The review of the current and future OBD regulatory requirements revealed the different levels and challenges that the sensors will confront. Lower mass limits, additional number limit, on-board and fleet monitoring with smart systems and more sensitive and effective in-service conformity checks, require advanced sensors able to be set-up and be ready for measurement in a short period. Calculation and delivery of real-time data in the framework of on-board monitoring necessitate integrating these sensors in smart systems similarly to already available smart emissions measurement systems (SEMS) for gaseous emissions. The desired level of accuracy will be different for each application or requirement, but undoubtedly, it will be better compared to the currently available resistive soot sensors. The method developed for current OBD using the resistive technology should be used as a template for advanced on-board applications.

Optical and electrical charge-based principles were presented as candidate sensor solutions. The laser induced incandescence (LII) sensor can provide an accurate and direct measurement of both PN and PM, but improvements are needed for OBD application focusing on contamination and cooling issues, and the high complexity of high-power laser. 3DATX parSYNC combines low-cost technology with advanced algorithms to calculate PN and PM levels. The available data though is not enough to extract reliable conclusions for the accuracy and sensitivity of the system. Electrostatic sensors are for many years in the market but the cross-sensitivities to high flow and their rather poor performance at low emission levels, entail the need for further investigation and improvements. Finally, sensors based on diffusion charge technology, have been proved accurate for OBD applications. Nevertheless, the sophisticated design and the need for clean pressurised air restrain their wide adoption for advanced OBD applications.

Acknowledgements

This was a long and exciting journey, but I could not get to the final destination without everyone standing next to me and supporting my efforts. Foremost, I would like to express my sincere gratitude to my supervisor Professor Zissis Samaras for his continuous support and guidance over the past years. He has given me all the freedom and the opportunities to expand my knowledge and research area, while at the same time helping me stay on course and focused on the target. I would also like to express my deep appreciation to Associate Professor Leonidas Ntziachristos as a member of the advisory committee, for his continuous support, and all the fruitful and insightful discussions we had. Also, I would like to sincerely thank Assistant Professor Savas Geivanidis for being my first port of call for everything. His knowledge and expertise for soot sensors helped me to keep in track and complete this thesis. I am also very grateful to the members of the examination committee, Professor Grigorios Koltsakis, Professor Ananias Tompoulidis, Professor Nikolaos Mousiopoulos and Professor Dimitrios Vlachos for taking the time to review my thesis and provide their invaluable feedback.

It was also a pleasure to collaborate with Dr. Pavlos Fragkiadoulakis, who significantly contributed to the completion of this study. I am also very grateful to PhD Candidate Elias Saltas for his invaluable contribution to my research study. My sincere thanks and gratefulness go to all the members of the Laboratory of Applied Thermodynamics, Dr. Dimitrios Katsaounis, Dr. Athanasios Dimaratos, Dr. Ilias Vouitsis, Dr. Stavros Amanatidis, Dr. Dimitrios Tsokolis, Dr. Georgios Triantafyllopoulos, Dr. Anastasios Kontses, Dr. Panayotis Pistikopoulos, PhD Candidates Zissimos Toumasatos, Stylianos Doulgeris and Alexandros Katsinos, Mr. Argyrios Tzilvelis, Mr. Giorgos Christou, Mr. Pavlos Ketikidis, Mr. Georgios Stamos, Mr. Dimos Melachrous, Mr. Georgios Varmazis, Mr. Arsenis Keramidas, Mr. Georgios Kasideropoulos, Mr. Grigorios Papanikolaou, Mr. Dionysios Mavrodis and Mr. Dimitrios Mavrodis for the great collaboration we had over the past years and the vivid discussions.

It was an honour and pleasure to collaborate with the members of Stoneridge Inc. (Novi, MI, USA) and I would like to specifically acknowledge Mr. Kayvan Hedayat and Mr. Thomas Essert for the great collaboration and fruitful discussions during the last four years. I would also like to thank Mr. Jeff Philbin, Mr. Lou Lamborghini, Mr. John Hart, Mr. Chris Chaput, Mr. Chris Parnin, Mr. Karsten Pietschmann and Mr. Rüdiger Emmerich for the great collaboration under our common research activity for the development of the soot sensors.

I would also like to express my appreciation to all the faculty members of the Department of Mechanical Engineering of the Aristotle University of Thessaloniki for sharing their scientific knowledge and for their invaluable support over the past 12 years.

In addition, I gratefully acknowledge the funding received from the State Scholarships Foundation (IKY) by providing the scholarship “Scholarships programme for post-graduate studies - 2nd Study Cycle”.

Apart from my colleagues and co-workers, I would like to sincerely thank my close friends, for their patience and invaluable moral support. Last, but not least, I would like to express my deep gratefulness to my parents Ourania and Panagiotis, and my brothers Anastasios and Iordanis for their unconditional love and for supporting my dreams in any and every way.

Contents

Executive Summary	7
Contents.....	13
1. Introduction	17
1.1. Air pollution and particulate matter emissions	17
1.2. Vehicular particles	18
1.2.1. Non-volatile particles.....	19
1.2.2. Volatile (and semi-volatile) particles.....	20
1.3. Reduction of particulate matter emissions	20
1.4. Aftertreatment devices-Failures of particulate filters.....	21
1.5. OBD systems for DPFs	22
1.5.1. Introduction to the OBD systems	22
1.5.2. The regulatory framework for OBD for particulate filters	23
1.5.3. Approaches for DPF on-board diagnosis.....	26
1.5.4. Development process of DPF OBD systems	27
1.6. Motivation, objectives, structure and novelty aspects of the thesis	28
2. Methodology	33
2.1. Resistive soot sensor and the OBD model for DPF diagnosis	33
2.1.1. Resistive soot sensor.....	33
2.1.2. The architecture of the OBD model.....	37
2.1.3. Definition of threshold in real conditions	39
2.1.4. Necessary conditions to start the DPF diagnosis	42
2.2. Testing and measurement campaigns.....	43
2.2.1. Engines and vehicles details	43
2.2.2. Artificially failed DPFs.....	47
2.2.3. AVL Micro Soot Sensor	50

2.2.4. Pegasor Particle Sensor.....	50
2.2.5. Steady-state points, legislative cycles, RDE routes	52
2.2.6. Surface and elemental analysis	55
2.3. Error propagation calculation.....	56
3. OBD model: development, calibration, validation and uncertainties.....	57
3.1. Simulation of engine-out soot emissions (Soot model)	57
3.1.1. Approaches for soot modelling.....	57
3.1.2. Methodology for the selected approach.....	60
3.1.3. Development of the necessary maps.....	64
3.1.4. Performance and validation	67
3.2. Simulation of filtration efficiency (DPF model).....	72
3.2.1. Approaches for DPF modelling	72
3.2.2. Methodology for the selected approaches	73
3.2.3. Development of the models	77
3.3. Simulation of the sensor response time (Sensor model)	85
3.3.1. Approaches for sensor modelling	85
3.3.2. Methodology for the selected approach.....	87
3.3.3. Development of the Transfer Function.....	89
3.3.4. Performance and validation	90
3.3.5. Summary.....	97
3.4. Sensor response time.....	98
3.4.1. Sensor output	99
3.4.2. Parameters affecting the response time	99
3.4.1. Calibration of sensor response time for the reference cycle (NEDC)-Sensor inaccuracy	101
3.5. OBD Algorithms	102
3.5.1. The error of the overall OBD model.....	103
3.5.2. Final diagnosis.....	103
3.5.3. Validation of the model	109
3.6. Summary and conclusions	110

4. Challenges and limitations of the sensor model and the resistive sensor	113
4.1. Performance of the Transfer Function under extreme driving conditions	113
4.2. Effect of supply voltage on sensor regeneration	117
4.3. Effect of sensor mounting orientation.....	119
4.4. Water protection.....	122
4.5. Optimisation of dew point strategy	123
4.6. Sensor cross sensitivities.....	127
4.6.1. Introduction	127
4.6.2. Effect of sulphur, methane, carbon monoxide, hydrogen, AdBlue (urea), sodium	129
4.6.3. NH ₃ effect	135
4.6.4. Ash effect.....	142
4.7. Summary and conclusions	149
5. Advanced PN/PM on-board diagnostics	151
5.1. Introduction.....	151
5.2. Regulation and market needs for advanced PN/PM sensors.....	154
5.2.1. Lower OBD threshold values for PM emissions	155
5.2.2. OBD limit for PN emissions.....	155
5.2.3. Fleet monitoring with on-board sensors and Smart Emission Measurement Systems (SEMS)	155
5.2.4. On-Board Monitoring (OBM) of PN/PM emissions	156
5.2.5. In-service conformity.....	156
5.2.6. Market requirements.....	156
5.2.7. Summary of needs and requirements.....	156
5.3. Advanced sensors.....	157
5.3.1. Optical principle	157
5.3.2. Electrical charged-based principle.....	159
5.4. Testing with Electrostatic sensor	163
5.5. Summary and conclusions	166
6. Summary, conclusions and future research	169
6.1. Summary and conclusions	169

6.2. Future research.....	171
Appendixes.....	175

1. Introduction

1.1. Air pollution and particulate matter emissions

Air pollution is a serious and worldwide concern for human beings and the natural environment (World Health Organization, 2006; European Environment Agency, 2019). Particulate matter emissions consist of solid or liquid particles suspended in the air. These are emitted in the atmosphere both by natural sources (e.g. forest fires, volcanos, dust, sea salt) and anthropogenic sources (e.g. power plants, transportation, industrial processes, household activities). Their effect on human health is the subject of several studies over the last decades (Sydbom et al., 2001; Delfino et al., 2005; Sioutas et al., 2005; Rückerl et al., 2011; Muñoz et al., 2019). The list of the health risks includes respiratory issues (altered pulmonary function, asthma), cardiovascular problems (ischemic heart disease, hypertension, blood coagulation, an increase of heart rhythm), reduced fertility and cancer (HEI, 2013; Kumar et al., 2014; WHO, 2018). More than 4 million deaths worldwide are related to particulate matter emissions annually (HEI and IHME, 2018). Also, the ecosystem is profoundly affected both directly and indirectly (Figure 1). The direct effects consist mainly of scattering and absorption of solar radiation with cooling and heating consequences on the atmosphere, respectively. The indirect effects are related to cloud formation and modification: water droplets are formed onto pre-existing aerosol particles which are known as cloud condensation nuclei (CCN) (Pandis and Cruz, 1997) and thus, increase the light scattering and the cloud lifetime.

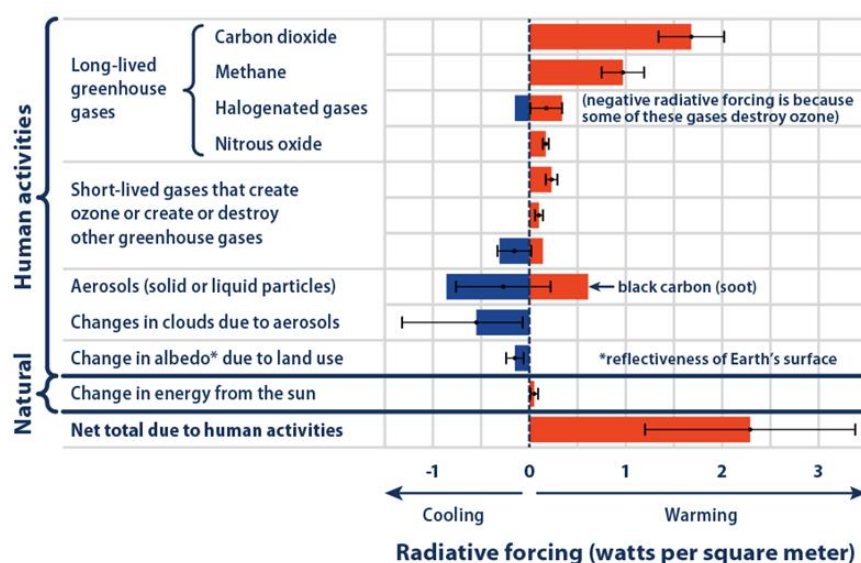


Figure 1: Radiative forcing caused by human activities and the results on climate cooling or warming (US EPA, 2019)

For air quality assessments and health effects, the following size bins are used to classify particulate matter according to their diameter D_p :

- Particles with $D_p < 10\mu\text{m}$ (PM_{10})
- Fine particles with $D_p < 2.5\mu\text{m}$ ($\text{PM}_{2.5}$)
- Ultrafine particles with $D_p < 0.1\mu\text{m}$ (UFP)
- Nanoparticles with $D_p < 50\text{nm}$

Particulate matter mass concentration limits in the ambient air are applied since the early '70s in the developed countries to retain air pollution at low levels. These limits are commonly referring to PM_{10} and $\text{PM}_{2.5}$ annual and daily average concentrations.

1.2. Vehicular particles

The transportation sector with the combustion process currently contributes to the total PM emissions by 13% in the European Union (for $\text{PM}_{2.5}$) although a significant reduction has been achieved the last two decades (European Environmental Agency (EEA), 2018). This was mainly achieved by policy actions through emission standards to reduce primary emissions for road and non-road sources, while the total activity of the sector were constantly increasing. Despite these measures, vehicles still account for approximately 25% of the total particulate matter emissions in urban areas (37% for developing countries) (Karagulian et al., 2015).

Particulate matter mass (PM), particle number (PN) and size are considered the most commonly used properties to characterise particulate matter emissions derived from internal combustion (Hinds, 1999). A typical particle size distribution of engine exhaust was introduced by Kittelson (1998) and comprises the three characteristic particle size modes named as nucleation mode, accumulation mode, and coarse mode. The nucleation mode (5-30nm diameter) usually contains most of the particles in terms of PN concentration. The accumulation mode (30-500nm diameter with average 40-80nm) includes most of the PM concentration. Finally, the coarse mode contains only a few large particles (Kittelson, 1998, Grose et al., 2006) (Figure 2).

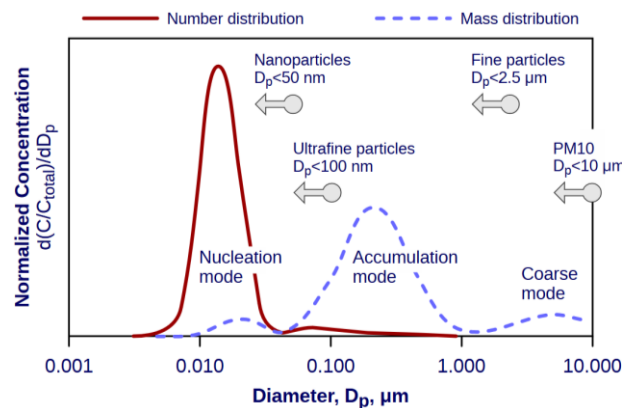


Figure 2. Size distribution of particles from combustion (“DieselNet. Exhaust Particulate Matter,” 2019)

Exhaust particle emissions from vehicles can be divided into two main categories: solid or non-volatile and volatile particles (Eastwood, 2008). The non-volatile category includes carbonaceous material and ash. Organic material (i.e. alkenes, alkanes, alcohols, esters, ketones, acids and PAH), nitrates (i.e. HNO_3 , nitric acid) and sulphates (i.e. H_2SO_4 , sulphuric acid) are the main constituents of volatile particles. After the release in the atmosphere, exhaust aerosol is cooled and diluted. New delayed primary particles can be created via condensation on primary particles or nucleation. As a next step, secondary particles can be created: the gaseous species of the exhaust gas (organic, nitrate and sulphate fraction) are oxidised in the atmosphere in the presence of sunlight, and these can be condensed on existing particles (e.g. soot particles) and nucleate to create new particles.

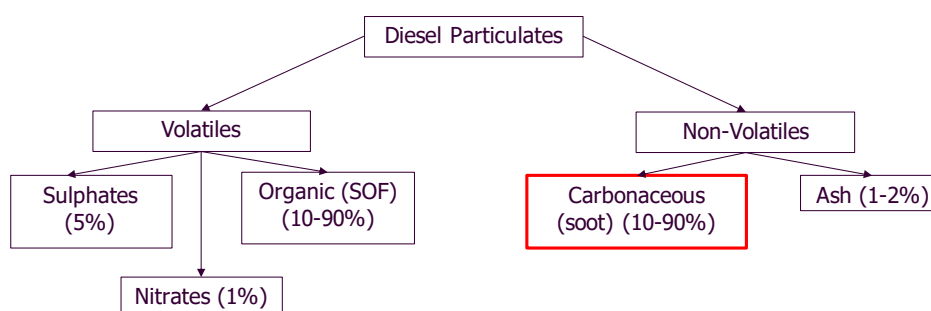


Figure 3: Particle composition. The focus of this study is on the carbonaceous part or soot, being usually the higher fraction of diesel particulates.

1.2.1. Non-volatile particles

Carbonaceous material is the main fraction of non-volatile particles. This part is also known as soot or elemental carbon or black carbon and is branch-like agglomerates with 0.1-10 μm diameter consisting of other spherical particles with 5-50nm diameter. The main aspects that contribute to the production of these agglomerates are combustion chamber temperature above 1900K and places inside the chamber with a fuel-rich mixture. These places are near the injector, where there is not enough space for the mixture process. Also, the low swirling of the incoming air and low fuel injection multiply the fuel-rich regions. The production of the particles starts a few crank angle degrees before the combustion initiation and lasts until the exhaust gas exits the tail pipe. Another important component of the non-volatile particles is the inorganic solid material or ash. The main components of ash are Calcium (Ca), Iron (Fe), Lead (Pb), Zinc (Zn), Manganese (Mn), Nickel (Ni), Vanadium (V) and Aluminium (Al). These elements derived from engine oil additives (for better lubrication characteristics), wear of engine parts such as oil pump, piston rings, camshaft etc., exhaust line processing residues and fuel additives for better fuel properties such as viscosity, cloud point and flashpoint.

1.2.2. Volatile (and semi-volatile) particles

This category comprises the organic fraction, the nitrates, the sulphates and other ions. The organic fraction (or hydrocarbons, HCs) can be further categorised into unburned hydrocarbons, oxygenated hydrocarbons and polycyclic aromatic hydrocarbons (PAH). The primary source for HC is the unburned fuel and the engine oil that has leaked in the combustion chamber. Sulphates (mainly sulfuric acid) and nitrates (mainly nitrate acid) just like hydrocarbons are mostly absorbed by the carbonaceous part. The main source of sulphates is fuel with a high concentration of sulphur (S). Sulphur in fuel and sulphates in emission gases are strongly related. Sulphates concentrations are negligible when ultra-low-sulphur diesel is used. Nowadays, the sulphur concentration in European diesel fuel is below 10 ppm (ultra-low-sulphur), which leads to only small amounts of sulphates in the exhaust pipe.

1.3. Reduction of particulate matter emissions

Historically, the focus was on the reduction of PM owing to the fact that legislation limits were referred only to mass until the European Union (EU) limits included in 2011 (Euro 5b exhaust emission standards) for the first time, the PN limit of 6×10^{11} [p/km] for diesel and recently also for GDI engines (Delphi, 2018). There are three groups of options in which manufacturers rely on to reduce the emissions:

- **Engine design:** Since the introduction of the first emission standards in the 1970s and until the first installation of particulate filters (2000), the focus of the engine manufactures was to improve the combustion and engine design to conform to the latest standards. The engine design includes mainly fuel injection, air induction, combustion and engine cooling.
- **Fuel and lubricants technology:** Fossil fuels have been the dominant source for engines for decades. Alternatives for lower particle's emissions, consumption and cost are considered the Biofuels (1st and 2nd Generation), synthetic fuels, gas to liquid diesel (GTL) etc. and every mixture of the above. These alternatives are quite promising in particulate matter emission reduction. Additionally, unburned lubricating oil can be a significant source of particles. But also, the chemical and physical characteristics of lubricants are important. Viscosity can impact the amount of oil that passes the piston ring and the oil layer that remains in the cylinder surface. The amount of sulphated ash, phosphorus and sulphur (SAPS) can affect the rate of ash accumulated in the aftertreatment devices.
- **Aftertreatment devices:** In this category, the exhaust particulate filters (Diesel Particulate Filter, DPF or Gasoline Particulate Filter, GPF) are the highly efficient

measure to reduce PN/PM emissions. The operating principle of the particulate filters is analysed in the next section. Also, Diesel Oxidation Catalyst (DOC) decreases volatile and semi-volatile particles.

1.4. Aftertreatment devices-Failures of particulate filters

Focusing on the aftertreatment system, nowadays, DPF is the standard equipment for particulate matter reduction in all diesel vehicles. The prognosis is that it will remain an indispensable part of diesel powertrains also in the future. In the heavy-duty sector, the DPF has also been widely implemented, both as equipment fitted by original equipment manufacturers (OEM) as well as in retrofit programs (Future Market Insights, 2019). Also, GPFs are currently introduced to conform to the PN limits for light duty applications (Demuynck et al., 2018), and their adoption is expected to be universal in the future.

The most common design of a particulate filter is the wall-flow monolith. Other designs are metallic foam, ceramic fibres, metal fibre filters and sintered metal filters (DieselNet [8], 2014). Monoliths which were firstly used in catalyst converters, are made of cordierite – a synthetic ceramic composition with very low thermal expansion coefficient and high-temperature resistance with good mechanical strength. Alternative materials for monoliths are silicon carbide with higher temperature resistance but also higher thermal expansion and cost and aluminum titanite which offer low coefficient of thermal expansion and similar durability with the silicon carbide filters. In particulate filters adjacent channels are alternatively plugged at each end, resulting in a wall-flow instead of flow-through in catalysts.

Filtration could be divided into depth filtration and cake filtration. In a clean filter, there is only depth filtration with three mechanisms: diffusion, interception and inertia. In diffusion, aerosol particles due to their random motion in the gas (Brownian movement), deviate from the gas streamlines and are collected by meeting the filter material. In the interception collection mechanism, particles that follow the streamline are collected by coming into contact with the filter material due to the low distance between the particle and the filter material. The larger the aerosol particles, the easier it is for the particles to be collected by inertia. The inertia arises where due to a rapid change in flow angle (such as at the back end of an inlet channel) the particles deviate from their flow line and collide to the material. Therefore, particles are captured inside the wall, and a few percentages of them may pass the wall and exit from the tailpipe. The filtration efficiency in this process is below 90%. When the pores are almost filled with particles, a layer of particles starts to be created on the wall's surface. This 'filtration cake' is now the filtering medium for the next particles with a filtration efficiency of almost 99%.

The captured particles inside the DPF create a pressure drop to the gas flow. If the filter becomes overloaded, this pressure drop could have a significant fuel penalty. To avoid these problems,

manufacturers provide a reliable in most cases regeneration mechanism. Regeneration is the oxidation of carbon particles to gaseous products, mainly to CO_2 . Regeneration of DPFs can occur either actively with fuel injection for temperature increase or passively during high load operation (especially in heavy-duty vehicles). In the case of the GPFs, the exhaust temperature is frequently high enough for passive regeneration during lean operation (e.g. fuel cut-off events) and therefore, no active strategies are currently used.

Regeneration may expose the filter material to very high temperatures, as well as rapid temperature changes. Since the distribution of soot is not necessarily uniform throughout the filter, the thermal stress frequently has a local character. Both high temperature and thermal stress, are responsible for most cases of filter failure, such as melting or cracking. Another reason for reduced filtration efficiency of a filter is the intentional removal of the DPF brick for tampering reasons. All these cases result in a reduced filtration efficiency and the risk of exceedance or violation of the legislative limits. Therefore, to ensure the functionality of the filter, emission regulations require On-Board Diagnostic (OBD) systems to monitor the particulate matter emissions (Kamimoto, 2017). Currently, the limit is based on the particulate mass emissions, as will be discussed in the next section.

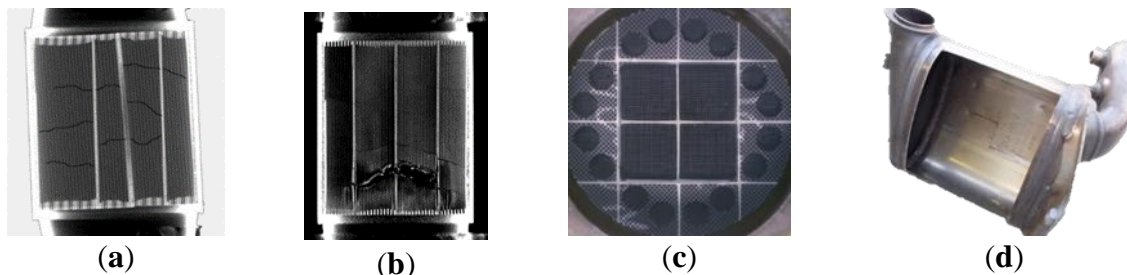


Figure 4. (a) Cracks on DPF substrate (LAT) (b) Melted DPF (LAT) (c) Partial unplugged DPF (LAT) (d) DPF removal (google image)

1.5. OBD systems for DPFs

1.5.1. Introduction to the OBD systems

OBD systems continuously monitor the engine components to make sure that emission limits are not exceeded during the vehicle's lifetime. Starting in California in 1988 from California air resources board (CARB), the first OBD stage (OBD I) required monitoring emission-related electrical components, storage of fault in the electronic control unit (ECU) and activation of a malfunction indicator lamp (MIL). The second OBD stage (OBD II), was introduced again in California in 1994 and in addition to OBD I, the functionality of the sensors was monitored. Furthermore, the fault codes were standardised according to ISO and SAE standards, and it also became mandatory that third-party scan tools could read the stored faults.

Since 1994 considerable changes and revisions took place for OBD II. After the latest updates, monitoring Air to Fuel ratio (A/F) for every cylinder, cold-start strategy and permanent error storage are additionally required for gasoline engines. For light-duty (LD) diesel engines, monitoring of the fuel, air and exhaust-gas systems are also required. For example, in a diesel engine with common rail, exhaust gas recirculation (EGR) and DPF the injected fuel quantity, the injection timing, the EGR response and the filtration efficiency of the DPF must be monitored. Finally, there are revisions under discussion to include more functions to OBD II, such as the CO₂ monitoring and services for hybrid vehicles (HV).

The MIL is an informative indicator which is used when a malfunction occurs in an engine. It is also known as a check engine light (CEL) and is located on the instrument panel of the car. When activated, it is either flashing or in a steady activated status. The first status indicates a severe fault and serious damage could occur in the catalytic converter or other after-treatment devices if the engine does not stop immediately. The latter is used for a minor problem in a sensor or an aftertreatment device, and a visit in an authorised service is mandatory. It is typically in yellow-amber, and its shape is a contour of an engine (Figure 5).



Figure 5: Malfunction indicator lamps (MIL)

Every time the MIL is activated, a fault code (Diagnostic Trouble Code, DTC) is stored in the ECU of the car. This code is different for every fault and could be read from a diagnostic device. For the activation of the MIL, an OBD model is used for the diagnosis of every component. In the next sections, the OBD system for the DPF is analysed along with the corresponding legislation.

1.5.2. The regulatory framework for OBD for particulate filters

Both light and heavy-duty vehicles require the monitoring of the particulate filter against the OBD threshold limit (OTL). This study is performed for LD applications, and therefore, all following sections refer to light-duty applications and especially passenger cars.

Focusing on the European legislation for better guidance through the different levels of PM and PN legislation, three main categories are presented in Table 1. The emission limits with the driving cycle as the core of every regulation for the type-approval of vehicles, the OBD requirements (OTL) for emission control through vehicle's lifetime and the RDE limits as a representative of the real-world operation of every vehicle. Euro 6-2 LD OBD legislation requires the monitoring of the particulate filter to ensure the proper performance of the system (UNECE, 2017). The ultimate requirement is to detect a malfunction of the system before the PM emissions exceed the current limit of 12 mg/km during the

legislative driving cycle and illuminate the MIL. This requirement is valid for compression ignition vehicles and positive ignition with direct injection system (GDI). This limit though is significantly higher than the engine-out emissions of current GDI vehicles. Therefore, this limit has no meaning for positive ignition engines which have high PN but low PM emissions. Currently, there is no PN limit for OBD, but it is included in the list of studies to be performed for the new EU limits, which are now developed (EU, 2018a). Also, the legislation requires only for the compression ignition vehicles, to diagnose the total removal or the complete failure of the DPF. This diagnosis is feasible with the delta-pressure sensor, which is installed in all DPF-equipped vehicles to control the soot load of the filter and the regeneration process.

Table 1: EU legislation limits for the first registration of vehicles (2014-2020)

	9/2015	9/2018	>2020
Emission	Euro 6a, b, NEDC		Euro 6c, d, WLTC
PM	4.5 [mg/km]		4.5 [mg/km]
PN	6×10^{11} [p/km] *		6×10^{11} [p/km]
OBD	OBD Euro 6-1		OBD Euro 6-2
PM	25 [mg/km]		12 [mg/km]**
PN	<i>No limit</i>		<i>No limit</i>
Filter removal	<i>DPF only</i>		<i>DPF only</i>

* 6×10^{12} [p/km] for GDI

** for all compression ignition engines and GDI

Regarding the two biggest automotive markets in the world, China has adopted the same OBD approach and limits as Euro 6-2 with the additional GPF removal requirement, and similarly, the United States regulation controls the PM below 17.5mg/mi with no limit on PN emissions and no practical reason for GPF removal detection as GPF is not required for the current type approval PM limit. All other markets use, as a reference, the EU and US limits to define their legislation. The current legislation needs for the US, China and EU, are summarised in Table 2.

Table 2: Main requirements of current legislation regarding the particulate filters

Requirements	EU-Euro 6-2	China-CN6	US-LEV III
Cycle	NEDC/WLTC	WLTC	FTP-75

PM Emissions	4.5 mg/km	3 mg/km	3 mg/mi
PN Emissions	6×10^{11} [p/km], <i>GDI only</i>	6×10^{11} [p/km], <i>GDI/PFI</i>	<i>No limit</i>
PM RDE	<i>No limit</i>	<i>No limit</i>	<i>Not applied</i>
PN RDE	9×10^{11} [p/km]	12.6×10^{11} [p/km]	<i>Not applied</i>
PM OBD	12 mg/km	12 mg/km	17.5 mg/mi
PN OBD	<i>No limit</i>	<i>No limit</i>	<i>No limit</i>
Filter removal	<i>DPF only</i>	Yes	Yes

Therefore, based on the current limits and the typical emissions of diesel and gasoline LD vehicles in terms of particulate mass, the OBD actual requirements are categorised below:

- **For DPF-equipped cars:**
 - PM < 12 mg/km (EU, CN) and < 17.5 mg/mi (US)
 - Diagnosis of total removal or total failure of DPF
- **For GPF-equipped cars:**
 - Only GPF removal for CN

Based on this analysis, a robust, accurate and precise way must be used to retain the PM emission below the OBD limits for diesel cars. The total removal can be effectively diagnosed by the delta-pressure sensors (paragraph 1.5.3.1), and therefore, no further investigation is needed.

To be in line with the certification procedures for approval of compliance of a vehicle to OBD requirements in both EU and US legislation, the test protocols for vehicle OBD type approval comprise two parts:

- The first part consists of a preconditioning period to stabilise the DPF filtration efficiency which for the EU is one or two consecutive NEDCs (or Worldwide harmonized Light-duty Test Cycle [WLTC]) and for the US one or two Federal Test Procedure (FTP-75), Supplemental Emissions Test (SET) or Unified cycle (an additional preconditioning cycle is possible upon request).
- The second part is the exhaust emission test. This test is a cold cycle, and at least 6h-soaking is needed before its start. Prior the end of the emission test cycle (or before the engine stop for FTP-75 cycle), a vehicle set with the criteria limits for the DPF diagnosis must diagnose the malfunction and illuminate the MIL (Figure 6, Figure 7).

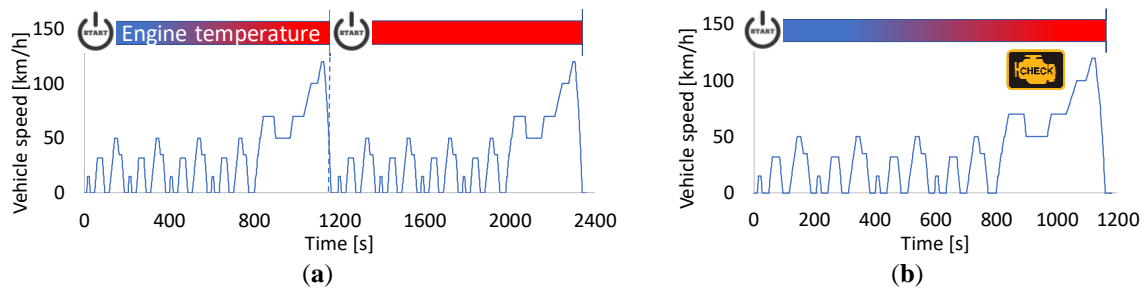


Figure 6. EU OBD legislation (a) First and second preconditioning cycles (b) Emission tests cycle (Example of NEDC)

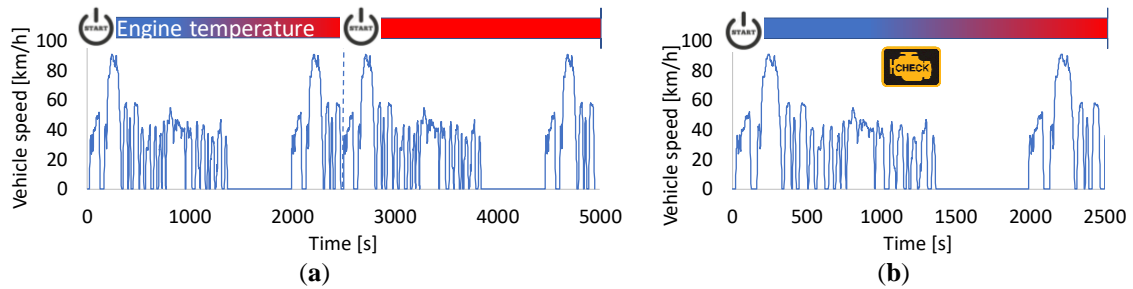


Figure 7. US OBD legislation (a) First and second preconditioning cycles (the second or even more preconditioning cycles can be applied upon request from the manufacturer) (b) Emission tests cycle

1.5.3. Approaches for DPF on-board diagnosis

There are two main approaches for on-board diagnosis of the DPF: monitoring with and without a particulate matter or soot sensor.

1.5.3.1. Monitoring without a particulate matter sensor

A solution that follows this approach is to use an advanced delta-pressure sensor for the DPF. It is feasible to distinguish an intact from a damaged DPF, but there are areas with high uncertainties, DPF needs to be at least partially loaded for diagnosis (not possible after regeneration), and the ash load of the DPF can significantly affect the accuracy (Figure 8). Thus, it can be a solution for specific projects and only for a diagnosis of total DPF removal (Finch et al., 2010).

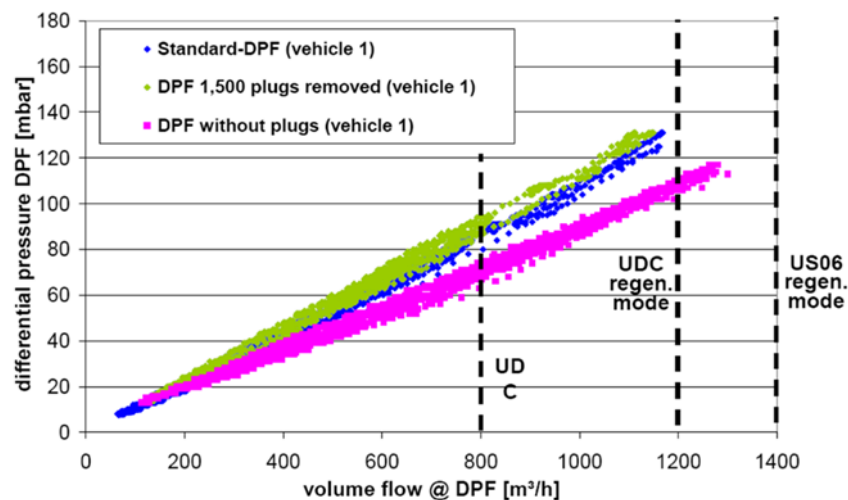


Figure 8: Delta pressure for two damaged and an intact (standard) DPFs (Daimler - ACEA OBD Seminar, January 23, 2008)

Also, another similar solution is the radio frequency sensors which have higher accuracy but are not currently used in the automotive sector. In this technology, the accumulated soot in a DPF absorbs and changes the microwave signal produced by an RF antenna. The correlation of the signal change with the soot accumulation is possible (Sappok et al., 2010). The temperature gradient between the inlet and outlet of the DPF is also used by some manufacturers to identify the total removal of the DPF in coupling with the temperature modelling (Surve, 2008). Finally, in the case of using an SCR coating on the DPF substrate (SDPF or SCRoF), the diagnosis of removal or even partial plugs removal, is feasible with the monitoring of the pre- and post-NO_x emissions.

1.5.3.2. Monitoring with a particulate matter sensor

The current DPF OBD models are based primarily on a particulate matter sensor to conform with the new Euro 6-2 OBD legislation. Currently, the adopted sensor technology from the automotive industry is the resistive soot sensor fitted into the exhaust line downstream of the DPF. These sensors are sensitive to the carbonaceous part of the PM, and the term soot sensor (instead of PM sensor) is used for this study because soot concentration is used as the parameter that mainly affects the sensor signal. PM emissions are used only to characterise the tailpipe emission levels according to the legislation.

Other sensor technologies that could be used for OBD applications are electrostatic or optical sensors which are currently developed for both PM and PN measurements. Thus, they will be applicable to future stringent legislations or schemes such as on-board monitoring (OBM). These sensors will be reviewed and analysed in the last chapter of this study.

1.5.4. Development process of DPF OBD systems

The development of ECU integrated OBD systems follows a few steps which represent the common approach of the automotive industry for such models. This procedure is depicted in Figure 9. As a first step, the concept of the operation is defined. In our case, the idea is to diagnose any malfunction of the DPF by estimating the emissions using a soot sensor. This step is followed by the analysis of the regulation needs, which - in principle - require to keep the emission below the OBD threshold limit. To this aim, the structure of the model and its detailed design are developed. This concept is designed in detail in the Matlab/Simulink® environment, which is the final step of the design section. The next part is the realisation of the idea, which concludes with the operation of the model in the vehicle. As intermediate steps in this section, the software is integrated into the ECU, tested, calibrated and validated under various conditions to ensure a reliable and accurate diagnosis. During the realisation phase, the need for re-designing for a few aspects may arise, and thus, the process must be repeated.

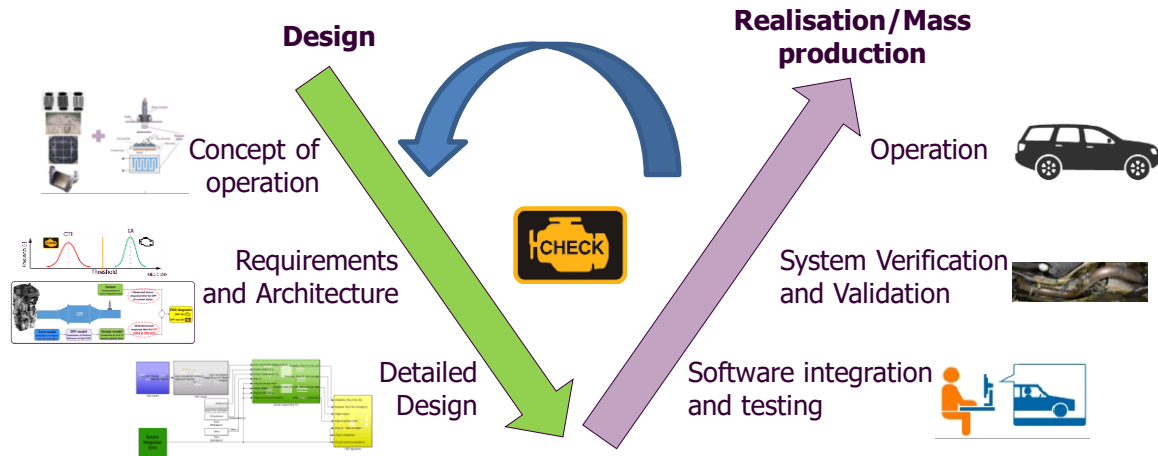


Figure 9: Approach for the development of the OBD model for the DPF. The design and the realisation are the two distinct levels for the final implementation.

1.6. Motivation, objectives, structure and novelty aspects of the thesis

Having analysed the general approach for the development of a DPF OBD system, it is obvious that several tests and calibration procedures are needed for each step. The motivation of this dissertation originated from the scientific and market need to develop and optimise the OBD DPF model focusing on the design phase and aiming to minimise the need for re-designing and applying changes in the architecture. In addition, special effort was applied to develop an optimised resistive soot sensor and investigate the possible sensor solutions for future legislation and market needs.

Several publications investigate the operating principle of the sensor and the parameters that affect and limit its operation. In terms of the overall OBD model, the number of publications is lower, and they provide a general approach to the topic. The signal of the resistive sensor represents the reduction of the resistance between the electrodes. A few studies explain the fundamentals of the operating principle of the sensor. For example, Hagen et al. presented a simple sensor element and some initial results for the response of the sensor (Hagen et al., 2010). Malik et al. also proposed a sensing element based on resistive technology for soot mass determination of an aerosol sample (Malik et al., 2011). A few publications followed about complete resistive sensor modules, ready for automotive applications for OBD purposes and some of them briefly presented the overall OBD model and the necessary models for the diagnosis (Ochs et al., 2010; Weigl et al., 2012; Brunel et al., 2013; Linke et al., 2016). Also, the deposition mechanisms have been investigated. For example, Delphi has developed an electrical model of a resistive sensor independently of the nature of the deposition mechanisms (Husted et al., 2012). Effect of thermophoresis was presented by Nordic Innovation Centre and VOLVO (Malik et al., 2011) and Grob and Schmid (Grob et al., 2012). Electrophoresis was investigated as a dominant parameter that affects particle deposition. Hagen and Müller stated that electrophoresis is the main drive of particle deposition in the case of their examined conductometric soot sensor (Hagen et al., 2014). Teike et al. modelled the deposition due to electrophoresis and validated the dendritic structure

of the soot bridges between the electrodes (Teike et al., 2012). To reduce the response of the sensor, increased electrophoresis via high polarisation voltage was tested, but this approach is limited by internally caused thermophoresis or Joule effect (Hagen et al., 2018; Grondin et al., 2019). Also, to the same aim, Bartscherer and Moos used an additional conductive cover layer (Bartscherer and Moos, 2013). The same approach was also tested by Hagen et al. (Hagen et al., 2016). Finally, Fragkiadoulakis developed a physical model for the simulation of sensor response time using all deposition mechanisms (Fragkiadoulakis et al., 2018).

Even though the available work is recently increasing, the examined approaches are either focusing on the sensor itself or - for those that deal with the overall OBD model - are industry-oriented and are approaching the topic only with an experimental assessment of the proposed solutions. To evaluate the available solutions and go beyond the current approaches, the objectives of the current study are to:

- Suggest and implement innovative approaches for the key-parts of the model and evaluate their effectiveness in DPF diagnosis.
- Investigate requirements and resolve early-raised issues after sensor first installation in pre-production vehicles for improved accuracy and robustness of the resistive sensor and the sensor model.
- Review the solutions for future PN/PM sensing and monitoring according to future requirements.

To achieve these objectives, the study has been organised into six chapters:

- Chapter 1 explains the need to study and control particulate emissions and sets the goal of doctoral research.
- Chapter 2 presents the methodology starting with the necessary equipment used at the various stages of the research. At the same time, the structure of the model is developed, and the way the DPF condition is diagnosed through the OBD Index is explained.
- Chapter 3 focuses on the design phase of the OBD model and provides the details of each sub-model used in the overall OBD model. The various solutions that can be used for each sub-model are presented, the accuracy obtained with each approach and the total error of the diagnosis is calculated considering all individual errors as well as the measurement error introduced by the sensor itself. In addition, ways and approaches of rejecting certain diagnostic events based on specific criteria are developed. Finally, the overall model is implemented offline in an engine test cell to evaluate its accuracy during transient conditions.
- Chapter 4 examines all issues arising from the final application of the diagnostic model and the sensor to a vehicle during the realisation phase. The tasks that were examined comprise

the effect of the supply voltage from the vehicle electrical system on sensor regeneration, the impact of mounting orientation in the exhaust, the point where the sensor and the model should start during cold start operation, the influence of contaminants in the exhaust gas and finally the limits within which the transport function developed is valid.

- Chapter 5 describes the needs of future legislation and the possible solutions. The new requirements that have emerged are presented in conjunction with solutions both at sensor level and at the level of infrastructure required to ensure (proper) operation of anti-pollution systems and to monitor the emissions of each vehicle in circulation.
- Chapter 6 summarises the main conclusions and observations that emerged from this study. Also, suggestions for future research on improving the diagnosis and behaviour of the sensor, and the review of the next generation of sensors and models for future legislation and market requirements are reported. Finally, the performance of an electrostatic sensor is examined as an alternative to resistive soot sensors.

The novelty aspect of the doctoral dissertation is summarised in the following points:

- A complete and detailed OBD model has been developed that incorporates different aspects and approaches for each sub-model and not only the standard approach of the automotive industry. The improvements that can be introduced are evaluated in detail, and the resulting uncertainties are quantified.
- The sensor model and the sensor hardware were further investigated, focusing on defining the limits for accurate diagnosis and resolving issues that emerged during the development phase and the first application on pre-production vehicles.
- The needs and solutions for future legislation on emissions monitoring of each vehicle were explored. Advanced OBD with lower PM limits or additional PN limits will render the resistive sensor insufficient for accurate diagnosis or monitoring. Solutions, including advanced PN/PM sensors, are presented and discussed in terms of their maturity level.

The core of the research and the innovation aspect are documented by peer-reviewed publications to scientific journals and paper published in international conferences:

Journal publications:

- I. **Kontses D.**, Geivanidis S., Fragkiadoulakis P., Samaras Z., “*Uncertainties in model-based diesel particulate filter diagnostics using a soot sensor*”. *Sensors*, 2019, 19, 3141.
- II. **Kontses D.**, Fragkiadoulakis P., Geivanidis S., Samaras Z., “*Performance of a resistive soot sensor physical model in transient vehicle operation*”, Submitted, under review in *Journal of Aerosol Science*, 2019

Conferences proceedings:

- I. **[Full paper] Kontses D.**, Geivanidis S., Samaras Z., “*Challenges and error propagation of PM sensor-based DPF diagnostics*”, Transport Research Arena (TRA), 16-19 April 2018, Vienna, Austria
- II. **[Full paper] Kontses D.**, Geivanidis S., Samaras Z., “*Review of methods for PN/PM estimation for advanced OBD applications*”, 23rd Transport and Air Pollution (TAP) Conference, 15-17 May 2019, Thessaloniki, Greece
- III. **[Presentation] Samaras Z.**, **Kontses D.**, Geivanidis S., “*Challenges of resistive PM sensor-based DPF diagnostics*”, SAE 2017 On-Board Diagnostics Symposium, 27 February – 1 March 2017, Turin, Italy
- IV. **[Presentation] Geivanidis S.**, **Kontses D.**, Fragkiadoulakis P., Samaras Z., “*Operation and implementation of a resistive soot sensor for DPF health diagnostics*”, 6th International Exhaust Emissions Symposium, 14-15 June 2018, BOSMAL, Bielsko-Biala, Poland
- V. **[Poster] Kontses, D.**, Amanatidis, S., Ntziachristos, L., Samaras, Z., Janka, K., Tikkanen, J., “*Application of the Pegasor Particle Sensor PM/PN PEMS on board of a diesel passenger car in real-world operating conditions*”, 9th PEMS International Conference and Workshop, 2014, CERT, Riverside, California

2. Methodology

The core of the study is the development of the OBD model for the diagnosis of the DPF, and the optimisation of the resistive sensor. In the first part of this chapter, the structure and the concept for the OBD model are presented along with the description of the Stoneridge resistive soot sensor.

In terms of testing, the study comprises several measurement campaigns for the development, calibration and validation of the models and the diagnosis with the resistive soot sensors, and some initial measurements with advanced PN/PM sensors. Most of the measurements were performed on the engines and vehicles available in the Laboratory of Applied Thermodynamics. For some calibration steps, a pre-production vehicle with the soot sensor installed as factory equipment was also used. The SEM analyses were performed in an external laboratory. Finally, the Simulink® environment was used for the development of the overall OBD model, and an error propagation analysis quantifies the accuracy of the model.

Briefly, the target of this chapter is to present:

- Details about the resistive sensors that were used in each test
- The structure of the OBD model and a general description of the necessary components
- The methods for creating the DPFs with a reduced filtration efficiency
- The engines, vehicles and their exhaust setups with the equipment that were used for the measurement campaigns
- The error propagation analysis

2.1. Resistive soot sensor and the OBD model for DPF diagnosis

2.1.1. Resistive soot sensor

A resistive soot sensor consists of a sensor probe and the electronic control module (ECM) or sensor control unit (SCU) (Figure 10a) necessary for sensor control and communication with the ECU of a vehicle. This box hosts several functionalities including the operating mode of the sensor, the dew point strategy, the sensor diagnostics, the configuration of the CAN messages to the ECU etc. The probe of a sensor consists of the sensor tip for flow conditioning before it reaches the sensing element (Figure 10c). The element is a ceramic plate from aluminium oxide (Al_2O_3) or zirconium dioxide (ZrO_2) (2 typical material examples according to the patent (Berger et al., 2009)) and is vertically fitted into the

exhaust line (Figure 10b). Two or more Platinum electrodes are mounted on the ceramic plate in a specific distance between them. When the sensor is clean from soot, the electrical resistance between these two electrodes is infinite. The operation of the sensor is separated in two periods (Figure 10d):

- **A-C: accumulation period:** This is the period where soot is accumulated in the clean sensor surface. During this period, the resistance is reduced due to the soot accumulation. The measurement of the resistance is performed indirectly either by measuring the voltage in a steady-current circuit or the current in a steady-voltage circuit. The resistance value is then transformed into the sensor signal depicted in the graph. In general, the resistance value could also be used, but it is preferred to convert it to an equivalent normalised value. As can be seen in Figure 10d, there are two distinct phases:
 - A-B: percolation phase or “deadband” during which the resistance is either infinite or too high (above a specific limit) and unstable to be accurately measured. During this period the signal is set to zero by the ECM, but soot is accumulated on the sensor.
 - B-C: main loading phase. The resistance between the two electrodes is reduced rapidly due to complete soot dendrites built between the electrodes.
- **C-D regeneration period:** The resistance of the sensor is now below a specified limit set by the ECM, and sensor regeneration is triggered. Thus, the accumulated soot is oxidised, and the sensor is ready for the next accumulation period. This resistance limit is calibrated for every sensor generation to ensure the same response time. During the regeneration process, the temperature is high enough to oxidise soot, but simultaneously below a specific threshold to protect the sensor’s material. This process lasts a few minutes, depending on the settings of the ECM.

The critical measurable quantity of a soot sensor is the duration of the sensor’s accumulation period (A-C), which is called “response time” (RT). The accumulation and regenerations periods are named as sensing mode of the sensor. To protect the sensor element from damage and to eliminate measurement discrepancies due to water condensation in the exhaust, the sensor is activated after the temperature in the exhaust reaches a predefined dew point. The selection of this point will be thoroughly analysed in section 4.1. Before the activation point, the sensor is in the preheating mode. During this period, the sensor is heated (e.g. at 100°C) to avoid particle accumulation due to thermophoresis. Also, during DPF regeneration the sensor is not operated (neither preheating nor sensing) and this is called standby mode.

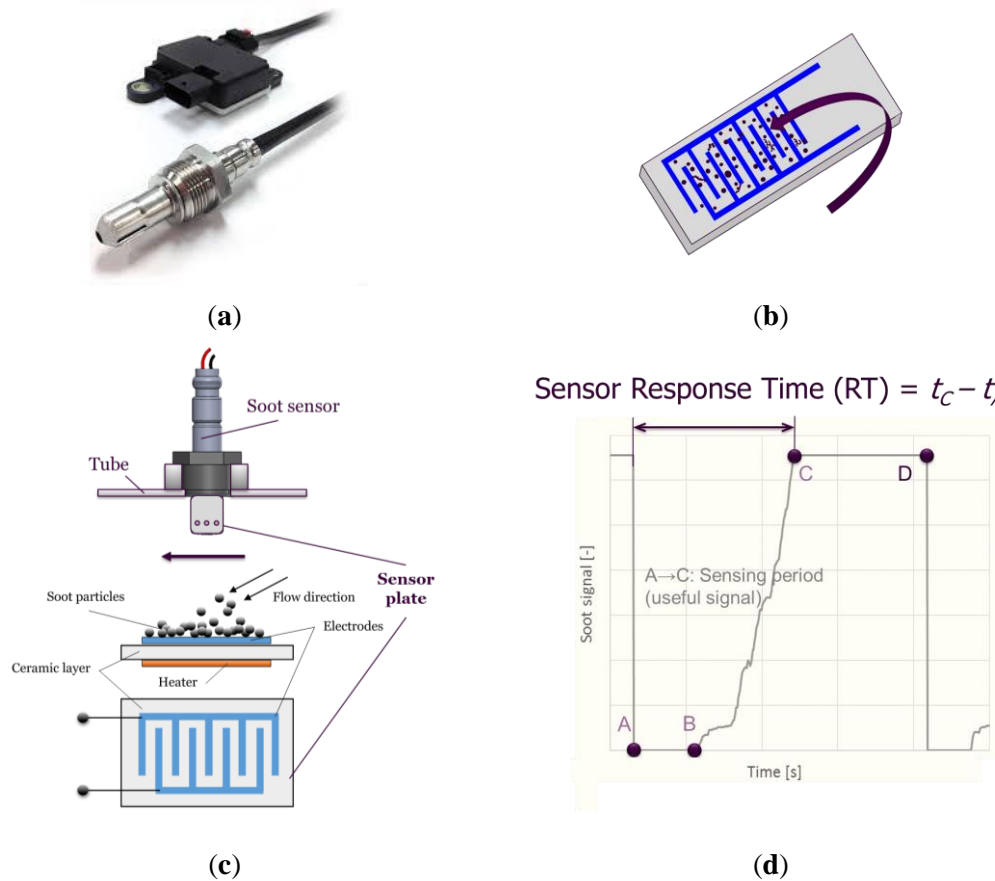


Figure 10: a) ECM with sensor tip b) sensor element (enlarged) c) operating principle and d) response time of the Stoneridge resistive soot sensor.

This study was based on prototype and commercially available soot sensors from Stoneridge Inc. Work on this sensor was initiated by a European project for the technical feasibility of different OBD limits for Euro 6 applications (Samaras et al., 2014a). The details of the different versions of the Stoneridge sensors (both in terms of hardware and software) can be found in two patents by Hedayat et al. (Hedayat et al., 2012, 2017). During the 4-year research with soot sensor within this thesis, several different versions of sensor hardware and software were tested. Also, many tests comprised comparisons of different sensor tip geometries, sensor packaging or software for better sensor management and protection from contaminants. Table 3 summarises the various sensors that were used for each test as it will be described in the following chapters. Briefly, the sensor tip was improved for better protection against water and ash contaminants, and the element change was induced by the tip improvements. The ECM changed according to the requirements of the light-duty and heavy-duty customers and did not affect the sensor operation. The improvements on the sensor body were necessary for better sensor durability and to accommodate additional sealing elements. Finally, the protection mode is a software improvement for ash protection. Gen6 sensors are currently developed for better protection to exhaust contaminants. The results of these investigations are not finalised yet and thus, they are not included in this study.

Table 3: Summary of the differences among the various sensor generations used for the study (HW: hardware, SW: software). Gen5 sensors were the most widely used in this thesis.


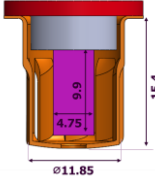


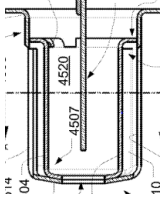
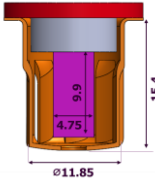


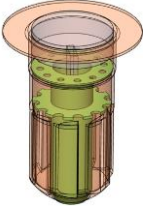
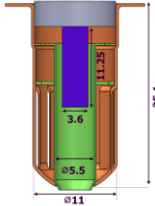


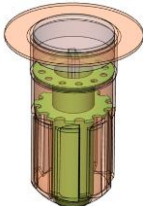
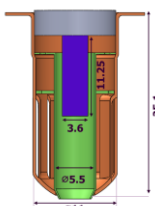


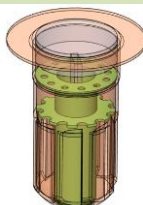
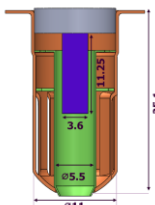


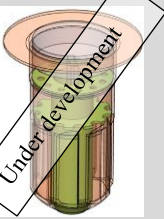
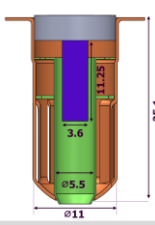


	HW-Tip	HW-Element	HW-ECM	HW-Sensor body	SW-Protection mode	Improvements
Gen1					P1	<i>Default</i>
Gen2					P1	HW-Tip: <i>Dual tip (initial design)</i>
Gen3					P1	HW-Tip and sensor body: <i>Dual tip design</i>
Gen4					P2	SW: Protection mode: <i>Improved ash protection</i>
Gen5 (current gen.)					P2	HW-Sensor body and ECM: <i>Additional internal sealing</i>
Gen6 (not tested yet)					P3	HW-Tip and SW-Protection mode: <i>Improved protection from exhaust contaminants</i>

Table 4: Summary of the sensor generations used in this work

Experiments	Chapter	Gen1	Gen2	Gen3	Gen4	Gen5	Gen6
Soot model	3.1					✓	Under development
DPF model	3.2					✓	
Sensor model	3.3				✓	✓	
Sensor response	3.4					✓	
Overall OBD Model	3.5					✓	
Sensor optimisation	4	✓	✓	✓	✓	✓	
Sensor model optimisation	4.1					✓	

2.1.2. The architecture of the OBD model

The aforementioned resistive soot sensor is part of an OBD model for the diagnosis of the DPF. The concept of the OBD model is to check if due to a DPF failure, the actual PM emissions of the vehicle are higher than the OBD threshold limit emissions (12 mg/km over NEDC). The legislation requires to perform this check for the evaluation of the effectiveness of the DPF over a legislative driving cycle. Emissions higher than the OBD threshold limit should turn on the MIL.

The diagnosis is achieved by comparing the actual sensor response time reported by the sensor (1st branch in Figure 11b) with the simulated response time when the PM emissions are at the OBD threshold limit (2nd branch):

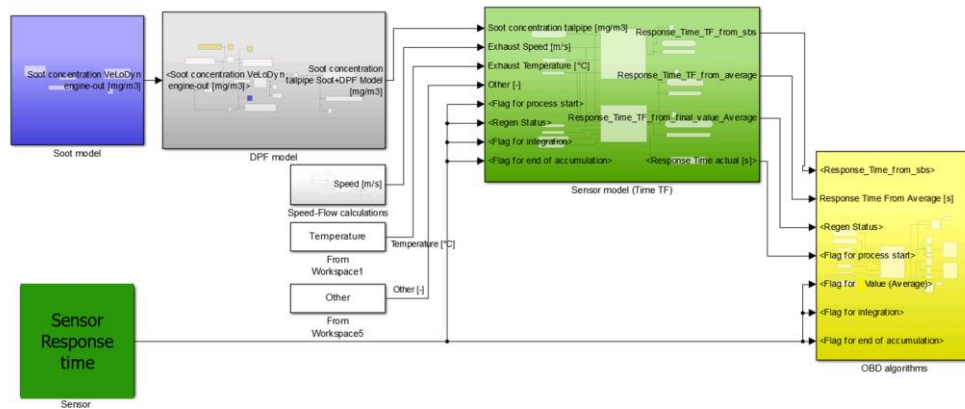
- Higher measured response time means lower than the OBD threshold limit emissions (DPF OK)
- Lower measured response time indicates higher than the OBD threshold limit emissions (DPF not OK)

The model was built in Matlab/Simulink (version 8.4, R2014b) (Figure 11a), and its architecture will be presented in this section (parts of the Matlab/Simulink model are shown in Appendix D). Also, for each sub-model, the different approaches will be described. The OBD model, as illustrated in Figure 11b, consists of the signal of the soot sensor (Sensor box), the OBD algorithms (Diagnosis) which execute the final DPF diagnosis and three sub-models:

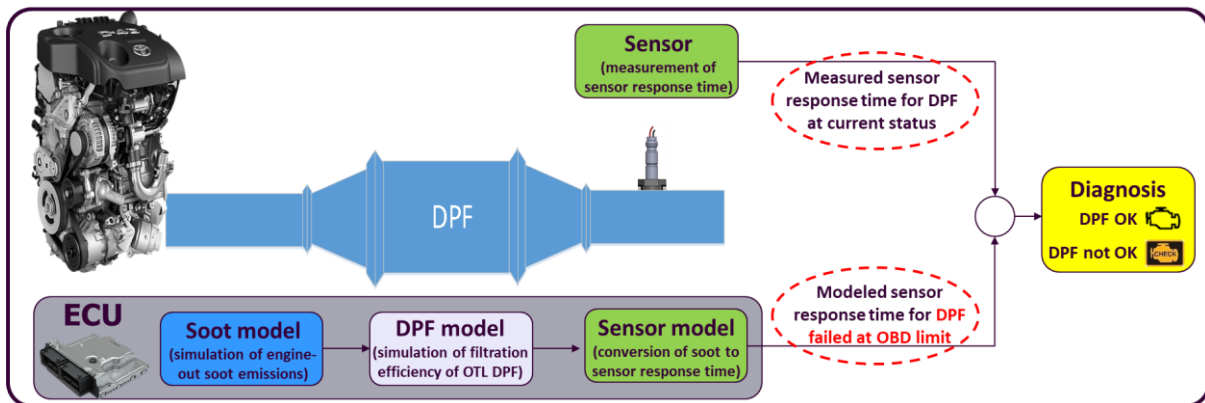
- **Soot model:** This model simulates the engine-out soot emissions produced as a function of variables available in the ECU. For OBD applications, a map-based model using the engine

speed and torque as inputs is the default approach offering adequate accuracy with low computational demands. For improved performance and accuracy, the steady-state base map can be corrected for transient operation.

- **DPF model:** The DPF model calculates the filtration efficiency of a DPF failed at the threshold limit and produces the DPF-out soot emissions to be used as input to the sensor model. The standard practice for simple DPF models is to use a constant filtration efficiency calculated based on measurement of soot concentration upstream and downstream of an OTL DPF (failed at the OBD limit=12 mg/km during the NEDC). A common practice is to perform these measurements also for a TA DPF (failed at the TA limit=4.5 mg/km during the NEDC). An example of an alternative advanced DPF filtration efficiency model is the Exothermia/Axisuite partial unplugged DPF model, which was also used in the current study.
- **Sensor model:** The sensor model calculates the response time of the sensor for given exhaust conditions. This is usually done with a statistical model. A physical model, as presented by Fragkiadoulakis (2018), can be used as an alternative approach to the statistical model.



(a)



(b)

Figure 11. Overview of the OBD model developed in Matlab/Simulink[®]

The direct comparison of the measured and modelled response times at the end of a sensor accumulation period is the simplest method as described above but requires full sensor accumulation periods which can take several minutes for a slightly damaged DPF. An indirect comparison though at every time step can increase the frequency of detection. In this case, the OBD Index is calculated at every time step (usually $dt=1s$) as:

$$\text{OBD Index}(t) = \int_0^{RT} \frac{1}{\tau(t)} * dt \quad (1)$$

where,

RT= measured Response Time (RT) (input from the sensor, 1st branch in Figure 11b)

$\tau(t)$ =Estimated Response Time at time t during the sensor loading (input from the sub-models, 2nd branch in Figure 11b)

For an OTL DPF (12 mg/km over NEDC) an “ideal” OBD model and an accurate sensor yield an OBD index=1 at the end of sensor accumulation and the DPF should be diagnosed as not OK. In summary for all emission levels during an NEDC:

- $\geq 12 \text{ mg/km} \rightarrow \text{OBD Index} \leq 1 \rightarrow \text{DPF not OK}$
- $< 12 \text{ mg/km} \rightarrow \text{OBD Index} > 1 \rightarrow \text{DPF OK}$

It is important to keep in mind that for the commercial application of the OBD model in case of “DPF OK”, the sensor regeneration is triggered immediately after the OBD Index reaches >1 value because the period after this point is not useful. This strategy allows for additional diagnostic events in the limited available time of one legislative cycle. In our study, sensors were not triggered to regeneration regardless of the diagnosis in order to be able to adjust the threshold offline after the execution of the test and perform the sensitivity analyses. Nevertheless, to avoid excessive loading times with high filtration DPFs (e.g. tests with full DPF), sensors were triggered to regeneration after 1800 seconds which is the duration of the WLTC during which at least one diagnostic event should be performed.

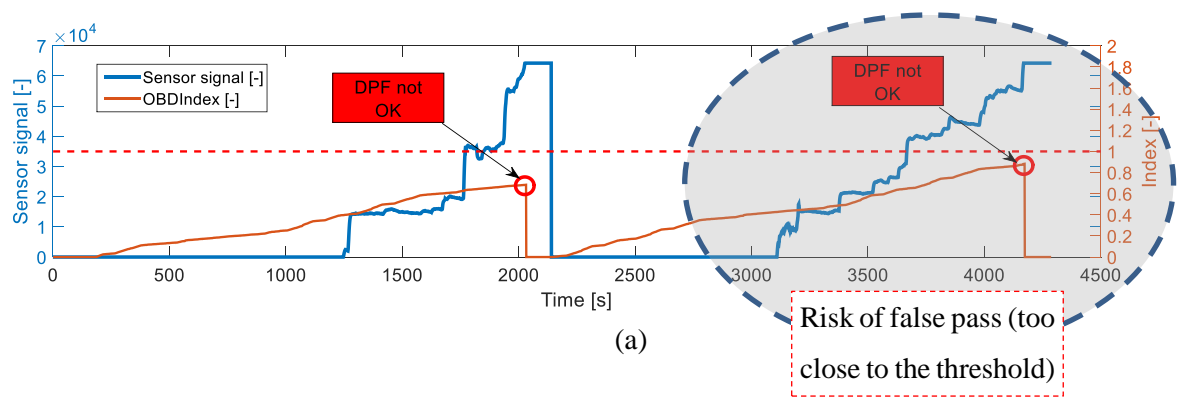
2.1.3. Definition of threshold in real conditions

The main issue with the OBD model though, is that a safety margin around the OTL (12 mg/km) is needed to compromise the uncertainties, to eliminate false passes and to ensure robust diagnosis in all conditions in a vehicle implementation. During real-world operation, it is possible that a DPF failed at levels leading to emissions above the OTL (e.g. exceedance of 1 mg/km) leads to OBD Index > 1 and thus, not being correctly diagnosed. This may appear during real-world operation due to sensor or model being faced with rare but possible operating conditions that were not predicted during model setup. This

situation though is not acceptable since, according to the legislation, no false pass (error of omission, type II error) is allowed. Therefore, detection should be designed to be performed against a threshold lower than the OBD threshold limit of the legislation, to serve as a safety margin, ensuring no error of omission under any operating conditions. This level is commonly set between a high limit (the OTL=12 mg/km) and a low limit (the TA limit=4.5 mg/km). According to the legislation needs, the low limit should have been the emission of a fully operational DPF (≈ 0 mg/km). The reason for selecting a higher limit is to minimise the number of false failures (error of commission, type I error) because this would lead to unnecessary costs for technical inspection and customers complaints. Therefore, the threshold should also be as close to the OBD threshold limit (12 mg/km) as possible. To this aim, a compromise between the two design competing targets is necessary for real-world applications, and the model and the efficiency need to be calibrated with respect to this requirement. The final threshold emissions should be as close to the OTL as possible according to the above theory (e.g. 10 mg/km). To adjust this limit, usually, the threshold filtration efficiency of the DPF model is calibrated. Therefore, a threshold value (either for the OBD Index or the emission level) is calculated, and the diagnosis is performed with respect to this limit.

- Tested emissions \geq threshold emissions \rightarrow OBD Index $\leq 1 \rightarrow$ DPF not OK
- Tested emissions $<$ threshold emissions \rightarrow OBD Index $> 1 \rightarrow$ DPF OK

Figure 12 illustrates two examples of successful diagnoses during transient operations with artificially destroyed DPFs above and below the OTL (13 mg/km and 6mg/km, respectively). The threshold was set at 12 mg/km. The diagnosis is correct in all cases, but it is obvious that there is the risk of false pass event in the second repetition of the above OTL DPF. For this reason, the selection of threshold emissions below the OTL is necessary.



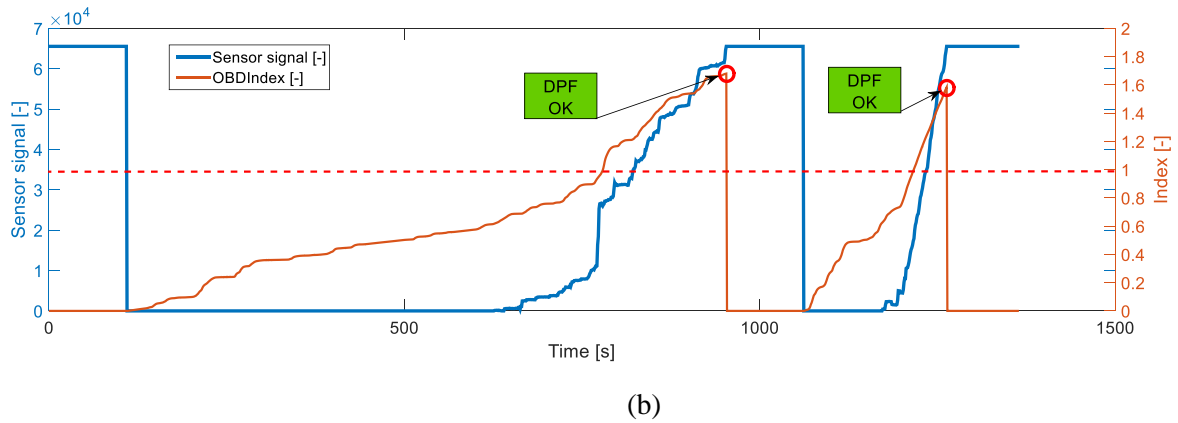


Figure 12. Example of OBD index and sensor signal across a transient operation for (a) an above the OTL DPF where both sensor accumulation periods result in a correct diagnosis of DPF not OK (b) a below the OTL DPF where both sensor accumulation periods result in the correct diagnosis of a DPF OK.

For setting up the model presented in this analysis, one should execute the following steps:

- Develop and calibrate the soot, DPF and sensor models for best correlation with reference measured emissions, filtration efficiencies and response times, respectively.
- Measure the sensor response times for the OTL and TA DPFs on different legislative driving cycles on the test bench and real driving conditions.
- Calculate the OBD Indexes for all sensor accumulations using the filtration efficiency for 12 mg/km over NEDC and create the distributions of the probabilities (Figure 13).
- Calculate the threshold Index, which allows minimum errors of type I and II (Figure 13). According to the needs of each calibration campaign, the threshold can be moved towards the direction of zeroing either the type I or type II error. In most cases, the priority is to ensure zero type II errors (legislation need), and thus, the Index threshold is moved towards lower values.
- Calibrate the threshold filtration efficiency, which brings the threshold OBD Index to 1. This step is not necessary for the case of the constant filtration efficiency but provides a better overview and understanding of the concept. Based on this threshold filtration efficiency, the threshold emissions on NEDC can also be calculated as a final reference value.

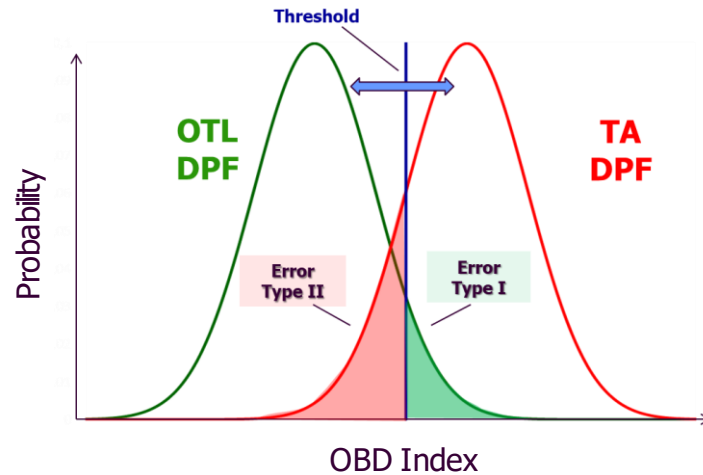


Figure 13. Definition of threshold OBD Index, and type I and II errors as derived from the measurements of an OTL and a TA DPF. The target is to find a compromise between low Type I and Type II errors.

2.1.4. Necessary conditions to start the DPF diagnosis

A successful diagnosis using the above OBD model requires respect at a few necessary entry conditions related both with the sensor but also with the overall engine and exhaust system:

- **Status of the sensor:** Before the execution of the diagnosis, the sensor must be totally clean from soot. To this aim, a sensor regeneration is performed before the first sensor accumulation after every key-on. This will oxidise the remaining soot from previous operation.
- **Dew point:** The sensor regeneration increases the temperature of the sensor element to 700-800°C. In the case of low exhaust gas temperature, water condensates can reach the hot sensor element and create cracks due to a thermal gradient. Also, after the regeneration and during the sensing mode, water condensates can create a bias on the sensor signal due to the high conductivity of water, which can lead to a decrease of the resistance between the electrodes. To avoid these issues, the first sensor regeneration is activated after a specific (calibratable) exhaust gas temperature which is usually called dew point and is the point after which there are no condensates in the exhaust (e.g. 120°C). This may not be a temperature level, but a calculation of gas enthalpy that has passed through the sensor. Currently, dew point-free oxygen sensors have been developed using a two-layer sensing element (NGK/NTK, 2019). This approach should also be investigated for the soot sensors to resolve this issue.
- **Active DPF regeneration and DPF load:** During DPF regeneration, both particle concentration and composition differ compared to regular operation (Dwyer et al., 2010). Also, a clean filter has significantly lower filtration efficiency than a loaded filter due to the absence of soot cake. These can lead to the wrong diagnosis of a functional DPF, and therefore, DPF diagnosis is deactivated during DPF regeneration and for a specific small

duration after the regeneration. Alternatively, a minimum soot load calculated by the ECU after the last DPF regeneration can be introduced. Most importantly, for the case of an artificially failed DPF, which is used during the homologation, the emissions are reducing with increased soot load after the soot cake formation period. Therefore, for the homologation procedure, preconditioning cycles are allowed after the DPF regeneration to sufficiently load the DPF and stabilise the emissions for consistent results among different driving patterns. These preconditioning cycles are usually one or two driving cycles, but additional cycles can be used upon request (UNECE, 2015).

- **Legislation limits for ambient conditions:** The OBD system can be disabled when engine starting temperature is below 266 K (-7 °C), or the vehicle is at elevations over 2,500 metres above sea level.

2.2. Testing and measurement campaigns

The development, calibration and validation of the sub-models and the overall OBD model require targeted testing campaigns both in laboratory but also in real-driving conditions. The engines, vehicles, equipment and set-up that were used in the different sections of this study are presented in the following paragraphs.

2.2.1. Engines and vehicles details

The characteristics of the engines and the vehicles that were used for this study are summarised in Table 5 and Table 6. We should clarify that the access on vehicle #3 was limited because it was a pre-production vehicle located in an automotive manufacturer in Europe. All modifications and measurements for this vehicle were performed by the manufacturer, and for this study, we used only data provided by Stoneridge.

Table 5: Engines used for the measurements

	Engine #1	Engine #2
Engine	Daimler 2.2 OM646	Toyota 1.4 1 ND
Fuel	Diesel	Diesel
Displacement [cc]	2148	1364
Fuel injection system	Common Rail, DI	Common Rail, DI
Max Power [kW/rpm]	110/4200	66/3800
Max Torque [Nm/rpm]	330/2100	205/1400-2800
Cylinders	4	4
Emission standards	Euro 4	Euro 6

Table 6: Vehicles used for the measurements

	Vehicle #1	Vehicle #2	Vehicle #3
Vehicle/Engine	Honda Accord 2.2 L i-CTDi	Peugeot 308 1.6 L HDi	N/A 2.2 L
Fuel	Diesel	Diesel	Diesel
Displacement [cc]	2204	1560	N/A
Fuel injection system	Common Rail, DI	Common Rail, DI	Common Rail, DI
Max Power [kW/rpm]	103/4000	88/3500	N/A
Max Torque [Nm/rpm]	340/2000	300/1750	N/A
Cylinders	4	4	4
Gearbox	6-speed	6-speed	6-speed
Emission standards	Euro 4	Euro 6b	Euro 6d Temp*

* Not officially type-approved, pre-production vehicle

For all applications, modifications of the exhaust lines were necessary to install the sensors and the measuring devices. Both engines shared the same exhaust aftertreatment architecture for the steady-state measurements to avoid bias of the aftertreatment when the same sensors were tested in both engines. The target application of the sensor is on vehicles equipped with NO_x aftertreatment devices (SCR, LNT, or combination of these systems) to conform with the strict NO_x legislation limits. Also, sensors are usually installed after these devices, and thus, the NO_x emissions will be low at the sensor location. To replicate these conditions, an LNT or SCR system was always installed upstream of the sensors as it is illustrated in Figure 14a and Figure 14b, respectively.

In detail, the steady-state setup consists of a Diesel Oxidation Catalyst (DOC), a Selective Catalyst Reduction (SCR) system for NO_x reduction and artificially failed DPFs for the control of particulate matter emissions. For the SCR, gaseous NH₃ was injected via uniformly arranged in the exhaust line spray elements, and the quantity was controlled by a mass flow controller (MFC) (Figure 14b). The NO_x emissions control during the transient measurements was performed by the original NO_x aftertreatment setup of the Toyota engine, which is a Lean NO_x trap (LNT) (Figure 14a). NO_x emissions for both configurations were measured before the sensor location via NO_x sensors. The measurement of the soot emissions was performed by the AVL Micro Soot Sensor (MSS), and for the steady-state tests only, the AVL Smoke Meter was additionally used to validate the repeatability in terms of soot emissions of the setup over a pre-defined reference point. For the tests which required the measurement of gaseous emissions (e.g. NH₃ tests), gas analysers were installed at the end of the tailpipe.

The engine parameters were controlled via the INCA software and temperature, and pressure values for the inlet and outlet of all exhaust devices were recorded by the ETAS ES650 hardware.

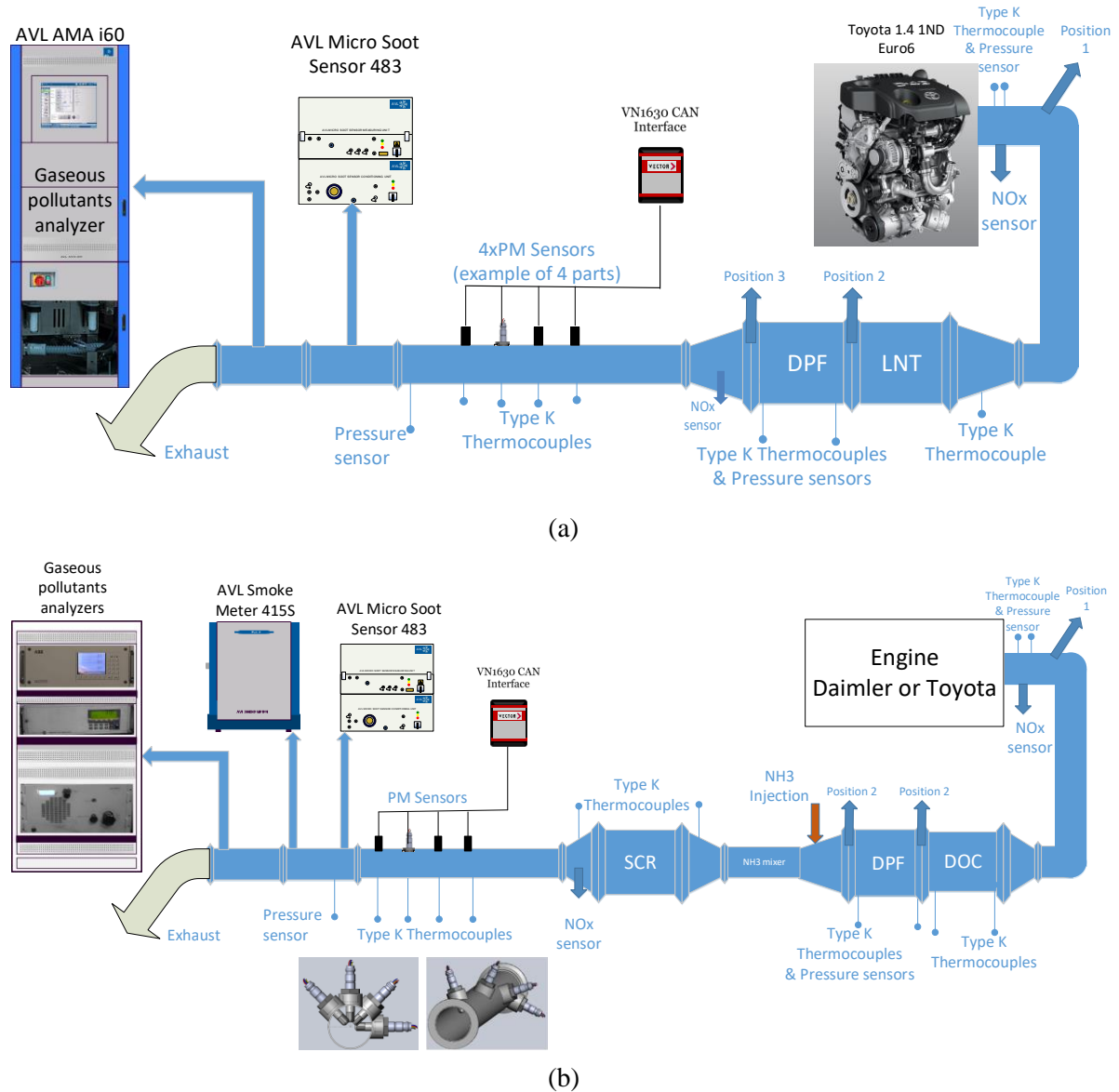
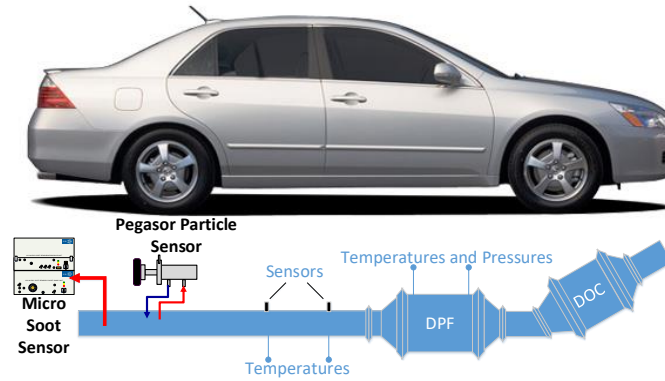


Figure 14: Exhaust setup for (a) Toyota engine for transient measurements (b) Toyota and Daimler engines for steady-state measurements

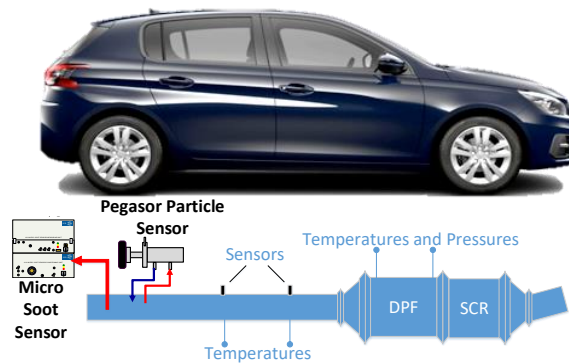
The exhaust setup of each vehicle was different due to the different emission standards and the different solutions adopted by the manufacturers to comply with the legislation limits. The Honda vehicle was originally equipped with a close-coupled DOC and an underfloor DOC which was replaced by the artificially failed DPF (Figure 15a). There was no DPF regeneration functionality for this vehicle, and thus the DPF was removed from the vehicle and regenerated regularly (also based on the threshold for the pressure drop through the DPF) in an engine bench. The Peugeot vehicle was originally equipped with an SCR catalyst followed by a DPF which was replaced by artificially failed DPFs (Figure 15b). Vehicle #3 was fitted with a close-coupled DOC and DPF, which was again replaced by a failed DPF and an underfloor SCR catalyst (Figure 15c).

Sensors were installed downstream of all aftertreatment devices. The exact installation point was selected to ensure adequate mixing of the exhaust gas after the unplugged DPFs and avoid the bends

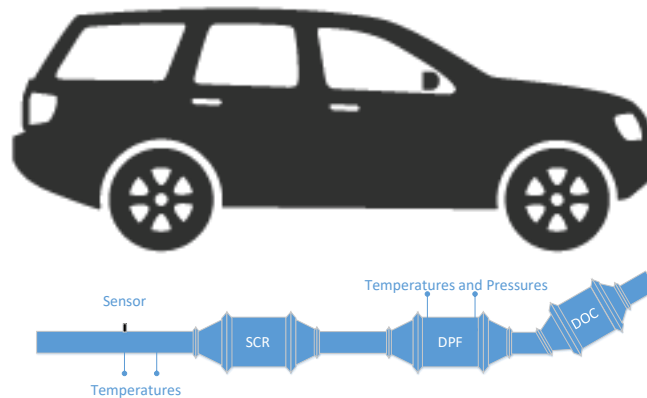
of the exhaust line. The soot concentration was measured with an MSS during the in-laboratory measurements over legislative transient cycles or with the Pegasor Particle Sensor (PPS) during the on-road measurements. This change was necessary due to the high technical requirements and demands of the MSS, which makes the on-road measurements impossible. Also, there was no soot measurement for the tests with vehicle #3.



(a)



(b)



(c)

Figure 15. Schematic of the exhaust set-up for in-laboratory and on-road measurements of a) Honda Accord vehicle b) Peugeot 308 vehicle c) vehicle #3.

The Daimler engine was mainly used for the sensor model development and the cross sensitivities tests. Toyota engine was selected for transient measurements of legislative driving cycles and replicated real-world driving conditions. Also, it was used for the development of the overall OBD model and the error propagation analysis.

The vehicles were used for the realisation of the concept, the validation and verification of the system and the collection of real driving data for the calibration of the OBD model and the optimisation of the sensor. Table 7 summarises the usage of each engine and vehicle in the current study.

Table 7: Overview of engine and vehicle used for every section of the study

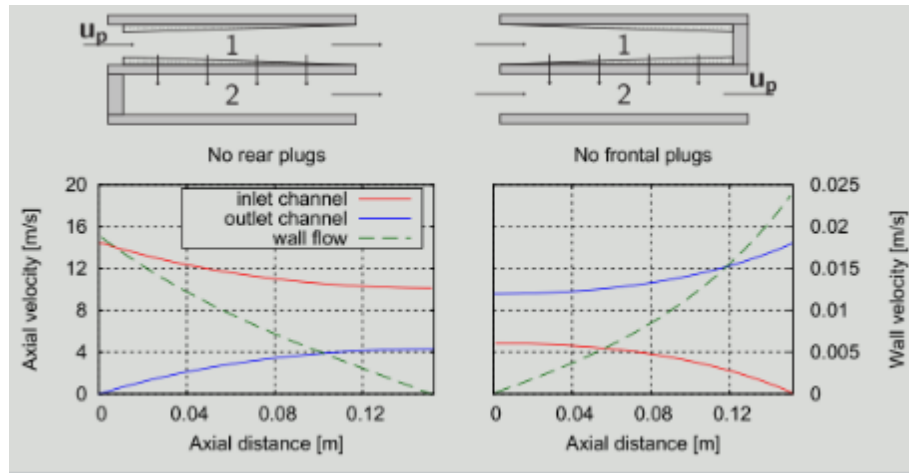
Experiments	Chapter	Engine #1, Daimler	Engine #2, Toyota	Vehicle #1, Honda	Vehicle #2, Peugeot	Vehicle #3, N/A
Soot model	3.1		✓			
DPF model	3.2		✓			
Sensor model	3.3		✓	✓	✓	
Sensor response	3.4		✓			
Overall OBD Model	3.5		✓			
Resistive sensor optimisation	4	✓				✓
Sensor model optimization	4.1	✓	✓			
Advanced OBD	5		✓			

2.2.2. Artificially failed DPFs

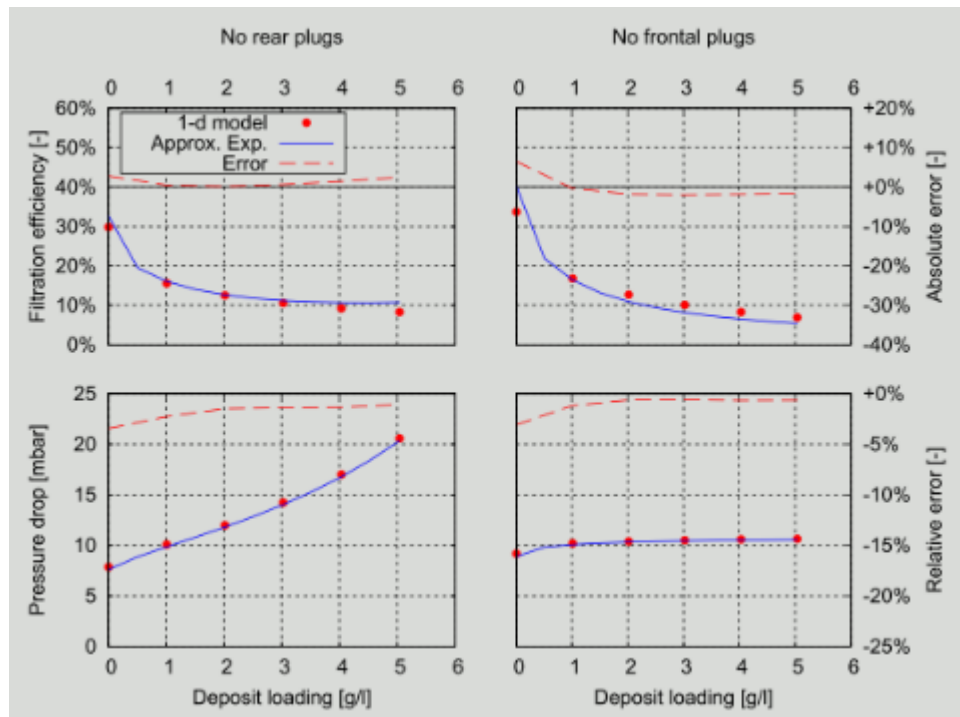
For most of the tests with the soot sensors, artificially failed DPFs were installed in the exhaust setups to adjust the soot emissions. There are four main approaches for reducing the filtration efficiency of a DPF:

- **Plug removal (front or rear):** In this technique, channel plugs are removed via milling either from the front or the rear of the DPF to create free paths for the exhaust gas. The number of removed plugs is correlated with the filtration efficiency of the DPF, and it is a common approach to uniformly and symmetrically remove plugs on the surface to obtain almost linear correlation (Figure 17a). It is worth mentioning that the front and rear plug removal techniques are different in terms of pressure drop and filtration efficiency evolution from a clean to a loaded filter. Simulation and measured data in Figure 16 illustrate these differences. The removal of outlet plugs can be considered more representative of the real

failures that may occur in a DPF: melting or cracks are usually towards the outlet of the DPF. Therefore, for this study, plugs were removed from the outlet of the DPF.



(a)



(b)

Figure 16: Differences between the rear and front plug removal technique (Haralampous and Kontzias, 2014) on a) axial and wall velocities and resulting soot cake pattern b) filtration efficiency and pressure drop.

- **Through holes:** This technique creates through holes in the filter and allows for free paths for the exhaust gas. This is the easiest method to simulate failed DPF, but the sensitivity is high, and it is challenging to achieve the desired levels (Figure 17c).
- **Bypass of the DPF:** In this implementation, a by-pass branch is created, which is controlled by an exhaust flap to regulate the filtration efficiency of the system. This technique is very

effective when the filtration efficiency needs to be continuously variable, but it is hard to implement it in a vehicle due to space constraints and the required modifications (Figure 17d).

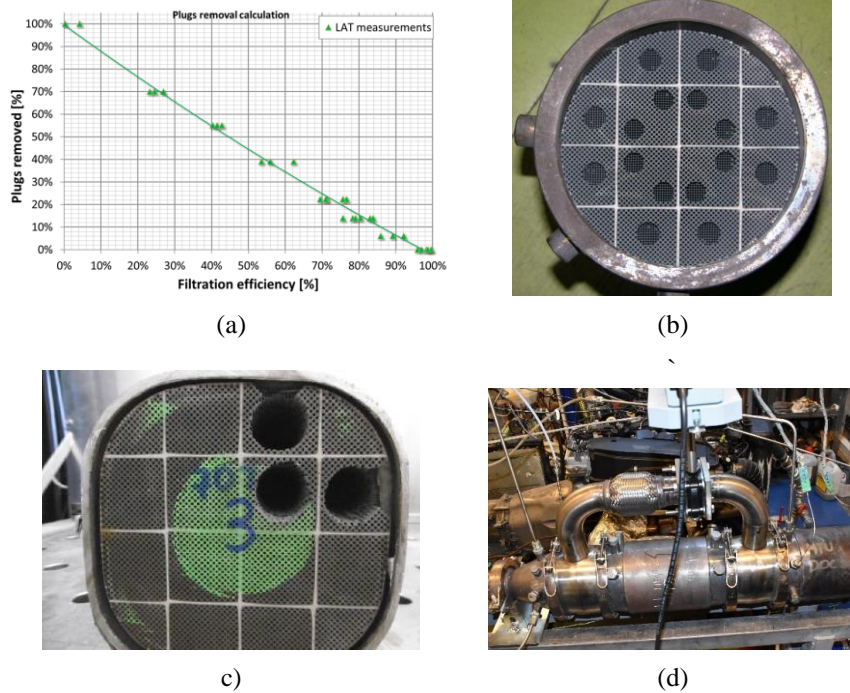


Figure 17: (a) Correlation between filtration efficiency and percentage of removed plugs (example for the removal of outlet plugs only) (b) Example of DPF removed plugs (c) Through holes in a DPF for failure simulation (d) Bypass of the DPF for controlling filtration efficiency

- **Ring-off cracks:** The last approach is to create ring-off cracks in the substrate by drop-to-idle of a heavily loaded DPF. The DPF inlet temperature is increased based on fuel post-injection, the oxidation initiates and the engine is dropped to idle to minimise flow and increase O₂ concentration. Very high temperatures are recorded inside the DPF due to uncontrolled regeneration and high thermal stresses are developed which lead to internal or ring-off cracks (Figure 18).

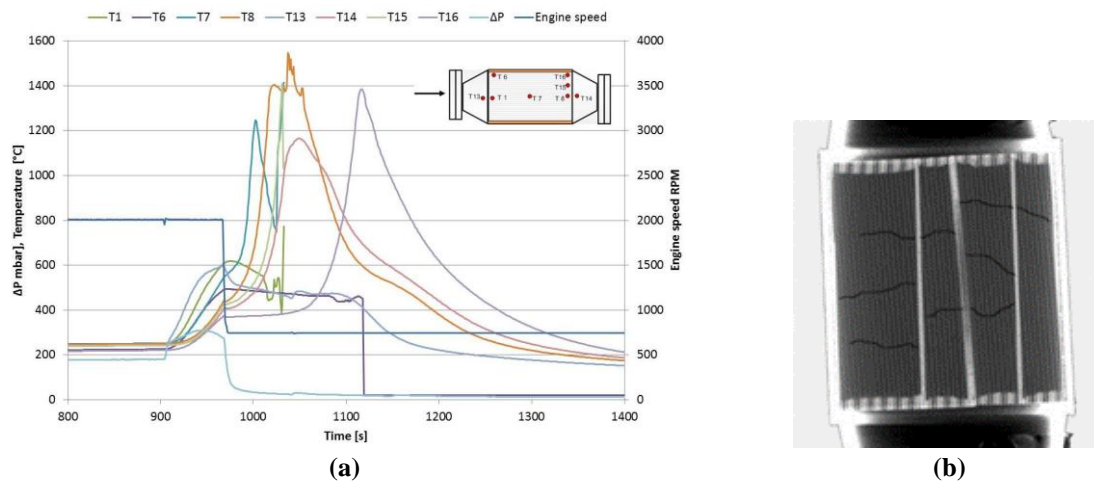


Figure 18: a) drop to idle technique for DPF cracking b) cracks on DPF (tomography)

For the needs of the current study, several DPFs were created based on the plug-removal technique. Especially for the development and validation of the OBD model, two levels were designed for each tested engine and vehicle (the discussion for the selection of these levels can be found in paragraph 2.1.3):

- “OTL DPF”: PM emissions on cold NEDC at the OBD threshold limit (OTL) = 12 mg/km
- “TA DPF”: PM emissions on cold NEDC at the type approval (TA) limit = 4.5 mg/km

2.2.3. AVL Micro Soot Sensor

The AVL Micro Soot Sensor (MSS) was the reference instrument for measuring the soot mass concentration of the exhaust aerosol during the in-laboratory tests. It is based on the photo-acoustic principle. Modulated light produced by an infrared laser source is absorbed by the airborne soot sample. This is thermally expanded thus creating acoustic waves which are detected by a microphone. Through calibration, the instrument can deliver the soot mass concentration. The MSS was installed in the tailpipe using a pressure and temperature reduction probe and heating line to avoid exhaust condensation. The dilution ratio of the MSS is an important parameter for the accuracy of the measurement, and it was set to the lowest possible value for each test according to the emission levels.

2.2.4. Pegasor Particle Sensor

The Pegasor Soot Sensor was used for the measurement of soot emissions during the on-road measurements. Its operation is based on the measurement of the electrical charge carried by pre-charged particles (Pegasor, 2014). A sample of the exhaust gas is pumped using negative pressure generated by filtered motive airflow in an ejector, built-in sensor's construction (Ntziachristos et al., 2013). A corona discharger has already ionised the filtered air. Afterwards, it is mixed with the particle-containing gas, and according to their size, particles are effectively ionised with different load. An ion trap removes the non-attached ions as their electric mobility is higher than the ionised particles. Detecting and measuring the escaping current of the flow results in the number and the mass flow concentration (Figure 19). PPS advantages are its compact design compared to other PN/PM sensor, its high resolution and sensitivity (10 Hz, 0.3 seconds response time) and the fact that particles are not collected but only pass through the sensor.

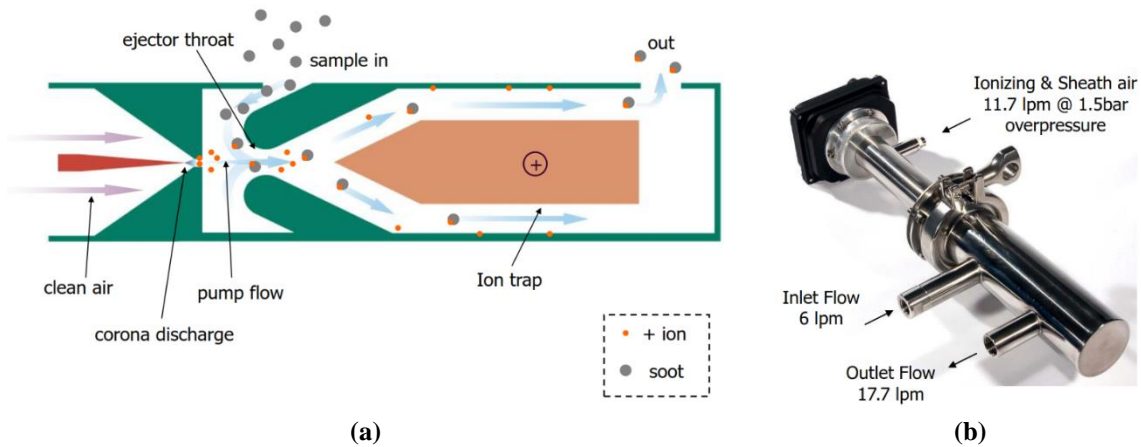


Figure 19: (a) Pegasor Particle Sensor operating principle (b) Measuring unit

The main parts of PPS installation in the vehicles are:

- Measuring unit (Figure 19b)
- Heated inlet pipe with heater controller
- Air supply unit
- Air pressure regulator
- Power equipment (12DC / 230 AC Inverter)

Heater on inlet pipe ensures that no condensation of the exhaust gas will occur until it reaches the sensor body. Internal sensor heater is pre-set at 200°C. There is also a control unit for the heater, which can be adjusted to a specific desired temperature. During on-road measurements, the heater was in the pre-set temperature. Power supply for the heater was from an AC/DC inverter. As it was pointed out, clean, dry and pressurised air in 1.5 bar is necessary for PPS operation. For on-road measurements, Pegasor has constructed an air pump along with filters and drying mechanism. Power supply for this pump is the AC/DC inverter. Due to the high electrical consumption of the heater during its operation, the air pump's operation was not steady, but thanks to air pressure regulator the air supply to the measurement unit was steady at 1.5 bar pressure.

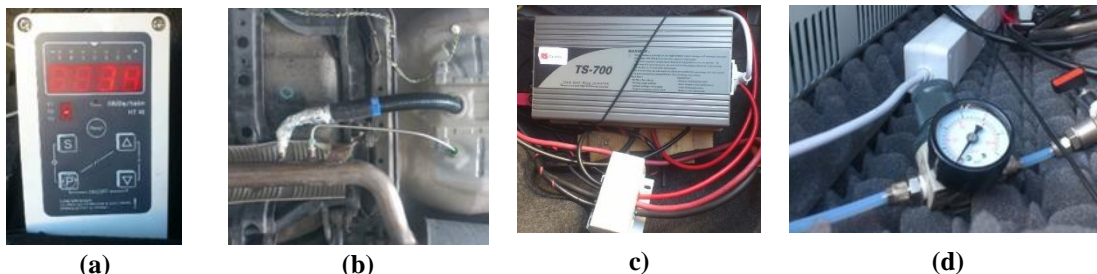


Figure 20: (a) Inlet gas heater's control unit (b) inlet heated pipeline (Honda Accord on-road measurements) (c) Power supply for every AC (d) air pressure regulator

2.2.5. Steady-state points, legislative cycles, RDE routes

All tests were performed over either steady-state points characterised by the exhaust soot concentration, gas velocity and gas temperature, or transient cycles characterised by the vehicle speed pattern.

2.2.5.1. Steady-state measurements

Every steady-state point in this study is characterised by three parameters: exhaust soot concentration, gas velocity and gas temperature. The desired combination of soot, velocity and temperature is achieved by changing the engine and ECU parameters (engine speed, torque, EGR, throttle, swirl valve, etc.). Enough time was provided for stabilisation of exhaust conditions at the targeted values, and during the whole duration of each point measurement, the three targeted values were constant. At least two sensors with the same geometry and from the same production batch were tested simultaneously for all tests to check the repeatable behaviour of all sensors. Also, at least four accumulation periods were measured at each point for all sensors to check their repeatability. For all steady-state points the target was to retain the NO_x emissions in the lowest possible limit and in parallel keep the NH_3 slip below 10 ppm (this is the limit for NH_3 slip on heavy-duty applications (EU, 2009a) and was adopted as the only reference value; there is no limit for passenger cars and light-duty applications). Details for the measured steady-state points are provided in the corresponding sections.

2.2.5.2. Legislative driving cycles and Real Driving Emissions (RDE) tests

For the needs of the current study, several legislative driving cycles (both cold (c) and hot (h) start) were measured for the Honda and Peugeot vehicles in the chassis dynamometer and the Toyota engine in the transient engine dynamometer. In addition, to evaluate the performance of the model and the sensors during real driving conditions, three different real driving routes were tested. Honda and Peugeot vehicles were tested over these routes, and also one driving pattern was replicated in the Toyota engine (Ntziachristos et al., 2016). Finally, vehicle #3 was tested for several hundreds of kilometres in road-driving conditions without any specific route. Table 8 summarises the cycles measured for each vehicle and engine.

Table 8: Legislative cycles and real-driving routes for the tested vehicles and engine (c: cold, h: hot)

Cycle	Toyota engine	Honda vehicle	Peugeot vehicle	Vehicle #3
NEDC (c), (h)	✓	✓	✓	
WLTC (c), (h)	✓	✓	✓	
FTP-75 (c), (h)	✓	✓		
Artemis road (h)		✓		
Real-driving #1 (c)		✓		
Real driving #2 (h)	✓		✓	
Real driving #3 (h)			✓	
Real driving #4 (c), (h)				✓

Real driving #1 is a combined route: 40% urban, 40% rural, 20% motorway (Figure 21). It was designed in the region of Thessaloniki, Greece and was repeated ten times under different traffic conditions. Real driving #2 (RDE compliant) was designed according to the requirements of the RDE legislation that was in force at the period of the measurements (EU, 2016) (Figure 22). Nevertheless, no PEMS was installed to check compliance with all RDE requirements. Real-driving #3 was a dynamic RDE route which does not comply with the regulation and aims to evaluate the performance of the sensor over an extensive/extreme range of operating conditions (Figure 22, Table 9). Finally, real driving #4 comprises random routes of everyday driving without any specific pattern or repeatable schedule.

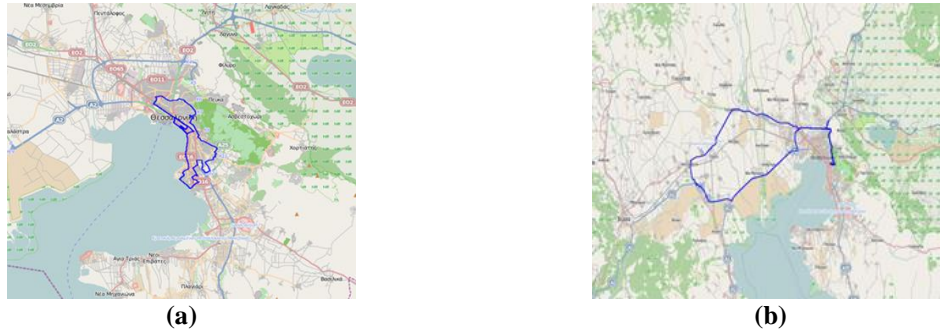
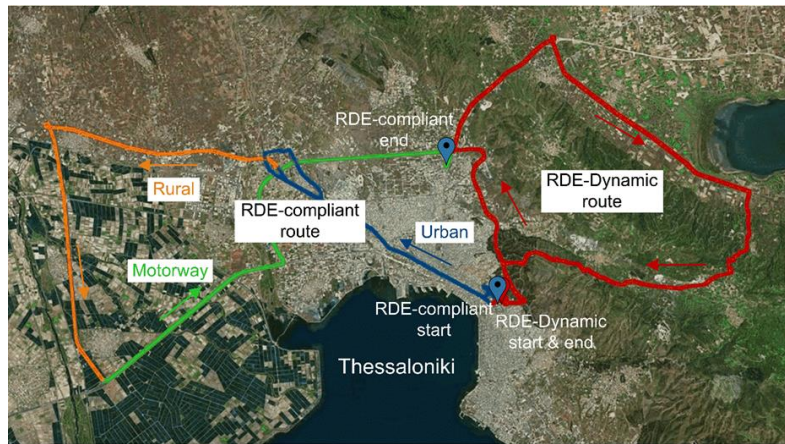
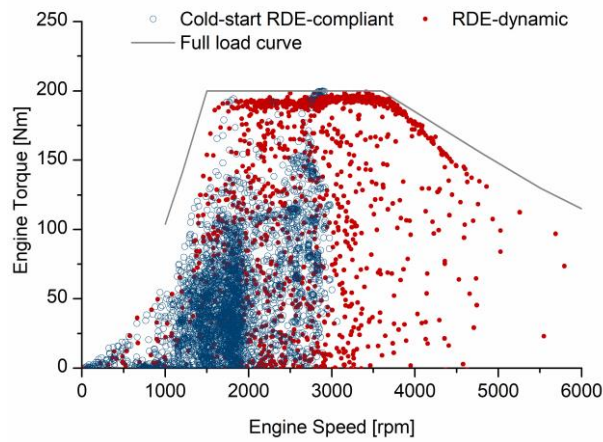


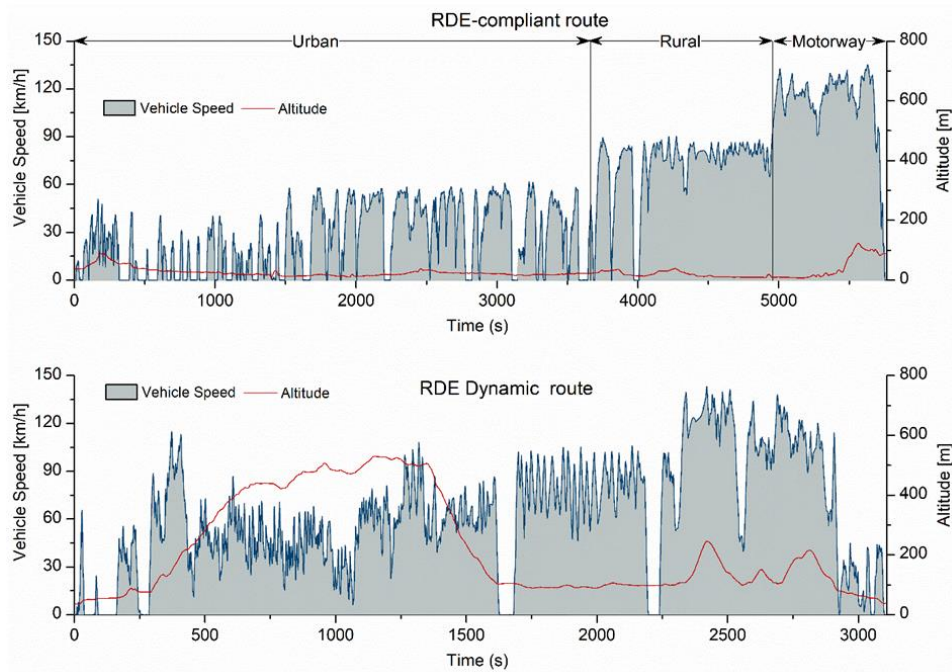
Figure 21: Real driving one route a) Urban part b) Extra-urban and highway part



(a)



(b)



(c)

Figure 22: a) Real driving #2 and 3 route (RDE-compliant route and RDE-dynamic) consisted of urban, rural and motorway parts (Triantafyllopoulos, 2018) b) torque and engine speed points for RDE-compliant and dynamic routes (Kontses, 2019) c) comparison of vehicle speed and altitude for RDE-compliant and RDE-dynamic routes (Kontses, 2019).

Table 9: Comparison of RDE-compliant and RDE-dynamic routes along with the legislation limits

Trip characteristics	RDE-compliant	RDE-dynamic	Regulation limits
Trip duration [min]	100	50	90 – 120
Stop duration [% of trip]	22	20	> 10
Trip distance [km]	77	54	> 48
Urban distance share [%]	37	30	29 – 44
Rural distance share [%]	33	36	23 – 43
Motorway distance share [%]	30	34	23 – 43
Urban average speed [km/h]	21	30	15 – 30
Rural average speed [km/h]	83	75	60 – 90
Motorway average speed [km/h]	118	110	100 – 145
Max altitude [m]	115	530	< 700
Positive elevation gain [m/100km]	507	1600	<1200
Total altitude gain [m]	-7	0	± 100

2.2.6. Surface and elemental analysis

In order to have a thorough characterisation and a better understanding of the accumulated particles on the sensor and to find their chemical elemental composition, ex-situ analyses are necessary. To this aim, Scanning Electron Microscopy (SEM) with Energy Dispersive Spectroscopy (EDS) were used to examine the sensing element after soot loading tests and exposure to contaminants. The procedure requires the sensors to be covered with a 5 nm gold layer to eliminate charge accumulations during the inspection. A JEOL JSM 6300 scanning electron microscope equipped with an X-ray EDS analyser (Oxford Isis 2000) was used. The goal is to visualise the morphology of the particles present on the sensor and distinguish the dominant chemical elements.

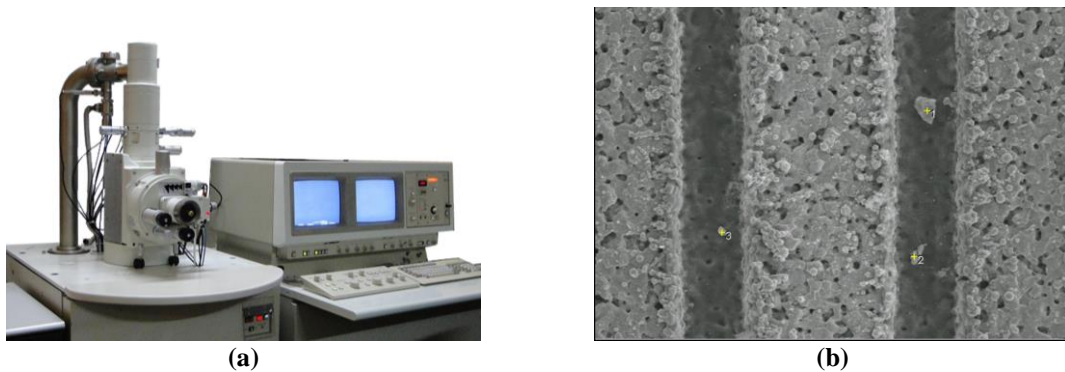


Figure 23: a) SEM equipment b) example of a resistive sensor after exposure to ash particles

2.3. Error propagation calculation

The implementation of the soot, DPF and sensor models in the OBD model, introduces errors closely associated with the input parameters and the method of execution of every sub-model. To separate, quantify and evaluate these errors, an error propagation analysis was performed. The individual errors, as described in the following tables, were calculated based on equation (2).

In general, if $q=f(x,y,...)$, δx is the error associated with variable x , δy the error related to variable y and δq the requested error, then:

$$\delta q = \sqrt{\left(\frac{\partial f}{\partial x} * \delta x\right)^2 + \left(\frac{\partial f}{\partial y} * \delta y\right)^2}, \quad (2)$$

where,

$\frac{\partial f}{\partial x}$ is the partial derivative of function $f(x,y,...)$ with respect to the variable x and cyclical with respect to the other variables.

This study evaluates the error propagation through the OBD model in a single sensor accumulation period over a type-approval NEDC.

3. OBD model: development, calibration, validation and uncertainties

The main parts of the OBD model are the three sub-models (soot, DPF, sensor models), the sensor response time and the algorithms for the final execution of the diagnosis (Figure 11b). In this chapter, the overall OBD model is built and applied to diagnose the DPF failure level according to the legislation needs.

The following headings can best describe the individual targets:

- Evaluation of the different approaches and methodologies for each sub-model
- Development and calibration of the sub-models
- Validation of the sub-models on other driving cycles
- Assessment of the performance of the overall OBD model
- Uncertainties and the error propagation through the the model for a reference NEDC
- Rejection criteria for improved diagnosis

3.1. Simulation of engine-out soot emissions (Soot model)

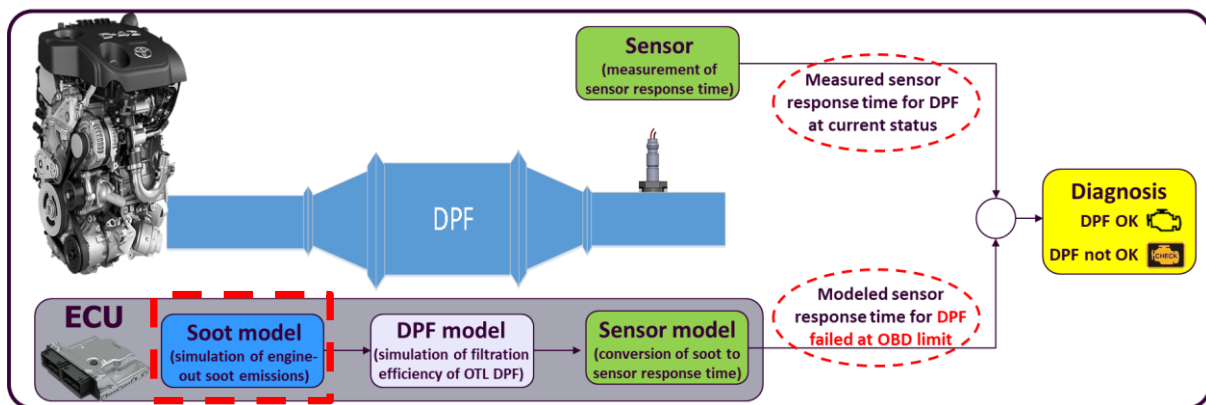


Figure 24: Overview of the OBD model. Focus on the soot model

3.1.1. Approaches for soot modelling

The target of this model is to calculate the engine-out soot emission in real-time operation (second by second basis). The modelling of soot emissions is a challenging part due to the various and complicated procedures that take place in a combustion chamber. The different chemical and physical

procedures for soot than need to be modelled are presented below (Heywood, 1989; Kirchen, 2008; Adlouni, 2011):

- **Formation stage:**
 - Pyrolysis of fuel to soot precursor and growth species, mainly acetylene (gas-phase hydrocarbons)
 - Condensation of the precursors to form the first particles/nuclei ($<2\text{nm}$)
 - Particle surface growth, aggregation, coagulation \rightarrow increased size, number, mass
- **Oxidation stage:**
 - Oxidation of the growth species and the soot particles

The engine-out soot emissions are the net result of the formation and oxidation procedures inside the cylinder. The balance between these procedures and the factors that affect it can be summarised in a ϕ -T graph (local fuel-air ratio or equivalence ratio versus temperature) (Figure 25).

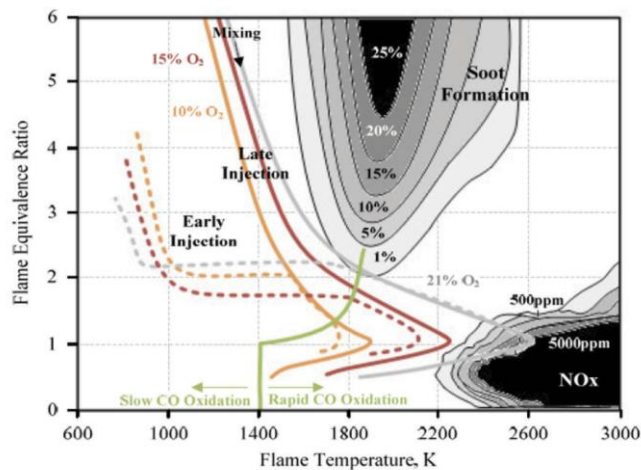


Figure 25: Equivalence ratio versus temperature region of diesel soot precursor formation (Dhal et al., 2018)

Despite that this type of graph is a powerful tool for understanding the chemical kinetics of soot, with emphasis on the effects of temperature and equivalence ratio, it does not provide information on combustion, heat transfer, inhomogeneities in the combustion chamber or chemistry of a real fuel. For this reason, analytical models have been developed to model the soot emissions. The analytical models are based on fundamental physical and chemical laws. Examples of analytical models can be found in several publications (Frenklach et al., 1985; Frenklach and Wang, 1991; Dec, 1997; Hong et al., 2005; Mosbach et al., 2009). Even today, the processes governing the soot formation and oxidation are not fully understood, but the accuracy of these models is considered high. Nevertheless, high computational effort is needed for this result. Thus, the real-time application of these models is not possible.

A much simpler and faster approach is the implementation of empirical models which are developed based on experimental data. These models are valid only for one specific engine (the engine

used for the experimental data collection), which is a significant limitation compared to the global validity of the analytical models. The low computational effort though is their main advantage, which is a priority for the on-board applications. Regarding the different approaches for empirical modelling, there are several levels of complexity. The simplest and fastest are the black-box models which do not assume any predefined structure and are mainly mean value statistical models (Fiorani et al., 2008). On the other hand, grey-box models have a specific structure and are the most commonly used models for real-time applications. In this category, phenomenological models (the most popular is from Hiroyasu (Hiroyasu, 1983)) and macro parameter-dependent models are included. The most important of these parameters as summarized by Adlouni et al. (Adlouni, 2011) comprise: equivalence ratio, engine speed, injected fuel mass, injection pressure, injection distribution CAD, injector geometry, injection timing, combustion temperature, in-cylinder pressure, combustion chamber geometry, compression ratio, exhaust gas recirculation, boost pressure etc.

The empirical models are mainly referring to steady-state modelling. During transient operation, some factors cause deviations from the steady-state modelling results. The transient operation during real driving conditions is usually a combination of tip-in (increased load with constant engine speed) and engine acceleration (increased engine speed with constant load). The physical meanings behind the soot emissions deviation between steady-state and transient operation are (Benajes et al., 2002; Adlouni, 2011; Barro et al., 2015):

- **The turbocharger lag:** During an engine acceleration, the turbo needs to increase its speed to allow an increased amount of air to reach the combustion chamber. The inertia of the system does not allow for a quick adaptation in the new requirements. This additional needed time is the turbo lag.
- **Mass and air transfer delays:** Increased time is needed to transport the air from the intake to the cylinder and the exhaust gas from the cylinder to the exhaust. This time is different for every engine speed and thus, can create delays during transient operation.
- **The thermal transient phase:** The combustion phase is highly related with the previous conditions in the chamber. This is affected by the heat losses in the exhaust manifold and in the turbocharger, but also by the heating-up of the liners, cylinder etc.

For the target of this study, a transient model is needed with low computational effort, capable of real-time execution and calibrated for a specific vehicle/engine. Therefore, a combination of a base black-box modelling for steady-state operation and an additional grey-box macro parameter modelling for a transient correction were used as described in the next section.

The different approaches for the engine-out soot emissions modelling and the selected method for this study can be summarised and classified as follows:

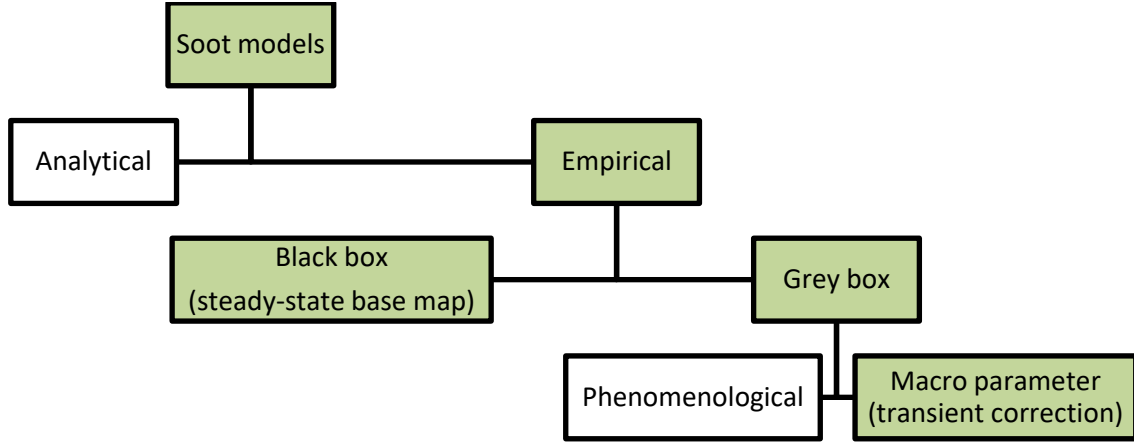


Figure 26: Classification of soot models. The green boxes are referring to the current analysis, which aims in developing an empirical, grey-box, micro parameter-dependent model for transient correction supplementary to a black box statistical model.

The target of this study is to develop an empirical model consisted of a basic black-box approach for steady-state operation and an additional grey-box macro parameter approach for the transient operation. This model simulates the engine-out soot emissions produced as a function of variables available in the ECU.

3.1.2. Methodology for the selected approach

For OBD applications, a map-based model using the engine speed and torque (or injected fuel mass) as inputs is the default approach offering adequate accuracy at low computational cost. For improved performance and accuracy, the steady-state base map was corrected for transient operation based on additional measurements according to the methodology presented by Neumann et al. (Neumann et al., 2012). The equation for the transient-corrected soot concentration is:

$$C_{Soot}(N, m) = C_0(N, m) + \sum_{k=1}^n \frac{\partial C_{0,k}}{\partial Z_k}(N, m) \times [Z_k(N, m) - Z_{0,k}(N, m)], \quad (3)$$

Where,

- N : Engine speed
- m : Injected fuel mass
- $C_{Soot}(N, m)$: Soot mass concentration [mg/m^3] at a specific operating point during transient operation
- $C_0(N, m)$: Soot concentration from base emission map (steady-state)
- $\sum_{k=1}^n \frac{\partial C_{0,k}}{\partial Z_k}(N, m) \times [Z_k(N, m) - Z_{0,k}(N, m)]$: Soot concentration from transient correction
- k : Influencing parameters for transient correction
- $\frac{\partial C_{0,k}}{\partial Z_k}$: Partial derivative of soot concentration against each influencing parameter
- $Z_k(N, m)$: Value of the influencing parameter at a specific operating point during transient operation

- $Z_{0,k}(N, m)$: Value of the influencing parameter at a specific operating point during steady-state operation

Before proceeding with the methodology for the development of the base emission map and the transient correction, it is necessary to identify the parameters/variables (Z_k) that need to be included in the analysis. As already discussed, there are several parameters which can be used to simulate the soot emissions. As an example, the equivalence ratio and cylinder temperature are crucial parameters (Figure 25). However, both values are not readily available in an ECU, which is a pre-requirement for global OBD applications. The examination of the influencing parameters that are responsible for the transient deviation leads to the inclusion of injection timing, rail pressure, air-to-fuel ratio (or lambda) in the exhaust, exhaust gas recirculation rate (EGR), mass airflow (MAF) and boost pressure. Lambda, EGR and MAF are interdependent, and thus, the MAF was selected as the representative value. Therefore, the transient correction is based on three ($k=3$) influencing parameters:

- MAF
- Rail pressure
- Injection timing

The soot model was developed, calibrated and validated in the Toyota engine (Table 5). The necessary emission measurement equipment was an MSS at the engine out position (position 1 of Figure 14a). Compared to an on-road application, the in-laboratory tests provide accurate measurement of the engine torque whereas, the fuel-injected mass is provided from the vehicle's ECU (calculation) or an additional laboratory fuel meter. In our study, the fuel meter was not available, and thus, it was decided to use the torque instead of the fuel mass. The final equation is presented below:

$$C_{Soot}(N, T) = C_0(N, T) + \sum_{k=1}^n \frac{\partial C_{0,k}}{\partial Z_k}(N, T) \times [Z_k(N, T) - Z_{0,k}(N, T)], \quad (4)$$

Based on equation (4), three map categories are needed for the calculation of the soot concentration in transient operation:

- The base soot map, $C_0(N, T)$
- Three steady-state maps with the values of the influencing parameters, $Z_{0,k}(N, T)$
- Three maps with the partial derivative for the influencing parameters, $\frac{\partial C_{0,k}}{\partial Z_k}(N, T)$

The value of the influencing parameters ($Z_k(N, T)$) and the engine speed (N) and torque (T) are the second-by-second inputs that are needed from the vehicle's ECU.

To develop the base soot map and the steady-state maps of the influencing parameters for the whole engine operation map, nine levels for the engine speed and twelve levels for the engine torque were used (Table 10). A few of the above speed-torque combinations are not possible as they are above

the full load curve of the engine. For the partial derivative values of the influencing parameters, the development was based on fewer levels compared to the base map to reduce the calibration effort (green font in Table 10).

Table 10: Operating point levels for the development of the soot model. For the partial derivative values of the influencing parameters, the development was based on fewer levels compared to the base map to reduce the calibration effort (green font).

Engine speed [rpm]	Engine torque [Nm]
800	0
1000	10
1400	20
1800	40
2200	60
2600	80
3000	100
3400	120
3800	140
	160
	180
	200

For the calculation of the partial derivative for each influencing parameter in each expansion point, a parameter step variation in a “short distance” around the corresponding expansion point was performed. The direction of the change in the influencing variables is relative to the direction of increased soot emissions: reduced mass airflow, reduced rail pressure and retarded injection timing. To perform the MAF variations, the engine was throttled to reduce the available airflow. For reduced rail pressure, the respective ECU variable was decreased through the INCA/ETAS ECU and bus interface module (ETAS, 2019). Similarly, for retarded injection timing, the respective ECU variable was used. Regarding the amount of the short distance change, it resulted after a try and error procedure aiming in creating the lowest accurately measurable increase in soot emissions (Table 11). An example of this exercise is presented in Figure 27. MAF is reduced by engine throttling and consequently, soot concentration increases. The repetition of this procedure for the selected points and influencing variable results in the partial derivative maps presented in the next section.

Table 11: Step changes for the influencing parameters

Influencing parameter	Step change
Mass air flow	4-6 [kg/h]
Rail pressure	20-40 [bar]
Injection timing	0.2-0.3 [degrees]

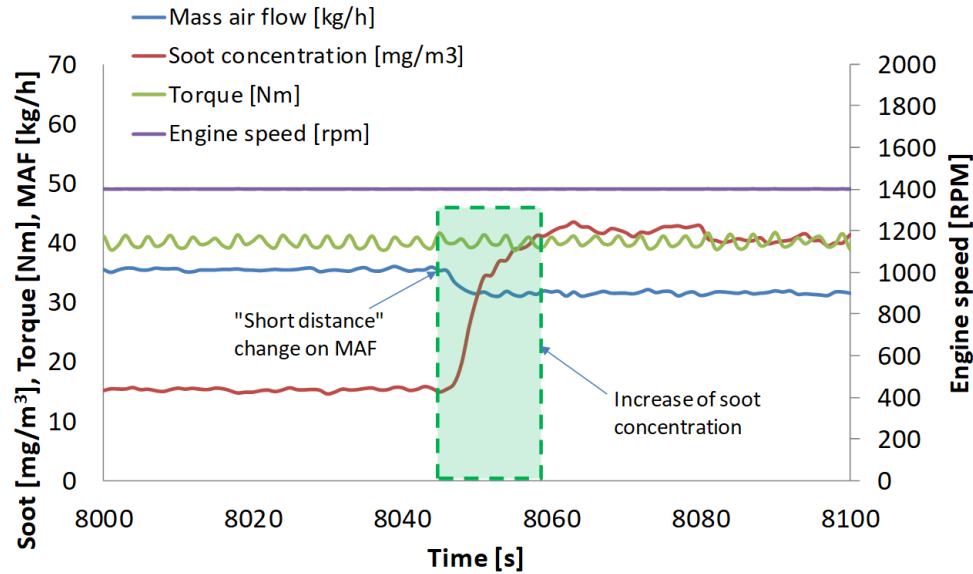
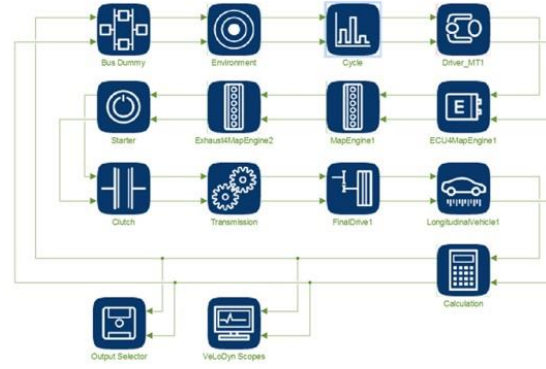


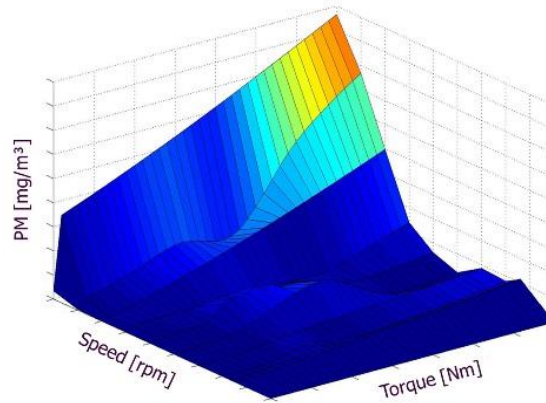
Figure 27: Step variation of MAF and recording of the resulting increase in soot concentration

Nevertheless, the transient correction demands considerable calibration effort for every application. Another possible future alternative for accuracy improvement is the calibration of the model based on several data and machine learning techniques for real driving operation of the vehicle (Linke et al., 2016). Also, the utilisation of additional input parameters could enhance accuracy without the need for extensive calibration. An example of this scheme is the signal of low-cost cylinder pressure sensors (Hidria, 2011). This approach is not further analysed in this study, but it is an interesting proposal for future work.

As discussed, for the implementation of the base map and the transient correction, the engine speed and torque are used as inputs. In a vehicle application though, the torque is a calculated value based on vehicle speed profile, gear ratios, road load, mechanical losses and vehicle characteristics. Also, the simulation procedures usually use as inputs the vehicle speed profile. By using IAV/Exothermia VeLoDyn software as a part of the Matlab® library, it is possible to simulate the emissions of a vehicle under different legislative test cycles or real-world driving profiles. VeLoDyn calculates the engine speed and torque for a given driving profile using a combination of vehicle and engine operation variables, environmental conditions, road load etc. Therefore, VeLoDyn allows the performance of sensitivity analysis on various vehicles or driving patterns.



(a)



(b)

Figure 28. (a) Overview of the VeLoDyn model for simulation of engine-out soot emissions (b) Soot map used for calculation of engine-out soot emissions in every time step according to engine speed and torque which are provided by the vehicle's ECU.

VeLoDyn is a tool for managing and simulating motor-vehicle powertrains, and it works as a part of the Matlab Library just like Simulink. The higher-order Model Manager simplifies the development and standardisation of the Simulink models. VeLoDyn works based on so-called carrier blocks. These blocks incorporate the signals from any Simulink block into a bus structure and provide a database holding all the information necessary for a model.

3.1.3. Development of the necessary maps

The first step is to develop the base soot map ($C_0(N, T)$), which is shown in Figure 29. The dots are the measured steady-state points, and the map is limited by the full load curve of the engine. Soot formation is highly correlated with the injected quantity and thus, the load of a diesel engine. This is partially the case for the map in Figure 29. The reduced emission above the 140Nm level is due to the EGR strategy, which is deactivated at high torque and high engine speed levels. This strategy leads to higher soot oxidation rates during the combustion process and thus, lower soot emissions at this area.

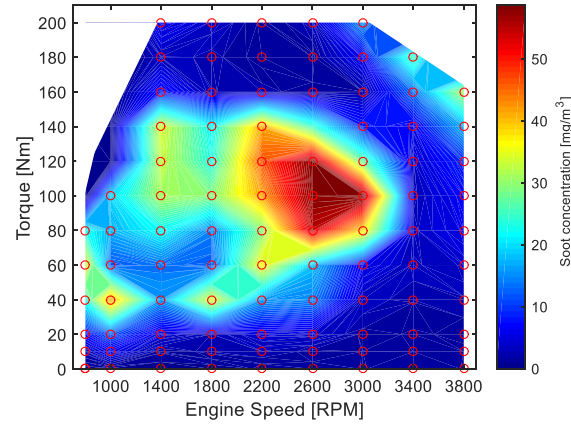
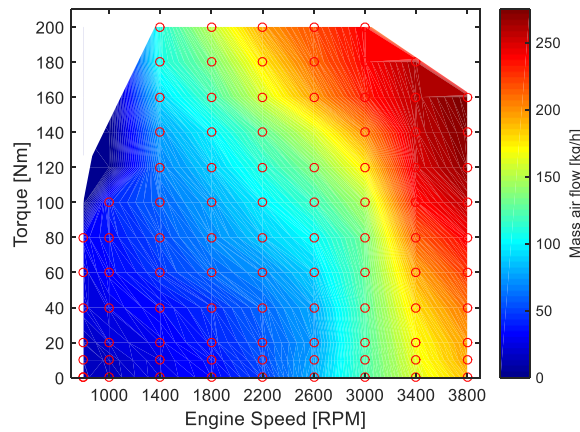
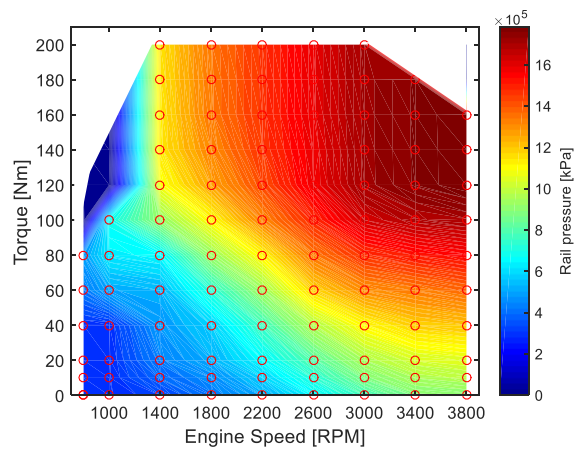


Figure 29: Soot concentration for steady-state operation (base soot map, $C_0(N, T)$). The red marks are the measured points (12 levels of torque, nine levels engine of speed).

The development of the steady-state maps of the influencing variables is the next step ($Z_{0,k}(N, T)$). Mass airflow (MAF), rail pressure and injection timing were the selected variables. The three maps are in Figure 30, along with the steady-state measurements (red dots). The positive values of primary injection timing refer to crank angle after the top dead centre (TDC). The MAF is positively correlated with the engine speed, the rail pressure increases -in general- when both engine speed and torque are increased, and the injection timing is also positively correlated with the engine speed.



(a)



(b)

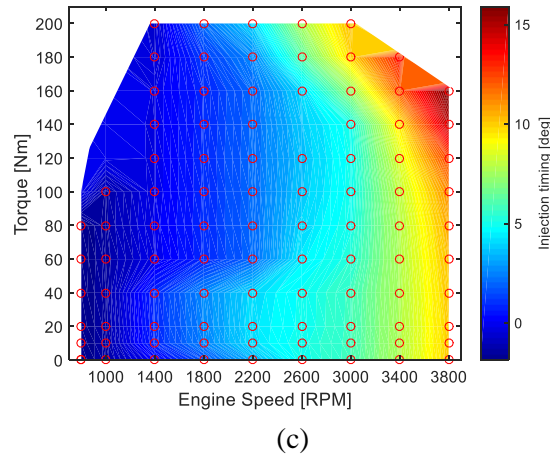
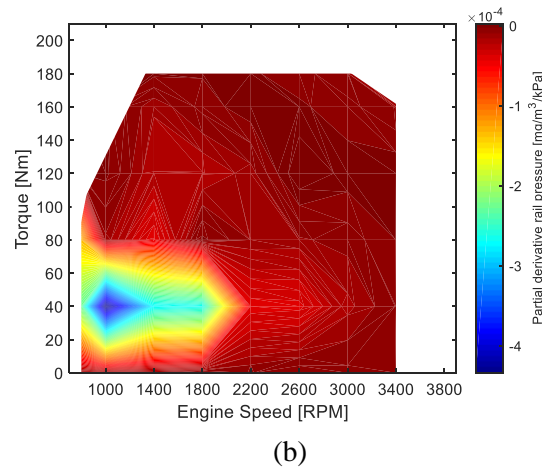
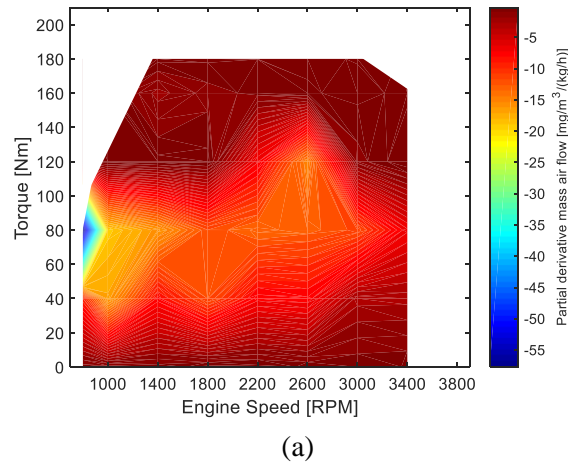
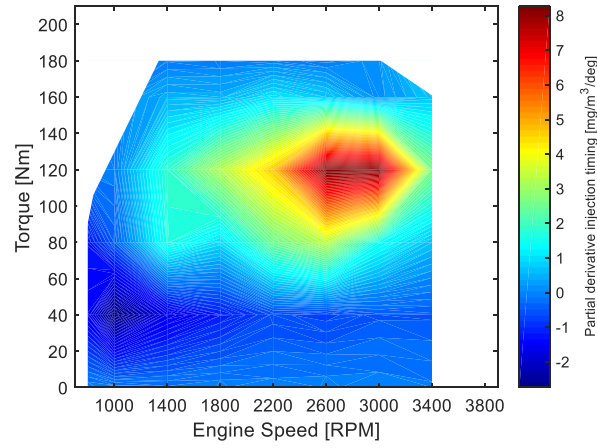


Figure 30: Steady-state maps ($Z_{0,k}(N, T)$) of (a) MAF (b) rail pressure (c) injection timing.

The last step is the development of the three maps with the partial derivative for the influencing parameters ($\frac{\partial C_{0,k}}{\partial Z_k}(N, T)$). The results are presented in Figure 31. The physical meaning of the partial derivative is the impact of the change of each influencing variable on soot emissions. A reduction of 1 kg/h in the intake air, can reduce the soot emissions up to 10mg/m^3 apart from low speed high torque area where the partial derivative of soot can be higher than 50mg/m^3 (absolute value). On the other hand, the effect on soot emissions of small changes in the rail pressure and injection timing are insignificant compared to the effect of mass airflow.





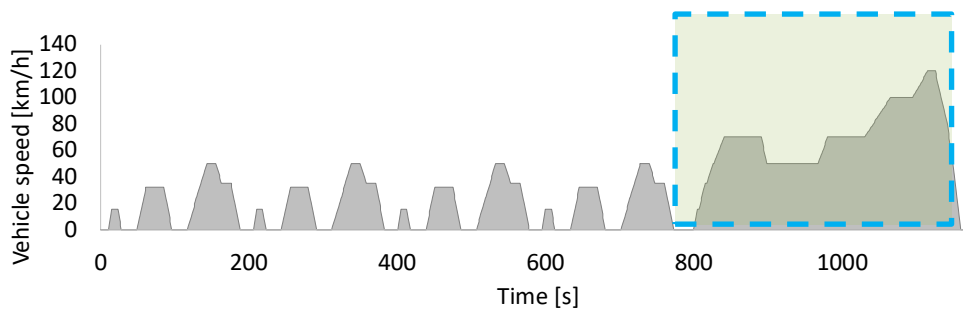
(c)

Figure 31: Partial derivative maps ($\frac{\partial C_{0,k}}{\partial Z_k}(N, T)$) for (a) MAF (b) rail pressure (c) injection timing

Having calculated the necessary maps, the soot mass concentration during transient operation can be calculated based on equation (4).

3.1.4. Performance and validation

For the base soot map without the transient correction, the modelled against the measured soot concentration over the NEDC is presented in Figure 32. In the urban part of the cycle (0-780 seconds), the error of the model is small in terms of cumulative values. The discrepancy in the modelled soot though is created in the extra-urban part of the cycle (780-1180 seconds) where the deviations in the second-by-second data due to the measured transient peaks lead to relatively high inaccuracy of the model (25% deviation). To improve the model in this area, the transient correction is necessary. It is implemented according to the methodology described in the previous section, and the results are presented in Figure 33.



(a)

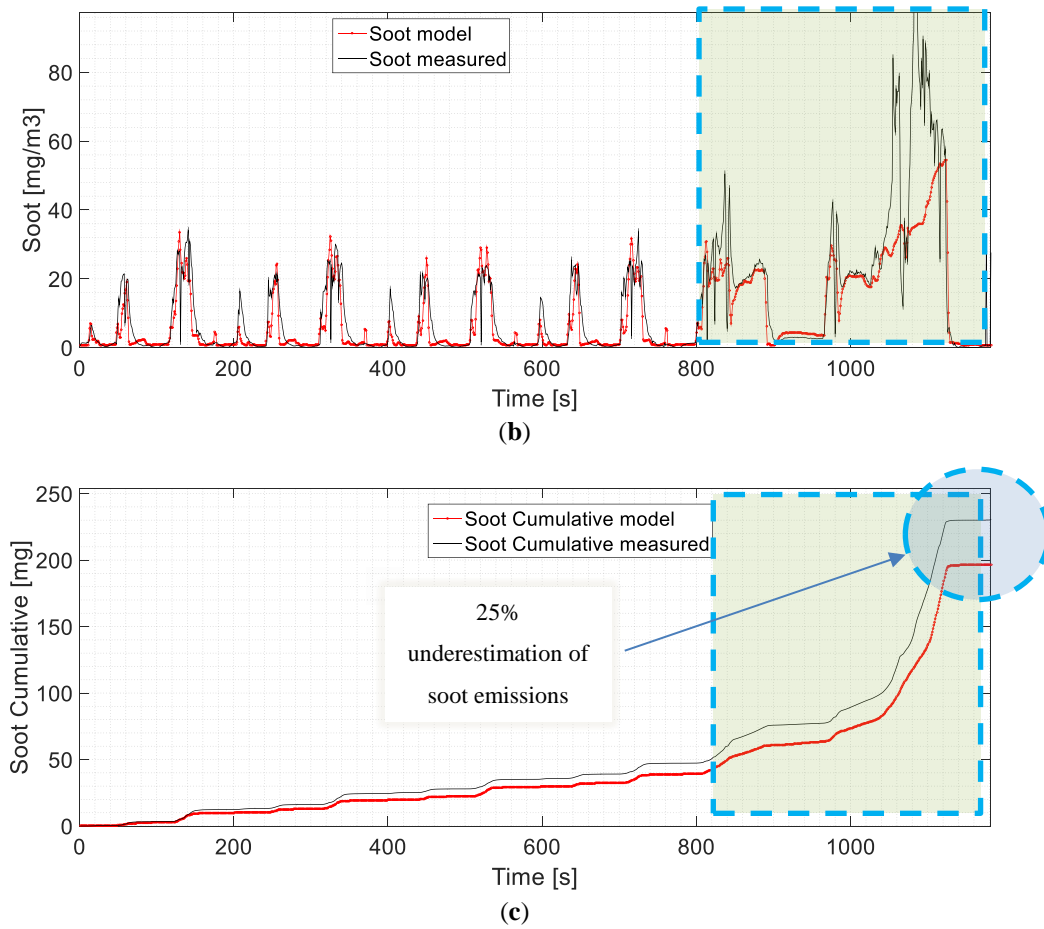
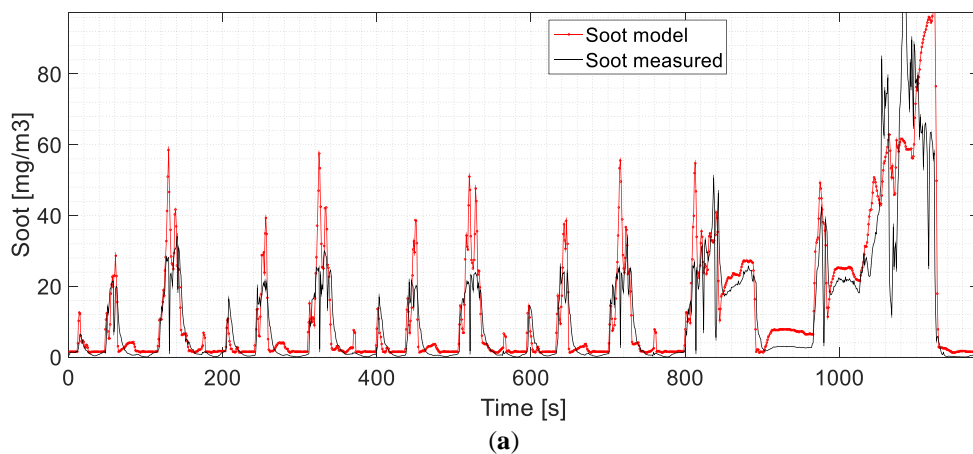


Figure 32: (a) Vehicle speed profile for NEDC cycle (b) Second-by-second soot concentration from the model (using only the base soot map) and the measurement (c) Cumulative soot concentration from the model (using only the base soot map) and the measurement.



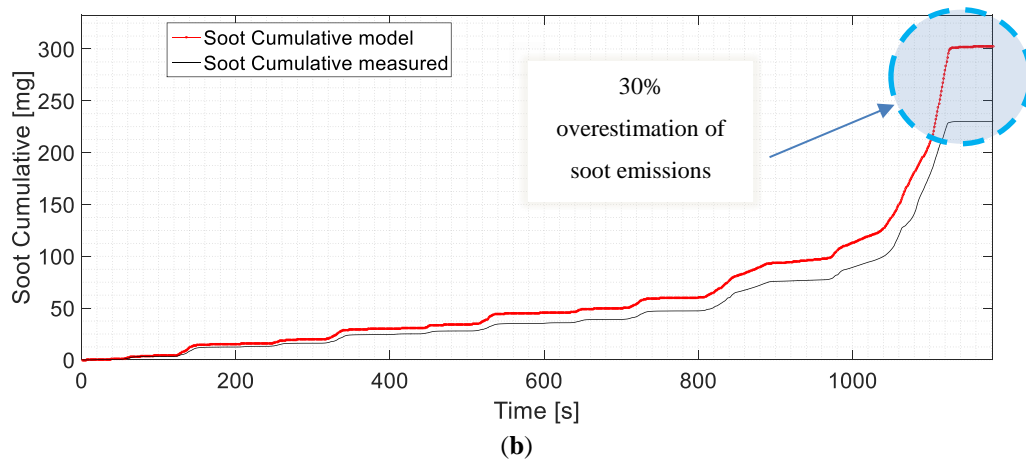


Figure 33: Soot estimation from the base soot map and the transient correction (a) Second-by-second soot concentration from the model and the measurement (b) Cumulative soot concentration from the model and the measurement.

It is obvious though that the model with the transient correction overestimates the soot peaks during the cycle (this is also reflected in the cumulative values). This can be attributed to the different EGR strategy in the transient operation. The engine demands lower EGR rates than the steady-state operation for the same operating points (same engine speed and torque) in order to meet the torque requirements. The lower EGR rate is expected to reduce the soot concentration due to the higher amount of oxygen for soot oxidation. The good correlation between the EGR deviation and the model overestimation verifies the above (Figure 34). Idle points show the opposite phenomenon in the EGR, but here the error is almost zero.

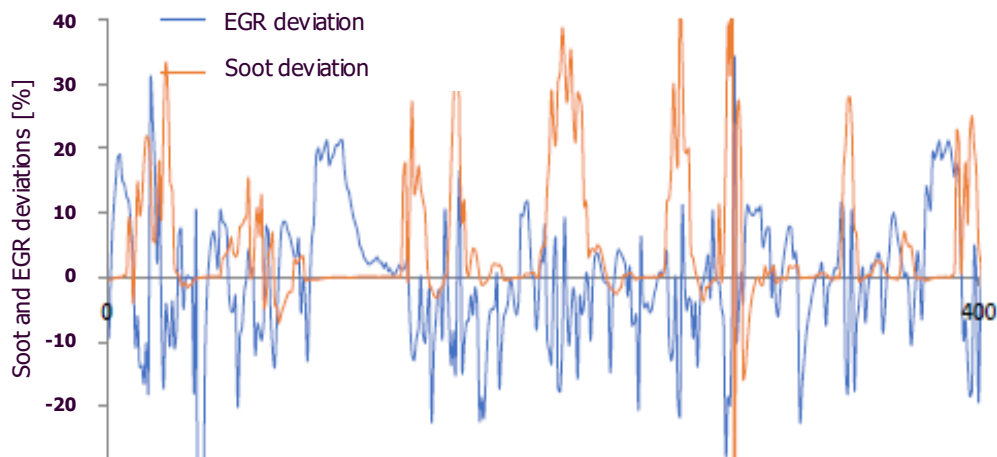


Figure 34: Correlation of EGR deviation with soot deviation

This leads to the need for introducing an EGR correction, but in this case, the additional term is expected to be in the direction of reducing soot emissions. Following the previously described methodology for the development of the steady-state maps of the other influencing parameters and the other partial derivative maps, the maps of Figure 35 are created.

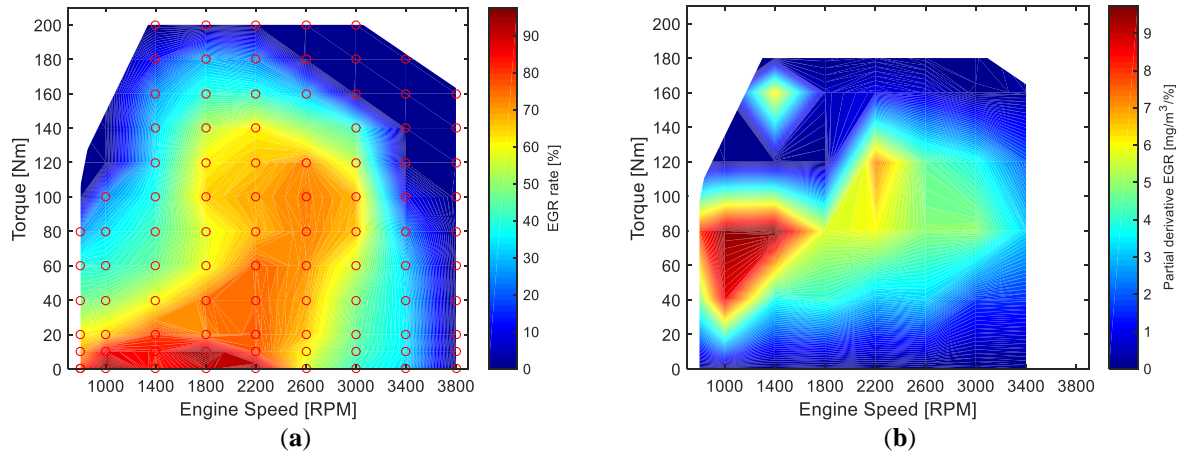


Figure 35: Steady-state maps for (a) EGR rate (b) partial derivative for EGR

With the introduction of the EGR correction, the soot model shows good correlation with MSS measurements and the final error is significantly reduced to 2% (Table 12). The improvement is in most significant in the extra-urban part of the cycle. In this part, the importance of the correction becomes clear, as here the dynamic phenomena are stronger, and therefore, the deviations stemming from the prediction based only on the base model map are more significant. It is noted that for some points where the EGR correction creates negative values in the instantaneous emission diagram, the corrective term is omitted.

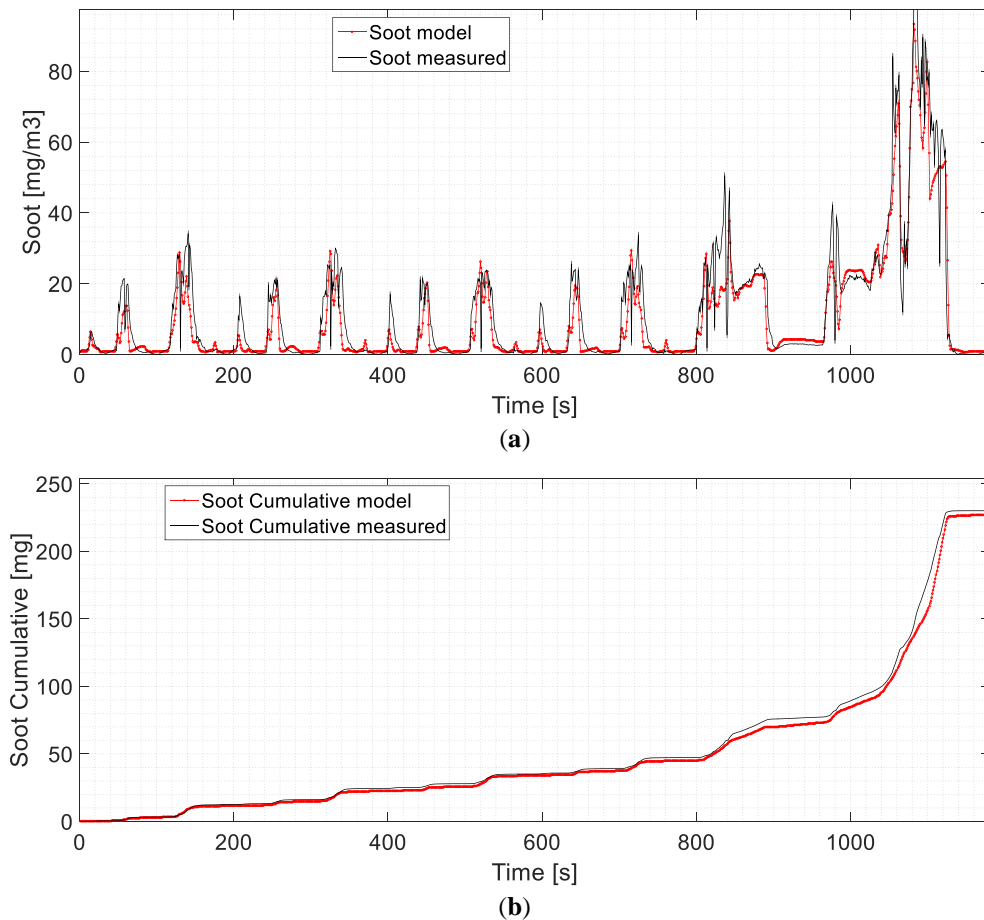
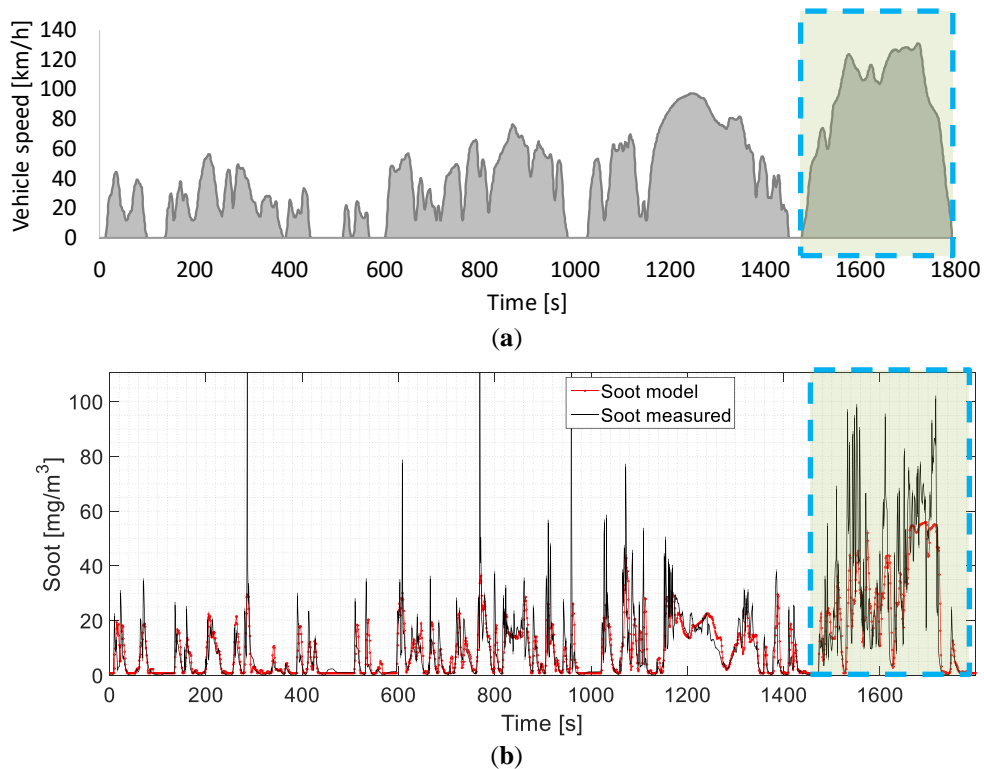


Figure 36: Final soot estimation from the base soot map, the transient correction and the EGR adjustment
 (a) Second-by-second soot concentration from model and measurement (b) Cumulative soot concentration from model and measurement.

Table 12. Errors of soot models

Model	Source of inaccuracy	Associated error
Base Soot model	Emission maps on transient	$\delta_{sv}=25\%$
Soot model with transient correction	operation	$\delta_{sv}=2\%$

Validation over different transient profiles is the necessary next step for the soot model. The validation is performed for the WLTC cycle (Figure 37a). Figure 37b shows that several peaks are reproduced by the model. Peak estimation is accurate, and despite some deficiencies in their values, the transient correction is reliable. In the range 1200-1250 seconds, the model deviates from the measurements as a result of the prediction from the static map. The engine here runs at very low torque gradients, which means that the correction term is almost zero, and the error is due to the first term of equation (4). Also, a deviation is observed in the last part of the cycle (motorway driving conditions). At these conditions, the model fails to predict the soot peaks accurately, but this creates a relatively small deviation on the final cumulative values (17%).



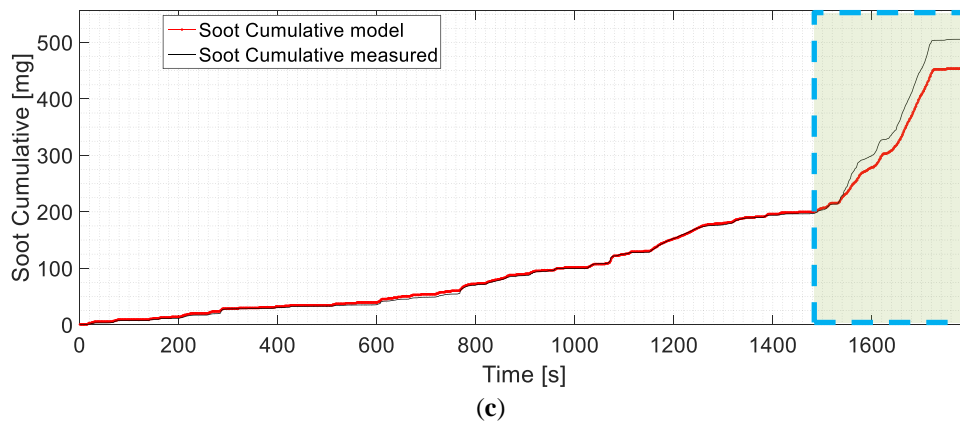


Figure 37: (a) Vehicle speed profile for WLTC cycle (b) Second-by-second soot concentration from model and measurement (c) Cumulative soot concentration from model and measurement

3.2. Simulation of filtration efficiency (DPF model)

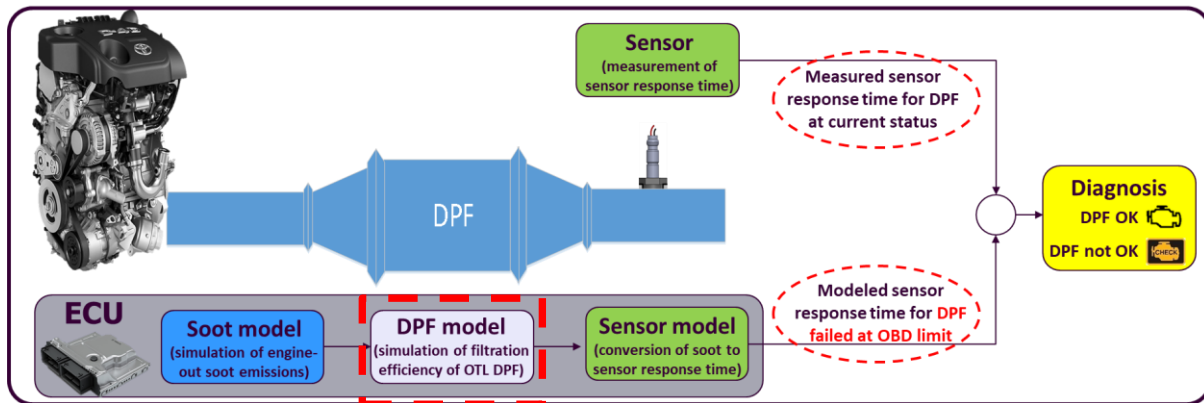


Figure 38: Overview of the OBD model. Focus on the DPF model

3.2.1. Approaches for DPF modelling

The calculation of the instantaneous DPF-out soot emissions requires the implementation of the filtration efficiency of the DPF. The standard practice for simple OBD DPF models is to use a constant filtration efficiency. Although this approach is valid for an intact DPF, the performance of partially failed DPFs cannot be accurately simulated with constant efficiency. The efficiency of the intact filter is reduced for a few minutes after the regeneration (depth filtration), but shortly after the build-up of the soot cake, the efficiency reaches almost 100%, regardless of the exhaust conditions or the DPF load. The challenge for the unplugged DPFs is that the efficiency (after the depth filtration) is affected by various parameters including the DPF load, the exhaust temperature and the exhaust mass flow. Available studies focusing on partially failed DPFs reveal that the filtration efficiency of a clean partially unplugged DPF is initially increasing as soot is accumulated on the channels (similarly to the intact DPFs) but shortly after the formation of soot cake, the efficiency exhibits a negative correlation with the

DPF load (Zhang et al., 2010; Basu et al., 2013; Haralampous and Kontzias, 2014; Haralampous and Mastellos, 2015). This behaviour is explained by the increased flow through the damaged area due to the reduced resistance compared to the intact area. Additionally, for an even higher accuracy during the transient operation on a second-by-second basis, the effect of the exhaust volume flow should be considered. X. Zhang (2010) investigated the effect of exhaust mass flow on the exhaust mass distribution between the intact and the damaged area and found that the fraction of exhaust mass flow going through the intact channels was increased with an increase in exhaust flow. Also, Linke (2016) referred to a possible dependency of temperature on filtration efficiency of a partially failed DPF. The last two comments are describing the effect of exhaust volume flow on the filtration efficiency.

Therefore, the advanced alternative approaches for the calculation of the filtration efficiency of the OTL DPF, need to consider the effect of the above parameters on the evolution of the filtration efficiency during the operation of the vehicle after a DPF regeneration. It is important to note that for OBD applications, the legislation allows the implementation of a delay factor or a minimum DPF loading before enabling the diagnosis. The reason is to avoid the rapidly changing filtration efficiency during the depth filtration period. Therefore, the following analysis focuses on the performance of the selected approaches after this threshold. The threshold loading is usually expressed in g/l, and typical values for DPFs are 0.05-0.5 g/l depending on the filter microstructure. It is a common practice to introduce some transient preconditioning cycles before the start of diagnosis to achieve the desired DPF loading.

Based on the above, four approaches were investigated to describe the behaviour of an unplugged DPF, covering both simple, low-accuracy solutions, and also complex and high-accuracy approaches:

- Constant filtration efficiency
- Linearly decreasing filtration efficiency
- Empirical model considering the exhaust volume flow and the DPF load
- DPF simulation using the commercially available Exothermia/Axisuite platform

3.2.2. Methodology for the selected approaches

For the investigation, development and calibration of the different approaches, the Toyota engine (engine #2) with the OTL DPF was used. The OTL DPF (12 mg/km over the NEDC) was created based on the plug-removal technique. 219 plugs were symmetrically removed from the rear face of the filter, and the filtration efficiency was measured at 92%. The calculation of the number of the removed plugs was based on a 2D design software. The selection of small drills (12 mm) in this study creates a

discrepancy on the number of plugs that were actually removed because it is possible that plugs in the periphery of each cycle are not fully removed. Therefore, the actual number of removed plugs could be significantly lower, as it will be discussed in the section with the Axisuite model. For better accuracy, it is preferable to reduce the number of drills and create two or four areas of removed plugs.

The exhaust measurement equipment comprised two MSSs, measuring upstream and downstream of the OTL DPF to define the filtration efficiency (for some calibration steps, a setup with 1 MSS coupled with two sampling lines connected with valves upstream and downstream of the filter was used due to unavailability of the second MSS). Based on the calculated exhaust volume flow and the soot concentration from the MSSs at each time step, the soot mass flow and thus, the measured efficiency can be easily calculated:

$$\text{Measured (reference) filtration efficiency} = 1 - \frac{\text{soot mass flow downstream of the DPF}}{\text{soot mass flow upstream of the DPF}} \quad (5)$$

The second-by-second calculation of the filtration efficiency during transient operation significantly fluctuates (e.g. due to small differences in the exhaust flow for the two MSSs, the different response of sensors etc.) and thus a moving average (e.g. 50 values) is preferred to better illustrate the transient efficiency.

Also, a steady-state soot loading test was performed to define the threshold DPF load before the implementation of the model. This soot loading level was then converted into a number of NEDCs, which is the common approach for DPF preconditioning. Finally, it is necessary to define the maximum DPF loading for the investigations. It is related to the regeneration strategy of every vehicle, and for this study, it was selected at 4 g/l. This is calculated by weighing the filter before and after the loading procedure. To experimentally obtain this load level, it was necessary to run 13 NEDCs with the current setup.

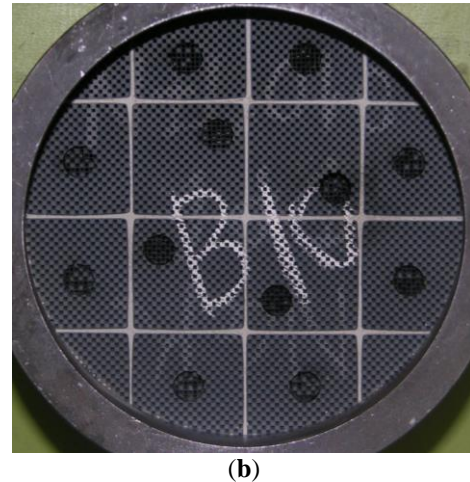
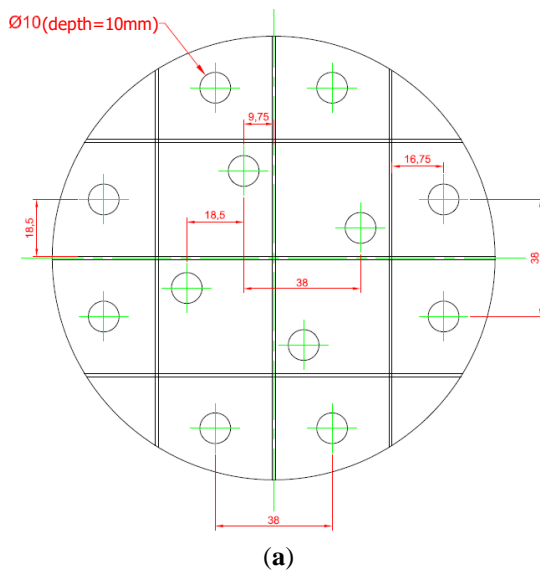


Figure 39: OTL DPF for the Toyota engine for the development of the DPF models. 219 plugs were symmetrically removed from the rear face of the filter a) 2D drawing b) photo after plug removal

3.2.2.1. Constant efficiency

The constant filtration efficiency, which provides a rough estimation for the needs of the initial calibration steps, is calculated based on the cycle after the preconditioning. The cumulative soot masses upstream and downstream of the DPF are used to calculate the efficiency:

$$\text{Constant filtration efficiency} = 1 - \frac{\text{cumulative soot mass downstream of the DPF}}{\text{cumulative soot mass upstream of the DPF}} \quad (6)$$

3.2.2.2. Linearly decreasing efficiency

With this approach, it is possible to account for the reduced filtration efficiency due to DPF soot loading. It was observed that the correlation could be defined by a linear function. To find the slope of the function of the efficiency for various DPF loadings, a protocol with several NEDCs was run until the DPF load reached the predefined level of maximum DPF load (4 g/l for this study). The first cycle was again neglected due to the unstable efficiency during depth filtration.

3.2.2.3. Empirical model

This method uses pre-calibrated filtration efficiency maps and interpolation technique for the second-by-second calculation of the filtration efficiency. In order to investigate the effect of both exhaust volume flow and DPF loading, the following test sequence is typically suggested and used:

- DPF regeneration
- DPF conditioning to avoid the impact of the depth filtration (DPF loading up to ≈ 0.1 g/l)
- Exhaust volume flow variations with slightly loaded filter
- DPF accelerated loading
- Exhaust volume flow variations with loaded filter

The last two steps were performed for three district load levels: 0.1 g/l, 1 g/l and 4g/l. The outcome of these experiments is a 3D map of the filtration efficiency as a function of the instantaneous exhaust volume flow and the DPF load.

3.2.2.4. Axisuite/Exothermia model

The Axisuite model (version 2017A) consists of two DPFs connected in parallel in the exhaust line. The first DPF (filter 1) is a typical full DPF (filtration efficiency almost 100%) and the second DPF (filter 2) is a fully unplugged DPF (filtration efficiency 0%) (Figure 40). In terms of simulation, the two

filters are identical except for the length of outlet plugs of filter 2 which is set to zero and the diameters which are calculated based on the number of removed plugs and the number of cells per square inch of the filter (cpsi). This DPF model can accurately and robustly determine the filtration efficiency in a second-by-second approach as long as the necessary boundary conditions are introduced.

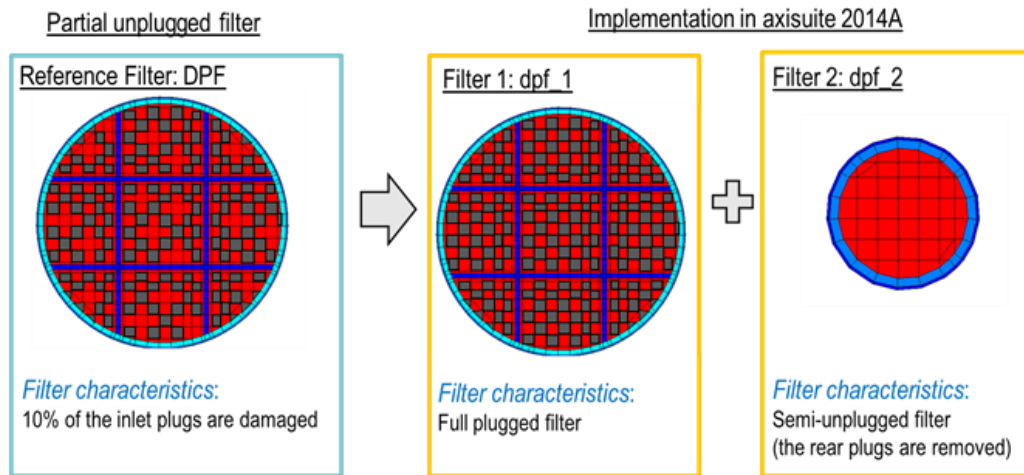


Figure 40. Simulation of a partial unplugged DPF (Axisuite)

The accurate simulation of Axisuite models demands some calibration effort. The procedure consists of two targets for the model calibration of the full DPF:

- **Soot and substrate parameters**
 - Soot permeability [m^2]
 - Substrate soot capacity [$\text{g}/\text{l}_{\text{wall}}$], permeability [m^2]
- **Filtration parameters**
 - Diffusion mechanism correction factor [-]
 - Interception mechanism correction factor [-]
 - Gradient parameter in wall filtration efficiency [-]

This calibration procedure is the same for all Axisuite DPF models and is described in detail by Karamitros (2016). It consists of three different test protocols: the “clean pressure drop” test for the definitions of the substrate parameters, the “filtration efficiency” test for the filtration parameters and the “soot loading” test for the soot parameters. All calibration steps were performed in the same way for the current study for a full DPF and the OTL DPF.

3.2.3. Development of the models

For the OTL DPF used in this study, the minimum (threshold) DPF loading was selected at approximately 0.12 g/l according to the filtration efficiency test in Figure 41. This load is achieved during transient operation (NEDC) within the first 1050 s of the cycle (Figure 42). Therefore, one NEDC is sufficient as preconditioning after the DPF regeneration.

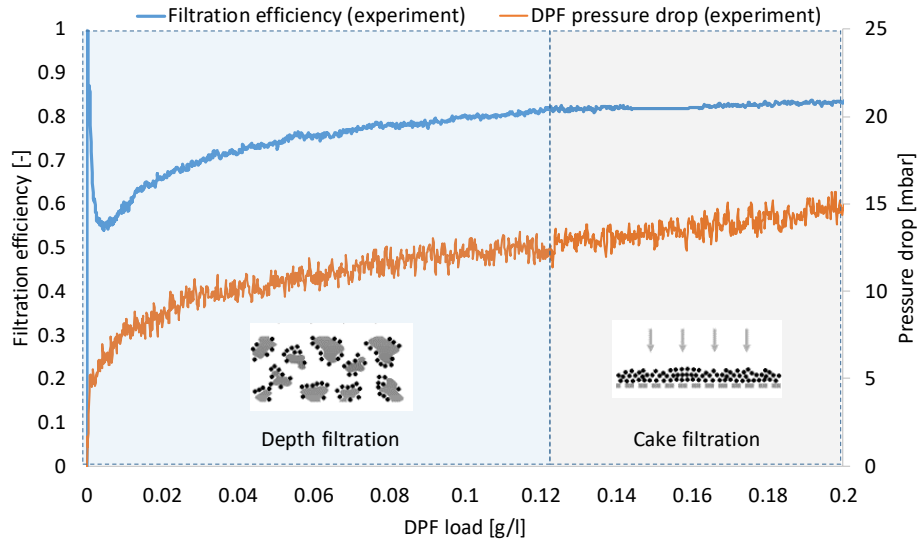


Figure 41: Evolution of the filtration efficiency and the pressure drop for a clean DPF during steady-state operation

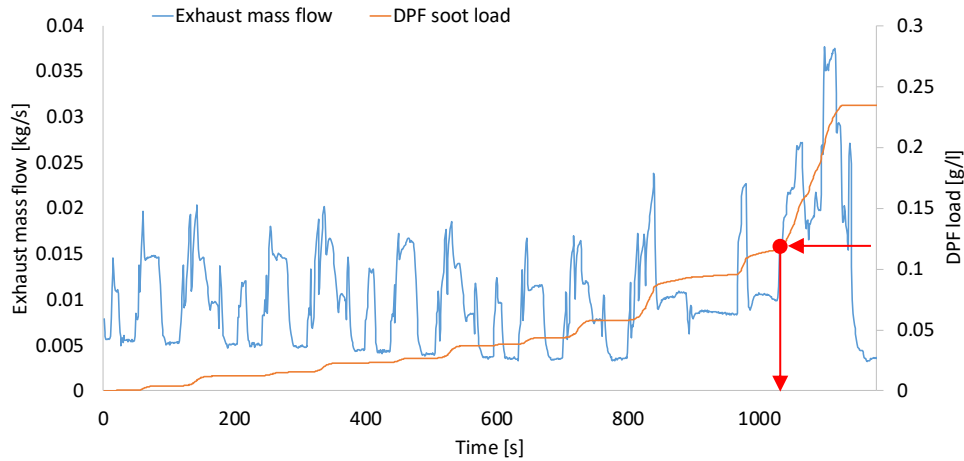


Figure 42: Exhaust mass flow profile and evolution of the DPF load for a clean DPF during an NEDC

3.2.3.1. Constant efficiency

After the preconditioning, a second NEDC was run to define the constant filtration efficiency. Based on the results presented in Figure 43, the efficiency is 92%, and it is approximately constant during the

cycle. Nevertheless, a slight trend for reduction of the efficient is observed (it is validated in the next experiments) and this is the reason for the insufficiency of the constant efficiency.

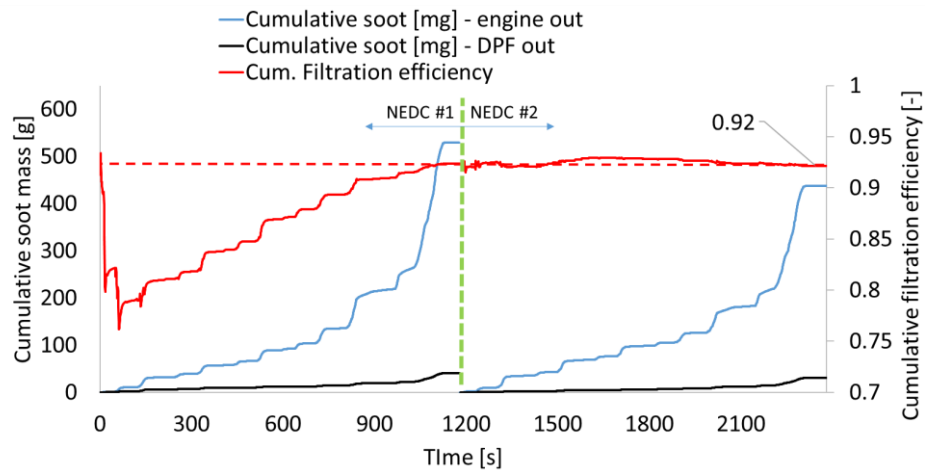


Figure 43: Constant filtration efficiency based on the 2nd NEDC for the OTL DPF. The 1st cycle is a preconditioning to avoid the depth filtration of the DPF. The cumulative values are calculated separately for each cycle.

3.2.3.2. Linearly decreasing efficiency

To define the correlation of the efficiency with the DPF soot load, a protocol with 13 NEDCs was used. The evolution of the efficiency is shown in Figure 44. The result indicates that the DPF load leads to a 13% reduction of the efficiency at the maximum DPF load. The reduction rate is approximately 3%/g/l.

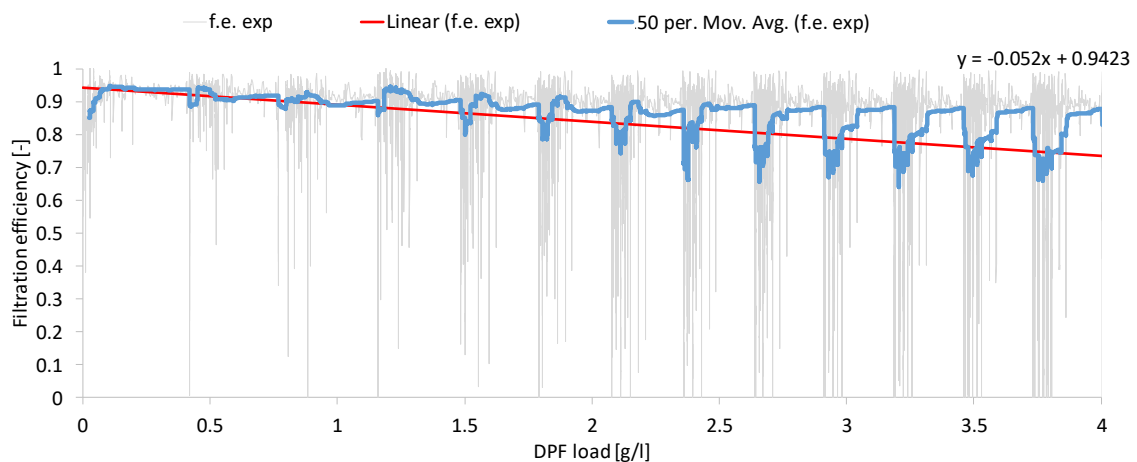


Figure 44: Evolution of filtration efficiency during 13 NEDCs

3.2.3.3. Empirical model

This approach comprises the development of a filtration efficiency map as function of the exhaust volume flow and the DPF soot loading. Figure 45a illustrates the effect of exhaust volume flow on the filtration efficiency for a moderate DPF load (1 g/l) and Figure 45b depicts the reduction of the filtration efficiency for increased DPF load. Despite the linear behaviour that was used in the previous approach, the best fitting is achieved with a polynomial function.

The combined behaviour is depicted in Figure 45c. Base on this map, the filtration efficiency is calculated in a second-by-second basis based on the exhaust volume flow and the DPF load. For low levels of DPF load, the efficiency is high and less sensitive to variations on exhaust volume flow. At higher DPF load levels, the efficiency is lower and more affected by the flow variations.

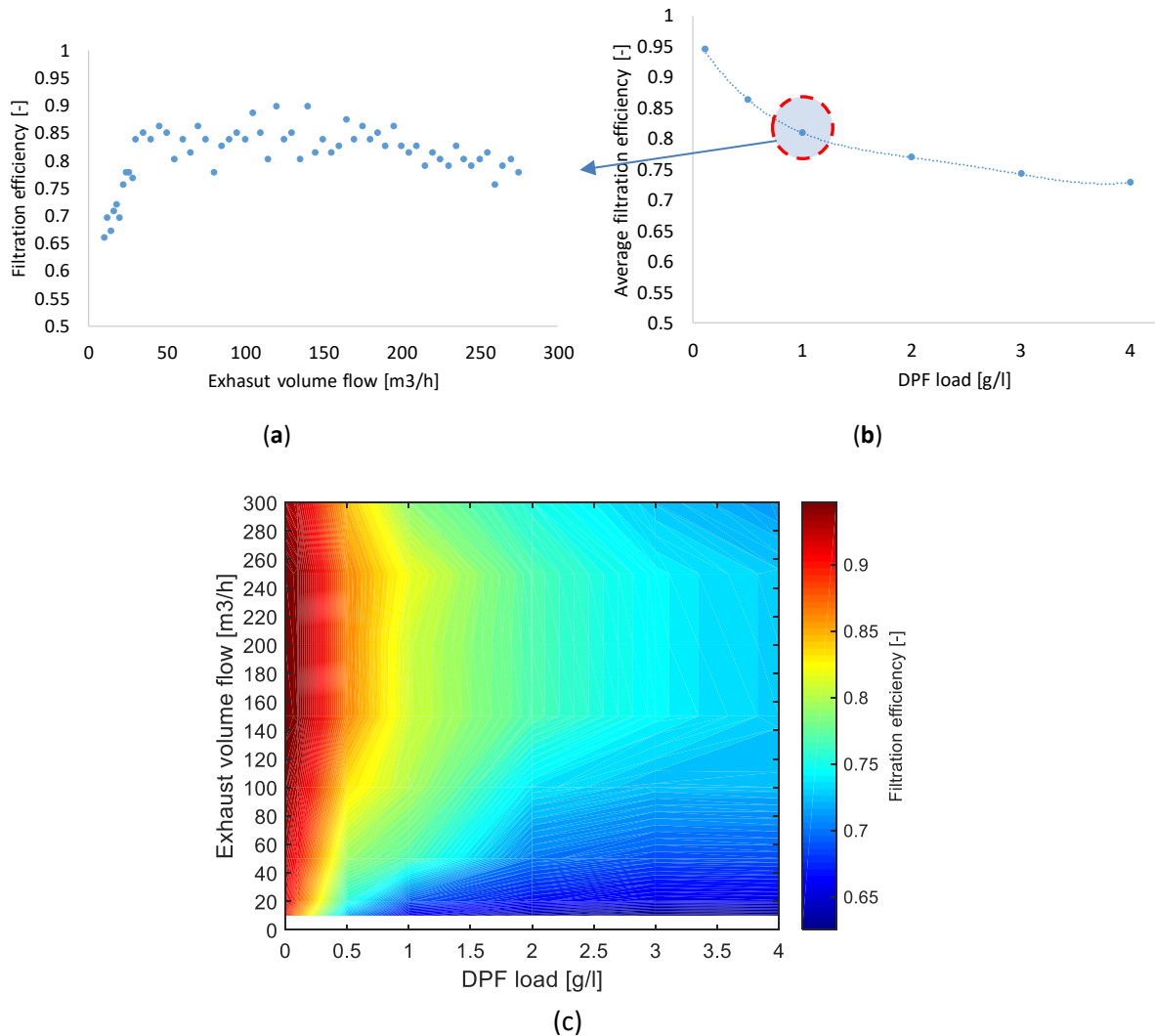
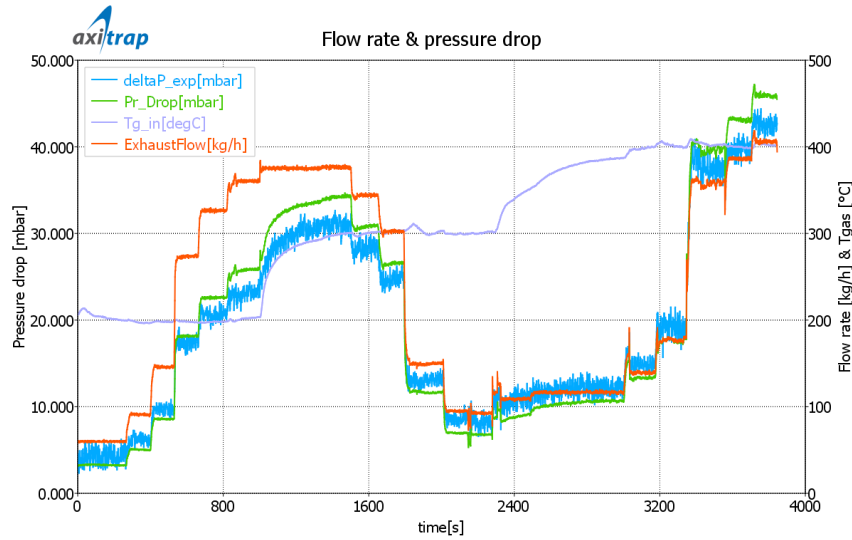


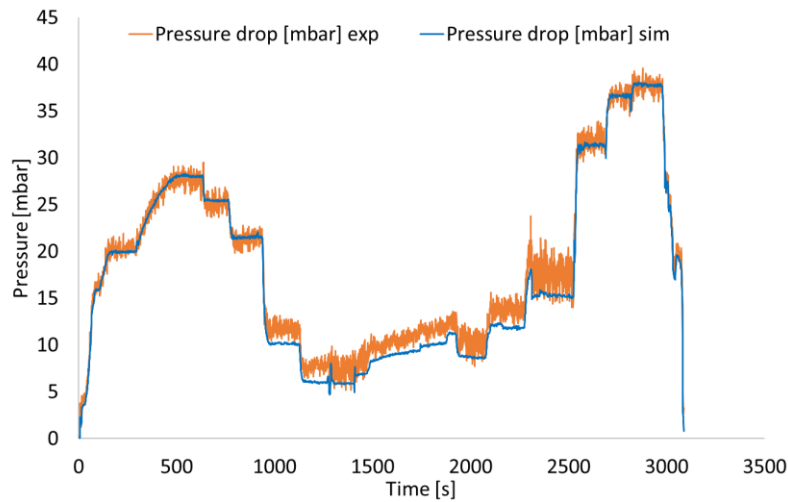
Figure 45: a) Effect of exhaust volume on filtration efficiency b) effect of DPF load on filtration efficiency c) 2D map for the filtration efficiency as a function of exhaust volume flow and DPF load

3.2.3.4. Axisuite

The clean pressure drop tests are performed with a DPF placed upstream of the clean OTL DPF to allow soot-free investigation of the pressure drop through the OTL filter at various flow rate and exhaust temperature levels. Based on this test, the clean wall (substrate) permeability is defined. This test was performed for both full and OTL DPFs (Figure 46a and b).



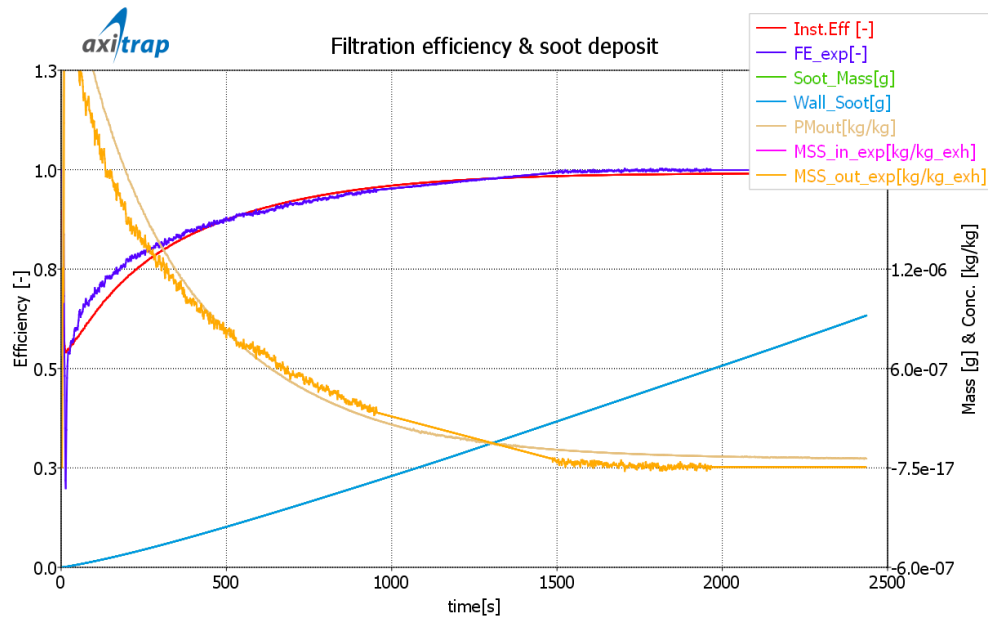
(a)



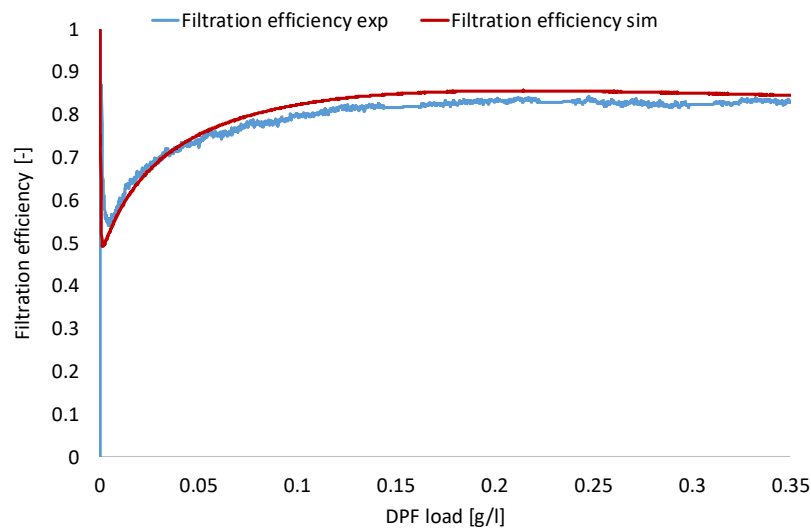
(b)

Figure 46: Clean pressure drop tests for a) full DPF b) partially unplugged OTL DPF

The second test protocol was the filtration efficiency test for the calibration of the correction factors for diffusion and interception, and the gradient parameter in wall filtration efficiency (Figure 47). The engine is operated at constant exhaust flow (150 kg/h), and the efficiency is monitored until it reaches a plateau due to the transition from depth to cake filtration.



(a)



(b)

Figure 47: Filtration efficiency tests for a) full DPF b) partially unplugged OTL DPF

The last test protocol is the soot loading test to investigate the evolution of the pressure drop for the loaded filter (up to 4 g/l). This test is used to calibrate the loaded wall permeability and the soot permeability. The engine is operated at a steady-state point with high soot concentration to accelerate the DPF loading. The last part of this protocol consists of high flow rate steps (similarly to the clean pressure drop test) to compress the soot cake and study its compression (Figure 48).

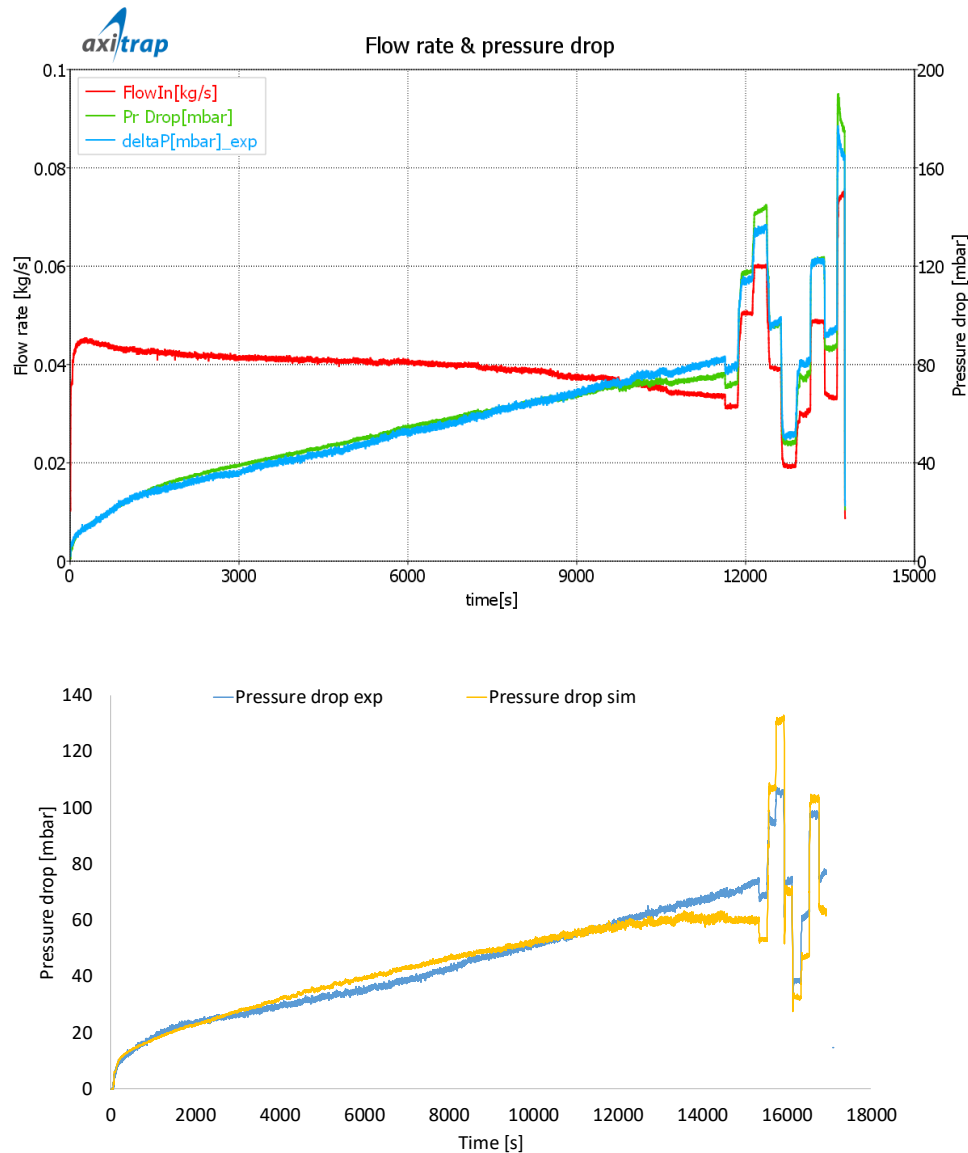


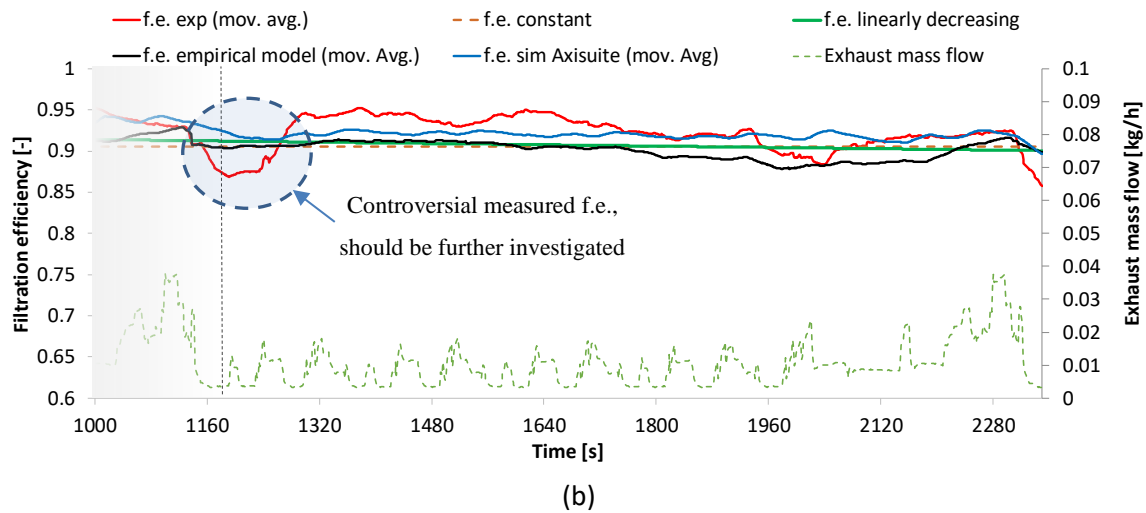
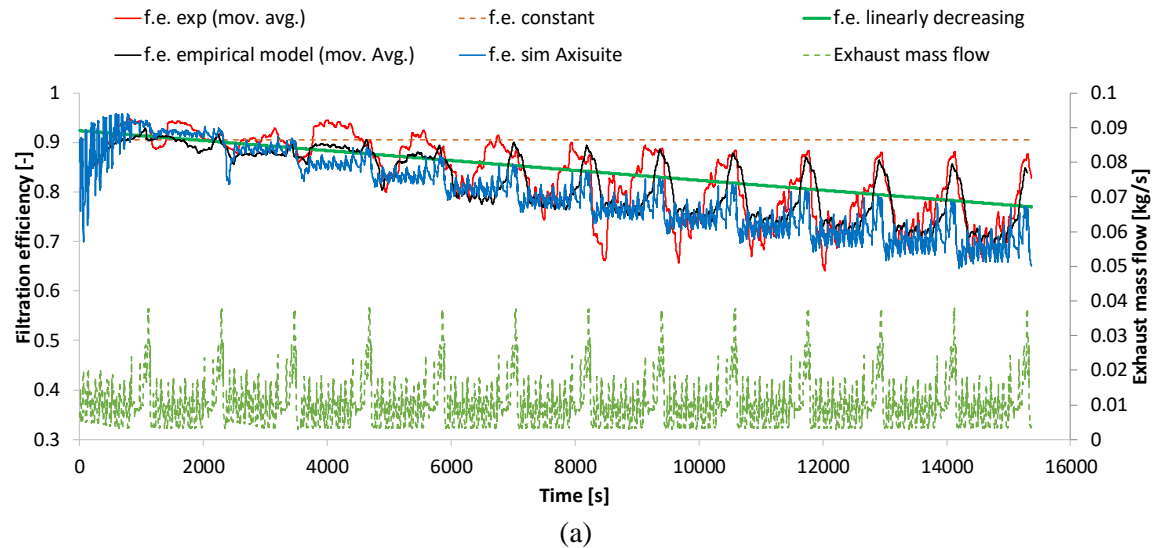
Figure 48: Soot loading tests for a) full DPF b) partial unplugged OTL DPF

3.2.3.5. Performance of the models over transient cycles

Figure 49a illustrates the results of the four approaches for the simulation of the filtration efficiency of the OTL DPF during transient operation (13 NEDCs). The constant approach is lacking accuracy as the DPF load increases. The linearly decreasing efficiency is able to predict the reduction of the average efficiency but neglects the impact of the exhaust flow. The empirical and the Axisuite models are able to provide a more accurate second-by-second prediction of the filtration efficiency.

The performances of the empirical and the Axisuite models are better compared in Figure 49b, which shows the second NEDC of the sequence of the 13 cycles. The first 180 s is the last part of the preconditioning cycle where the efficiency is significantly reducing, and this affects the moving average efficiency (average of 50 values) of the next cycle. This low efficiency at the end of the preconditioning can be partially attributed to the prolonged low exhaust flow due to idle operation at the end of the cycle.

But a closer look at the measured MSS data downstream and upstream of the DPF reveals a possible measurement-related issue (Figure 49c). Due to extremely high soot emissions (up to 400 mg/m^3) of the preceded seconds, possibly either the MSS or the DPF have an unpredicted behaviour (e.g. blow-offs or sensor stability issues). Therefore, the low measured efficiency in this area should be further investigated before trying to create a model to predict this behaviour. Focusing on the comparison between the empirical and the Axisuite models (Figure 49b) after the controversial initial period, their performances are considered similar, and they are both following the trends of the measured efficiency.



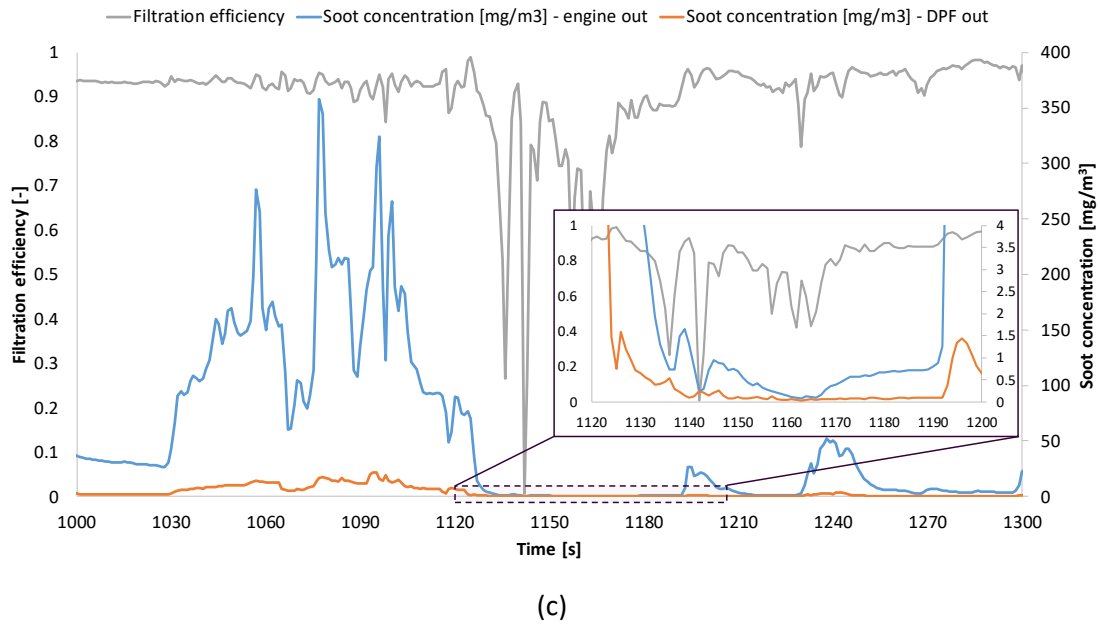


Figure 49: Filtration efficiency a) during 13 consecutive NEDCs b) focus on the second NEDC which is the reference cycle after the preconditioning c) focus at the end of the preconditioning cycle (are with low filtration efficiency)

3.2.3.6. Summary

To summarise, the associated error yields as the average value from the comparison of estimated and measured by MSS soot emissions in every time step for the first NEDC cycle after the preconditioning (Table 13). The empirical and Axisuite models have the highest accuracy during the cycle.

Table 13. Errors of DPF models

Model	Associated average error
DPF model-Constant	$\delta_{cf}=9\%$
DPF model-Linearly decreasing	$\delta_{lf}=7\%$
DPF model-Empirical model	$\delta_{cf}=5\%$
DPF model-Axisuite model	$\delta_{af}=5\%$

3.3. Simulation of the sensor response time (Sensor model)

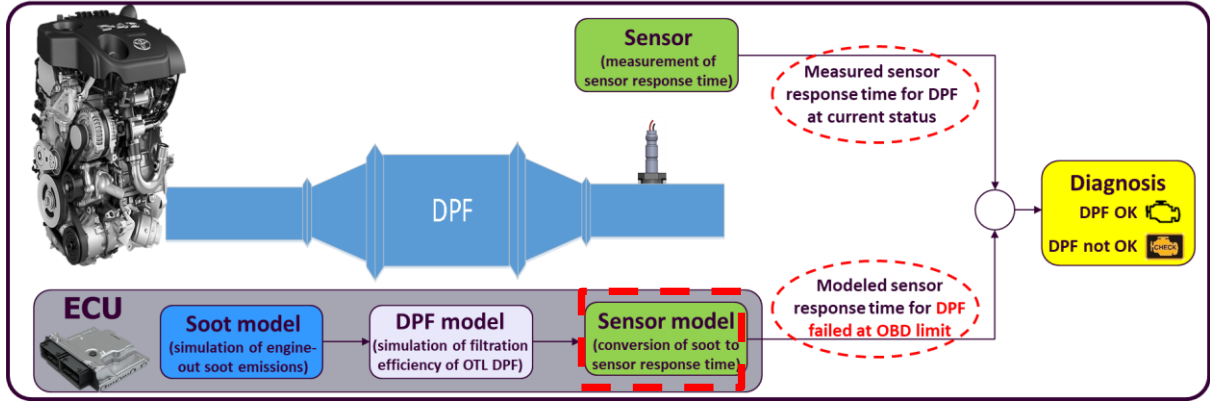


Figure 50: Overview of the OBD model. Focus on the sensor model

3.3.1. Approaches for sensor modelling

The measured value of the sensor is the response time, and thus, the sensor model should also yield the same quantity. This can be performed based on either a statistical model or a physical model. The current study develops a new statistical model and utilises a previously developed physical model to investigate their performance under different conditions.

A physical model was developed and presented by Fragkiadoulakis (2016) and can be used as an alternative approach to the statistical model. The physical model includes five deposition mechanisms: thermophoresis, electrophoresis, convective diffusion, inertial impaction and turbulent impaction. From these five mechanisms, the latter was found to be negligible in comparison with the others, thanks to the sensor design. Once the deposition mechanisms (represented by the total corresponding particle flux) have been determined, the variability of the sensors is expressed in terms of a sensor-specific constant, called “Sensor Constant”. The Sensor Constant is a measure of the cumulative number of particles deposited on the sensor plate during the response time interval (per time unit per sensor plate area). Based on this procedure, the response time of the sensor may be predicted using the following equation:

$$RT_{modeled}[s] = \frac{\overline{n'_A}}{\overline{J_t}}, \quad (7)$$

where $\overline{n'_A}$ is the Sensor Constant defined by a set of steady-state measurements and $\overline{J_t}$ the average particle flux over a time interval. The model considers the deposition velocity of particles of the same size and charge distributions (Maricq, 2006) and accounts for five deposition mechanisms (Equation (8), Table 14) which are thoroughly discussed by Fragkiadoulakis (2016):

$$V_{dep,total} = \sum V_{dep,i} = V_{th} + V_{el} + V_{diff} + V_{imp} + V_{turb} \quad (8)$$

Table 14: Particle deposition mechanisms in a resistive soot sensor

Mechanism	Driver	Main equation
Thermophoresis	Temperature gradient	$V_{th} = -K_{th} \cdot \frac{v_g}{T} \cdot \nabla T$
Electrophoresis	Electric field attracts charged particles	$V_{el} = \frac{J_{el}}{n_0} = \frac{\frac{Z \cdot E \cdot A \cdot n_0 \cdot \Delta t}{A \cdot \Delta t}}{n_0} = Z \cdot E$
Brownian diffusion	Particle concentration gradient	$V_{diff} = 0.664 \cdot Re_L^{1/2} \cdot Sc_p^{1/3} \cdot \frac{\mathfrak{D}}{L}$
Inertial impaction	Velocity component normal to the surface	$V_{imp} = \frac{J_{imp}}{n_0} = \frac{\frac{E_I \cdot A \cdot dx \cdot n_0}{A \cdot dt}}{n_0} = E_I \cdot V_0$
Turbulent impaction	Eddy motion near the surface	$V_{turb} = u^* \cdot \min \left[6 \cdot 10^{-4} \cdot (\tau_p^+)^2, 0.1 \right]$

Where:

- for thermophoresis: K_{th} is the thermophoretic coefficient, v_g the kinematic viscosity of the gas and ∇T the temperature gradient between the sensor and the exhaust gas in proximity to the sensor.
- for electrophoresis: Z is the electrical mobility and E the electric field intensity
- for diffusion: Re is the Reynolds number, Sc_p the Schmidt number, \mathfrak{D} the particle diffusion coefficient and L the sensor plate characteristic length
- for inertial impaction: E_I is the impaction efficiency and V_0 the exhaust gas velocity component which is vertical to the impaction plate
- for turbulent impaction: u^* is the friction velocity and τ_p^+ the dimensionless particle relaxation time

Blow-off events, stickiness probability, different conductivity of particles, soot oxidation on the element, cross sensitivities and contamination of the sensor were not investigated. This simplification would be an issue for a physical model targeting to replicate the second-by-second sensor signal. Our target though was to model and estimate the sensor response time for the OBD model, which relies on cumulative results rather than instantaneous signals. Therefore, all these effects can be compensated through a correction factor, as will be presented in the Scale Factor section.

Based on the analysis from Fragkiadoulakis (2018), each sensor, even with the same geometry needs a different Sensor Constant for the ultimate fitting of measured with modelled response times. It is not possible though, for full vehicle production to calibrate and provide separate Sensor Constants for each part installed in the vehicles. In general, the automotive industry needs a global OBD calibration for all sensors of a vehicle model equipped with the same engine.

Therefore, in this study, a global physical model was used, which is defined by the universal deposition mechanisms (Fragkiadoulakis et al., 2018) and a universal Sensor Constant. This Sensor Constant is the average of all tested sensors and should be valid for all sensors with the same tip and element geometry (different geometry requires a new calibration of the Sensor Constant). Also, in that study, a secondary Sensor Constant was introduced to improve the accuracy at high response times (> 1500 seconds), i.e. very low particle concentrations. All sensor responses in the current study were found to be below the above threshold; therefore, a single Sensor Constant was considered sufficient for the current study.

3.3.2. Methodology for the selected approach

As discussed, the current study focuses on the development of a statistical model. This procedure was repeated several times for all generations of the sensors, but in the next sections, the statistical model for Gen4 sensors is presented. In addition, all results are compared with the performance of the physical model to evaluate the accuracy of both models. The evaluation of both the physical and the statistical models is performed based on the coefficient of determination (R^2) and the Root Mean Square Error (RMSE).

3.3.2.1. Statistical model or Transfer Function

The statistical sensor model was developed in the Toyota engine (Table 5). The necessary emission measurement equipment was an MSS at the sensor position (position 2 of Figure 14a). For the validation of the statistical model, several driving cycles and on-road data were used. The resulting transfer function is a multiple-input single-output function which is typically generated with statistical regression tools, using a sensor measurement steady-state dataset based on a Design of Experiment (DoE) representative of the range of vehicle operating conditions. For the needs of the current study, a function with three inputs was developed. The inputs were selected based on their expected effect on the sensor response time: soot concentration is the main input parameter based on the operating principle of the sensor, and exhaust speed and temperature were found to affect the response time for low soot concentration levels. Enough time was provided for stabilisation of exhaust conditions at the targeted values, and during the whole duration of each point measurement, the three targeted values were constant. In total, three sensors (named Sensor 1 to Sensor 3) with the same geometry and from the same production batch were tested simultaneously. These are Gen4 sensors. Also, at least four accumulation periods were measured at each point for all sensors to check their repeatability.

Figure 51a shows the example of a statistical model for the calculation of the response time. When the exhaust speed increases for a specific exhaust gas temperature, the response time decreases. In this example, temperature affects the response time in a milder manner (Figure 51b): an increase of the exhaust gas temperature causes a decrease in the response time, especially at low soot concentrations.

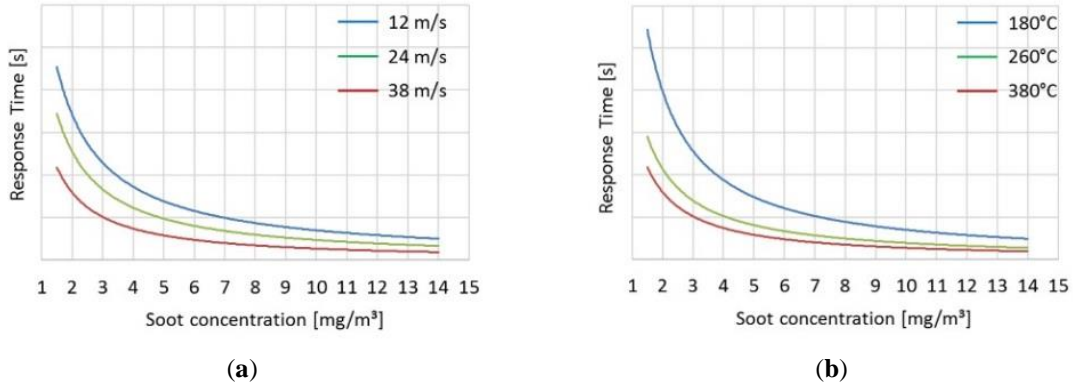


Figure 51. Example of performance of the statistical model over different levels of soot, velocity and temperature. (a) Sensor response time at 220°C for three exhaust gas velocity levels (b) Example of sensor response time at exhaust speed of 24 m/s for three exhaust gas temperature levels

Regarding their shape, the most common empirical function contains natural logarithms (and thus is hereon called “logarithmic function”):

$$\begin{aligned} Time = \exp(a_0 + a_1 \cdot \ln(Soot) + a_2 \cdot \ln(Speed) + a_3 \cdot \ln(Temp) + a_4 \cdot \ln(Soot) \cdot \ln(Speed) \\ + a_5 \cdot \ln(Soot) \cdot \ln(Temp) + a_6 \cdot \ln(Speed) \cdot \ln(Temp) + a_7 \cdot (\ln(Soot))^2 \\ + a_8 \cdot (\ln(Speed))^2 + a_9 \cdot (\ln(Temp))^2) \end{aligned} \quad (9)$$

where, Time corresponds to sensor response time (s), Soot corresponds to soot concentration (mg/m^3), Speed to exhaust gas velocity (m/s) and Temp to exhaust gas temperature ($^{\circ}\text{C}$).

3.3.2.2. Scale Factor (SF)

In both statistical and physical models, the inputs are limited to avoid extensive development effort and keep resulting equations sufficiently simple for OBD application (implementation to vehicle engine control units - ECU). Therefore, there are remaining parameters that are not considered and might be significantly different under specific conditions in a way to affect model performance. In similar cases, calibration factors can correct for zero drift and/or sensitivity drift (Doebelin, 1990) (p68-69). As will be presented in the results section, a constant factor is able to compensate for the remaining parameters. For this study, it was named Scale Factor (SF):

$$RT_{model,calibrated} = SF \cdot RT_{model} \quad (10)$$

The remaining unaccounted parameters may include:

- The blow-off events and stickiness probability of the particles on the sensing element under different conditions (Fragkiadoulakis et al., 2018).
- The conductivity of particles which can be affected by the exhaust aftertreatment devices or the operating point due to different carbon content, amount of ash particle and organic fraction (Maricq, 2006; Grob et al., 2012).

- The soot oxidation on the element induced by the heating of soot bridges due to Joule effect caused by the voltage supplied for electrophoresis (Grondin, 2018).
- The sensor installation as discussed by Linke et al. (Linke et al., 2016) which includes both the orientation of the installation of the sensor in the exhaust line but also the orientation of the sensing element inside the sensor tip as depicted in a CFD analysis for the current sensor (Gkantonas, 2016).
- The particle characteristics such as the particle size or morphology, which may be affected by the operating conditions (Harris and Maricq, 2001; Burtscher, 2005). In our measurements though, in all the DoE steady-state points for the calibration of the physical model (Fragkiadoulakis et al., 2018), the particle diameter size was found to be adequately represented by a lognormal distribution - regardless of the DPF -, with an average geometric mean of $\mu_g = 65 \text{ nm}$.
- The aftertreatment devices (such as SCR with urea injection) that can create new particles or transform the emitted particles in terms of size (Robinson et al., 2016).
- The production/assembly method of the sensor which can create small deviations on the response time.
- The calibration of the regeneration threshold which can directly and significantly change the responses.

Therefore, the physical and the statistical models should be corrected for each project or application similarly to the calibration of the signal behaviour model in a relevant publication (Linke et al., 2016).

3.3.3. Development of the Transfer Function

The development of the statistical model is performed based on steady-state measurements. In order to select the measured levels for soot concentration, exhaust gas speed and temperature, the highest values of these parameters were derived from several legislative cycles that were run for the Toyota engine with the “Above OTL” DPF. Table 15 presents the steady-state dataset.

Table 15. Steady-state levels for the tested sensors (Sensors1-3).

Soot [mg/m ³]	Velocity [m/s]	Temperature [°C]
1.5	10	160
4	20	260
8	30	

The result is a logarithmic function. Its performance is presented in Figure 52 in comparison to the measured data. The performance of the statistical model in most of the measured points is excellent. The only exception is the highlighted point of low exhaust soot, velocity and temperature. The sensor is faster than the model, but this difference is considered within the accepted limit of $\pm 20\%$. Nevertheless, the main focus should be on the validation of the statistical model over input parameters different than those used to develop the model.

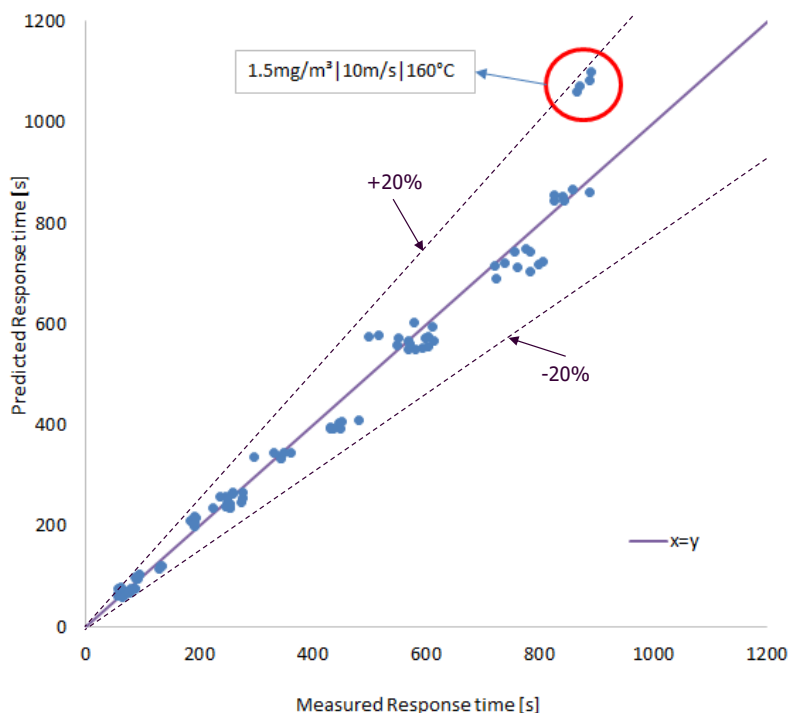


Figure 52. Performance of the empirical function compared to measured data.

3.3.4. Performance and validation

The performance of the statistical model is examined in three different testing protocols: steady-state points different from those used for the development, legislative driving cycles and on-road driving conditions.

3.3.4.1. Steady-state measurements

Before the evaluation of the model over transient conditions as it was described in the objectives of the current study, a different set of steady-state points was examined. These points covered even higher exhaust speed levels (up to 36.5 m/s), and higher temperature levels (up to 300°C) compared to the tested levels during the calibration procedure. These high levels are encountered in the on-road tests, and therefore the performance of the models on this extrapolated area is of high interest. Table 16 summarises the tested levels.

Table 16. Steady-state levels for the validation of the statistical model

Soot [mg/m³]	Velocity [m/s]	Temperature [°C]
2.5	14.5	180
4	25.5	240
8	36.5	300

As discussed in the methodology, for each sensor, at least four consecutive accumulation periods were measured for every point to evaluate the repeatability of the sensors. High dispersion on the horizontal axis (measured response) for a specific point is an indication of low repeatability of the sensors having in mind that all engine and exhaust conditions are constant. The repeatability is good for all points except for one steady-state point (2.5 mg/m³, 14.5 m/s, 180°C) (Figure 53a, highlighted area). The fastest response time should be treated as an outlier. After a closer look at the sensor signal, a possible explanation could be that a soot flake reached the sensor element and suddenly reduced the sensor resistance, leading to response time lower than the anticipated one. This point was included in the analysis to examine the worst-case scenario, which contains outliers due to unpredictable reasons.

Focusing on the accuracy of the physical model compared to the measured response times, the model is found to generally underestimate the sensor response, a behaviour similar to the statistical model (Figure 53c). This may be an indication of a systematic error introduced in the measurement of this extrapolated dataset. More specifically, in order to measure the high exhaust speed and temperature levels, the engine was forced to operate out of the normal ECU calibration. This could have led to significantly different particle characteristics (number, mass, size, stickiness, conductivity). Given that the signal depends directly on soot in the exhaust (Feulner et al., 2015; Reynaud et al., 2019), such differences are expected to appear.

As mentioned above, the differences in the current dataset dictate the need for the introduction of a scale factor which would calibrate the model to adapt it to the measured data. A closer look at the data, reveals that such an SF could be the inverse of the slope of the linear trendline. Using a universal SF for all sensors, a new (calibrated) estimation of the model response time is calculated (Figure 53b).

In terms of precision, the performance of the physical model reasonably agrees with the performance of the model over the data used for its development (Fragkiadoulakis et al., 2018). A good indication of the good precision is the high R^2 and the relatively low RMSE values, which is below 10% of the highest value (Figure 53b). Summary results of the final models shown in Table 17 indicate that the statistical behaves slightly better than the physical model (based on R^2), but both are considered highly accurate.

Comparing the results with the generally accepted rule in the automotive industry that accuracy of $\pm 20\%$ is considered sufficient for DPF OBD (Fragkiadoulakis et al., 2018), Figure 53b and d, show that most of the points are within these limits. The physical model though performs slightly worse in a few of the low response time points.

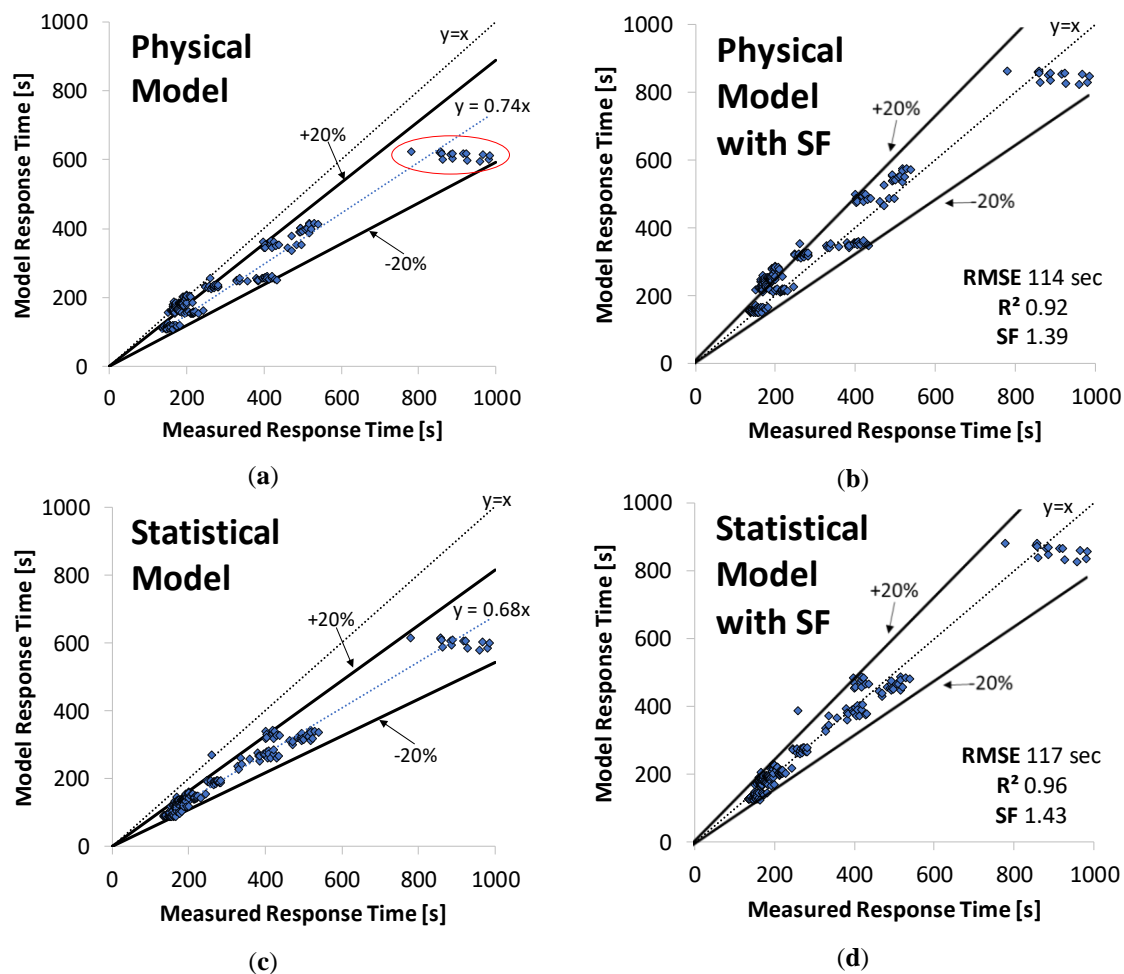


Figure 53. Physical model (a and b) and statistical model (c and d) for all sensors (steady-state tests). Calibrated results (b and d) with the use of the SF shows good performance of both models with a slight advantage of the statistical model.

Table 17. Comparison of R^2 , RMSE and SF between the physical and the statistical model (steady-state tests).

Model	R^2	RMSE	SF
Physical	0.92	114 s	1.39
Statistical	0.96	117 s	1.43

Overall, the global physical model with a universal SF can be both accurate and precise even for high exhaust speed levels and for all tested sensors which is essential for a reduced error of propagation in the OBD system.

3.3.4.2. Driving cycle tests

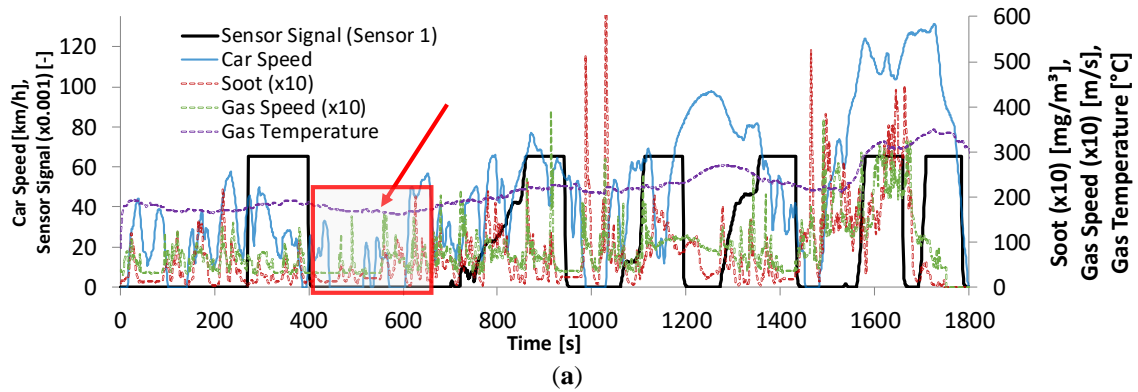
The same sensors, which were employed in the steady-state tests, were also used in a series of transient tests. In these tests, several driving cycles were run on the Honda Accord 2.2 L i-CTDi vehicle (market diesel fuel, lube oil according to manufacturer's specifications), to gather a sufficiently large amount of data, measuring as many sensor intervals as possible. Both hot and cold cycles were tested.

The tested cycles were NEDC (cold) and NEDC hot, WLTC, Artemis Road, FTP-75 (cold) and FTP-75 hot.

Five DPFs at different failure states were used in these tests. The DPFs, characterised based on their total emission in the NEDC cycle, were ranging from 5.2 mg/km to 14.3 mg/km PM emissions, respectively. The sensors communicated with the computer via a Vector CAN Interface (VN 1630), while an AVL 483 Micro Soot Sensor (MSS) was used for the soot emissions measurements.

Figure 54a shows the general characteristics of the performed measurement with the example of a WLTC. Figure 54b is a representative picture of the deposition velocities for all mechanisms (except for turbulent deposition, which is negligible) zooming in a randomly selected part of the first sensor response region for the case of WLTC for better clarity. At the beginning of each sensor interval, the temperature drops from a start value of $\sim 800^{\circ}\text{C}$ due to sensor regeneration (not shown in the graph). At that time interval, the sensor does not attract particles due to thermophoresis. Particle attraction to the sensor due to thermophoresis is induced when the temperature is stabilised approximately after 10-20 s.

Figure 54b also shows that thermophoretic deposition is about twice the effect of electrophoretic deposition for this sensor technology. In some gas speed peaks, the deposition due to impaction increases significantly, while in most cases its effect is negligible and similar to the diffusion. The same behaviour is observed for other driving cycles shown in Appendix A (Figures A1-A3).



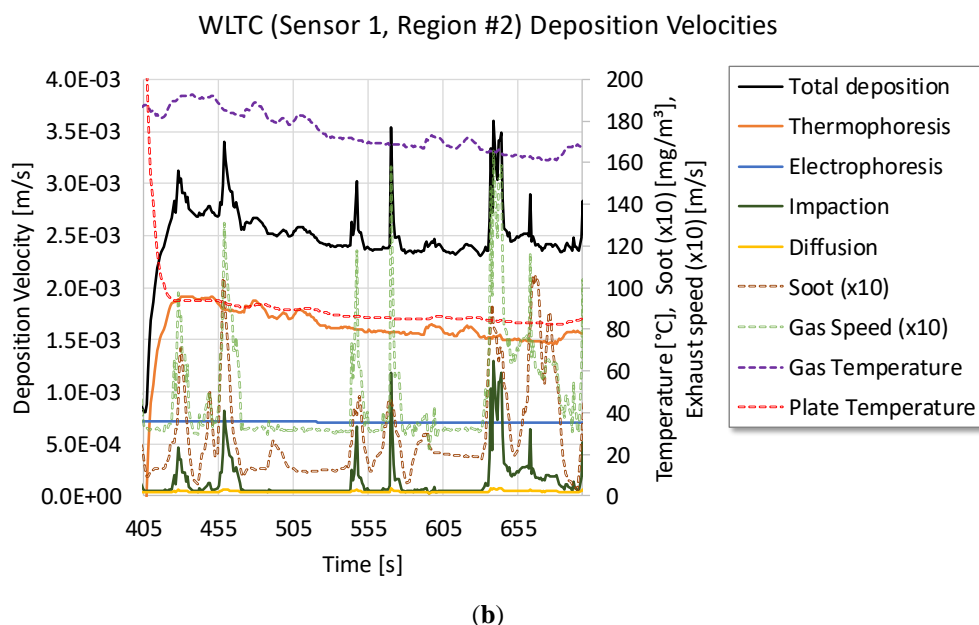


Figure 54. (a) Basic parameters of a WLTC measurement with high PM emissions (DPF emission: 13.1 mg/km). The sensor signal is described by the soot value (no physical meaning of the numbers). Part of the first (valid) loading of the Sensor 1 (highlighted area) is selected to analyse the deposition mechanisms. (b) Deposition velocities at the specified time interval

The same approach - as in the case of steady-state measurements - for the scale factor is applicable for the driving cycles to improve the accuracy of the models. Figure 55a and b show the modelled response time after the application of the scale factor, which was calculated based on data from all sensors. Both the physical and the statistical models perform equally well in terms of precision based on R^2 and RMSE values (Table 18). In addition, there are a few points for both models which are outside of the $\pm 20\%$ limit, but this does not weaken the generally good performance.

The scale factor needed for this dataset is different compared to the steady-state measurements. This can be explained by the differences in the exhaust line set-up and exhaust characteristics used for the transient measurements. The exhaust set-up of the Toyota consisted of straight lines with no bends, whereas the Honda vehicle uses its original exhaust line with compromises in the sensor installation. Therefore, variations of the flow profiles are expected. Also, particle characteristics can be significantly different during the transient tests because the engine is operating under the normal ECU calibration while this calibration is bypassed during steady-state tests and the engine is operating out of its normal calibration maps for most of the points. In addition, the characteristics of particles generated during transient operation may be significantly different due to differences in transient control of the engine (e.g. EGR rate, boost pressure, rail pressure, etc.). This is not the case in steady-state testing since engine control parameters are locked to specific values. The latter is not possible in real-world operation, even during use of vehicle cruise control. An indicative example of the particle size distribution during a WLTC on a Euro 6b diesel vehicle equipped with a partially unplugged DPF is presented in Appendix B. The second-by-second profile of the geometric mean diameter reveals significant deviations of the nominal mean value used in the development of the model.

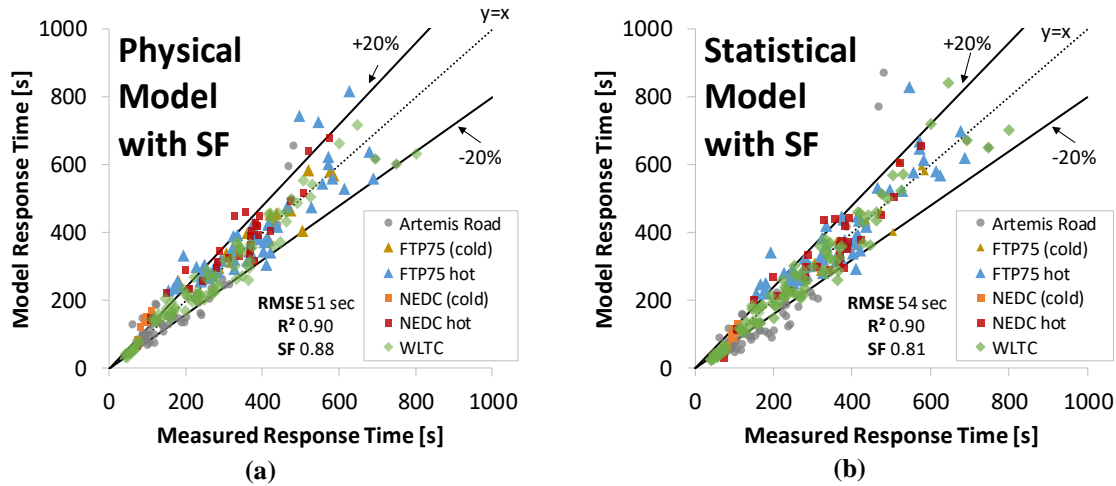


Figure 55. Satisfactory performance of the SF-corrected models for Sensors 1-3 on all driving cycles (a) Physical model (b) Statistical model.

Table 18. Comparison of R^2 , RMSE and SF between the physical and the statistical model (driving cycles tests).

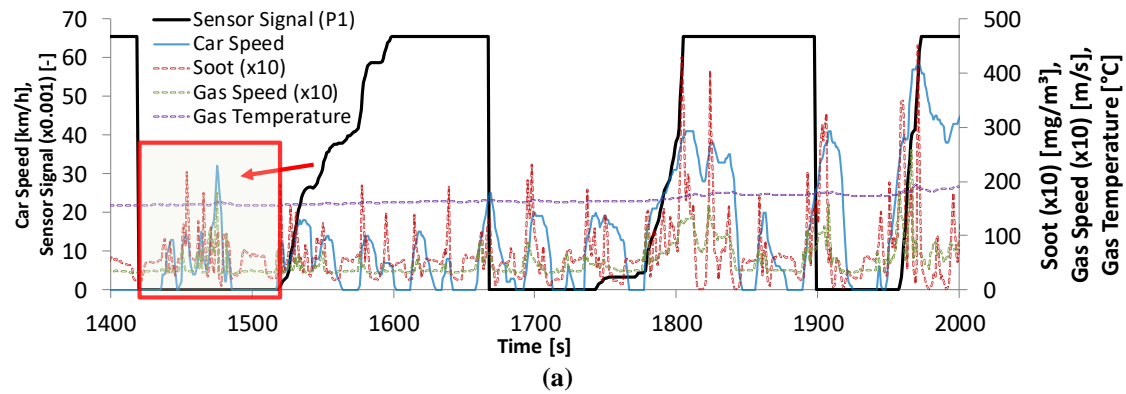
Model	R^2	RMSE	SF
Physical	0.90	51 s	0.88
Statistical	0.90	54 s	0.81

3.3.4.3. Real driving tests

The models were also tested on the dataset that was produced by on-road measurements. The on-road measurements took place with the same Honda Accord 2.2 L i-CTDi vehicle as described in Chapter 2. For these tests, a Pegator Particle Sensor (PPS) which is suitable for OBD applications, was used for monitoring the soot concentration in real-time. The PPS was initially calibrated against the MSS so that the soot concentration measurements are consistent. The PPS was also used in measurements on the same vehicle, during laboratory measurements on driving cycles (Ntziachristos et al., 2011). Along with the PPS, two Gen4 soot sensors (called P1 and P2) were installed in the exhaust line. These sensors share the same geometry with the sensors used before (Sensors 1-3) but different regeneration thresholds. Two artificially failed DPFs were installed on the Accord: a DPF with filtration efficiency calculated at 85% (named as “1.5 x Type Approval” or simply “1.5xTA”) in NEDC and one with filtration efficiency calculated at 65% (named as “Above OBD Threshold Limit +20%” or called “Above OTL” for simplicity) in NEDC.

The on-road measurements consisted of various driving conditions representative of typical real driving conditions. Figure 56a presents an example of urban driving for the first 400 seconds and extra-urban for the duration of the remaining tests. A representative picture of the soot deposition mechanisms can be seen in Figure 56b. Similarly, to the driving cycle tests, thermophoresis is found to be the most

prominent mechanism, with the electrophoresis coming second. The temperature of the sensor plate is - on average - lower than the temperature of the exhaust gas due to heat losses to the environment, and the temperature gradient enhances soot deposition. Impaction is also becoming significant when there are spikes in the exhaust gas speed. Soot deposition due to diffusion does not change significantly and (in most cases) is found at similar levels as the impaction deposition.



Run #1 (Sensor P1, Region #2) Deposition Velocities

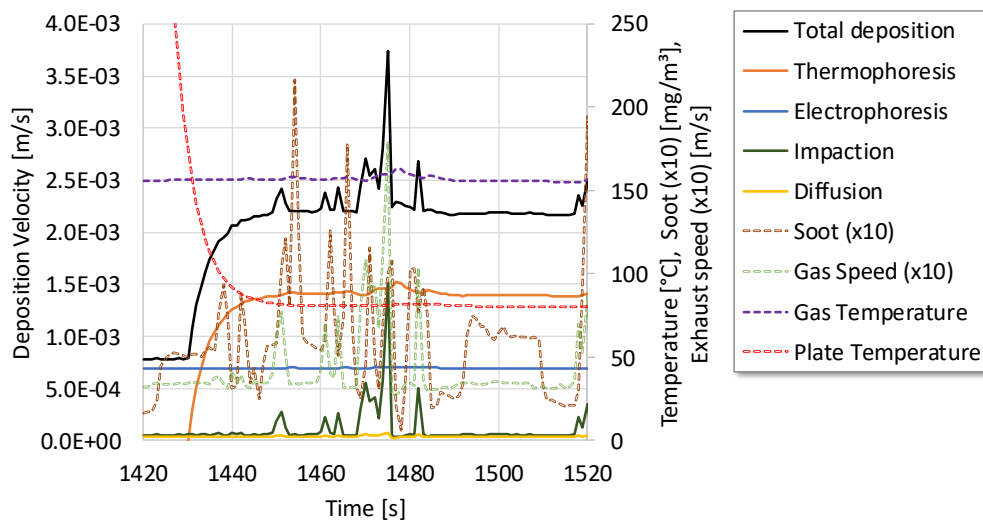


Figure 56. (a) Example of 600 seconds of on-road tests with urban and extra-urban driving. Zoom-in a sample loading of the P1 sensor during the urban route with Above OTL DPF, (b) Deposition velocities for the specified time interval.

The needed scale factor and the final performance of the physical and statistical models are presented in Figure 57a and b and summarised in Table 19. The physical model outperformed the statistical; however, the performance of the statistical model was satisfactory as well.

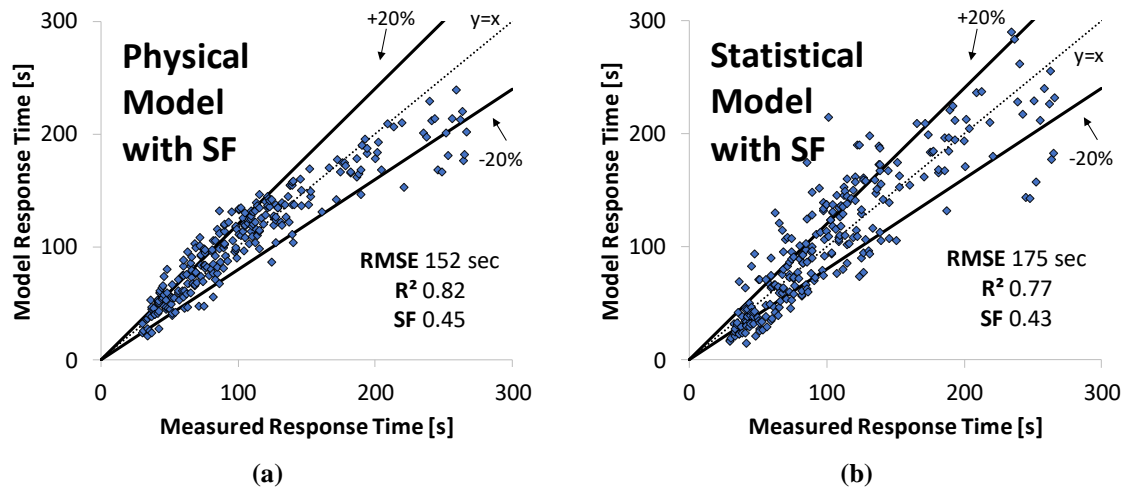


Figure 57. Performance of the SF-corrected models for sensors P1 and P2 (on-road tests). The physical model outmatches the statistical model (a) Physical model and (b) Statistical model.

Table 19. Comparison of R^2 , RMSE and SF between the physical and the statistical model (on-road tests).

Model	R^2	RMSE	SF
Physical	0.82	152 s	0.45
Statistical	0.77	175 s	0.43

Again, a universal SF calibration was found to be sufficient for the analysis. The absolute value though, was found to be significantly lower than the SF used for the driving cycles. The need for a different factor for good model accuracy can be mainly attributed to the various sensors examined in these tests compared to the driving cycles. It was not possible due to practical constraints to use the same sensors in these activities. P1 and P2 sensors were from a different production batch with a different threshold for regeneration triggering than Sensors 1-3. However, they share the same geometry (same-tip and element) and thus, the global model is similarly precise to the driving cycles (expressed by the R^2 and RMSE).

3.3.5. Summary

The analysis of the performance of the model over different conditions concluded to specific accuracy compared to measured response time. In order to calculate only the error due to the implementation of the statistical model, each input of the Transfer Function is associated with the inaccuracies shown in Table 20. Regarding soot concentration, the introduced error is based on the actual soot measurement, which is the targeted accuracy of the soot model.

Table 20. Sensor model variables and associated errors

Variables	Source of inaccuracy	Associated error
Exhaust soot concentration [mg/m ³]	AVL 483 Micro Soot Sensor	$\delta_s=5 \mu\text{g}/\text{m}^3$
Exhaust temperature [°C]	Thermocouple Type K	$\delta_c=3.4^\circ\text{C}$
Exhaust gas velocity [m/s]	Engine intake hot wire and ECU calculated value	$\delta_v=0.23\%$
Intake mass flow [kg/h]	Engine intake hot wire	$\delta_m=2\%$
Fuel injection mass [kg/h]	ECU calculated value	$\delta_j=2\%$
Exhaust Pressure [Pa]	Pressure sensor	$\delta_p=300 \text{ Pa}$
Sensor model [-]	Empirical function	$\delta_{sm}=7\%$

δ_s : The inaccuracy of MSS is specified in the operation manual of the device (AVL, 2011). It is derived from the resolution accuracy of the measurement device ($5 \mu\text{g}/\text{m}^3$) and the dilution ratio accuracy of the conditioning unit ($2 + (\text{DR} \cdot 0.5) \%$). For the current analysis, the dilution ratio was 10, with 7% accuracy.

δ_c : Temperature is measured via a Type K thermocouple, and the corresponding accuracy originates from the probe ($0.75\% \cdot T$) and the recording device (0.25°C).

δ_v : The exhaust velocity is calculated based on the engine intake mass flow measured by a hot wire with 2% accuracy, the fuel injection mass calculated from the ECU (its accuracy is considered same to the one of mass flow) and the pressure measured by a differential pressure sensor with $\delta_p=300$ [Pa].

Therefore, the propagated error based on the above three variables is calculated at 7% based on equation (2), and this can be used as the inaccuracy introduced when a statistical model is used for the OBD model.

3.4. Sensor response time

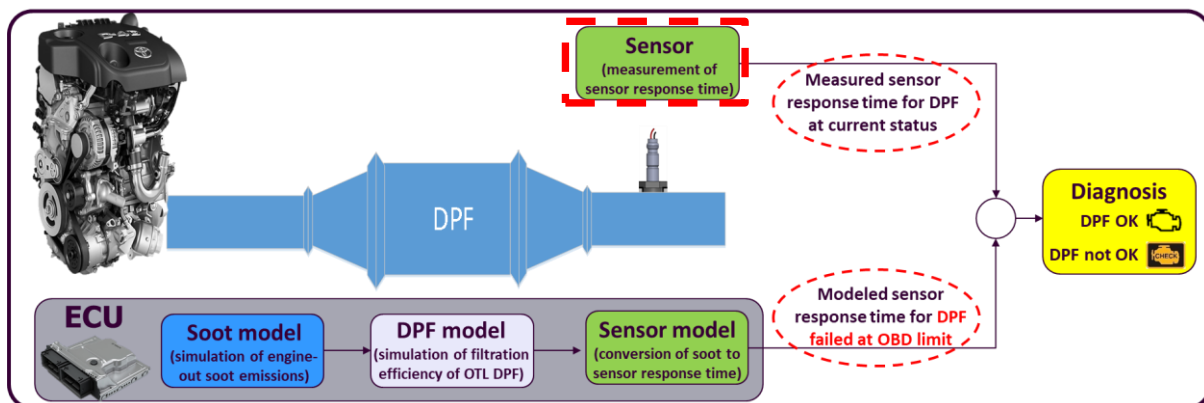


Figure 58: Overview of the OBD model. Focus on the sensor response time

3.4.1. Sensor output

The measured value of the sensor is the response time, which is the duration of the accumulation period. There are also alternative approaches for the useful signal of the sensor which comprise the use of the deadband duration, the slope of the signal during the main loading phase, a part of the response time (e.g. up to the 50% of the signal maximum value), the duration of the regeneration in the case that it is not fixed by the ECM or a combination of the above. Nevertheless, the use of response time is the most reliable and accurate method as was separately studied in a previous analysis.

3.4.2. Parameters affecting the response time

The sensor response time is a calibratable value, which in principle is defined by:

- **Sensor specific characteristics (these are determined during the sensor development)**
 - The geometry of the sensing element. For example, the distance between the electrodes is crucial for the construction of the dendrites.
 - The conditioning of the exhaust gas before it reaches the sensor element. This is performed by the sensor tip and defines the exhaust volume reaching the element, the exhaust velocity, the cut-off limit for big particles etc.
 - The enhancement of the accumulation mechanisms that contribute to the soot accumulation as was described by Fragkiadoulakis et al. (2018) and comprise electrophoresis, thermophoresis, impaction and diffusion. The contribution of these mechanisms is defined by physical limits but also by calibration factors. For example, electrophoresis is induced by a polarisation voltage applied between the electrodes. High voltage, though, leads to local heating of the element (Joule effect), which can oxidise the accumulated soot (Grondin et al., 2019).
 - The threshold set by the ECM for regeneration triggering.
- **Exhaust characteristics (their effect is considered by the sensor model discussed in section 3.3):**
 - The soot emissions in the exhaust line: high soot emissions lead in general to a rapid decrease of the resistance.
 - The exhaust velocity which affects the deposition mechanisms
 - The exhaust temperature which changes the soot resistivity and affects the thermophoresis due to the effect on the temperature gradient between the element and the exhaust gas.
 - The electrical conductivity of the accumulated particles: highly conductive particles or increased conductivity due to low temperature can lead to a rapid decrease of resistance for the same amount of accumulated particles.

- The particle stickiness probability is also an important parameter that defines the accumulation rate.
- **Additional characteristics named as sensor bias or cross sensitivities (these are discussed in section 4.5):**
 - The concentration of contaminants that can either change the conductivity of accumulated particles (e.g. by the accumulation of salts or hydrocarbons) or corrode the platinum, reduce the adhesion of the Platinum on the ceramic, and create cracks on the sensor element.

As an example, three different resistive sensors (different tips and elements) were tested simultaneously under the same exhaust conditions for the same duration (Figure 59). Since the exhaust conditions were identical, only the sensor-specific characteristics were examined. To further reduce the effecting parameters, the same polarisation voltage was used. Therefore, the differences among the three sensors are the geometry of the sensing elements and the conditioning of the exhaust gas in the sensor tip.

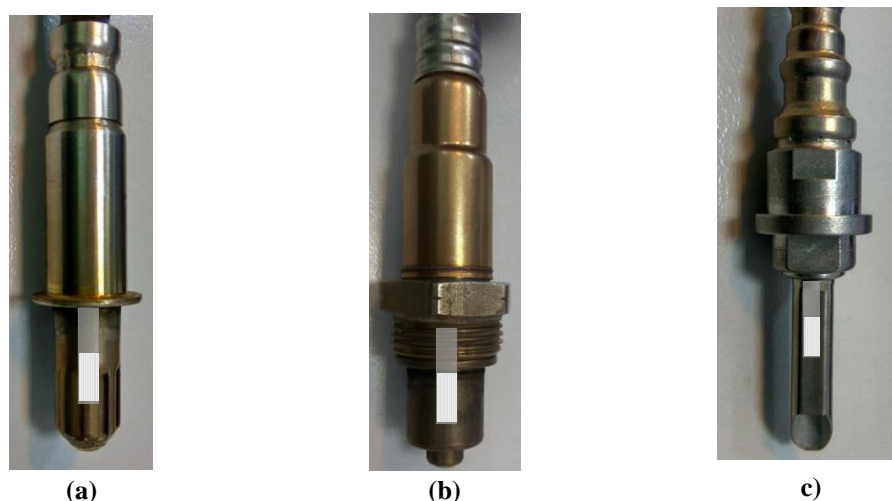


Figure 59: 3 different resistive sensors. (a) Stoneridge resistive sensor (b) Resistive sensor b (c) Resistive sensor c

The SEM images reveal significant differences among the sensors. Stoneridge sensor has mainly semi-completed soot bridges, and there is visible soot build up along the wall of the channel. This can be attributed to the high contribution of thermophoresis which tends to create soot layers, and less effect of electrophoresis which is responsible for the electric field induced growth of soot particles into bridges and dendritic structures (Maricq and Bilby, 2018). Regarding the resistive sensor b, its element consists again of semi-completed soot bridges, but less soot builds up along the wall of the channel, which indicates that electrophoresis should be the primary deposition mechanism for this sensor. Finally, on sensor c, the channels are full of completed soot bridges, and there are considerable areas with high accumulation of soot. This is mainly due to the different geometry of the sensor tip compared to the

other two sensors, which allows significantly higher soot amounts to reach the sensing element. This allows for lower response times, but possibly other contaminant or water condensates can much easier reach the element and affect the robustness of the diagnosis or even the durability of the sensor.

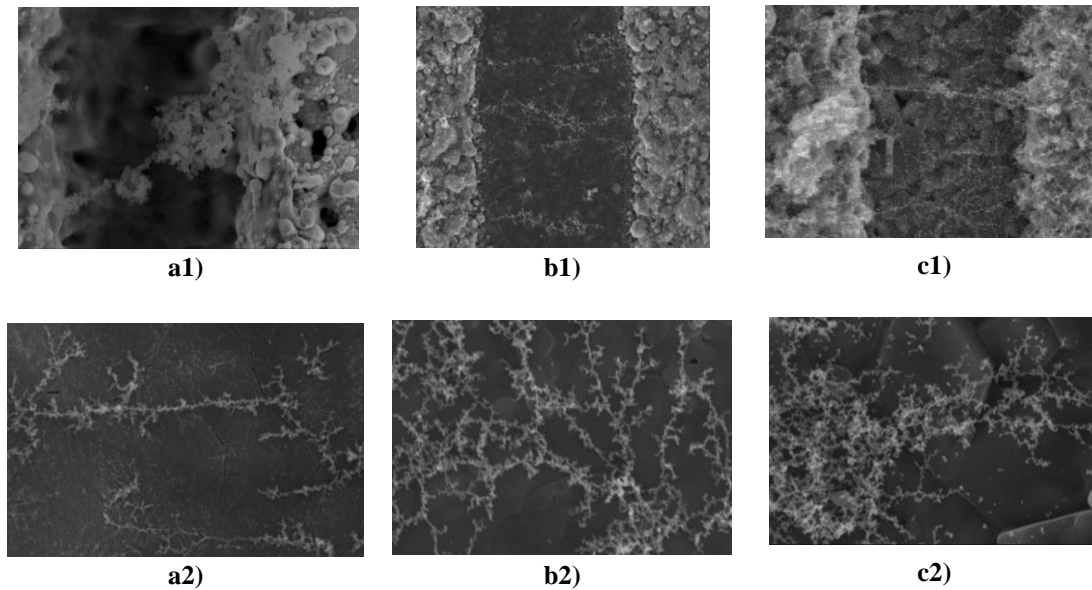


Figure 60: Soot accumulation and construction of dendrites for (a1,2) Stoneridge sensor (b1,2) Resistive b (c1,2) Resistive c.

3.4.1. Calibration of sensor response time for the reference cycle (NEDC)-Sensor inaccuracy

The last part of investigation in the OBD model is the sensor response time. This is not a model but the actual response of the sensor which was also used in the steady-state points of the DOE for the development of the sensor model.

Soot sensors have limited accuracy compared to laboratory measurement equipment. As an example, Khalek evaluated six different soot sensors in several steady-state points and concluded in 60% accuracy in soot concentration measurement compared to a reference device (Khalek and Premnath, 2013). This deviation is considered encouraging taking into account the small size and the low maturity level for the tested sensors (“DieselNet. Soot (PM) Sensors.,” 2019). In the current study, contrary to Khalek’s review where the soot concentration was the sensor output, the response time is the output of the sensor. Thus, its accuracy should be calculated and discussed from this point of view based on several steady-state points. To this aim, 18 steady-state points were measured (Table 21). To compare the measured response time to a reference response time, the empirical function developed in the methodology (Sensor Model) was used to calculate the response time based on the soot measurement of the reference instrument (MSS). The other two necessary input variables of the function (velocity and temperature) were calculated and measured, as described in section 3.3. The measured and the calculated

response times are compared in Figure 61a. The relative errors are presented in Figure 61b. The maximum relative error is 25% and includes both the inaccuracy of the sensor and also the error introduced by the empirical function used for the modelled response time, which is 7% according to Table 20. Therefore, the remaining error can be attributed to all parameters (except for the three inputs of the soot model) that affect the sensor operation. This can be expressed as the inaccuracy of the sensor, which is calculated at 18%.

Table 21. Steady-state levels for the tested sensors (Sensors 1-3).

Soot [mg/m ³]	Velocity [m/s]	Temperature [°C]
1.5	12	180
4	24	240
14	38	

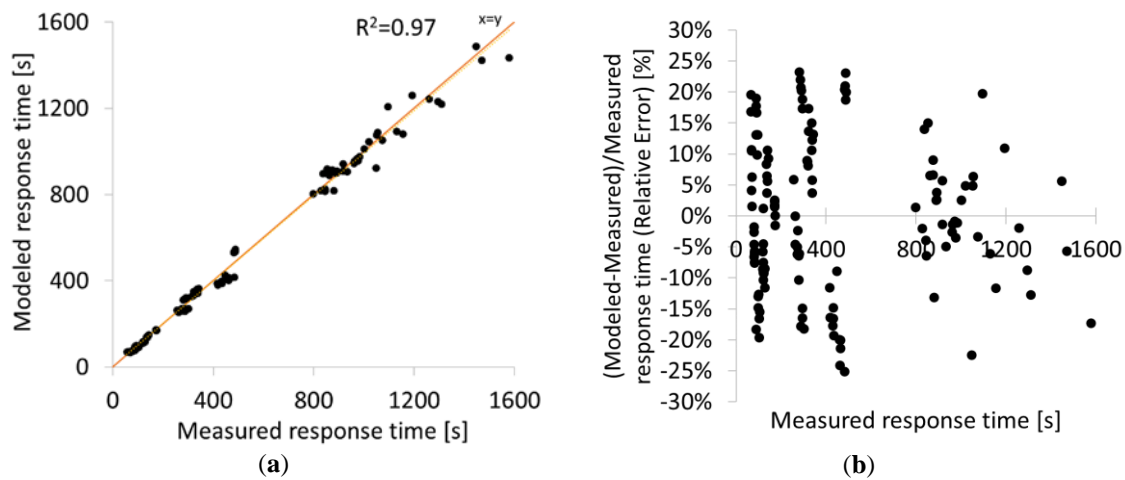


Figure 61. Measured compared to modelled response times in steady-state points, depicted as (a) x=y diagram (b) relative error. The maximum error is 25%.

3.5. OBD Algorithms

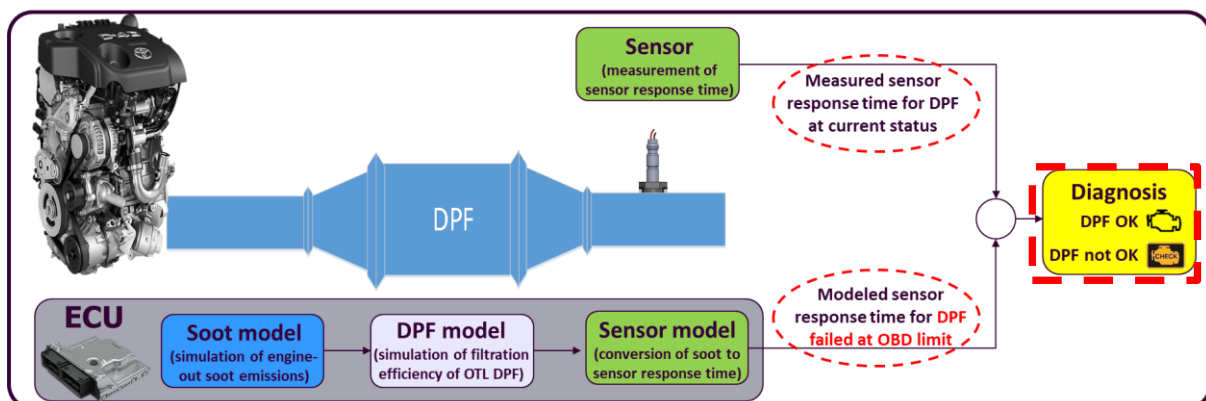


Figure 62: Overview of the OBD model. Focus on OBD algorithms

Having developed the soot, DPF and sensor models, and calculated the errors in every step along with the error of sensor hardware, the final step is to perform the diagnosis, calculate the overall error

of diagnosis (over the reference cycle NEDC) and validate the performance of the model under different transient conditions (both legislative cycles and real-driving conditions).

3.5.1. The error of the overall OBD model

The final implementation of the OBD model in the ECU includes all sub-models. Therefore, the calculated accuracy at this step reflects the accuracy of the DPF diagnosis. The development of the soot, DPF and sensor models, comprised two options: the simple and the advanced. For the soot model, the simple solution was the steady-state soot map, and the advanced was the implementation of the transient correction. Regarding the DPF model, a constant factor was the simple solution, and the advanced considered the DPF load and the exhaust volume flow. Finally, the statistical model was characterised as the simple and the physical model as the advanced solution. Based on our experience, the automotive industry prefers simple solutions to eliminate development and calibration costs, whereas the legislation authorities need advanced solutions for better accuracy, which will allow for lower future limits.

Starting from the automotive industry point of view using the simple approaches, the propagation of the estimated error in all steps lead to the final inaccuracy of 28% (Table 22). This was calculated based on the examined scenario for an NEDC. WLTC and RDE, which represent more aggressive and closer to the real-world driving conditions, are expected to increase the individual inaccuracies and consequently, the overall error of diagnosis.

The soot model using the transient correction and the DPF model based on the Axisuite simulation, lead to a significantly reduced error of the diagnosis (19%). This agrees with the conclusion from Linke (2016) for a resistive soot sensor, who suggests that the highest effort should be put on the soot model calibration.

Table 22. OBD model variables and associated errors

Variables	Associated error (simple models)	Associated error (advanced models)
Soot model	$\delta_{em}=25\%$	$\delta_{em}=2\%$
DPF model	$\delta_{dm}=9\%$	$\delta_{dm}=5\%$
Sensor model	$\delta_{sm}=7\%$	$\delta_{sm}=7\%$
Soot sensor accuracy	$\delta_s=18\%$	$\delta_s=18\%$
Overall OBD model [-]	$\delta_{OBD}=28\%$	$\delta_{OBD}=19\%$

3.5.2. Final diagnosis

The calculated error of 19% in the diagnosis using the advanced models quantifies and validates the statement on the methodology that the threshold for a valid and robust diagnosis must be much lower than the OTL (12 mg/km over NEDC). To define this threshold, additional tests are required with two

emission levels: OTL and TA limit. The Toyota engine (engine #2) with the transient exhaust setup and 2 Gen5 sensors were utilised for this exercise.

The first step is the measurement of the sensor response times (1st branch of Figure 11b) for the OTL and TA DPFs on the tested engine over the NEDC (cold start). The TA DPF was created by symmetrically removing 950 plugs from the outlet of the DPF and the OTL DPF by removing 1750 plugs with the same process. The filtration efficiencies were 71% and 52%, respectively.

We must note here that this OTL DPF (1750 removed plugs) is different from the one that was used on the DPF model (219 removed plugs) despite measuring on the same engine. This is caused by the increased engine-out emissions during the DPF model development due to the failure of the fuel injectors. All DPF modelling approaches (constant, linearly decreasing, empirical and Axisuite models) were calibrated at that time based on the increased emissions, and therefore, their direct implementation on the overall model and the final diagnosis is not possible. For this reason, the empirical DPF model was re-calibrated for the current engine-out emissions, and this is the approach used in the following section. The empirical model was preferred because it offers good accuracy with relatively low calibration effort.

Due to the low engine load during the urban part of the NEDC, the temperature remains at low levels. As previously mentioned, the sensor is activated after the temperature surpasses a pre-defined dew point which for the case of our measurements was set at 90°C (an explanation of the dew point calibration can be found in section 4.5). This temperature is reached only after 720 seconds in the example below (Figure 63), which limits the available time for sensing (only two diagnostic events per cycle). Therefore, for a more robust calibration, data from WLTC were also used (Table 23).

The next step is to calculate the response time for the OTL DPF (2nd branch of Figure 11b). To this aim, the following models were implemented:

- Soot model with transient correction
- Empirical DPF model
- Statistical sensor model

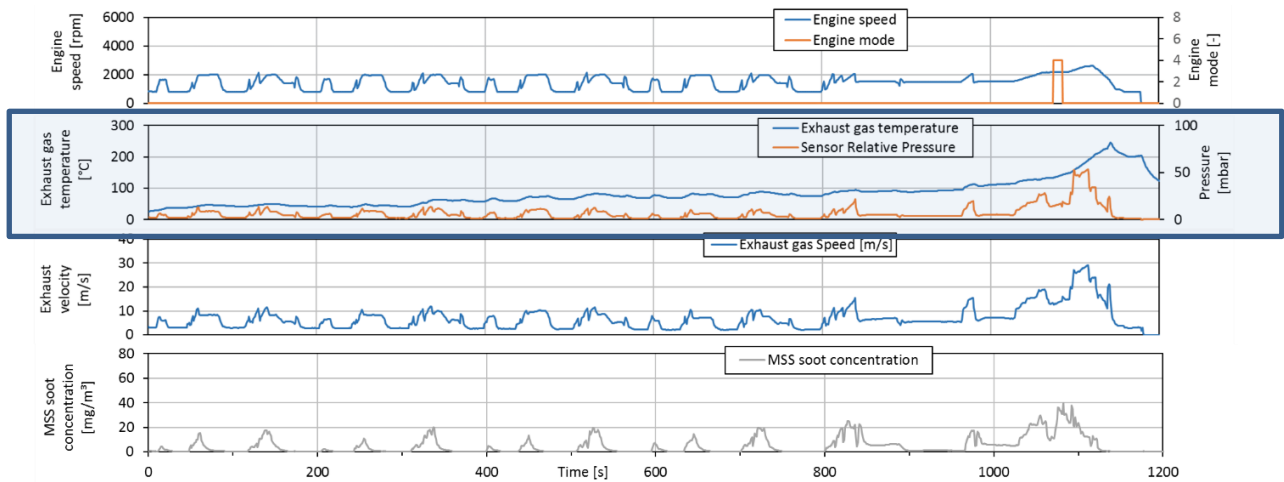
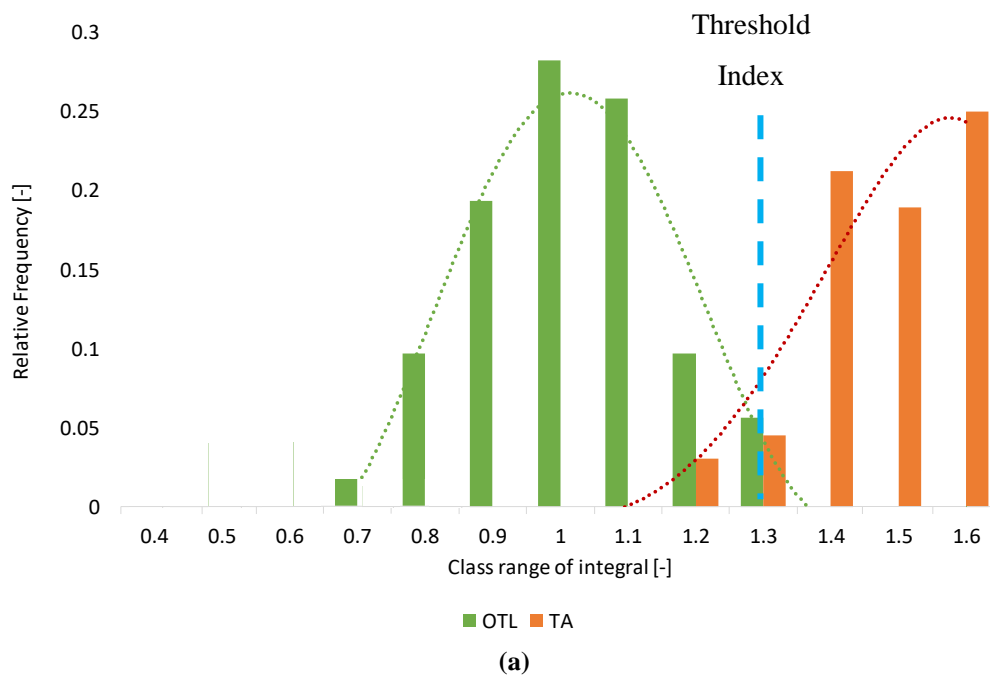


Figure 63: Engine and exhaust parameters during an example cold start NEDC. The temperature remains below the dew point (90°C) for more than the half duration of the cycle. The engine mode (0 or 4) indicates the normal or rich operation of the engine for NO_x release and conversion into N_2 , respectively.

The results of the OBD model for the measurements with the two DPFs (TA and OTL) over the NEDCs and WLTCs create the distributions of the probabilities for the OBD index (integral) presented in Figure 64a. Considering the legislative requirement for zero false passes, the threshold index must be higher than 1.3. As a next step, one can calibrate the threshold filtration efficiency to bring the threshold Index to 1 (this step is not necessary but provides a better overview and understanding of the concept) (Figure 64b). Therefore, the final threshold Index is 1, the threshold efficiency is calculated 58% (average value) and the threshold emissions are 9.7 mg/km . Based on this calibration, there are some false failure events in the case of the TA DPF, which can be reduced or eliminated with rejection criteria and debouncing strategies as will be discussed below.



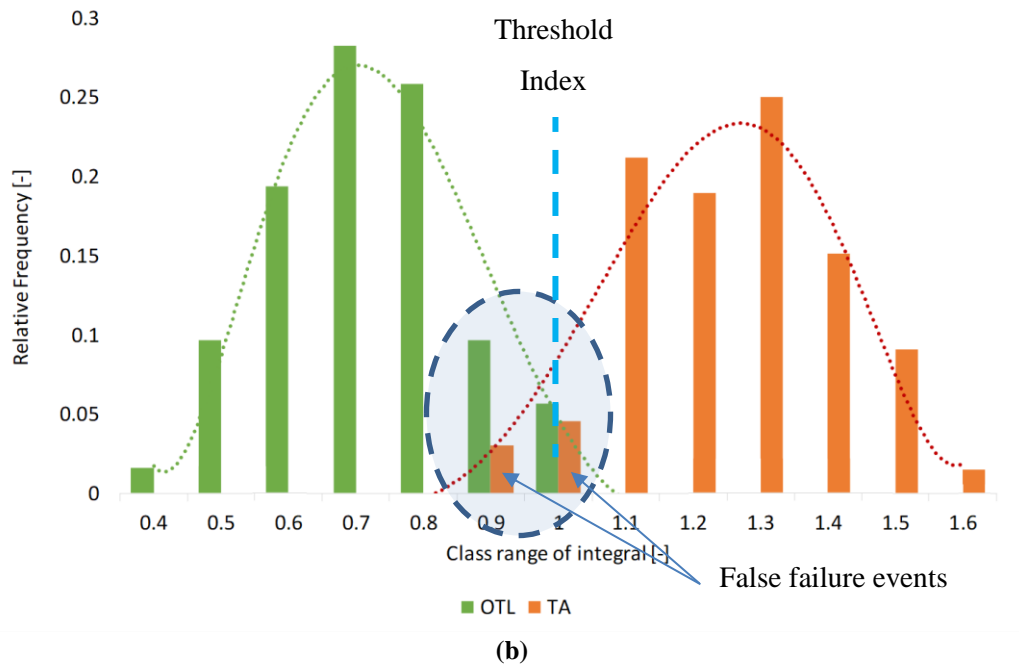


Figure 64: (a) Definition of threshold Index (b) Calibration of the threshold filtration efficiency to adjust the threshold Index to 1.

Table 23: Number of accumulation periods, corresponding emissions and false events for the calibration of the Threshold filtration efficiency (final calibration)

Driving Cycles	Sensor repetitions (2 sensors)	PM emissions [mg/km]	False pass events	False failure events
WLTC OTL	70	16.1	0	0
NEDC OTL	25	11.7	0	0
WLTC TA	51	7.7	0	4
NEDC TA	20	5.2	0	3
Total	166	-	0	7

3.5.2.1. Rejection criteria

The false failures events in the example above, can create warranty costs and customers complain, and thus, should be eliminated. Also, despite the focus of the calibration to ensure zero false passes, such events can still be possible either due to extreme or unpredictable conditions. Therefore, it is necessary to develop rejection processes to improve the robustness of calibration and eliminate false events. The next criteria are based on the fact that Stoneridge sensor is fast enough for at least two diagnostic events during the homologation procedure with an OTL DPF (12 mg/km). To validate this hypothesis, a threshold DPF was created and measured over 10 NEDCs. In all cycles, the minimum number of events was two, so the hypothesis is considered valid.

3.5.2.1.1. Elimination of false failure events-Derivative of the sensor signal

An example of a part of a real driving profile is used to elucidate the issue (Figure 65) with a Gen5 sensor on the Toyota engine. The DPF is at the TA level, so the diagnosis must be “DPF OK”. Nevertheless, the second and fourth diagnostic events fail to provide a successful diagnosis. This can be attributed to an aggressive operation, which leads to a sharp increase in sensor signal (sensor peak). This can be quantified by the derivative of the sensor signal. The implementation of a calibratable limit on the derivative can reduce false failure events. To avoid the rejection of “DPF not OK” when the emissions are always high (e.g. due to OTL DPF or total DPF removal), this criterion is activated only after a “DPF OK” event. Therefore, if there are two consecutive “DPF not OK” events with high signal derivative, the event is accepted, and the diagnosis is valid. In the case that this criterion fails to filter the false failure, according to the legislation, it is possible to erase the “DPF not OK” after 40 consecutive warm-up cycles (UNECE, 2015). This is though accepted only by the EU legislation.

The highlighted areas indicate that a threshold derivative (e.g. 5000) can successfully reject the false failure events in this example. To validate the above rejection scheme, it was evaluated for the WLTC TA and NEDC TA data of Table 23. The false failure events decreased from 7% to about 2%.

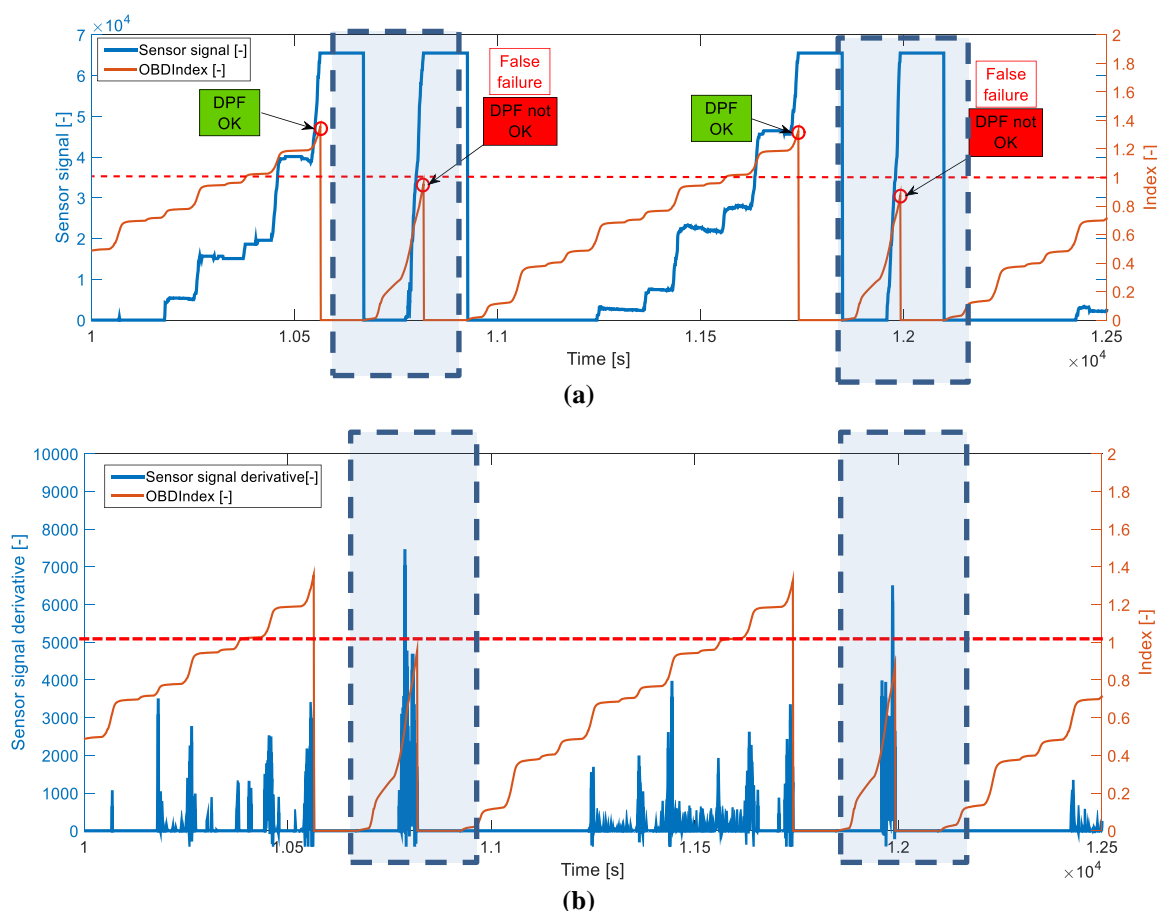


Figure 65: Real driving cycle with a TA DPF and two wrong diagnoses (false passes).

3.5.2.1.2. Elimination of false pass events-Debouncing strategy

In principle, debouncing is the development of timers or counters that run as a function of boundary conditions for decision making. Debouncing strategies for DPF diagnosis can be used to prevent false pass events in the case that the sensor is fast enough to complete more than one accumulation periods during the legislative driving cycle with an OTL DPF. The initial counter at engine start is kept from the previous operation. For every diagnostic event (i), (i=1,n):

- If the diagnosis is “DPF OK” \rightarrow Counter (i)=Counter (i-1) -1 (min. Counter=-1)
- If the diagnosis is “DPF not OK” \rightarrow Counter (i)=1

The final diagnosis after the debouncing is as follows:

- Final Counter=1 \rightarrow “DPF not OK”
- Final Counter=0 \rightarrow Repeat the diagnosis, 1st stage for DPF OK
- Final Counter=-1 \rightarrow “DPF OK”

Therefore, for a “DPF OK” diagnosis, there is a need of at least two consecutive false pass events. On the other hand, if the last event is a “DPF not OK” diagnosis, there is no need for an additional event.

Having in mind that the debouncing strategy is introduced to prevent false pass events during the homologation procedure with the OTL DPF, Figure 66 presents an example of an FTP-75 driving cycle with an OTL DPF. The sensor that was used was a Gen5 sensor. In this case, the first event is a correct “DPF not OK” diagnosis, whereas the second is a false pass event. Without debouncing the final diagnosis would be “DPF OK”. With debouncing, the final counter is 0 and therefore, repetition is needed, which is allowed by the legislation. A more aggressive scenario to ignore the false pass would be to declare the counter=0 case as “DPF not OK”, and in that case, there is no need for repetition.

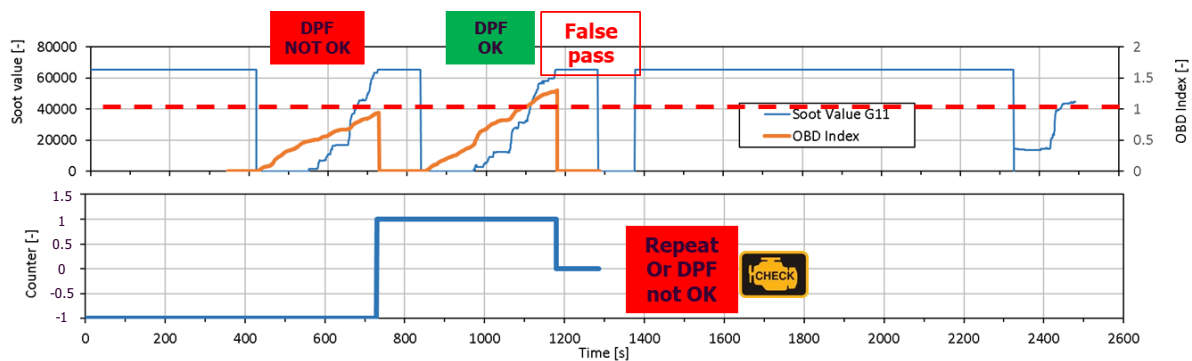


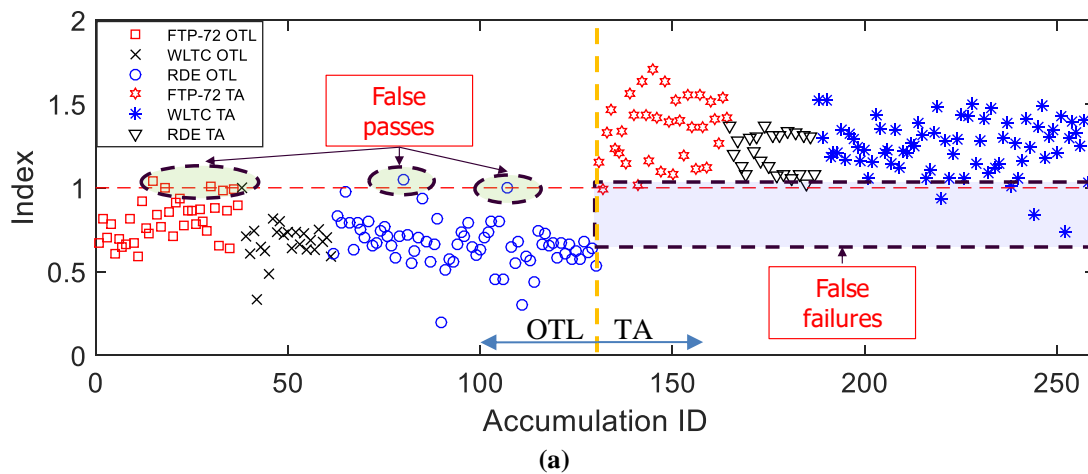
Figure 66: Example of debouncing strategies for DPF diagnosis over an FTP-75 driving cycle

3.5.3. Validation of the model

Up to this point, the three models (soot, DPF, sensor models) and the OBD algorithms were separately developed in NEDC and validated in WLTC (FTP-75 for the debouncing) for the Toyota engine. The target of an OBD system is to perform well in real driving conditions. For this reason, 2 Gen5 sensors were measured in the Toyota engine over the real driving #2 route. This a reproduction in the engine dyno of an RDE compliant route with a Toyota vehicle with the same engine (Ntziachristos et al., 2016). The test was repeated for 2 emission levels (TA and OTL DPFs). The following models were implemented:

- Soot model with transient correction
- Empirical DPF model
- Statistical sensor model
- OBD algorithms with rejection criteria

Figure 67a summarises the performance of the overall OBD model before the implementation of the rejection criteria. There are a few false passes and false failures which can be successfully eliminated by using the debouncing strategy and the derivative of the sensor signal, respectively (Figure 67b). Figure 67c contains the same data as the previous image depicted in a bar chart. The outcome is that the model is able to distinguish the two emission levels using the rejection criteria since there is no overlapping of the OBD indexes: all OTL measurements yield indexes below 1 and all TA measurements overcome this threshold.



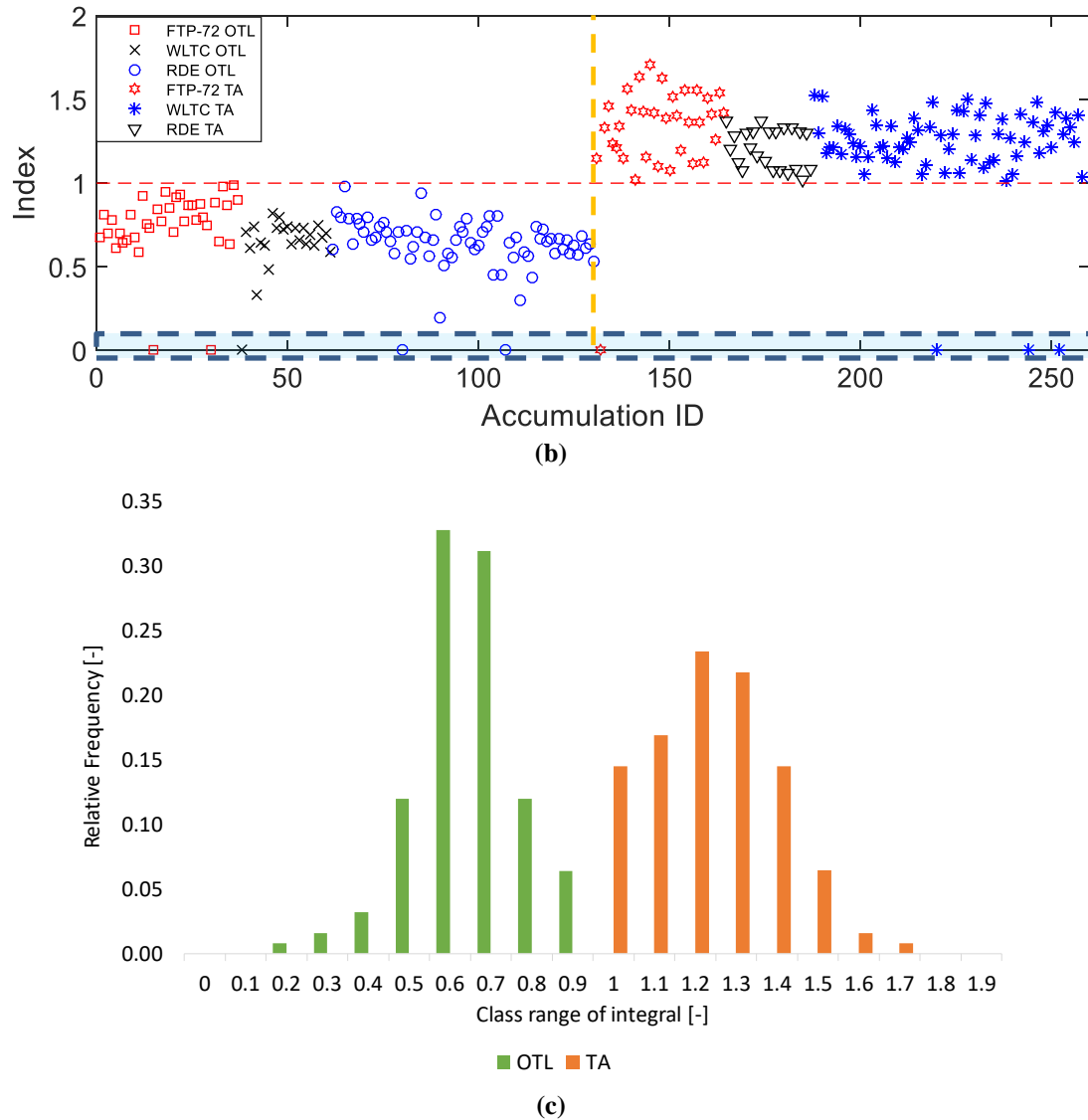


Figure 67: a) OBD Indexes without rejection criteria b), c) with rejection criteria

The last question that needs to be answered is whether the model can successfully diagnose the performance of a full DPF (filtration efficiency=99.9%). To this aim, a few RDE tests were also performed with a fully operational DPF. The model behaved as expected, and the sensors were triggered to regeneration after 1800 seconds before completing a full accumulation.

3.6. Summary and conclusions

An OBD model for the diagnosis of the DPF was developed in this chapter. The different options for every sub-model, the accuracy and the validation of the selected approaches and the performance of the overall model were discussed. The primary outcomes of this investigation can be summarised as follows:

- The soot model can be accurate enough when a transient correction is used. The final error was calculated at 2% compared to MSS measurements over the NEDC
- The advanced DPF model (Axisuite/Exothermia) by considering the effect of DPF load on filtration efficiency, improves the performance of the constant filtration efficiency approach and leads to a DPF model error of 5%.
- The sensor model predicts the sensor response time of the threshold emission either with a statistical or a physical model. The implementation of each of these models returns the same error of 7%.
- The accuracy of the resistive sensor is calculated at 18%.
- The cumulative error of the OBD model over the NEDC is calculated to be 19% (28% for the base models).
- The advanced OBD model was implemented to distinguish two emission levels: the TA and OTL. Using rejection criteria, it is possible to eliminate false pass and false failure events.

4. Challenges and limitations of the sensor model and the resistive sensor

Chapter 4 is dedicated on the sensor model and the resistive sensor. The implementation of the OBD model using a resistive sensor in the ECU of a vehicle requires i) the optimum performance of the sensor model under all driving and exhaust conditions ii) the fulfilment of a few technical specifications provided by the automotive industry and iii) the resolution of early-raised issues after sensor first installation in pre-production vehicles (realisation phase). This chapter focuses on:

- Evaluation of the performance of the sensor model over wide/extreme exhaust and operating conditions
- Evaluation of sensor installation limits: supply voltage, sensor orientation and water protection
- Calibration of dew point to allow enough time for sensor operation during cold start cycles and in parallel, avoid cracks and bias of sensor signal due to humidity (supplementary to water protection)
- Assessment of the possible effect of exhaust contaminants with focus on NH_3 and ash

4.1. Performance of the Transfer Function under extreme driving conditions

The statistical model, as presented in section 3.3, is the sensor model that is currently implemented in the vehicle applications that use the Stoneridge resistive soot sensor. The performance of the model for Gen4 vehicles has been already validated for steady-state points, legislative driving cycles and real driving with Honda vehicle. The target of this section is to first develop the new Transfer Function for the latest sensor generation (Gen5) and mainly examine the behaviour of the model on extreme conditions. For this reason, a new campaign of real driving was set with the Peugeot vehicle (vehicle #2). The measurement protocol comprised two driving profiles:

- Real-driving #2 (RDE-compliant) according to the RDE legislation requirements for the test route (EU, 2016) (reference conditions).
- Real-driving #3 (RDE-dynamic) with wider engine operation and aggressive driving.

The new Transfer Function was developed following the methodology described in section 3.3. Steady-state points were measured on the engine dyno (Toyota engine). The selection of the points was based on the analysis of transient data with an OTL DPF (after dew point reached at 120°C) and the technical constraints for measuring steady-state points, similarly to the development process on section 3.3. The difference, in this case, it that the transient data were the RDE-compliant routes with the Peugeot vehicle. The analysis of the three input variables (soot, exhaust velocity and temperature) are presented in Figure 68 (colour-filled boxes) and the finally selected levels for the DoE in Table 30.

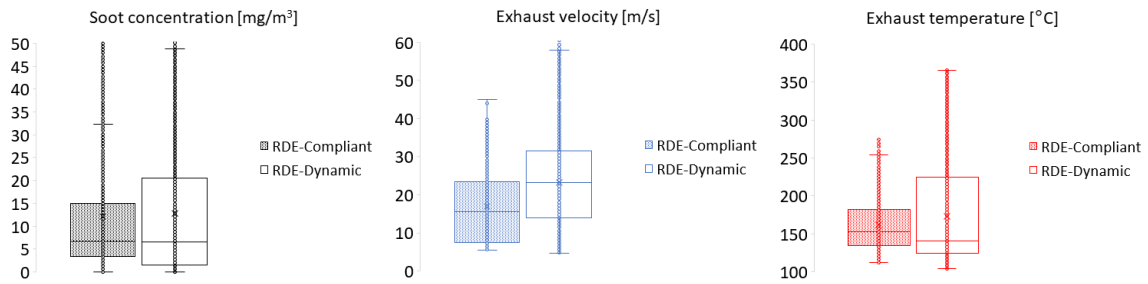
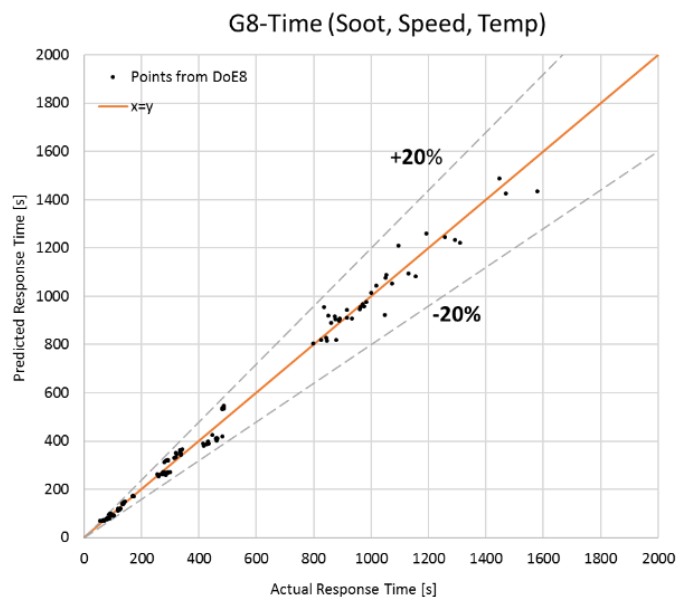


Figure 68: Soot, velocity and temperature for RDE-compliant (colour-filled boxes) and dynamic routes (no-fill boxes)

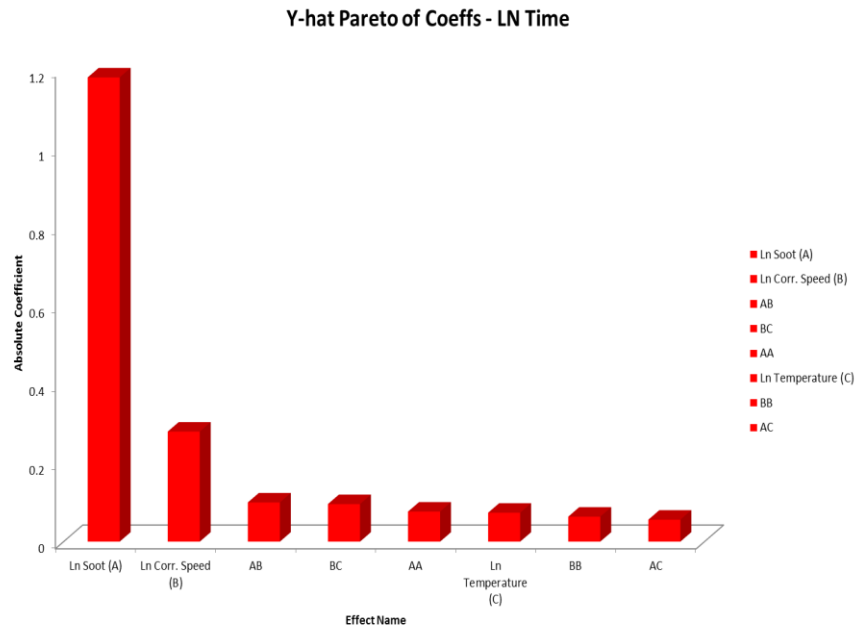
Table 24. Steady-state levels for the development of the new Transfer Function.

Soot [mg/m³]	Velocity [m/s]	Temperature [°C]
1.5	12	180
4	24	260
14	38	

The performance of the Transfer Function over the DoE levels is shown in Figure 69a. As expected, the performance of the TF is perfect. The next question to be answered for the new TF is its performance on RDE-compliant and dynamic routes.



(a)



(b)

Figure 69: a) Performance of the TF on DoE steady-state points b) Pareto charts for the contribution of each term of the TF. Soot is the most significant input parameter.

Plug removal was followed to create the OTL DPF for the Peugeot vehicle over the NEDC (reference cycle). Having installed the OTL DPF in the exhaust, the vehicle performed several repetitions of real-driving 2 and 3 routes (RDE-compliant and RDE-dynamic). The TF was calibrated using a scale factor based on the RDE-compliant data (reference data). The performance of the new TF is depicted in Figure 70. During the dynamic driving, there are a few events with significantly lower measured than predicted response times (highlighted area). These events are attributed to high soot peaks due to aggressive driving, and the criterion of the derivative of the sensor signal on the OBD algorithm is able to reject them from the final diagnosis. In principle, the TF is slower during dynamic driving, which indicates that aggressive driving can accumulate soot faster than what is predicted.

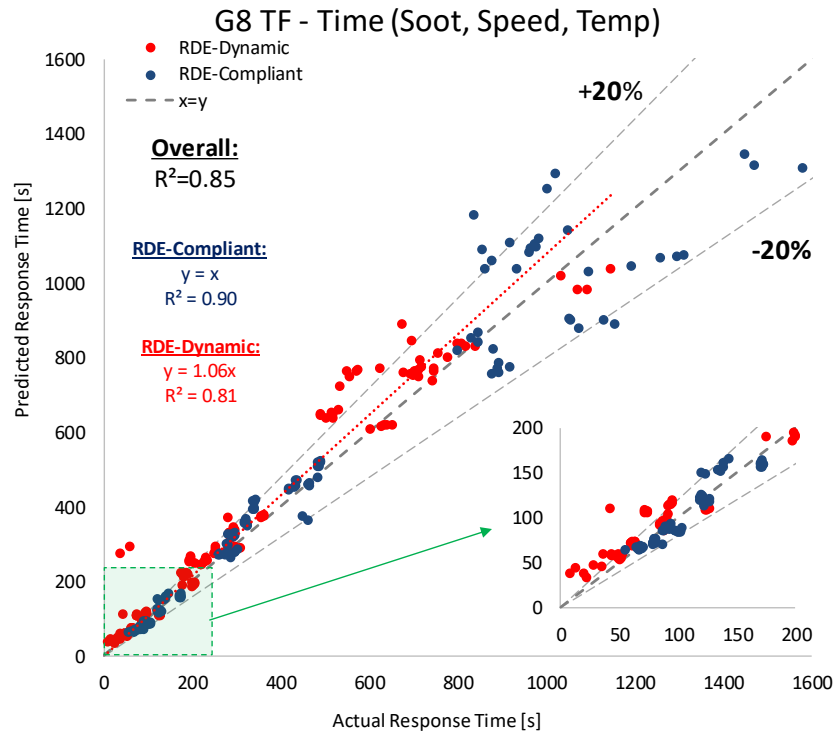


Figure 70: TF performance on RDE-compliant and RDE-Dynamic routes

Also, based on Figure 68, the main difference between the two driving patterns is observed at the higher values for all three input parameters. A closer look on the shape of the TF (Figure 51), reveals that the investigation of higher soot levels will not improve the performance of the TF since the sensitivity is low for higher than 12 mg/m^3 . On the other hand, additional speed and/or temperature levels will probably improve accuracy. Therefore, an extra speed level of 60 m/s and an additional temperature level of 380°C were added in the DoE. A new TF was developed, and the comparison between the two RDE routes is illustrated in Figure 71. The performance is slightly better, which indicates that improvement is possible with additional effort on the development of the TF with extended input levels.

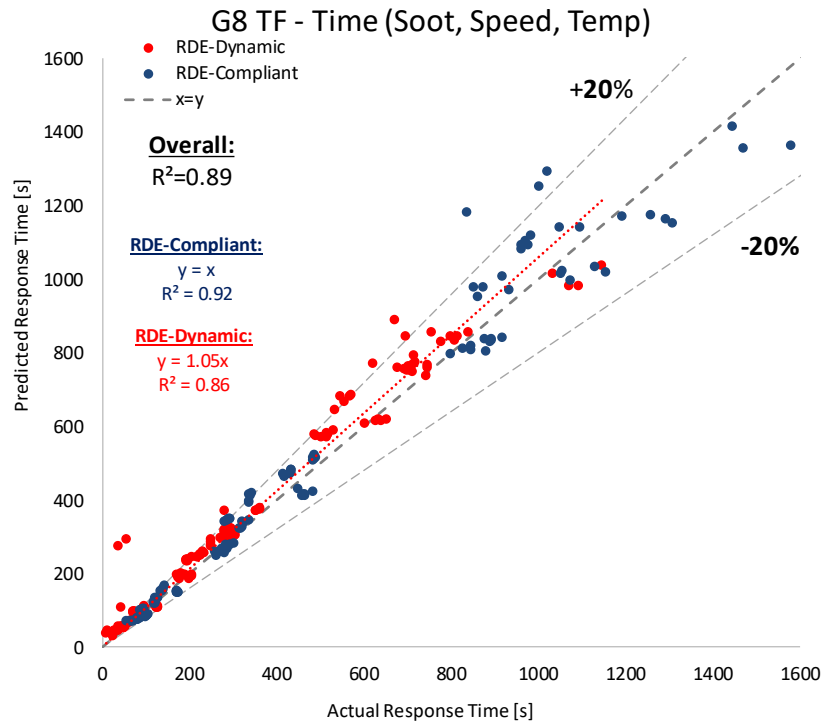


Figure 71: TF performance on RDE-compliant and RDE-Dynamic routes with improved TF

4.2. Effect of supply voltage on sensor regeneration

The nominal voltage for sensor operation in a non-commercial vehicle is 12 V. This value is usually stabilised by the alternator of the car, but due to the battery or other electrical issues it is possible to fluctuate between 9 and 16 V. Under these conditions, the sensor should be unaffected and operate normally. The effect of the three voltage levels (low, normal, high) must be examined in the sensing and the regeneration mode. In the sensing mode, though, the voltage does not affect the sensor operation. The excitation voltage used for electrophoresis is controlled by the sensor control unit and can be effectively kept at the desired levels due to its low current demand. During the regeneration process, the current demand is up to 3 A retrieved directly by the supply circuit. Low voltage can reduce the provided current resulting in insufficient temperature for soot oxidation. To examine this situation, a regeneration mapping was performed for different exhaust velocities and temperatures. The soot concentration was 8 mg/m³ for all tests. The levels for the supply voltage were 9, 12 and 15.5 V (16 V was not possible for the power supply). This test was performed on the Daimler engine with two Gen4 sensors, and the evaluation was based on the duration needed to complete the regeneration process.

Table 25: Steady-state points and voltage levels for the investigation of voltage effect on sensor regeneration

Soot [mg/m ³]	Speed [m/s]	Temperature [°C]	Supply voltage [V]
---------------------------	-------------	------------------	--------------------

8	20	220	9
	36	300-320	12
	45	420	15.5
	50		
	110		
	155		

Based on Figure 72, the regeneration duration is mainly affected by low supply voltage at high exhaust speed points. This behaviour was observed in both sensors and can be attributed to the insufficient control of regeneration temperature. High exhaust speed leads to high convection rates, which require additional thermal power to oxidise the accumulated soot, but this is not possible due to the low supply voltage.

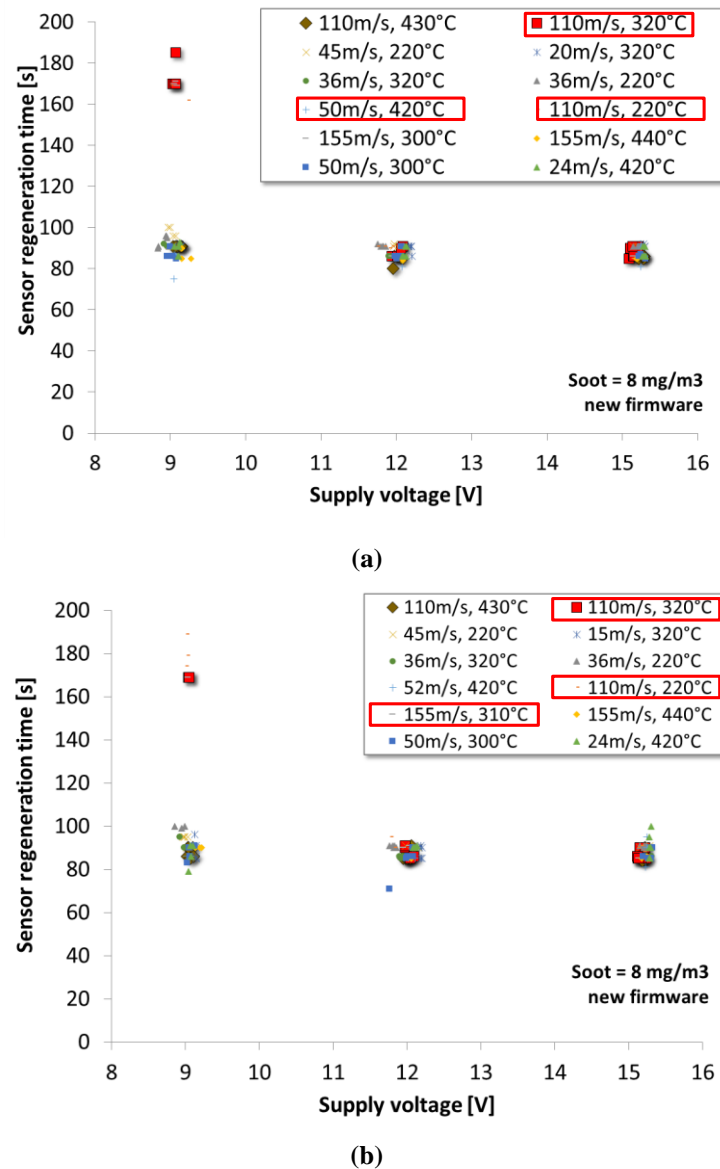


Figure 72: Regeneration duration for two sensors. Low voltage increases the regeneration time

To validate the theory, two sensors operated in standard and low supply voltage were examined in the SEM after the same duration of regeneration (90 seconds). In the first case, the sensor was clean from soot, whereas in the second case, the sensor element had a few areas with large soot deposits (Figure 73). To resolve this issue, the regeneration temperature was increased by 5% and the steady-state points with the high regeneration duration were repeated. The conclusion was that all regeneration durations were 90 seconds and thus successful.

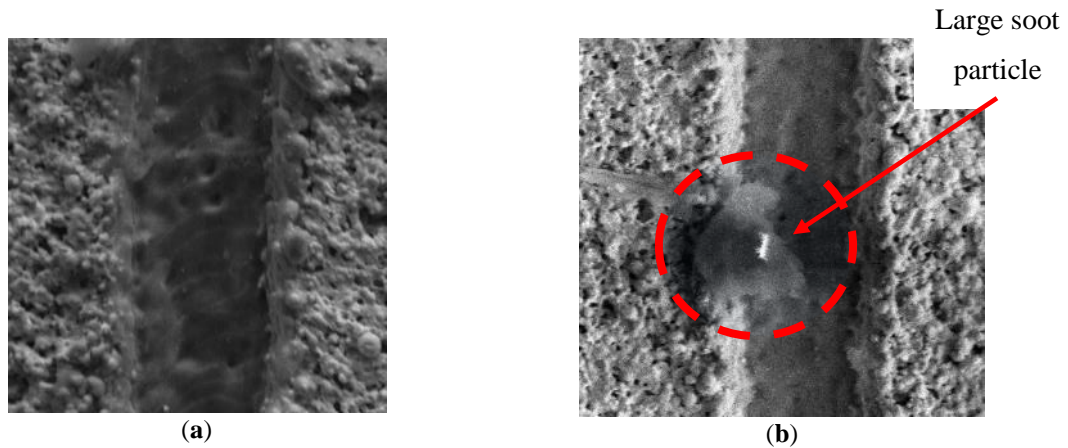


Figure 73: SEM images after 90 s of regeneration a) 12 V power supply; clean sensor b) 9 V power supply; sensor with soot deposits

4.3. Effect of sensor mounting orientation

The soot sensors are vertically installed in the exhaust line of the vehicles similarly to the gas sensors (Figure 74b). The mounting angle or sensor orientation is random during the sensor installation (Figure 74c). Therefore, one of the main requirements during the tip design is to ensure that the conditioning of the exhaust flow in the sensor tip is independent of the orientation. The first design of the sensor tip (Gen1 sensors) was focused on allowing a significant amount of exhaust flow reaching the sensing element. This was beneficial for the frequency of diagnostic events, but the sensors were sensitive to mounting orientation, and an orientation mark was needed to ensure proper installation. The effect (decrease for rotation from the nominal 0° orientation) on response time was up to 17% depending on the exhaust characteristics (mainly exhaust speed) and the mounting orientation (Figure 75).

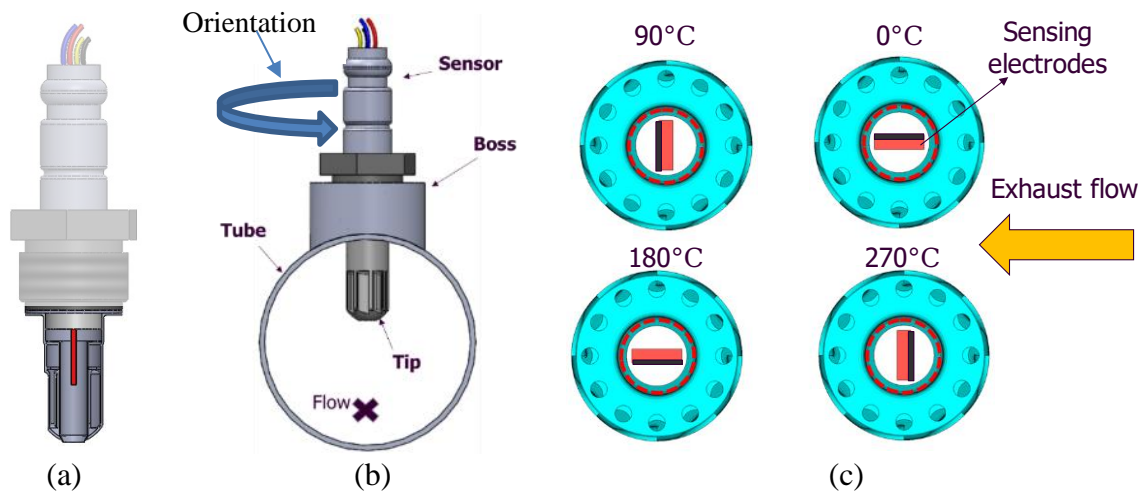


Figure 74: a) Side view of the latest tip design, b) installation in the exhaust line and definition of orientation c) bottom view with orientation positions

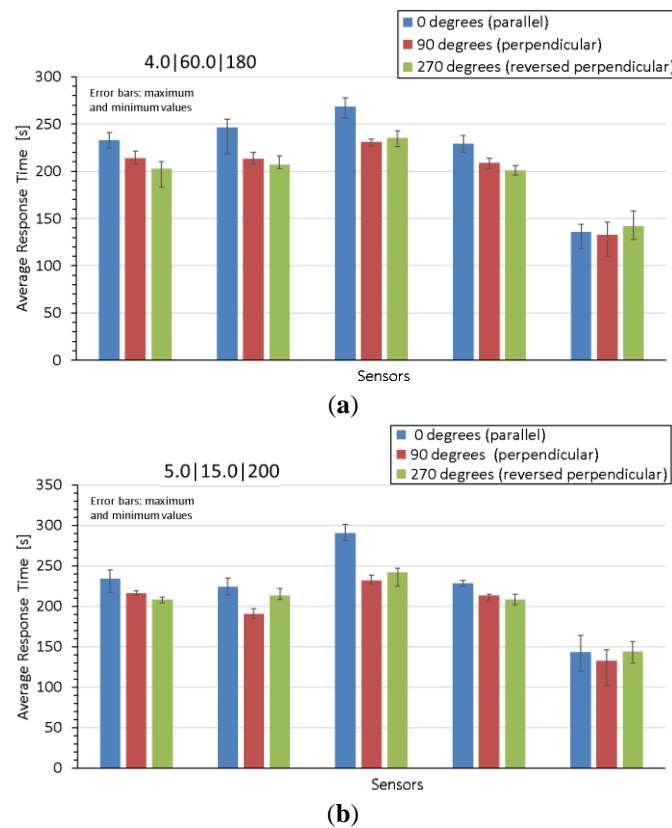


Figure 75: Effect of orientation on 5 Gen1 sensors a) high exhaust velocity b) low exhaust velocity

The current tip design (Gen3-Gen5 sensors) has been developed with respect to the requirement of independence of mounting orientation and sensor response. Gen6, which is currently developed, is based on Gen5 with additional features for water and contaminants protection, and thus, the independence of the mounting orientation remains.

The first step was to use Computational Fluid Dynamics (CFD) modelling to optimise the design, and afterwards to verify the results with experimental data. The CFD model was developed in a

separate study (Gkantonas, 2016), and it was used in the current work to investigate the orientation effect. The reference orientation is 0° to the exhaust gas (Figure 74c), and five additional orientation angles were studied: 10, 45, 90, 180 and 270 degrees. The simulation was run for a steady-state point (5 mg/m^3 , 15 m/s, 210°C for soot concentration, exhaust velocity and exhaust temperature, respectively) which is considered the reference point for the evaluation of the sensor. The results are presented in Figure 76a. Except for the normal velocity, there is no significant change in the flow characteristics near the sensor element (0.5 mm). But even the increase in the normal velocity does not affect the particle deposition rate because its absolute value is negligible compared to the total velocity. Therefore, no effect of orientation on sensor response time is expected according to the CFD analysis.

Figure 76b presents the experimental evaluation of the effect of different orientations on the response time of 2 sensors. The selected orientation angles are the same examined in the CFD modelling. Five sensor accumulation periods were recorded for each sensor and orientation. The bars illustrate the average values and the error bars depict the maximum and minimum response times. Sensor 1 is slightly slower than sensor 2 at the reference point, and this is consistent for all orientations. The experimental data validate the CFD model, and only minor differences are observed for the different orientation angles for both sensors. Therefore, this tip design is independent of the sensor orientation.

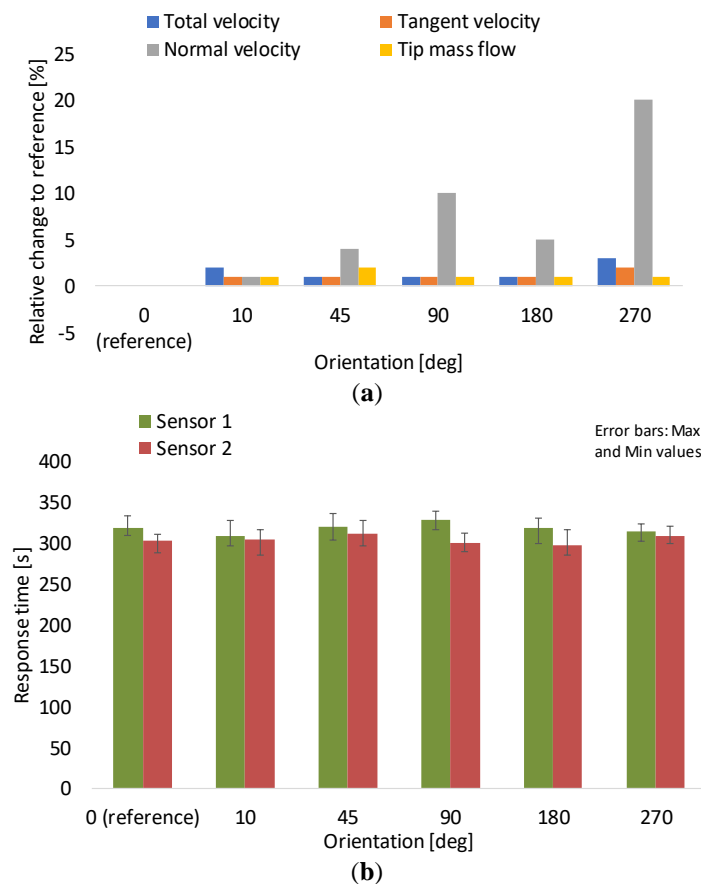


Figure 76: a) CFD analysis for the effect of sensor orientation b) Experimental results for the same sensor orientations. Sensor response times are independent of the orientation.

4.4. Water protection

Exhaust gas contains water vapours as a product of the combustion process. As exhaust gas cools down towards the tailpipe, condensation of the water vapours on any surface colder than the dew point temperature is possible (indicative dew point for exhaust gas is 50°C). The inner side of exhaust pipes, the substrates of the exhaust aftertreatment devices (DOC, DPF, SCR), the periphery of these devices or the tips of the exhaust sensors are examples of condensation hot spots. This phenomenon is intense during cold start operation or at low ambient temperature. Focusing on the exhaust sensors, condensation can reach the sensing element with the following mechanisms:

- Water droplets can directly condense on the sensing element in case of low element temperature. To resolve this issue, the sensing element can always be heated above the dew point (e.g. at 120°C) during cold start operation.
- Water droplets which have been previously condensed before the engine cranking or on a cold surface before the sensor location can reach the sensor. The solution, in this case, is the proper design of the sensor tip to prevent water from reaching the sensing element.
- Water pooling inside the exhaust line can be a source of an excessive amount of water that can reach the element. The latest exhaust aftertreatment configurations, contain U-shaped pipes in the exhaust in an effort to package all necessary devices in the limited space underneath the vehicle and as close to the engine as possible to provide high temperature for short light-off periods of the catalytic converters or enable conditions for SCR injection. Soot sensors are commonly the last component in an exhaust line, and thus, they are vulnerable to water droplets from the pooling areas.

The water amount in the exhaust can be calculated based on CO and CO₂ concentrations in the exhaust line (Heywood, 1989). Typical values for diesel vehicles are 5%-10%.

The main effect of water condensates on the resistive sensors is the risk for low element durability due to thermal stresses. Also, water condensate can create a bias on the sensor signal due to the high conductivity of water, which can lead to decreased resistance between the electrodes. Therefore, specific measures must be taken to protect the sensor against water droplets. These are divided into two categories:

- **Optimum design of sensor tip.** During sensor development, five different tip geometries were developed and tested. The target was to find the best compromise between water protection and in parallel adequate soot deposition for fast diagnostic events. The various geometries had been initially designed and optimised using CFD analysis, and afterwards, tested in an experimental setup using water and a dying medium to allow visual inspection

of water penetration. This study was performed by Stoneridge Inc. and was not part of the current study.

- **Optimisation of “dew point reached” strategy.** Even if the tip geometry successfully hinders water droplets from reaching the sensor element, during the cold start operation water vapours can condense on the sensing element if its temperature is below or close to the dew point. To diminish this possibility, the sensor element is heated during lower than the dew point temperatures, and it is only after a safe limit that the sensor triggers the initial regeneration and switches to sensing mode. This limit was experimentally defined as presented below.

4.5. Optimisation of dew point strategy

The dew point of exhaust gas can be accurately calculated based on the water molar percentage in the exhaust, the exhaust pressure and the saturation pressure of water as function of the temperature. During vehicle operation, though, the different devices in the exhaust line such as the sensor probe have a temperature gradient compared to the exhaust gas temperature. Therefore, it is a challenge to define the limit for safe sensor operation to avoid thermal stresses due to condensed water impingement on the sensing element. The calculated dew point of the exhaust gas is a useful indication, but it is necessary to perform tests in different exhaust conditions to define the “dew point reached” strategy.

In parallel, the dew point strategy must allow enough time for sensor operation in a cold legislative cycle. Otherwise, the homologation procedure will fail. For a WLTC cold start cycle, an indicative response time for a failed DPF at OBD limit is 500 seconds. Considering the need for debouncing with two accumulation periods during the homologation cycle (3.5.2.1.2), it is evident that the dew point should be reached as early as possible. Also, a safe dew point strategy is necessary to reduce the cold-start interference due to unburned hydrocarbons which can create a conductive layer on the sensing element that reduces the resistance between the electrodes and creates a sensor signal bias. Finally, the difficulty in defining the dew point is amplified by the start and stop strategies on modern vehicles. The strategies for the Start-Stop system, which switches off the engine when the vehicle is stopped (e.g. at traffic lights) are continuously improved toward lower CO₂ emissions. For example, the so-called second-generation systems switch off the engine even during vehicle deceleration. These frequent engine stops keep the exhaust temperature at low levels, and there is a risk for the sensor to fail to complete the necessary accumulation periods during homologation due to late “dew point reached” point. Figure 77 shows an example of the start-stop operation during the WLTC for the cold and hot start.

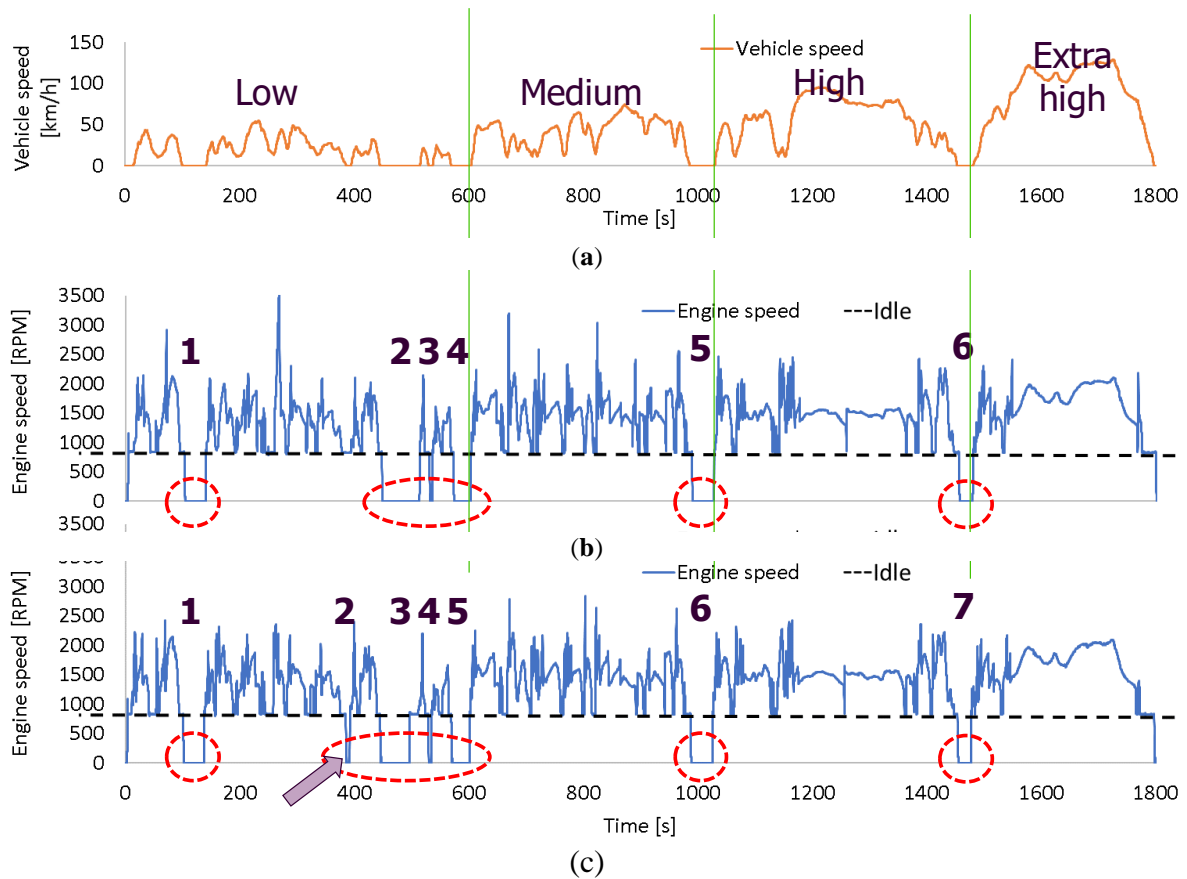


Figure 77: Example of start-stop operation during a WLTC cycle for a Euro 6 diesel vehicle a) driving profile b) start-stop during cold cycle c) start-stop during hot cycle

For the needs of the current study, the calibration procedure was performed on the test vehicle #3 (Table 6), which encounters all the above difficulties and challenges. The equipment that was used comprised:

- A resistive soot sensor which was used as an indicator of water on the element. This sensor was reporting the sensor resistance and was constantly in sensing model. The deposition of water droplets between the electrodes creates a resistance drop. To avoid any decrease on the signal due to soot accumulation, a full DPF was installed upstream the sensor. This method cannot quantify the water amount, but it is a reliable indication of water presence on the sensor element. The best solution to monitor the water amount is to use a humidity exhaust sensor, which is available in the market and can quantify the water amount (ETAS, 2011) but it was not available for the current study.
- A sensor with a thermocouple on the backside of the sensor element and a thermocouple on the sensor tip.
- Three thermocouples for the exhaust gas temperature before the DPF, before the SCR and in the sensor area, and two thermocouples in the inner and outer surface of the exhaust pipe.

The target was to correlate the exhaust gas temperature near the sensor area with the element and wall temperatures and experimentally define a safe threshold for sensor operation.

The tests were performed in cold ambient conditions, but for the final application in the market-available vehicles, extreme cold conditions are used by testing in climatic cold chambers or at the Arctic area. All tests were cold start with different preconditioning cycles and driving patterns. The vehicle was driven until the exhaust temperature at sensor position reached enough high temperature to ensure water-free exhaust (e.g. 200°C for exhaust gas temperature at sensor position).

Figure 78 shows an example of dew point tests. The measured temperatures are in the first graph and the sensor signal in the second graph (used as a humidity sensor).

The water condensation on the elements started 150s after the engine start, as indicated by the resistance drop, and these conditions continue for the next 10 min. Excessive water was observed in the exhaust based on the reading of the thermocouples in the highlighted area. The exhaust wall inner temperature seems to have a plateau, which is an indication of water pooling. Also, a few seconds later, the exhaust gas temperature at the sensor area has a significant drop, which is possibly due to water reaching the thermocouple. Nevertheless, the increasing temperature of the sensor element in this area and the unaffected sensor resistance indicate that the pooled water did not reach the sensing element. This can be attributed to the design of the sensor tip and also the installation of the sensor in the exhaust, which is always at 45° above the horizontal level. The final increase on exhaust gas temperature in the sensor area indicates that the pooled water was evaporated or blown out of the exhaust. To summarise, the indications for water presence in the system are:

- Drop on sensor resistance (water droplets)
- Plateau in inner wall temperature (water pooling)
- Significant drop for the exhaust gas temperature (water droplets)
- High difference between inner wall temperature and temperature of the sensor element (water pooling)

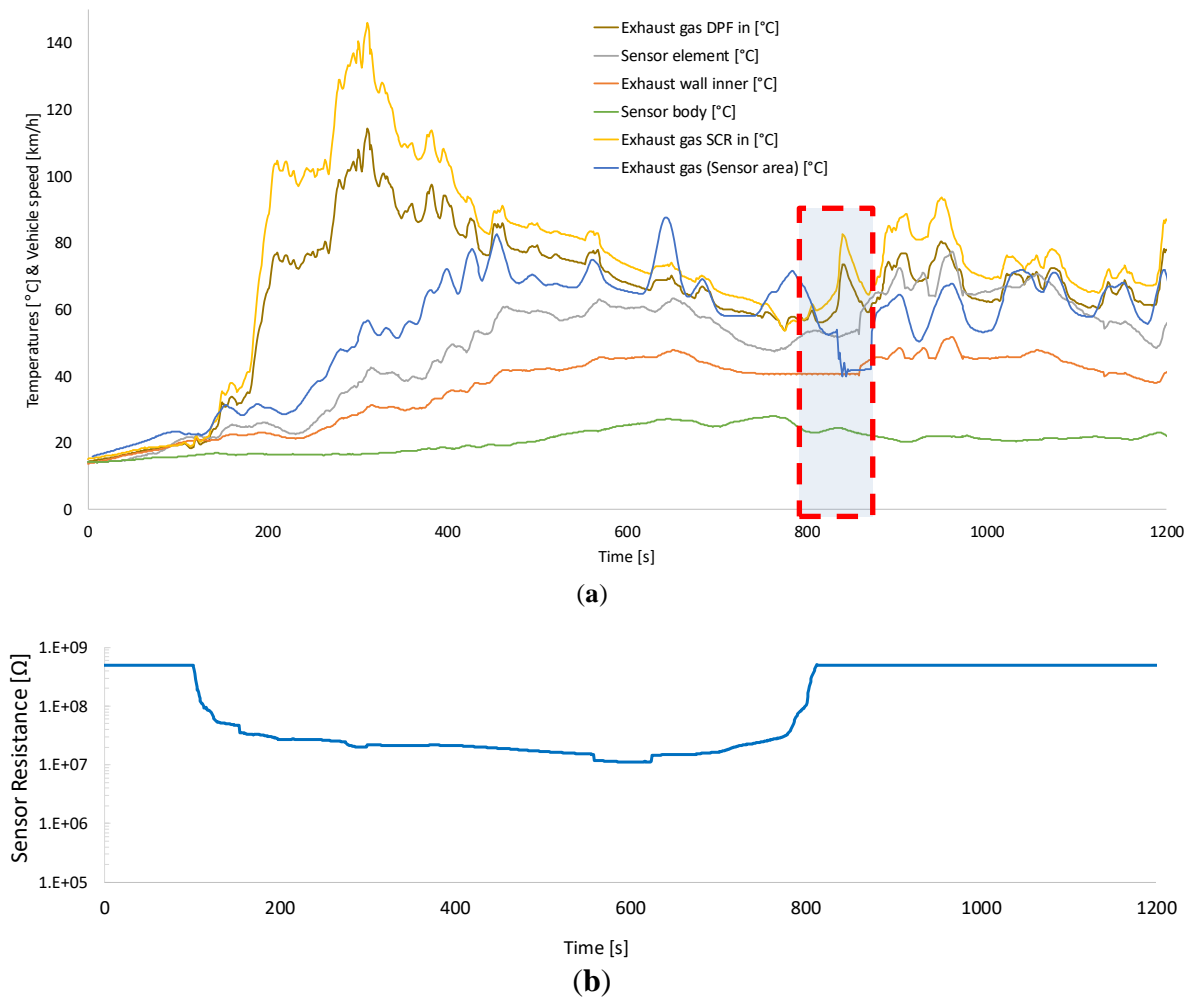


Figure 78: a) temperature profiles during cold start operation b) sensor signal

The outcomes of these tests are summarised in Table 26. The pre-selected dew point of 90°C seems to be adequate in most of the tests except for test #2. The idle operation before the soaking created water condensation inside the exhaust which was trapped due to the geometry of the exhaust line (U-shape before the sensor area). Surprisingly, this water amount did not evaporate during the first minutes of the following urban driving, and more water was trapped due to the cold-start and reached the area of the sensor after more than 10 minutes (Figure 78a). Nevertheless, the sensor was not affected by this phenomenon in this specific test, but the risk of sensor failure is high in a similar situation. The proposed solution is to increase further the dew point to ensure that the whole amount of trapped water is evaporated. In parallel, it is strongly advised to the automotive manufacturers to avoid U-shaped geometries before the sensor installation point.

Table 26: Correlation of exhaust, wall and sensor temperatures with the dew point temperature.

Test ID #	Pre-condition	Driving Profile	Time to reach 90°C (exh. gas at sensor position) [min]	Exhaust gas DPF in	Exhaust gas SCR in	Exhaust gas at sensor location	Sensor element	Exhaust wall inner	Sensor body	Comments
1	8h soaking at <10°C	RDE urban	16	190	120	90	75	59	25	Dew point safe, can be lower
2	Idle for 15 min and 4h soaking at <10°C	RDE urban	11	140	120	90	85	48	23	Water was observed during the transient operation (see previous figure). Probably the idle operation trapped some water in the exhaust (pooling)
3	High load for 2 min and 5h soaking at <10°C	RDE urban	9	150	105	90	72	64	28	Dew point safe, low wall temperature is risky for condensation
4	Same as test#1	RDE urban (aggressive)	6	200	160	90	Not available	60	35	Dew point safe
5	Same as test#2	RDE urban (aggressive)	5	210	120	90	Not available	65	39	Dew point safe, wall temperature still low
6	Same as test#3	RDE urban (aggressive)	6	180	100	90	Not available	69	31	Dew point safe

4.6. Sensor cross sensitivities

4.6.1. Introduction

The measured response time of the resistive soot sensor is used as input for the OBD Model which compares - using OBD algorithms - the measured and the modelled sensor response times for a DPF failed at the OBD limit (Linke et al., 2016). The modelled response time is calculated based on three sub-models: The soot model for the simulation of engine-out soot emissions, the DPF model for the simulation of the threshold filtration efficiency of a failed DPF and the sensor model which converts the soot emissions to sensor response time applying a mathematical transfer function or a physical model. There are many challenges related to the operation of the algorithms and each model. In this section, the focus is on the deviations of the measured response time that are not predicted by the transfer function or the physical model and can be attributed to sensor cross sensitivities.

Thermophoresis due to the lower temperature of sensing plate than the exhaust gas (Malik et al., 2011) and electrophoresis created by an electric field of a voltage applied between the electrodes (Kittelson et al., 1986), (Grondin et al., 2015), (Grondin et al., 2016), (Hagen et al., 2016), are the governing deposition mechanisms on the sensing element of a resistive soot sensor. Inertial impaction

and convective diffusion are also analysed as important mechanisms at high and very low exhaust velocities, respectively. The input parameters of the developed physical model are directly related with the sensing element (geometry, temperature, electric field, shear stress), the particle characteristics (soot concentration, particle size and charge distribution) and the exhaust gas flow parameters (temperature, velocity) which are calibrated based on engine data acquired by dedicated laboratory measurements. Similarly, the developed transfer function of the statistical model is based on exhaust soot concentration, gas velocity and temperature to simulate the sensor response time. A calibrated sensor constant is also used to improve the convergence of the transfer function or the model and the sensor measurement for different batches of sensors with different response duration.

Nevertheless, both the transfer function and the physical model at their current form do not account for specific parameters and characteristics of the exhaust aerosol that can occur during extreme conditions compared to what was measured or modelled during the design phase of the OBD model. These are called cross-sensitivities of the sensors, are characterised by the main chemical element of the substances and could not have been estimated based on pre-calibrated models available in the vehicle's ECU. Table 27 presents the tested cross sensitivities (NH_3 and ash are highlighted because they are examined in separate protocols). The levels that were examined are at least two: zero and the highest possible level according to the requirements of the automotive industry. For the ash and the NH_3 tests, several levels were examined as will be presented in section 4.6.3.

It is important to keep in mind the way that sensors were evaluated during the cross-sensitivities tests. The impact of the various elements was evaluated based on:

- i) The direct effect on sensor response time during the exposure
- ii) The remaining effect after a short exposure (comparison before and after the exposure)
- iii) The sensor-lifetime cumulative effect or sensor aging

The significance of the effect is compared to the inaccuracy of the sensor hardware (section 3.4). Any contaminant resulting in less than 10% effect on response time is considered insignificant. This is a condition that was adopted for our study to quantify the various contaminant effects and does not imply any additional inaccuracy of the sensor or the diagnosis.

In principle, the effects can be attributed to two main mechanisms as will be discussed in the results sections:

- Change of the deposition velocities, the growth of the dendritic structures, the conductivity of the particles and the stickiness of particles (Schmid et al., 2011; Grob et al., 2012; Grondin et al., 2016; Soysal et al., 2017; Maricq and Bilby, 2018). These conditions can lead to a direct effect on the response time.

- Salts or non-combustible particles deposition, corrosion of the platinum, platinum degradation, porous in platinum, reduction of the adhesion of the platinum on the ceramic, cracks on sensor element (Galusková et al., 2009; Papitha et al., 2013; Lei et al., 2016). These conditions can create a remaining or cumulative effect which raises durability and reliability concerns.

Table 27: Cross sensitivities, the way they were investigated and the tested levels. (RT: response time). NH₃ and ash are examined separately.

Cross sensitivities (elements)	Investigation	Levels
Sulphur (S)	Effect on RT (remaining)	0, 100 ppm (fuel)
Methane (CH₄)	Effect on RT (direct, remaining)	0, 1000 ppm (exhaust gas)
Carbon monoxide (CO)	Effect on RT (direct, remaining)	0, 1000 ppm (exhaust gas)
Hydrogen (H₂)	Effect on RT (direct, remaining)	0, 1000 ppm (exhaust gas)
AdBlue (Urea)	Effect on RT (remaining)	0, 50, 100, 150, 200 ml (on sensing element)
Sodium (Na)	Effect on RT (remaining)	0, 1000 ppm (exhaust condensate)
NH₃	Effect on RT (direct, remaining, cumulative)	0-700 ppm (with intermediate levels) (exhaust gas)
Ash	Effect on RT (direct, remaining, cumulative)	0-200 g (with intermediate levels)

During the analysis of cross sensitivities, the evaluation of the effect of ash and NH₃ emissions were considered as priorities, and thus, they are both separately examined in separate sections for direct, remaining and life-time cumulative impacts. The results and conclusions of all tests are useful to realise the limitations on the operation of soot sensors, define the effect of the tip design and software characteristics, and propose further investigations.

4.6.2. Effect of sulphur, methane, carbon monoxide, hydrogen, AdBlue (urea), sodium

4.6.2.1. Theoretical background

In this section, the sources of the elements are discussed:

- **Sulphur:** Sulphur originates from fuel and lubricant oil additives. EU sulphur limit for diesel fuels is 10 ppm (EU, 2009b) and a typical concentration level for a low sulphur-content lubrication oil is 2000 ppm (“DieselNet. Diesel engine lubrication,.” 2019). These levels can be significantly higher for other markets. Sulphur leaves the combustion chamber primarily in the form of sulphur dioxide (SO₂>95%) and a small proportion of sulphur trioxide (typically SO₃=2-5%). The proportion of SO₃ may be significantly increased by

oxidation of SO_2 in oxidation catalysts (30-40% conversion rate). Afterwards, the trioxide may react with water to produce sulphuric acid. Also, in the three-way catalyst, under favourable conditions, sulphur dioxide may be reduced to H_2S . SO_2 , COS and H_2S are also produced during the LNT desulfation. For the current study, the target was to examine the remaining effect of all gas products in an exhaust line downstream the DOC as they can occur due to high sulphur content in the fuel. The possible formation of sulphate particles in the catalyst was not investigated since the control of the operating point was based on the stabilisation of the soot concentration value via tuning of engine parameters (e.g. engine load, EGR etc.).

- **Methane:** Small quantities of methane can be produced when the hydrocarbons in fuels are not completely combusted. The carbon content of the fuel, the engine type, the amount of non-combusted hydrocarbons passing through the engine, and post-combustion emission controls, influence methane in the exhaust. In non-calibrated engines the proportion of methane emissions is generally highest at low speeds and when the engine is at idle.
- **Carbon monoxide and hydrogen:** Low exhaust temperatures during cold start lead to poor catalyst performance, and the conversion of CO (and HCs) is close to zero. The delayed or extended post-injection operation creates high amounts of H_2 and CO (mainly for LNT applications).
- **AdBlue (Urea):** Sensor position could be close to AdBlue injection. This installation is rare but can be possible in layouts with two urea injectors and installation of the soot sensor after the DPF. Also, for sensor positioning downstream of the DPF in case the AdBlue injection starts at low temperature, urea may not be decomposed and reach the sensor area. To avoid any issue, limitations can be applied to sensor installation and the temperature limit for the operation of the SCR system, but experiments are necessary to quantify any possible effect on sensors.
- **Sodium:** Sodium hydroxide is commonly used in the refining process to produce ultra-low sulphur diesel (ULSD) fuel from crude oil. Sodium can also be found in lubricant oil. Also, it is used as a lubricant during the cutting and bending process of exhaust pipes and can reach the sensors during the first operation in a vehicle.

4.6.2.2. Methodology

- **Sulphur:** Regarding the measurement equipment and setup for the sulphur exposure, sulphur enhancing compound Dibenzyl Disulphide (DBDS) was mixed in the diesel fuel of the Toyota engine. The additive is completely dissolved in the fuel, and therefore the mass of sulphur in the exhaust gases is equal to the mass of sulphur contained in the fuel mixture. The concentration of SO_2 in the exhaust is approximately 10% of the sulphur content in the

fuel (DieselNet, 2019). The measurement of the exact sulfuric gas compounds was not possible as this requires a specific gas analyser (e.g. FTIR analyser) which was not available at that period at LAT. Therefore, the sulphur content in the fuel was used to characterise this test, assuming SO₂ was the majority of the gas products. The remaining effect of sulphur on RT was the target of this test. The response times were measured in the three operating points of Table 28 which were repeated before (baseline) and after the 100-ppm exposure (the measurement after the 100 ppm was performed with 0 ppm of sulphur in the fuel). The direct effect of high sulphur-content in the fuel needed a different protocol and will be assessed in a future work. The reason is that due to the requirement to keep the soot emissions in the defined levels (3, 5, 7 mg/m³) during the sulphur exposure, the engine parameters were continuously tuned (e.g. EGR, torque). Therefore, the effect of the sulphate particles cannot be accurately examined.

- **Methane, carbon monoxide, hydrogen:** For the gaseous exposure (methane, carbon monoxide, hydrogen) high-pressure bottles, a mass flow controller (MFC) and three injection points were used to contaminate the exhaust gas of a diesel engine (Daimler and Toyota engines). The evaluation of the sensors was performed based on the response time in the three steady-state operating points before, during and after the exposure to assess both the direct and the remaining effects (Figure 79, Table 28).
- **AdBlue (Urea):** The AdBlue cross-sensitivity was examined with a drop-test of AdBlue fluid on the sensor element out of the exhaust. The flow of one droplet (10 µl) per 10 sec on the sensing element was applied, and sensors were then evaluated over the three steady-state points every 50 ml up to the final target of 200 ml. With the followed protocol, only the remaining effect was examined.
- **Sodium:** In a similar way, sodium effect was examined with sodium formate powder (HCOONa) added on deionised water and injected on the sensing element. Two droplets of 28 µl Na solution were injected on the element (total injected quantity=56 µl). After the injection, all sensors were soaked for 12 hours at room conditions (25°C). Immediately after soaking, the sensors were installed and tested in the exhaust over the three steady-state points to calculate the remaining effect (Table 26) again.

For all these tests, two Gen5 sensors were used.

Table 28: Steady-state engine operation at three soot concentration levels.

Soot [mg/m ³]	Velocity [m/s]	Temperature [°C]
3	15	210
5		
7		

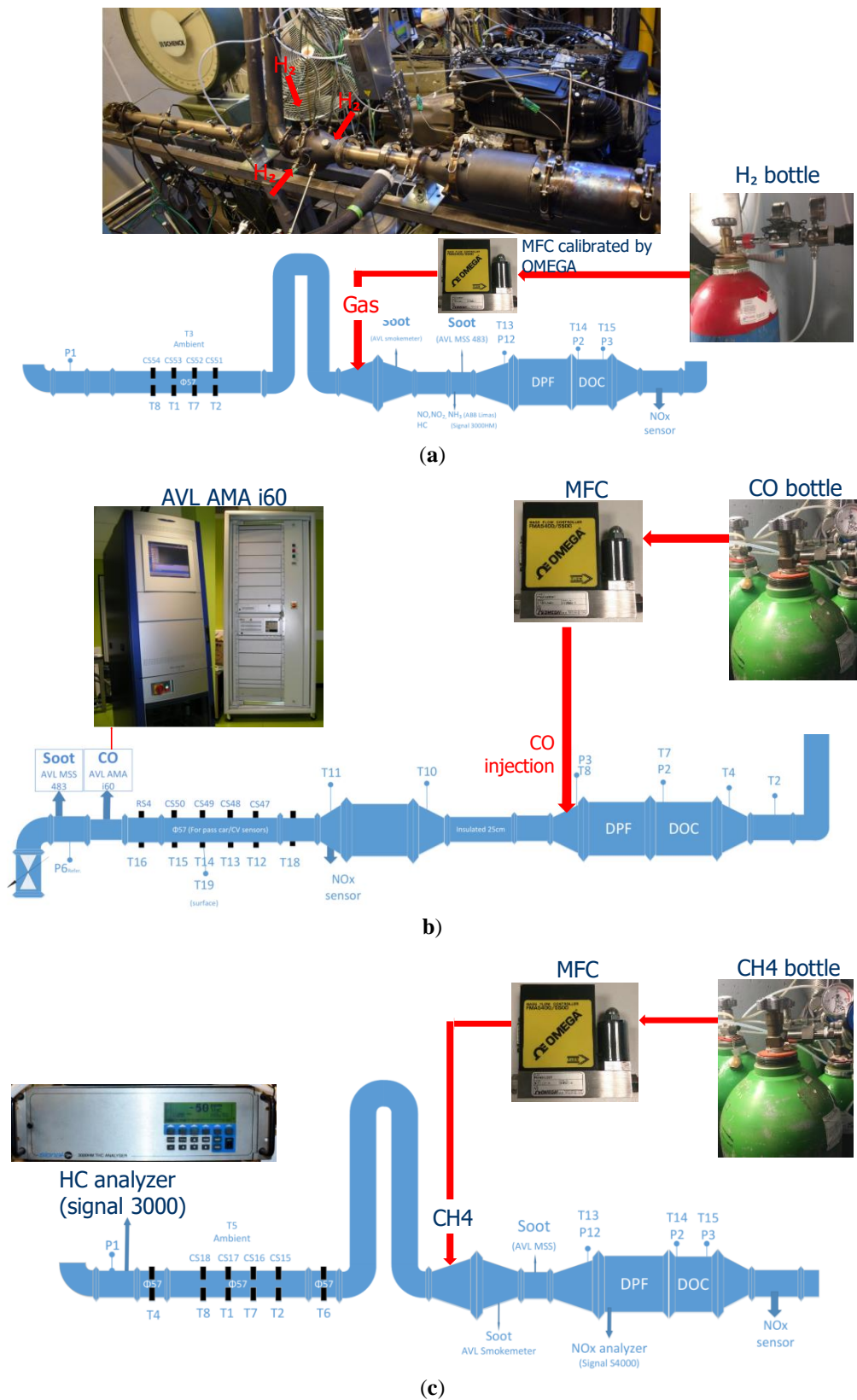


Figure 79: Experimental setup for gaseous exposure (H₂, CO, CH₄). Example of a) H₂, b) CO and c) CH₄ exposure.

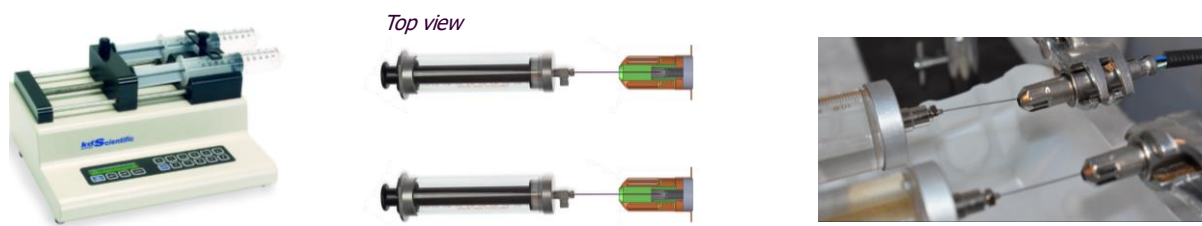


Figure 80: Experimental setup for AdBlue and Na exposure.

4.6.2.3. Results and discussion

The results of the cross sensitivities tests are summarised in Table 29.

The tested levels for S, CH₄, CO, H₂ and Na do not create any direct or remaining effect on resistive soot sensors. On the other hand, AdBlue seems to generate a remaining effect.

For S, the selected level was 10x higher than the maximum allowed level in ultra-low sulphur content diesel fuel in Europe (10 ppm (EU, 2009b)). Sulfuric components in the exhaust gases after combustion of the sulphur additive with diesel fuel are primary sulfuric compounds forming SO₂ in concentration 95-98% and SO₃ in 2-5%. H₂SO₄ is also produced by the reaction of SO₃ and water (SO₃ + H₂O → H₂SO₄). These components do not seem to either react with the platinum electrodes and the aluminium substrate or create salt particles that can affect the measurement resistance of the sensor. The possible increase of soot concentration due to the formed sulphate particles (mainly nucleation mode) (Meyer and Ristovski, 2007; Vouitsis et al., 2009) was not examined.

The experiments with the gas compounds (CH₄, CO, H₂) did not reveal any effect on the response time of the sensors. Therefore, the rich mixture for LNT applications is not an issue for resistive sensors.

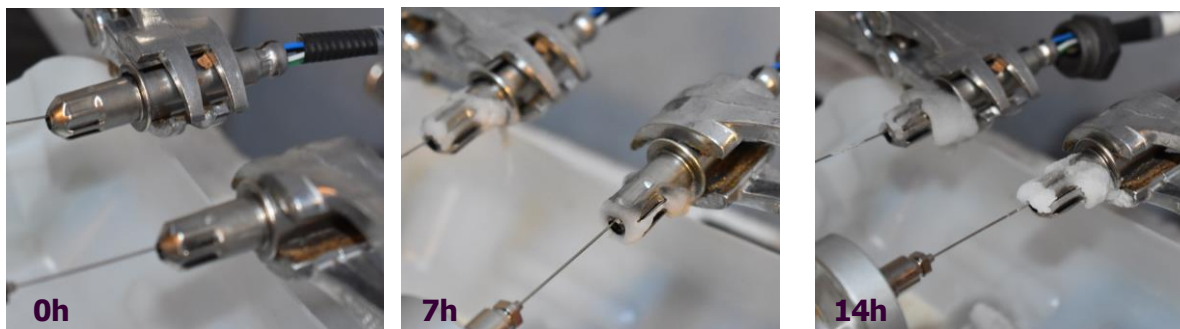
The results for AdBlue show that there is a slight remaining effect. The second sensor (CS11) was functional after the exposure, and the response times were the same in average values before and after the exposure. But the behaviour of the first sensor (CS7) was different. The response times were increased by up to 35%. This can be attributed to urea crystallisation due to evaporation of water occurring at low temperature. The main components are biuret and triuret, cyanuric acid, ammelide, ammeline and melamine (Wallin, 2014). Most of the deposits, though are temporary and become decomposed once the temperature and the flow rate increase after the installation in the exhaust. Complete decomposition of urea-based deposits should occur at temperatures of around 360°C to 400°C. A fraction of these deposits possibly remained as non-conductive salts between the electrodes of the CS7 sensor. Soot particles cannot be accumulated in these areas and thus, the accumulation period last longer. The main concern though, for the CS7 is the regeneration time-out error that reported during the last evaluation point after 3 hours of operation on diesel exhaust. The physical meaning of this error is

that the sensor was not able to totally clean its surface during sensor regeneration. To perform this check, the sensor compares its resistance after the regeneration with a threshold resistance set by the SCU. We were not able to clarify the reason for this failure, but these sensors are currently further investigated with SEM images to find the root cause of the issue. Despite the outcome of the further investigation, the different behaviour of the two tested sensors showed that the excess of AdBlue reaching the sensors is a potential risk for sensor and OBD model robustness.

For Na, the concern was about the increase of Pt porosity, which can create porous for contaminants and thus, Pt degradation (Galusková et al., 2009) and change on the response time of the sensor. The performed test though, did not reveal any issue. Nevertheless, an additional investigation will be conducted in the near future. This investigation was induced by findings of Na traces near the area of delaminated and cracked sensor elements from the first application on production vehicles and also by similar issues on BOSCH sensors which are presented in a recent patent (Tiefenbach, 2018). The ceramic aluminium substrate has excellent strength and electrical resistivity wear and is chemically inert to very high temperatures. But, due to stresses from transient thermal gradients, thermal cracks can occur. Ceramics are stronger in compression than in tension, so failure due to thermal shock is more likely due to rapid cooling, e.g. due to water droplets on the hot sensing element.

Table 29: Commonly found contaminants in the diesel exhaust and their effect (direct or remaining) on the resistive sensors.

Contaminant	Direct effect on RT	Remaining effect
Sulphur (S)	<i>Not tested</i>	Unaffected ✓
Methane (CH ₄)	Unaffected ✓	Unaffected ✓
Carbon monoxide (CO)	Unaffected ✓	Unaffected ✓
Hydrogen (H ₂)	Unaffected ✓	Unaffected ✓
AdBlue (Urea)	<i>Not tested</i>	(Slightly) increased ↑
Sodium (Na)	Unaffected ✓	Unaffected ✓



(a)

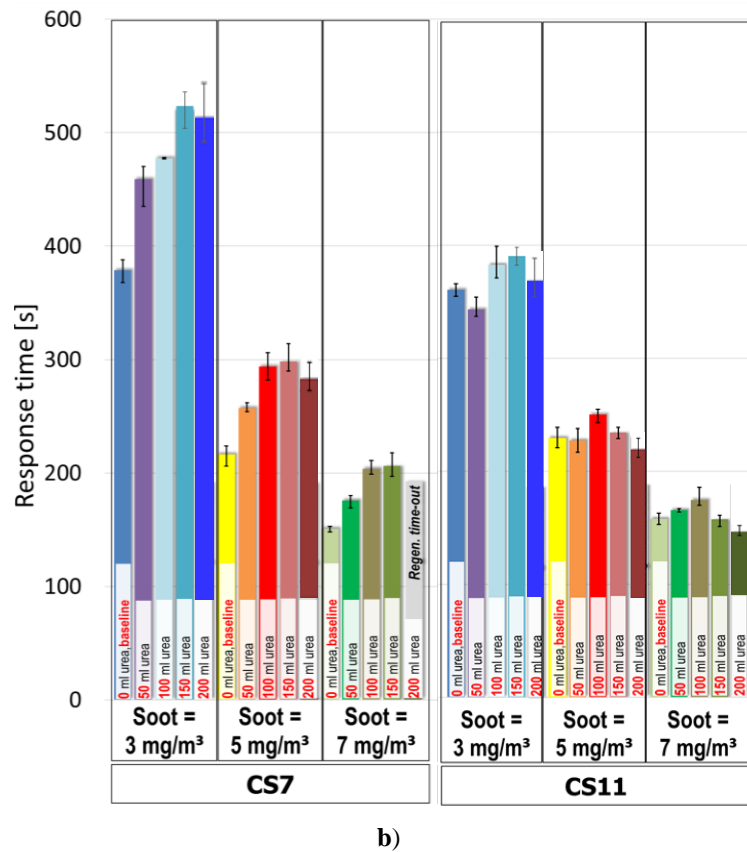


Figure 81: a) Urea deposits during the AdBlue test b) effect of Urea injection on sensor response time

4.6.3. NH₃ effect

4.6.3.1. Theoretical background

The Lean NO_x Trap (LNT) and the active Selective Catalytic Reduction (SCR) system with urea injection are currently used by the automotive industry to retain the NO_x emissions below Euro 6d Temp limit (ACEA, 2019). A combination of a close-coupled LNT and an underfloor SCR (either active or passive) is also used and will be more widely deployed for low NO_x emissions over RDE to conform with Euro 6d final NO_x limit (Ntziachristos, 2017), (RICARDO, 2018), (AECC, 2018)(Umicore, 2018). In addition, a passive NO_x adsorber (PNA) has been lately developed and uses NO_x absorption at low temperature and passive desorption with simultaneous active SCR at a higher temperature (Chilumukuru et al., 2017).

For LNT applications, although N₂ is the main product of reactions on the catalyst, NH₃ and N₂O are undesirable products of its operation during rich conditions and temperature below 200°C (DiGiulio et al., 2013). In the case of active SCR systems (either standalone or combined with an upstream LNT or PNA) with injected urea which is hydrolysed to NH₃, poor calibration of urea injection in terms of injected quantity can lead to high NH₃ emissions. Methods that are used or investigated to

improve SCR strategy and eliminate NH_3 comprise stoichiometric NH_3 injection (Robinson et al., 2016), closed-loop control systems with an additional downstream NO_x or ammonia sensor (Wang et al., 2010) and methods to calculate the catalyst NH_3 load (Moser et al., 2019) and the ammonia distribution in the exhaust gas stream. Also, for heavy-duty applications, EU legislation has already a limit of 10 ppm for NH_3 emissions, and this is plausible by mainly using an Ammonia Slip Catalyst (ASC) after the SCR.

Nevertheless, on light-duty applications, NH_3 emissions can be significantly high to raise questions about the impact on resistive soot sensors that are installed downstream (Husted et al., 2012). Recent researches show that vehicular NH_3 emissions are continually increasing in contrast to other legislative emissions and are comparable to agricultural NH_3 emissions (Hill et al., 2015), (Fenn et al., 2018), (Elser et al., 2018). Suarez-Bertoa et al. (2017) measured high on-road NH_3 emissions for a Euro 6b diesel SCR-equipped vehicle. It is evident that despite the detailed calibration of these systems, low tailpipe NH_3 emissions cannot be guaranteed in all driving conditions and thus, the investigation of any possible impact on the resistive soot sensor is necessary.

4.6.3.2. Methodology

For the SCR, studies have shown that the urea excess leads to the increase on particle number concentration downstream the SCR catalyst (Schwelberger et al., 2019), (Lee et al., 2010), (Robinson et al., 2016). Also in experiments with NH_3 injection instead of urea, the increase on particle formation was again significant (Amanatidis et al., 2014) but lower compared to urea excess (Robinson et al., 2016) which was partially attributed to the absence of urea-originated particles. Hence, to exclude the effects of urea, liquid NH_3 was injected upstream of the examined sensors. The effect of urea was discussed in a previous section (4.6.2.3). Two different protocols and approaches for the NH_3 effect were examined, one for the direct and remaining after short exposure and one for the lifetime cumulative effect.

In the first approach, the direct and the remaining after short exposure effects of NH_3 emissions on sensor response time was examined according to a steady-state protocol. The aim was to cover the legislative limit for heavy-duty applications (10 ppm) extended up to 50 ppm (with small steps of 10 ppm) which is slightly higher than the maximum instantaneous peak value for SCR overdosing events on diesel vehicle as summarized by relevant studies by (Herman et al., 2010), (Suarez-Bertoa et al., 2016). In addition, it was decided to evaluate the sensors under two very high levels of 350 ppm and 700 ppm of NH_3 slip. These two levels were examined as a worst-case scenario which should cover extremely aggressive NH_3 dosage strategies on SCR (e.g. to reduce NO_x emissions during cold start operation or dynamic driving) or frequent rich operations on LNT-equipped vehicles with high CO and H_2 emissions which lead to NH_3 formation. The protocol contains a medium engine operating point of 15m/s, and 200°C exhaust velocity and temperature, respectively and the soot concentration was 5

mg/m³. The soot level was selected to warrant frequent soot accumulation periods for the sensor to evaluate the effect of NH₃ based on ten accumulation repetitions on the same point.

The second approach covers the possibility of a cumulative effect on sensors after exposure in equivalent to full vehicle life conditions NH₃ emissions. Sensors were examined under an accelerated protocol and were exposed for 300 hours on 350 ppm of NH₃. The temperature profile was alternated between 150°C and 270°C every 50 hours to cover both low and medium exhaust temperatures. To examine the effect with a normally operated sensor, the test was performed with typical for a failed DPF exhaust conditions to allow frequent loadings and regenerations. Considering the high duration of the test and the targeted levels of temperature, the exhaust soot and velocity conditions were not possible to be strictly controlled in specific target-values. Therefore, the soot concentration was 2-4mg/m³, and the exhaust velocity was 14-18m/s. Based on previous tests with the current sensors in our laboratory, the response time from 2 to 4mg/m³ can be reduced by more than 50%. Hence, the evaluation of the sensors during the NH₃ injection would not have been reliable and was not examined. The evaluation of the sensor was performed every 50 hours over a reference point for only the cumulative effect on NH₃ exposure (4 mg/m³, 22 m/s, 300°C).

A mass flow controller (MFC) calibrated for NH₃ was used to control the dosage rate of NH₃. The resulting concentration in the exhaust was measured via an ABB Limas 11HW analyser along with the NO₂ and NO concentrations. Preliminary tests were performed to find the dosage rate needed for the desired NH₃ concentrations in the exhaust. The soot mass concentration was measured by the AVL Micro Soot Sensor (MSS). During the accelerated tests of high NH₃, the MSS only periodically measured the soot concentration as a reference for the stability of operating point.

Sensors were measured in the Daimler engine (engine #1). Market fuel diesel was used for all tests (EN-590) with Sulphur content <10 ppm. Also sulphur content of the engine lubricant was 0.2% weight (Total Quartz Ineo ECS 5W-30). The exhaust aftertreatment systems consisted of the originally commercially installed DOC and different downstream components between the two approaches:

- **Low NH₃ concentration test (for the first approach):** An uncoated SiC DPF was installed downstream of the DOC followed by the NH₃ injection system and a commercial Fe-Zeolite SCR flow-through catalyst. The filtration efficiency of the DPF was compromised by partial removal of plugs on the outlet of the brick (Samaras et al., 2013). Preliminary tests were performed to achieve the desired level of NH₃ slip.
- **High NH₃ concentration tests (for first and second approaches):** The same as the low NH₃ test exhaust components were used. During the low-temperature level (150°C), an additional U-tube as a heat exchanger was added in the exhaust to allow same engine conditions with lower exhaust temperature.

The sensors used for this study were pre-production parts (Gen3 sensor), but their accuracy and repeatability were close to the targeted values for the final market product. In total, three sensors were used in parallel for this study.

4.6.3.3. Results and discussion

4.6.3.3.1. The direct and remaining effect of NH₃ on response time (first approach)

The NH₃ slip up to 50 ppm after the SCR, does not seem to affect the sensor response time. The small fluctuation on the average values (red bars) is covered by the error bars which illustrate the maximum and minimum values.

For the 350 ppm and 700 ppm, there is a reduction in the response time (15% as average). A theory behind this increase could have been the formation of additional solid ammonium nitrate or sulphate particles inside the exhaust (Amanatidis et al., 2014). The increase of total particle number downstream the DPF and SCR as examined by Amanatidis (2014) is significant (129% as an average for solid >23nm particles). Nevertheless, in terms of absolute values of particle number, the increase is $2 \times 10^5 \text{ p/cm}^3$ at its maximum level which based on the generally acceptable equation (11) for mass and number correlation for diesel exhaust (Maricq and Xu, 2004), corresponds to the mass of less than 0.01 mg/m^3 which is validated also by the stabilised soot concentration measured by the MSS. This increase is below the sensitivity of 0.1 mg/m^3 of the resistive sensor that was used in this study and constitutes a negligible amount compared to the soot emissions of the evaluation points of the protocols. Consequently, a decrease in sensor response times due to additional particle mass should be excluded.

$$M = N_0 \frac{\pi}{6} \rho_0 d_{0e}^{(3-d_f)} \mu_g^{d_f} e^{d_f^2 (\ln \sigma_g)^2 / 2} \quad (11)$$

Nevertheless, we should notice the possible effect of the high solid ammonium particulate number concentration (on the exhaust gas), on the construction of the dendrites. Ammonium particles acquire high positive charges, and this can increase both the particle deposition rate and the conductivity of dendrites. The theory for increased probability for physical conducting pathways is validated by a relevant publication (Grob et al., 2012). According to the same study, carbonaceous samples mixed with ammonium particles can lead to hygroscopic behaviour. In this case, water can also be absorbed and increase conductivity, which will make the sensor faster.

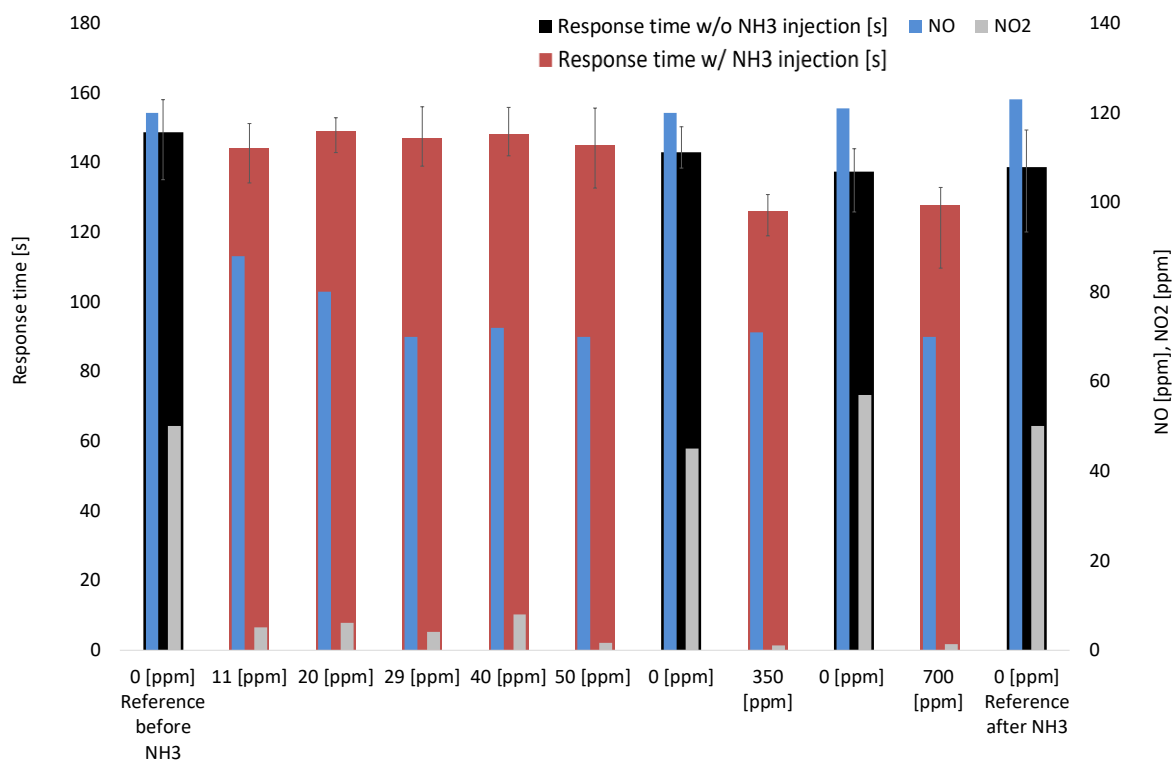


Figure 82: NH_3 direct effect on sensor response time. All measurements are for a medium engine operating point of 5 mg/m^3 soot concentration, 15 m/s exhaust velocity and 200°C exhaust temperature.

4.6.3.3.2. The cumulative effect of NH_3 (second approach)

The second test protocol for the NH_3 effect was a 300-hour test aiming to cover the full useful life of the sensor in a vehicle and investigate for durability and contaminations issues due to NH_3 excess. The evaluation points every 50 hours were used to quantify the effects on the sensor response time and on the ability of the sensor to fully regenerate. The examples of the first evaluations after 50 hours of exposure at the low-temperature level (150°C) and additional 50 hours (100 hours in total) at the high-temperature level (270°C) are presented in Figure 83a and b, respectively.

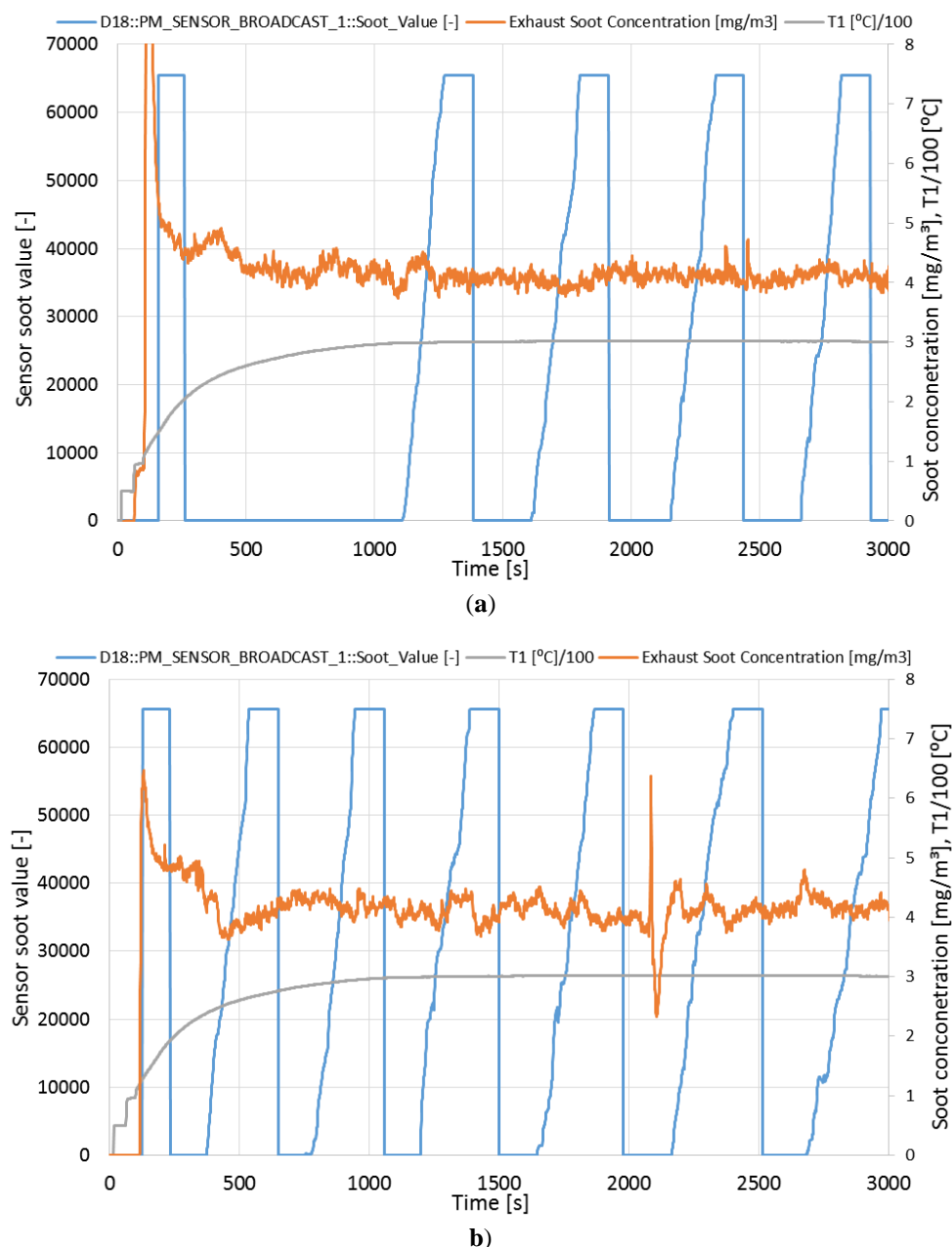
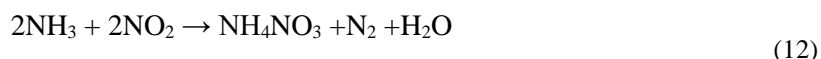


Figure 83: Evaluation of cumulative effect after 50 hours of NH_3 exposure a) low-temperature exposure
b) high-temperature exposure

The behaviour of the sensor during the first accumulation period is significantly different between the two measurements. It seems that the 50-hour exposure with low temperature creates a temporary effect on the sensor for one accumulation period. We should note again that during the evaluation points of this protocol, there was no NH_3 injection. Therefore, the mechanism that creates the response time increase can be only attributed to incombustible salts, which were previously formatted by the NH_3 excess and were already deposited on the sensing element. The formation of ammonium nitrate due to the low exhaust temperature during the NH_3 injection can explain this delay (Koebel and Madia, 2002):



These particles were possibly deposited either as solid or liquid on the sensing element during high NH_3 exposure and incommode the construction of soot dendrites or create a bias on the resistance between the electrodes due to their movement on the element. The above theory cannot be validated by SEM images because both sensors fully recovered after the first accumulation period. The high temperature of the first sensor regeneration partially decomposed the depositions (Koebel and Madia, 2002), but a few more minutes were needed for the full decomposition. After this period, the sensor response time was as expected based on the exhaust characteristics. Therefore, the effect of NH_3 excess during low exhaust temperature conditions is temporary, and sensors can recover after a few minutes with normal NH_3 levels in the exhaust.

On the other hand, there was no effect after the 50-hour exposure over the high-temperature level where the formation rate of ammonium nitrate is slowing down due to competing reactions of NH_3 with NO/NO_2 to N_2 and H_2O (Ciardelli et al., 2007).

The average response times (5 repetitions, excluding the first long duration discussed earlier) after each 50-hour exposure, are illustrated in Figure 84. It can be observed that there is no significant cumulative effect after the total length of 300h of operation with high NH_3 excess. The average response time of D14 sensor was reduced by 27% but on the other hand, the response time of the D21 sensor was increased by 13%. This difference can be explained by the mounting position of the sensors in the exhaust: D14 was installed close to the NH_3 injection point, followed by D13 and D21 which were installed slightly further from the injection point. Therefore, the concentration for the first sensor could have been higher due to insufficient mixing of NH_3 with the exhaust gas. The overall conclusion is that deviations from the reference values are expected to be low or in normal levels compared to the limited accuracy of the sensor itself and can be related with the mixing of NH_3 with the exhaust gas in this specific exhaust setup. This is important as it proves that despite a temporary effect after events with excessive NH_3 slip in an SCR system, the sensor can recover and operate normally.

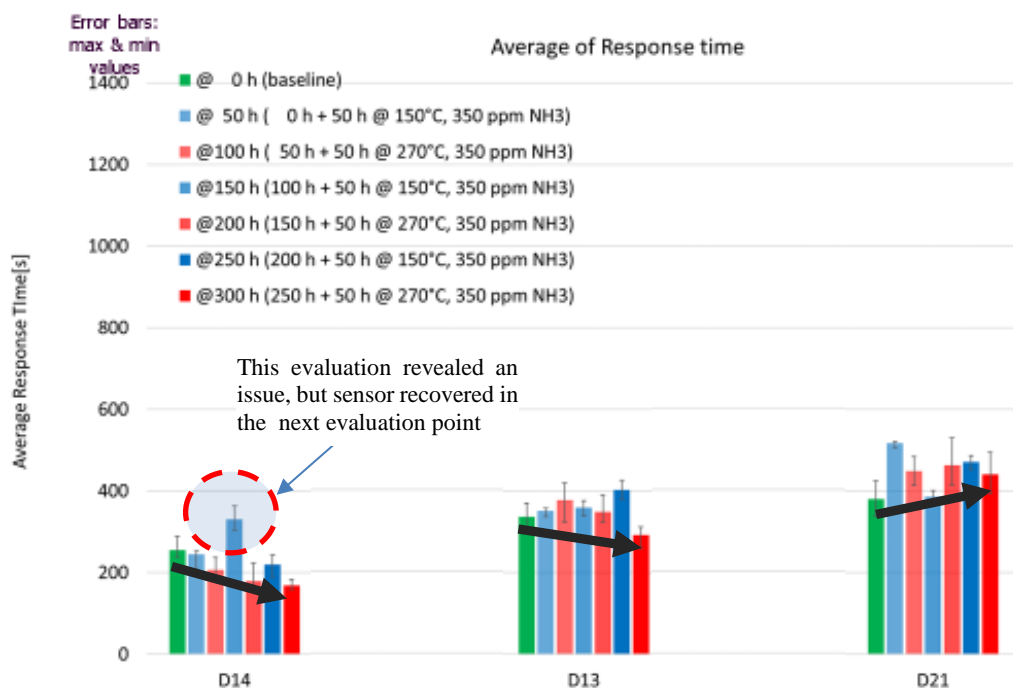


Figure 84: Evaluation of cumulative effect after NH₃ exposure (summary of all evaluation points)

4.6.4. Ash effect

4.6.4.1. Theoretical background

A small fraction of the solid particulate matter of engine-out emissions is composed of ash (Kittelson, 1998). Ash is mainly originated from the lubricant oil and more specifically from the inorganic additives of modern lubricant, which is consumed primarily in the engine cylinder (Johansson, 2008). Lubricant-derived constituents are Ca, Mg, Zn, S, Cl, Na and P. Additional but less significant sources of ash are the engine wear, corrosion of engine parts or exhaust line, metals in the fuel and fuel-borne additives that are used to enhance DPF regeneration (Sappok and Wong, 2007). The main constituents of this fraction of ash are Fe, Pb, Al Cr, Cu, Ni, Sr, Ti and Si can also slip in the exhaust through the intake air or the urea injection system as an impurity of the urea mixture used on modern SCR-equipped vehicles.

DPFs of modern diesel vehicles, significantly reduce the ash emissions (Vouitsis et al., 2011). The ash though is not combustible and is accumulated in the DPF. The accumulation of ash inside the channels reduces the active filtering area, increases the frequency of active regenerations and the backpressure which may lead to significant fuel penalty or in the worst case, filter blockage and necessity of filter cleaning or replacement (Tan et al., 2017). The high ash filtration efficiency is beneficial for the durability and contamination resistance of the soot sensor. Nevertheless, the ash-slip from or through the DPF can be significant during the following situations (Hedayat et al., 2017) (Liatl et al., 2013):

- **Cold start operation:** During cold engine start, the exhaust gas, line and components temperatures are below the dew point of exhaust gas water. The condensed water inside the DPF can act as carrier of ash particles to penetrate the filter wall and slip downstream of the DPF.
- **Clean DPF:** A recently cleaned filter with active or passive regeneration, has low filtration efficiency due to the high permeability of filter walls compared to the soot layer permeability (Suresh et al., 2000). Also, during DPF regeneration, particles can escape through the clean walls of the DPF assisted by the high exhaust flow.
- **Frequent engine stop and start events:** Measurement data proves that a blow-off event is possible, especially for clean DPFs.
- **DPF damage or removal:** low filtration is caused by cracks on the DPF substrate and melting of the substrate due to extreme temperature during the regeneration and intentional removal of DPF plugs or DPF brick for tampering reasons. Although it is the scope of the implementation of the resistive sensor to promptly diagnose the DPF damage, partial damage below the OTL can allow significant amounts of ash reaching the sensor.
- **Escape of large agglomerates through DPF walls:** The mechanism comprises the accumulation of ash particles in the filter substrate during normal operation, the grow into larger particles which block the pores of the substrate and the escape due to the increased pressure caused by the pore blockage.

The evidence discussed above suggests that exposure of soot sensors to high ash amounts cannot be ruled out and it is of interest to be investigated based on the measurement protocol presented in the section that follows.

4.6.4.2. Methodology

Previous studies concluded that the ash content, the consumption rate of the lubricant oil and the transfer rate of the lubricant ash are the key factors that determine the final ash mass in the exhaust of an engine (Givens et al., 2003), (Bardasz et al., 2010), (Tornehed and Olofsson, 2011):

- **Oil ash content:** It can be below 0.5% in new oil formulations and approximately 1.5 % for older technologies. The lubricant of the Daimler engine uses a low ash content oil of 0.69%, which is a typical value for modern lubricant oils.

- **Oil consumption rate:** It varies from 0.05 to 0.15% of the diesel fuel consumption (“DieselNet. Exhaust Particulate Matter,” 2019) depending on engine technology and oil characteristics. For modern engines, 0.1% is used as an indicative value.
- **Transfer rate of oil ash-component:** Predominantly, the oil creates inert ash particles which are accumulated in the DPF (Tan and Wang, 2018). The rate of the conversion of oil into particles is the transfer rate. The reported values vary, starting from less than 20% for Molybdenum (Mo) and Phosphorous (P) and reaching 70% for Calcium (Ca) as summarised by Tornehed, 2011. For sulphur, the transfer rate was found to be higher than 100% due to the contribution of fuel content (US Department of Energy, 2007). In this study, the fuel sulphur content was <10ppm to eliminate its effect. Thus, an average of around 50% can be used as a reference, but in this study, the worst-case scenario of 70% was used.

To assess the direct effect of ash particles, a worst-case scenario was selected for oil ash content and the oil consumption rate:

- Oil ash content = 1.9%
- Oil consumption rate = 0.25%

An evaluation point was selected with 5 mg/m³ soot concentration, 15 m/s exhaust speed and 210°C exhaust temperature. Sensors repeated five accumulation periods, and the average value was calculated for the evaluation of the sensors.

Regarding the cumulative effect after long exposure, based on the above values for a modern light-duty vehicle, the engine-out ash mass after the full useful life of 160,000km with assumed average fuel consumption of 6 l/100km, is around 33g. As discussed, most of this amount is filtered by the DPF, but it is possible under specific conditions to slip from the DPF and reach the resistive sensor. It was decided to expose the sensors on the whole amount of ash, ignore the DPF filtration efficiency and include intermediate evaluation points to examine the cumulative effect of ash exposure of the sensors.

The cumulative effect was examined every 18h on a different evaluation point with 15 mg/m³ soot concentration, 19 m/s exhaust speed and 260°C exhaust temperature. Sensors repeated five accumulation periods, and the average value was calculated for the evaluation of the sensors.

For our accelerated test, the desired ash amount was produced by high ash-contented oil (1.9%), which was mixed in the fuel (Takeuchi et al., 2003). The oil to fuel ratio was 0.5%, and the engine was operated in a semi-transient profile. This profile consisted of 4 district areas (Figure 85):

- Warming period up to 220°C

- Torque increase up to a specific temperature level at the sensor location: 450°C (5 repetitions)
- Aggressive torque increase up to a temperature of 520°C (1 repetition)
- Cooling for 10 minutes

This pattern was repeated until the desired ash quantity was produced based on the fuel consumption calculated from the ECU and measured in the fuel tank. This target was achieved after 80 hours of operation.

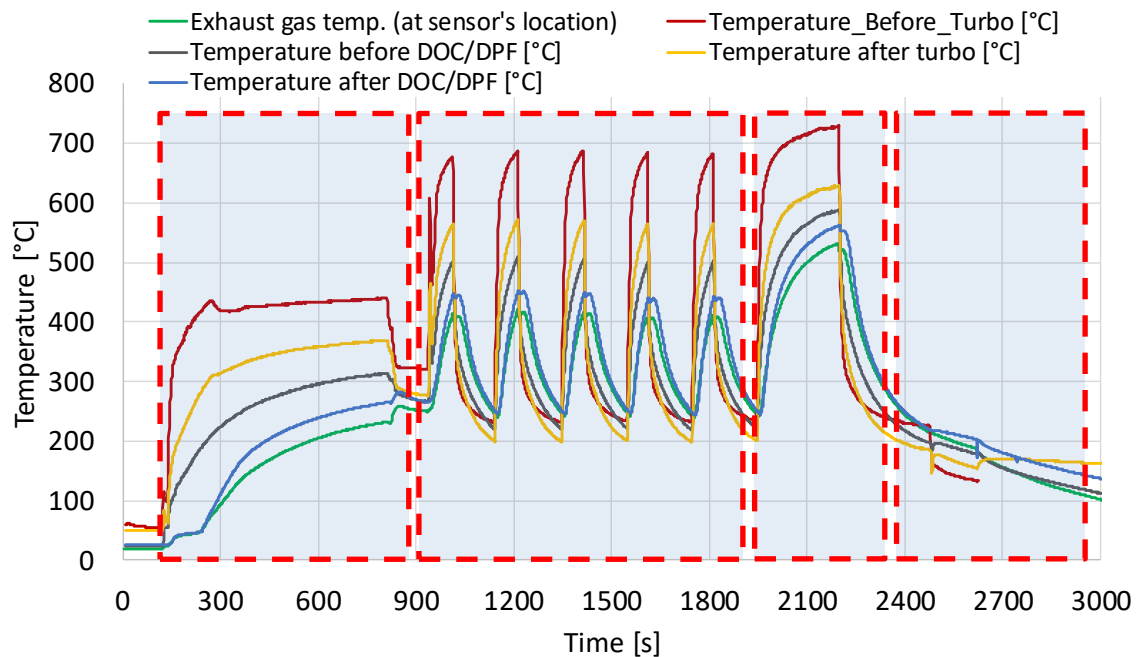


Figure 85: Transient pattern for ash exposure

Regarding the sensor characteristics, the target was to compare the contamination resistance of different software and hardware designs. Three different tip designs were tested and two different software.

- The first tip design was a short tip (Fragkiadoulakis et al., 2018) (Gen1)
- The second design was the alternative dual-tip design (Gen2), (Hedayat et al., 2017)
- The last was the currently used dual-tip design (Gen3-5).
- The P1 software was the default software of the sensors without any provision for protection from contamination
- The P2 software uses a pulsed electrostatic repelling voltage in the electrodes to periodically remove ash particles. This is usually done after the sensor regeneration and before the sensing mode to avoid any effect on the response time of the sensor and is called contamination prevention model (CPM) (Hedayat et al., 2017).

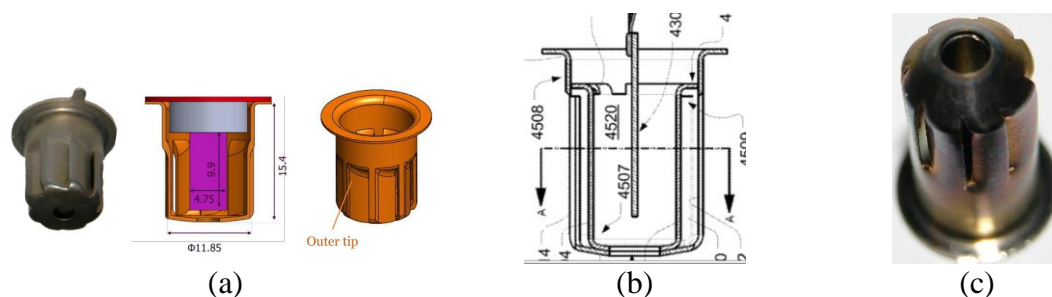
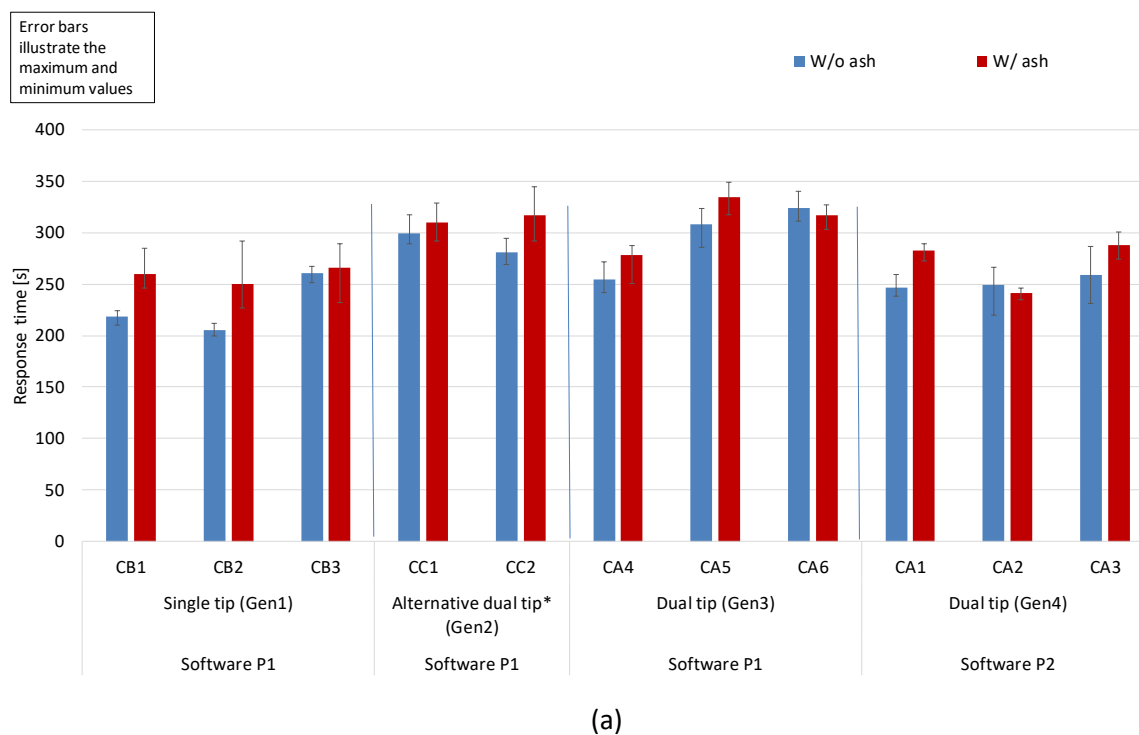


Figure 86: Design of sensor tips used for the ash experiment a) single-tip b) alternative dual-tip c) dual-tip

Sensors were measured in the test cell equipped with the Daimler engine (engine #1). Market fuel diesel was used for all tests (EN-590) with low sulphur content (<10 ppm). Also sulphur content of the engine lubricant was 0.2% weight (Total Quartz Ineo ECS 5W-30). The exhaust aftertreatment systems consisted of the originally commercially installed DOC. The DOC was intentionally installed in all experiments to avoid artefacts of unburned hydrocarbons (Grob et al., 2012). To prevent the accumulation of ash particles in the exhaust components, no exhaust aftertreatment device was installed after the DOC.

4.6.4.3. Results and discussion

Figure 87 a and b illustrate the results of the direct and the cumulative effect of ash exposure, respectively.



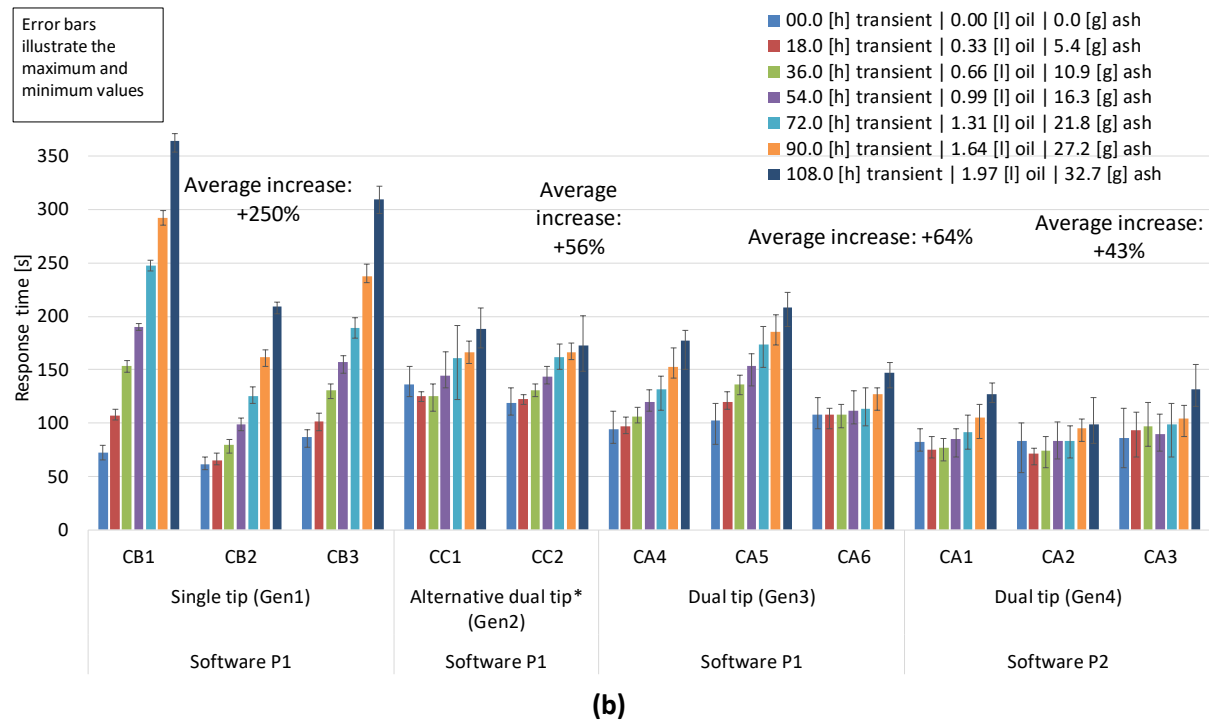


Figure 87: a) Direct effect on the response time of ash exposure b) Cumulative effect after long evaluated every 18h of ash exposure

Regarding the direct effect, all sensors are becoming slightly slower during high ash exposure (Figure 87a). This can be explained by the effect of ash on the construction of the dendrites. Soot particles, due to their high conductivity, create dendrites between the electrodes due to electrophoresis (Figure 88a). This is explained because the new particles that reach the electric field are focused onto the edges of particles previously deposited due to the distortion of the electrical field which creates a stronger electrical field at edges which are the previously accumulated particles (Riehle and Wadenpohl, 1995). On the other hand, ash particles are significantly less conductive and create a layer on the surface of the electrodes (Figure 88b). This mechanism delays the dendritic formation and increases the sensor response time. Also, no significant difference is observed between the different sensor tip designs of software, possibly due to the short duration of the exposure.

The evaluation of the cumulative effect reveals a few significant differences among the tested sensors. The single-tip compared to the dual-tip, fails to protect the sensor from the cumulative effect of ash particles. This should be attributed to the high contribution of the impaction as the deposition mechanism during the high ash exposure for the single-tip sensor (Fragkiadoulakis, 2016). The ash particles after the long exposure test are deposited onto the whole surface of the element because they cannot be removed by sensor regeneration. This ash layer prevents the soot particles from creating conductive paths, and the sensor needs a significantly higher time to reach the threshold resistance. On the other hand, the electrophoresis which dominates on dual-tip sensors attracts particles (both soot and ash) during the high ash exposure on specific areas with a high electric field, leaving limited but enough

space for the construction of soot dendrites. The above assumption is validated by the SEM images: the single-tip sensor is covered by ash particles whereas, for the dual-tip sensor, the ash particles are accumulated on the non-grounded electrode, leaving enough space for the construction of the dendrites (Figure 89).

The alternative dual-tip has equally good behaviour with the normal dual-tip because they have a similar design principle, and both rely on electrophoresis.

An important difference is observed between the two software. Software P2 compared to P1 helps to repel ash particles (comparison of dual-tip Gen3 and Gen4 sensors only). P2 uses a pulsed electrostatic repelling voltage in the electrodes to remove ash particles after the sensor regeneration and before the start of the accumulation period (Hedayat et al., 2017). This is validated by the SEM images in Figure 90. The whitish flakes (ash particles) are lower for the P2 software.

Even with the best tip design and software approach, there is a cumulative effect on the resistive sensor (Figure 87b). As expected, the P2 software has the best performance in terms of protection of the sensors of a significant remaining effect (increase by 43% after the total duration of the test). Currently, additional measures are investigated for further protection of the sensor from contaminants (analysed in the future work).

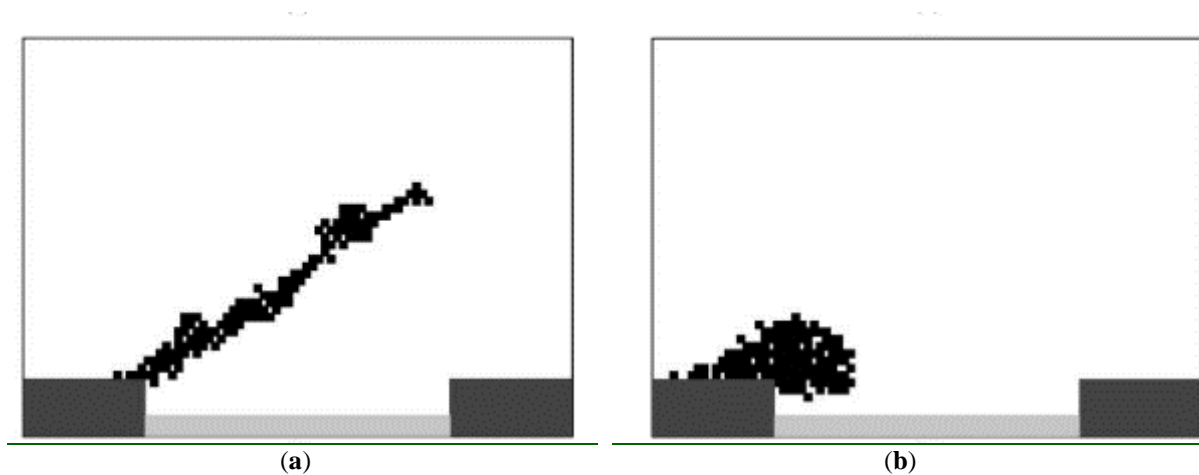


Figure 88: Accumulation pattern for a) soot particle b) ash particles. The higher conductivity of soot particles leads to the construction of dendrites between the electrodes instead of a particle layer on the element (Teike et al., 2012)

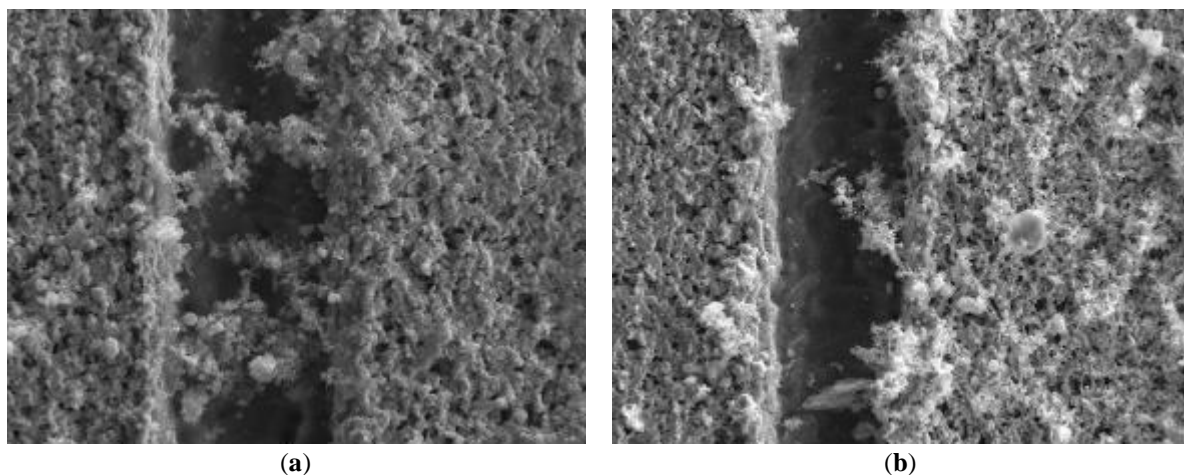


Figure 89: Comparison of single and dual-tip sensors. a) ash layer onto the whole surface for single-tip sensor b) ash accumulated on the non-grounded electrode leaving enough space for soot dendrites

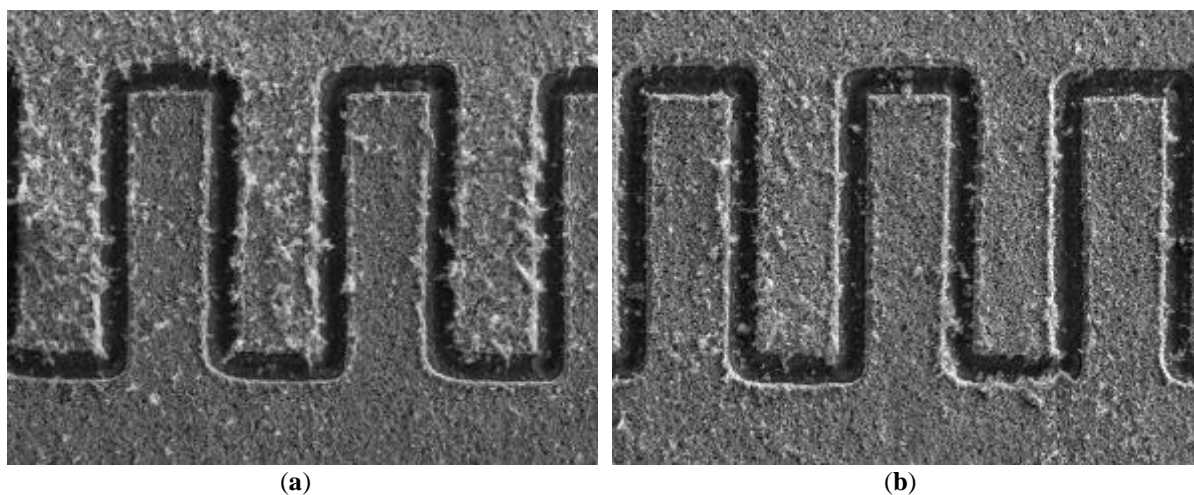


Figure 90: a) Extensive ash contamination (whitish flakes) on the upper electrode due to electrophoresis for the dual-tip sensor with P1 software b) lower contamination for the dual-tip sensor with P2 software.

4.7. Summary and conclusions

The challenges and the limitations related to the resistive soot sensor that came up during the realisation of the OBD model on a vehicle application were analysed in this chapter. The main results of this study can be summarised as follows:

- The low supply voltage can create regeneration issues in the sensor, but an increased regeneration temperature-target can tackle the issue.
- The latest tip design successfully overcomes the mounting orientation issue of the single-tip design.

- In parallel, this design offers enhanced water protection. The optimisation of the dew point strategy through dedicated cold-start measurements also makes sensors less vulnerable to the effects of water condensates.
- Experiments for the evaluation of direct or permanent effects on resistive sensors of various exhaust contaminants showed the effect of urea, NH_3 and ash as the most critical. Proper tip design and software solutions can diminish the impact on sensors.
- In the last part of this chapter, the focus is on the operating limits of the statistical sensor model, which derived from the comparison between the RDE-compliant and the RDE-dynamic. Additional measured levels during the development phase, can improve the performance on RDE-dynamic.

5. Advanced PN/PM on-board diagnostics

5.1. Introduction

Particulate filters are considered the key-device to reduce particle emissions and comply with current and future PN/PM type approval limits. This is the case for most gasoline engines and all diesel engines, either on light-duty or heavy-duty vehicles (Figure 91).

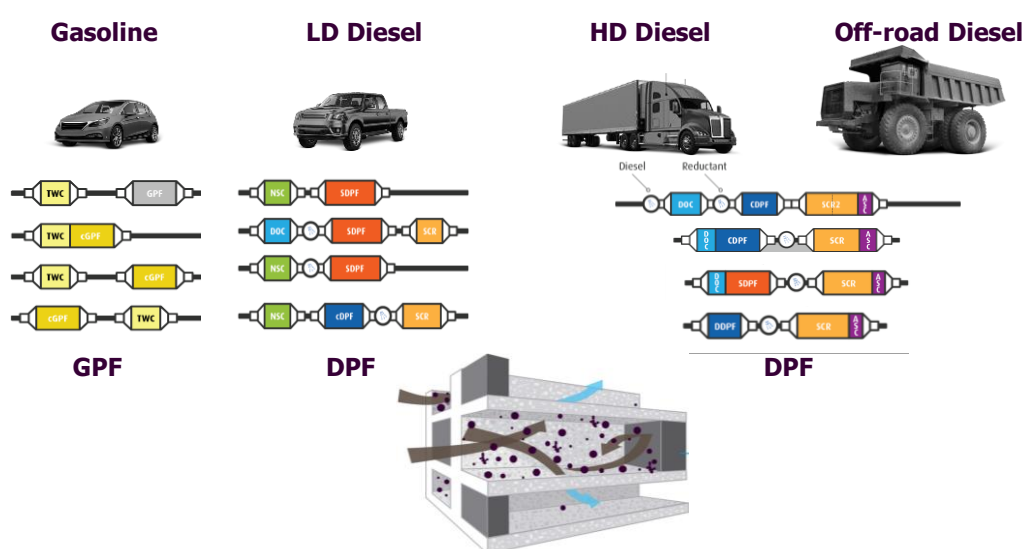


Figure 91: Exhaust aftertreatment of all vehicles. Particulate filters are the key-devices for the reduction of PN/PM emissions

It is important though to ensure the effectiveness of these systems during the vehicles life through the OBD system. The resistive sensor is a reliable and robust solution for DPF diagnosis according to current OBD requirements. Nevertheless, due to low particulate mass emissions of GDI vehicles, the response time of the resistive sensor is too high and not effective for GPF diagnosis. This is validated by literature data (Jessen et al., 2018) and also by measurements that were performed for this thesis (Appendix C). Alternative solutions that are investigated for GPF diagnosis comprise the use of advanced Delta-pressure sensors similarly to the current solution for DPFs, or temperature sensors upstream and downstream of the filter to monitor the temperature differences, or monitoring the oxygen storage capacity of a coated filter with lambda sensors, or combination of the above techniques (Jessen et al., 2018).

Also, besides the discussed current legislation, the next step for EU emission legislation which is currently prepared (EU, 2018a), contains work-packages for assessment of lower limits and additional

features of emission legislation such as OBD PN limit, on-board monitoring schemes (OBM) and in-service conformity of the vehicles. Current sensors are not able to provide reliable solutions for these demands. On the other hand, Portable Emissions Measurement Systems (PEMS) can accurately measure PN emissions according to the latest Real Driving Emissions (RDE) legislation (European Commission, 2017) but due to their negative aspects such as their high cost, weight and power consumption or the limited maximum continuous operation, are not suitable for current and future OBD applications. Also, the target group of customers for these devices is limited in companies, laboratories and authorities that perform RDE tests in the framework of type approval or market Surveillance related projects.

Based on the above, there is lack of improved PN/PM sensors. These sensors should be able to combine the positive aspects of current OBD sensors with PEMS merits aiming to monitor the emission levels rather than accurately measure them.

Also, it is worth mentioning that the future OBD as a system and approach will be significantly broader and enhanced with advanced capabilities and functionalities. The future OBD approaches and initiatives can be classified, into three levels:

- Emission data tracking from devices and sensors
- Emission data recording, retrieval, reporting and collecting from the vehicle
- Emission data processing and browsing of the results

The advanced sensors are part of the data tracking, but it is obvious that in the final version of future OBD, they will be part of smart systems, connected with a cloud (local or worldwide) to collect and analyse data targeting to distinguish and report high-emitters (Figure 92).

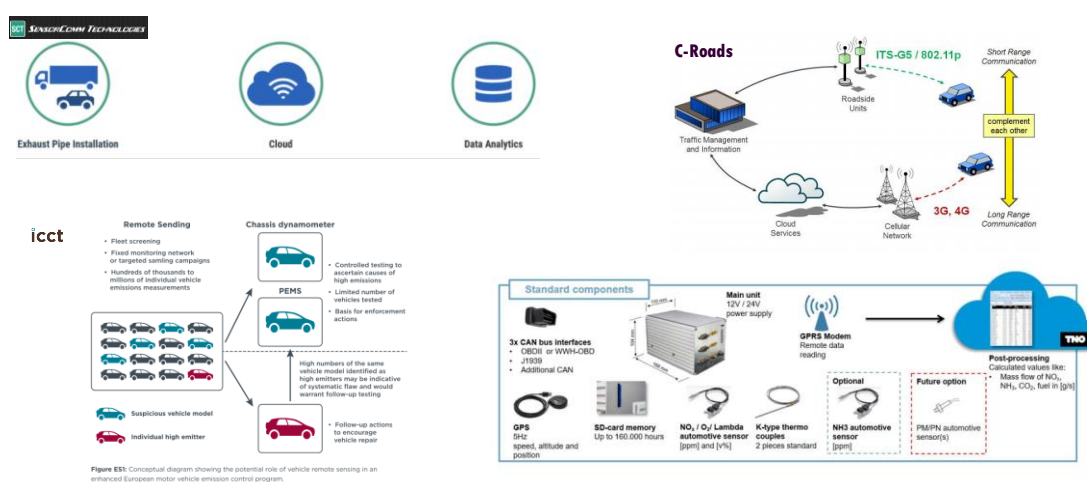


Figure 92: Sensors as part of future online emission monitoring systems (ACEA, 2018; TNO, 2018; TRUE, 2018)

An example of such systems is the on-board fuel consumption monitoring (OBFCM), which is currently developed in the EU. The EU takes the first steps towards the future OBD with the development of the new obligation for on-board fuel and energy consumption monitor of both LDVs and HDVs covering the data tracking, recording and processing. The goal is to develop detailed procedures for monitoring and assessing real-world CO₂ emissions through the tracking and collection of real-world fuel or energy consumption data from OBFCM devices. Instantaneous used fuel rate, the accumulated consumed fuel and total driven distance should be calculated by the ECU and be available via the OBD interface. Specifically, the signals to be used are:

- Total fuel consumed (lifetime) (l)
- Total distance travelled (lifetime) (km)
- Engine fuel rate (g/s)
- Engine fuel rate (l/h)
- Vehicle fuel rate (g/s)
- Vehicle speed (km/h)
- PHEVs: data categorised between charge increasing/depleting mode; also grid energy into the battery (kWh)

The work towards this new obligation needs to cover the following specific aspects:

- Development of accuracy requirements of OBFCM devices
- Development of a method for the on-board monitoring of HDV payload
- Development of standardisation requirements for on-board data recording and retrieval
- Development of a procedure for collecting and processing real-world fuel consumption data

Despite the focus on fuel consumption, one additional target of the OBFCM study is to explore whether data related to pollutant emissions could be recorded on-board. This addition is induced by California's regulation for the future HDV OBD which will require (starting from MY 2022) the tracking and reporting of both CO₂ and NO_x emissions in real-world use using the existing sensors and hardware.

Looking to the future of other markets, US have taken specific initiatives focusing on i) remote OBD to transmit OBD fault information for LDVs (OBD III), ii) NO_x emissions and fuel consumption tracking in real-world use for HDVs (REAL) and iii) OBD as the primary methodology for HDVs I/M enhanced with additional features.

The remote OBD for LDVs will collect on-board data (e.g. fault on an exhaust aftertreatment device) and transmit the OBD fault information to roadside receivers (e.g. through cellular networks). Retrofitted equipment and the roadside infrastructures are needed to transmit the vehicle's OBD data. This approach which is currently studied by states (including California) through pilot programs, does

not include the tracking or reporting of emission data (e.g. NO_x emissions) but aims to enhance or even replace the LDVs I/M programs through automated inspection of emission-related devices.

The REAL initiative for monitoring of HDVs NO_x and CO₂ emissions after the certification during the real-world use of the vehicle, will be in force starting from MY 2022. The tracking relies on existing sensors and hardware and the emission data will be used to assess potential high emission issues and to inventory for the future development of regulations. The provision is to use the OBD port and a scan tool to access the data (no provision for remote functionality) which are stored in the ECU of the vehicle using data binning technique (for NO_x emissions).

The new I/M for HDVs based on enhanced OBD functionalities, according to a recent report, can provide significant and tangible emission benefits. The different methodologies that were examined comprise the current OBD hardware for data tracking and alternative solutions for wired or remote data collection from the vehicle along with an analysis of the costs for implementation and operation of each system. OBD coupling with additional sensors or devices (e.g. mini-PEMS or RSD) could also play a smaller role towards a more comprehensive I/M program.

Similarly, China has launched a pilot program to equip nearly 5000 vehicles (mostly HD) with remote on-board sensing systems to monitor real-time on-board NO_x emissions in a second-by-second approach. This program includes a type of real-time Telematics gateway or terminals that communicate with an (authority) data server and sends upon request emission, engine and fault-related information (e.g. vehicle speed, engine speed, NO_x sensor output, DPF pressure difference value, MIL lamp status, fault codes etc.). Additionally, GPS positioning monitoring, GSM network transmission, high-speed CAN communication, ultra-low power consumption and other features are provided.

In the following analysis, the focus is on the advanced sensors, and the demands and methods for PN/PM estimation as it may be required by future legislation for advanced on-board diagnostics and monitoring are reviewed. To support this analysis, experimental data of an advanced PN/PM electrostatic sensor are presented and discussed. Finally, the conclusions include the discussion of the readiness and maturity of each technique for OBD applications.

5.2. Regulation and market needs for advanced PN/PM sensors

Resistive sensors are an accurate and robust solution for the current OBD legislation needs. Taking as an example, the future EU legislation, which is currently under discussion, several use-cases for advanced PN/PM sensors may arise. The next sections summarise the possible legislation and market needs for such sensors focusing on the EU.

5.2.1. Lower OBD threshold values for PM emissions

Euro 6-2 PM standard of 12mg/km was a reasonable limit considering the maturity of the available technology for PM estimation. Delta-pressure and resistive soot sensors are the current solutions for DPF diagnosis. Improved and new sensors can aid in further reducing the limit for a quicker and more effective DPF diagnosis. Nevertheless, this will not improve the expectations for correct GPF failure detection. The range of mass emissions from a gasoline engine before the particulate filter is significantly lower even than the type-approval limit of 4.5mg/km. An additional PN limit is discussed in the next paragraph to solve this issue.

5.2.2. OBD limit for PN emissions

Currently, there is not an OBD limit for PN emissions. DPF failures can be sufficiently diagnosed based on the PM OBD limit, but the correct diagnosis of the GPF is not secured due to the low PM emissions of gasoline vehicles which allow a non-GPF equipped vehicle to fulfil the legislative requirements (AVL, 2017). Jessen et al., (2018) presented the four solutions that Bosch examined for GPF diagnosis. Starting from the resistive particle sensor which is used in DPF diagnostics, it appears to be unsuitable for GPF diagnosis. The Oxygen Storage Capacity (OSC) method, which uses two lambda sensors, can effectively diagnose only the total removal of a catalysed filter. The temperature sensor-based method can additionally recognise the total failures of a non-catalysed filter but again fails to diagnose any partial failure. Finally, the differential pressure sensor seems to be the most promising concept, being able to diagnose a partially failed filter, but the achieved accuracy is not considered robust. Therefore, a limit of particles per km is of paramount importance for a flawless diagnosis of GPF removal or functional failure.

5.2.3. Fleet monitoring with on-board sensors and Smart Emission Measurement Systems (SEMS)

The lifetime emission compliance of a vehicle is guaranteed through the OBD system and the periodic inspection (Denis and Lindner, 2005). There are, though, clear evidence of OBD tampering, especially for DPFs (European Commission, 2018). Also, periodic inspections have been proved outdated due to low sensitivity, and a New Periodic Technical Inspection (NPTI) is investigated (Kadijk and Mayer, 2017). In addition, there are ongoing discussions for new approaches on taxation and traffic regulations such as “polluter pays” schemes. Advanced on-board PN/PM sensors incorporated in smart systems, is a requisite for the adoption of fleet-monitoring.

5.2.4. On-Board Monitoring (OBM) of PN/PM emissions

Emission monitoring can augment the significance and value of new OBD legislation on the target of emission reduction. The vision is to be able to measure, record and share data for the performance of vehicle environmental protection systems. This is going to be implemented in the near future for NO_x emissions in the US (CARB, 2018) and China (Wu, 2019). For the particulate matter emissions, it could be feasible through the advanced sensors, coupled with the necessary software and infrastructure for data sharing (e.g. over-the-air (OTA) vehicle connectivity) and online processing.

5.2.5. In-service conformity

The questionable effectiveness of current in-service conformity specifications (EU, 2018b), forces the legislation authorities, to assess new methods for laboratory tests but also for real-world driving evaluation with PEMS in the light of extended lifetime operation of a vehicle. SEMS with advanced sensors can be considered effective tools in this direction to replace or complement the expensive and complicated PEMS.

5.2.6. Market requirements

Apart from the legislative requirements, there are additional market needs that justify the demand of advanced sensors for OBD applications. The automotive industry could utilise these sensors to improve the new engines and aftertreatment devices or strategies through the plethora of data from the fleet that can be gathered with SEMS. Many research laboratories and organisations, could also be benefited by supplementation of PEMS or laboratory equipment and procedures (such as PMP protocol, SPN method) for creating different layers of particulate matter data in less time and resources consuming manner. The aim is to monitor the emission levels rather than accurately measure them.

5.2.7. Summary of needs and requirements

These requirements have created a demand for improved PN/PM sensors which are directly installed in the exhaust line and able to combine the positive aspects of current OBD sensors with advantages of PEMS.

Advanced sensors could be incorporated in a sensor-based measurement system which includes an on-board power source, weigh less than 7kg in total, can be quickly set-up and ready for measurement and have accuracy within 10% of current PEMS (Wikipedia, 2019). This system can be easily installed into a vehicle to measure, calculate and deliver real-time data for real-world tailpipe emissions and allows for on-board monitoring in large scale with minimum or no calibration requirements. Example of such a system has been already presented as a prototype for gaseous emissions SEMS from TNO and

Horiba (Kadijk et al., 2016) (TNO, 2018). It records the way the vehicle is operated, enables emission monitoring during the regular operation and provides new insights into real-world nitric oxides (NO_x) and ammonia (NH₃) emissions.

5.3. Advanced sensors

Future PN/PM sensors need to combine characteristics of current OBD sensors and PEMS and to be integrated into smart systems and advanced OBD models for efficient on-board diagnosis and monitoring. A list of the candidates which are close to the market or in an advanced development phase apart from the resistive sensor is presented and categorised based on their operating principle (Table 30).

Table 30: Overview of methods for PN/PM estimation

Operating principle	Particle property	Application
Resistive	PM	OBD
Optical	PN/PM	Advanced OBD
<i>Absorption</i>		
<i>Scattering</i>		
<i>Extinction</i>		
Electrical charge-based	PN/PM	Advanced OBD
<i>Electrostatic</i>		
<i>Diffusion charger</i>		

5.3.1. Optical principle

Optical sensors are benefitted from the result of the interaction between the exhaust particles with a laser beam. The incident light can be scattered by a particle, and in parallel, a portion of its energy can be absorbed by the particle. The combination of both effects is extinction. Sensitive detectors are used in all cases to measure and quantify this interaction based on scattering, absorption or extinction. A plethora of laboratory PN/PM instruments are based on the optical method: Condensation Particle Counter (CPC), Photoacoustic Soot Sensor (PASS), opacity meters, spot meters and aethalometers are typical examples (Giechaskiel et al., 2014). For OBD applications, only a few candidates could cope with the demands for low cost, compact dimensions, no need for calibration during lifecycle and accurate PN/PM measurement. At a mature research level, Johannes Kepler University Linz (JKU) has presented a Laser-Induced Incandescence (LII) sensor based on light absorption (Zhang et al., 2017, Zhen Zhang, 2016, Zhen Zhang et al., 2014). Also, 3DATX par SYNC device combines three low-cost environmental sensors based on scattering, extinction and ionisation technique (Johnson et al., 2018).

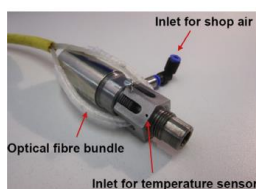
5.3.1.1. Laser-Induced Incandescence

In the LII technique, the temperature of the particles is increased approximately to 4000K just below the soot sublimation temperature due to particles interaction with the laser beam and the consequent light absorption. Because of the higher temperature, the particles radiate more strongly. This increase in radiation (incandescence) is the LII signal. Its peak is proportional to soot mass and is measured using collection optics and photodetectors. After being heated, the soot particles cool and the incandescence signal will decay with time. This decay time lasts approximately 200–500 ns depending on the size of the primary particles (excitation time=5–20 ns). From the measured LII signal and by application of energy transfer process models, one can obtain the information about the mass fraction (PM) and size distribution of the illuminated particles. Afterwards, the calculation of PN is feasible. The probe is vertically fitted in the exhaust and needs externally cooling (e.g. by pressurised air) which is an issue for OBD applications. Also, concerns are raised about the signal drift due to the clogging of the optical window, but this has been addressed by delivering the laser beam and collecting the incandescent light through the same access. Thus, only one optical window is in contact with the soot in the tail-pipe, and the high power pulsed laser radiation continuously cleans it.

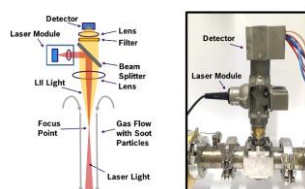
5.3.1.2. 3DATX par SYNC

The unit consists of 3 different sensors sensitive to different size fractions: ionisation for fine/ultrafine particles (up to 500nm), scattering for intermediate particulate groups (300nm to 2.5µm) and opacity for coarse particles (approximately 2.5-10+µm). It also provides surrogate outputs for PN and PM. The unit is light-weight (3.7kg) and compact for SEMS applications. Post-processing of the three signals with appropriate transfer function and models can provide reasonable estimations of mass and number for OBD applications. Few studies are available for its performance. Also, there are no data for the performance against instruments compatible with the legislation needs for OBD evaluation.

LII prototype from AVL and Johannes Kepler University Linz, Austria



LII prototype from BOSCH



3DATX



Figure 93: Optical sensors. LII sensors are still under development. AVL and BOSCH have presented prototypes for portable applications. 3DATX is commercially available and combines three low-cost sensors.

5.3.2. Electrical charged-based principle

Exhaust particles carry a physical, electrical charge. According to Maricq, (2006) and Bilby et al., (2016), the exhaust particles can be considered electrically neutral. 30-45% of particles are positively charged, 30-45% negatively, and 10-40% are neutral following a Boltzmann charge distribution (Maricq, 2008). This charge distribution was found to be the same for engine-out and post DPF measurements of a diesel engine and similar to gasoline engines (Maricq, 2006).

5.3.2.1. Electrostatic sensors

Electrostatic sensors exploit this natural charge. Continental (Continental Automotive GmbH, 2019), EmiSense (Allmendinger et al., 2013) and Honeywell (Honeywell Laboratories Plymouth, 2010) have developed or evolved sensors based on the electrostatic principle. The EmiSense sensor seems to have the most highly evolved design consisting of two coaxial electrodes protected by an optimised sensor tip and is positioned vertically to exhaust gas flow. The principle of operation is to separate the positive and negative particles into two electrodes, create dendrites of particles in each electrode which carry an amplified charge and afterwards measure the produced current from the electrically induced mobility created by the bouncing of agglomerates between the two electrodes. Owing to the high amplification gained by charge accumulation on the agglomerates (2-3 order of magnitude higher than the natural charge) the insulators and amplifiers of the sensor are simple and low-cost. The measured current is well correlated to PM (Steppan et al., 2014). Correlation to PN has not been validated yet. Also, cross-sensitivity to exhaust flow was investigated by Maricq et al., (2018). High flow increases the drag force of the dendrites and tilts them away from the opposite electrode without significant fragmentation. This phenomenon creates a quiescent period with artefacts on the sensor signal. Low concentration can deteriorate this phenomenon. Finally, contrary to the accumulation sensors, cross-sensitivity to ash is not a significant issue for the lifetime of the sensor.



Figure 94: Electrical charge-based principle; electrostatic sensors. The University of Texas (Austin) started the development of an electrostatic sensor to make use of the amplified charge of particles in 1999. EmiSense presented the first prototype for OBD applications in 2010. Continental redesigned the electronics and introduced its sensor in 2015, but the development suspended and is currently available only for agriculture applications. CoorsTek acquired EmiSense technology (2013) and is the only supplier today for this technology. In parallel, Honeywell developed and presented a sensor which uses the natural charge directly, but the development suspended.

5.3.2.2. Diffusion charger sensors

Particles are also able to acquire additional electrical charge by diffusion, field and flame charging and static electrification. A corona diffusion discharger achieves highly concentrated unipolar ion charging. Dekati investigated this ionising technique by diffusion as a miniature device or sensor with ETaPS (Electrical Tail Pipe Sensor) (Rostedt et al., 2009) which was further refined and developed by Pegasor with the PPS (Pegasor Particle Sensor). Recently NGK/NTK presented a miniature PPS which is highly portable, cost-effective and integrated into the NGK/NTK compact emissions meter (NCEM) along with NO_x and lambda sensors. Rostedt et al., (2017) presented a miniaturised sensor for OBD applications, which is also a compact PPS in terms of operating principle and hardware components. Details of the operation of the PPS and the first results on a diesel engine were presented by Ntziachristos et al., (2009). A series of publications followed in the next years about the operating principle, sensor calibration and various applications for Pegasor-type DC sensors. These are all summarised by Besch, 2016 and are briefly described below.

A high voltage corona discharge produces unipolar ions. Particles are pumped inside the sensor body by an ejector diluter using sheath air and subsequently are charged by ions via diffusion charging. The excess of ions that are not attached to particles is removed from an ion trap. The escaping current of the particles exiting the sensor body, demands an additional current to maintain the electrical balance of the isolated part of the sensor. This current is measured by an electrometer and is proportional to the particle surface area. Proper calibration with diesel exhaust of this signal was performed by (Ntziachristos et al., 2013), to report the PM and the PN concentration. Enhanced performance and accuracy on PN/PM estimation can be achieved using two Pegasor sensors in parallel with different ion trap voltages. This set up yields two distinct signals because of the different fraction of the size distribution collected by the two sensors. The comparison of the two signals provides information for the particle size distribution, which ameliorates the performance of PN and PM calculation and significantly reduces the PPS error (Amanatidis et al., 2016). Nevertheless, this complicated set-up is not suitable for OBD applications. A critical drawback of Pegasor-type sensors is the requirement for compressed air. This needs to be addressed for OBD applications (Rostedt et al., 2017). Finally, durability tests are not currently available, and the drift of the sensor due to internal contamination should be investigated.



Figure 95: Electrical charge-based principle; Diffusion Charging. Dekati investigated the ionising technique by diffusion as a miniature device or sensor with ETaPS (Electrical Tail Pipe Sensor), which

measures the escaping current. It was further refined and developed by Pegasor with the PPS (Pegasor Particle Sensor). Recently NGK/NTK presented a miniature PPS which is highly portable, cost-effective and integrated into the NGK/NTK compact emissions meter (NCEM) along with NO_x and lambda sensors. Rostedt et al., (2017) presented a miniaturised sensor for OBD applications, which is also a compact PPS in terms of operating principle and hardware components. Pegasor was acquired by CoorsTek in 2014. Testo has also developed a handheld nanoparticle counter based on the measurement of charge acquired by particles.

Table 31 contains a summary and comparison for the advanced PN/PM sensors. The last column contains as a reference, the characteristics of the resistive sensor even though it cannot be considered an advanced solution.

Table 31: Summary table of PN/PM sensors for future applications

	NGK/NTK (NCEM)		Miniaturized PPS		3DATX parSYNC		EmiSense-Continental		LII-JKU		Stoneridge	
	PM	PN	PM	PN	PM	PN	PM	PN	PM	PN	PM	PN
Operation principle	Diffusion charge		Diffusion charge		Opacity, Scattering, Ionization		Electrostatic		Absorption-Laser Induced Incandescence		Resistive	
Sample rate	0.2Hz		0.2Hz		<1Hz		0.1Hz		0.1Hz		0.1Hz	
Upper range	50 [mg/m ³]	1E+8 [p/cm ³]	80 [mg/m ³]	1E+8 [p/cm ³]	Not available	Not available	600 [mg/m ³]	Not available	Not available	Not available	25 [mg/m ³]	Not available
Resolution	0.001 [mg/m ³]	125 [p/cm ³]	0.001 [mg/m ³]	5000 [p/cm ³]	Not available	Not available	0 [mg/m ³]	Not available	Not available	Not available	0.1 [mg/m ³]	Not available
Particle size range	10-2500nm		10-2500nm		10 to 10000nm		23-10000nm		Not available		10-2500nm	
Uncertainty	±10%		±8%	±17%	Not available	Not available	±10% above 5mg/m ³ ± 0,5mg/m ³ at 2-5mg/m ³		Not available	Not available	±18	Not available
Sampling	Sensor in exhaust		Sensor in exhaust		(Heated) sampling line		Sensor in exhaust		Sensor in exhaust		Sensor in exhaust	
Dilution or conditioning	Sheath clean compressed air		Sheath clean compressed air		None		None		None (Compressed air cooling is needed)		None	
Calibration	Generic calibration		Generic calibration		Generic calibration		Generic calibration		Generic calibration		Vehicle-specific	
Cross sensitivities	None		None		None		Relevant impact of ash,		Not available		See 4.6	
Performance on different applications	Accuracy depends only on particle size		Not tested yet		Available tests for heavy-duty only		Not tested		Not tested yet		Diesel OBD optimised	
Size/weight	Sensor: Miniature, ECM:<12kg		Sensor: Miniature		3kg		Spark-plug size		Miniature		Sensor: 'Spark-plug' size	
Implication on the use	Continuous operation, Needs compressed air		Continuous operation, Needs compressed air		Continuous operation, needs replacement of consumables		Needs time to built-up initial dendrites, cross-sensitivity to flow		Not tested in-vehicle, Requires cooling		Blind windows for regeneration	
User friendly	<1h installation duration		<1h installation duration		<0.5h instal. duration		<10min instal. duration		<0.5h instal. duration		<10min instal. duration	
Communication	CAN, ECM in the trunk		CAN, ECM near the sensor		Wireless		CAN, ECM near the sensor		Not available		CAN, ECM near the sensor	

5.4. Testing with Electrostatic sensor

The basic operation principle of the electrostatic sensor was described in section 5.3.2.1. Briefly, particles are entering the sensor tip, and due to the electric field, the charged particles are accelerated towards the positive or negative electrode. Particles are then discharged, accumulated to filaments and brake off due to the electric force applied from the opposite electrode. During the movement between the electrodes, an amplified current is created, which is measured and correlated with mass concentration. The exhaust velocity is a vital cross-sensitivity in this operation, which is analysed below. Figure 96 illustrates the details of the Continental sensor that was used in this study. The sensor probe is fitted vertically to the exhaust line similarly to the resistive sensor, and the exhaust flow is conditioning in the sensor tip before reaching the sensing area.

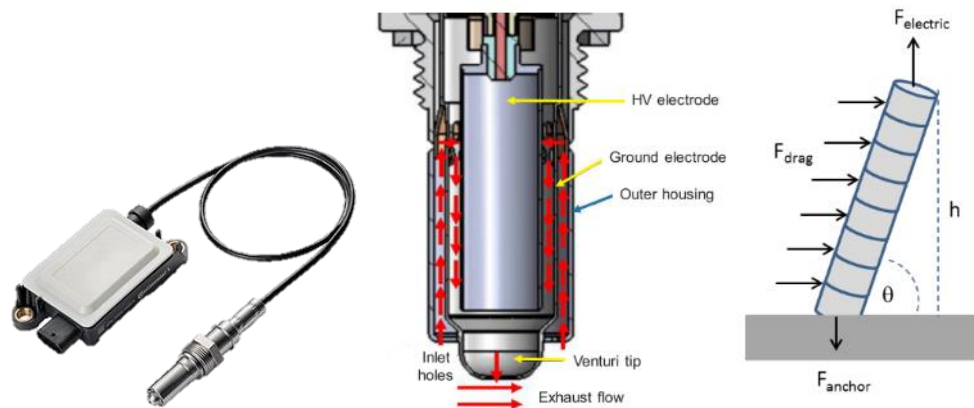


Figure 96: Electrostatic sensor a) sensor probe with the sensor control unit (SCU) b) details of sensor probe (Maricq and Bilby, 2018) c) forces on particles accumulated in one of the electrodes (Fitzpatrick et al., 2018).

Having described the OBD model with the resistive sensor for DPF diagnosis, it is evident that the use of the electrostatic sensor instead of the resistive sensor could add some merits in the OBD system, and this was the target of the measurement campaign with the electrostatic soot sensor that is described below. Also, considering the future legislation and market requirements discussed earlier, one could consider this sensor a prominent candidate for these applications. A full investigation of the performance of the electrostatic sensor for advanced PN/PM applications though was beyond the scope of this study and will be investigated and presented in a future publication. Focusing thus on OBD application and particulate mass measurements, a measurement protocol was developed for the Toyota engine (engine 2).

Both steady-state and transient measurements were performed with 3 Continental sensors (Conti 1,2,3). The targets were to investigate:

- The cross-sensitivity of the sensor to exhaust flow or velocity
- The sensor running-in time (or quiescent period) over different driving cycles

- The accuracy of the sensor against reference laboratory equipment

The measurement protocol comprised legislative driving cycles (NEDC, WLTC, FTP-75, LA92) and steady-state measurements. Two DPF failure levels were measured: engine-out emissions and EU OTL (NEDC).

As a first step, the sensor signal for the electrostatic sensor was compared to the measurement of the MSS. A second-by-second comparison indicates that there is an offset on the sensor signal, which is well-correlated with the transient characteristics of the exhaust gas. Figure 97a illustrates the needed correction for different exhaust velocity levels. With the application of the velocity correction, the signal of the sensor is in good agreement with the MSS (Figure 97b).

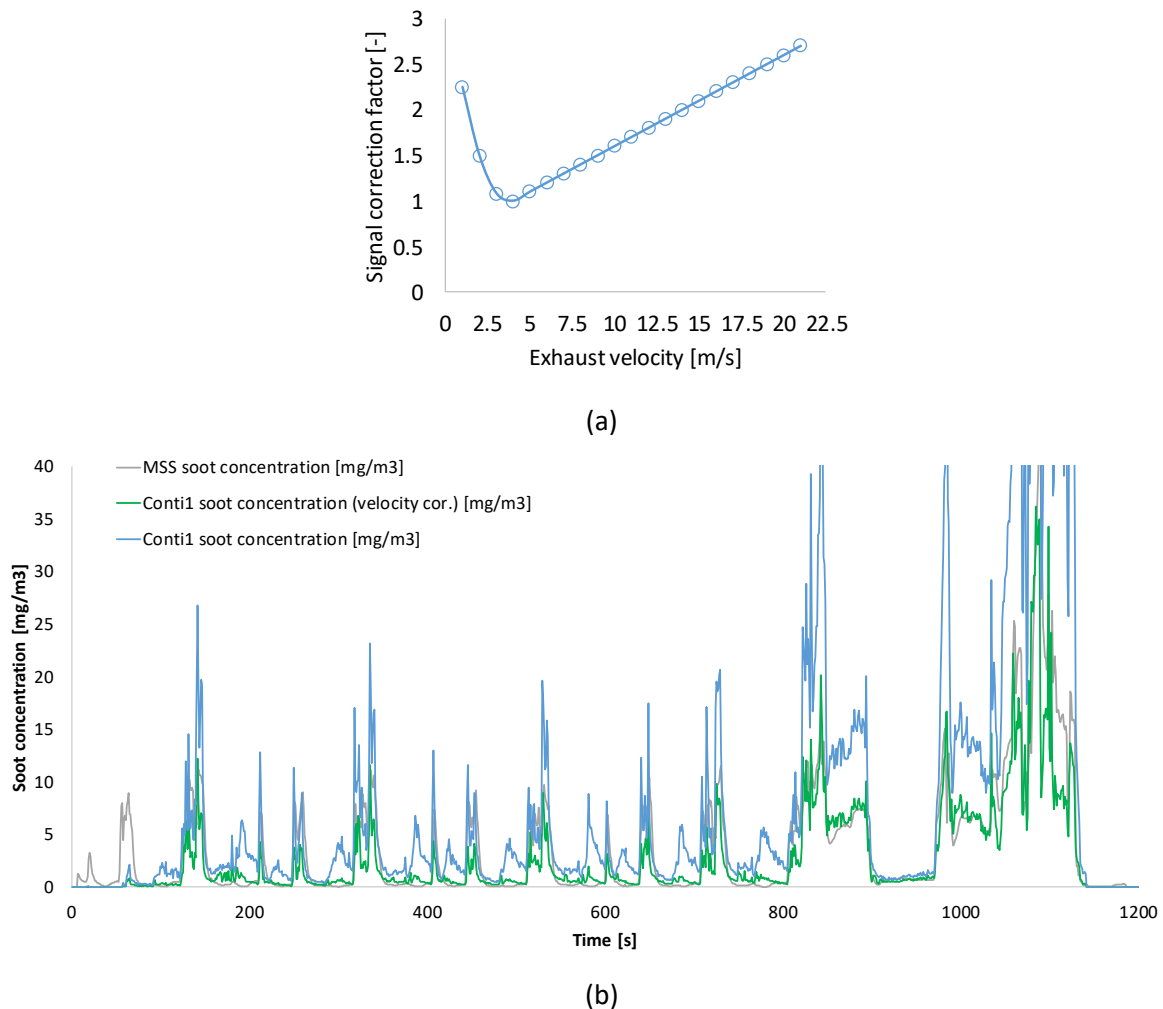


Figure 97: Correlation of exhaust velocity with the signal correction factor

The running-in time was investigated during several driving cycles using flow correction. This is the time needed for the first agglomerates to be built and reach a critical length and start the debouncing process. To simulate the scenario of obligation to diagnose a DPF failure in the first minutes after the occurrence of the issue, sensors were cleaned with pressurised air before the start of each cycle,

and the emission level of the cycles was at the OTL (12 mg/km over NEDC). In all cycles, sensor #3 had an abnormal behaviour and was excluded from the investigation. The worst performance is observed for NEDC cold where the running-in time was higher than 500 seconds (or 42% of the cycle duration). On the other hand, the result for FTP-75 was significantly better; 170 seconds (or 12% of the cycle duration before the 10-minute engine stop) were enough for the running-in time. The performance during the WLTC, and the LA-92 was in the moderate compared to the other two cycles (Figure 98a). These differences are correlated with the cumulative soot mass for every cycle (Figure 98b). The running-in time was significantly lower for operation without cleaning the sensor. In this case, the small differences that were observed should be attributed to the different temperature increase rate among the driving cycles. During cold operation, unburned HCs and water may be present in the exhaust, which possibly leads to delayed initial capturing of the particles.

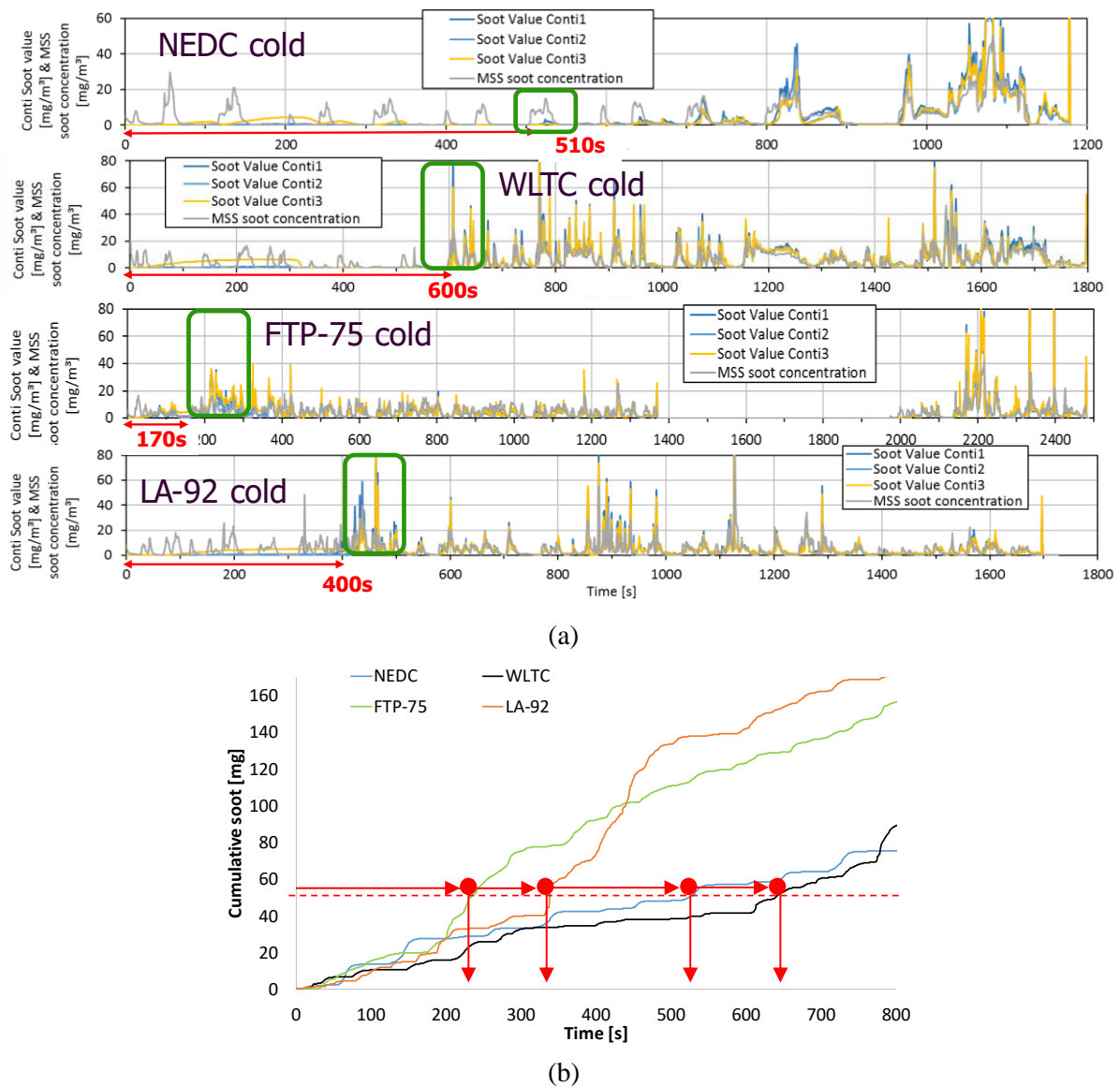


Figure 98: Running-in time for different driving cycles

Figure 99a illustrates the correlation of the electrostatic sensor (with flow correction) with the reference instrument (MSS). The signals exhibit a close match, and only some peaks are higher in the case of the electrostatic sensor. Figure 99b summarises the results of all steady-state and transient tests with the electrostatic sensors. The overall performance is close to the MSS regarding of the transient or steady-state operation.

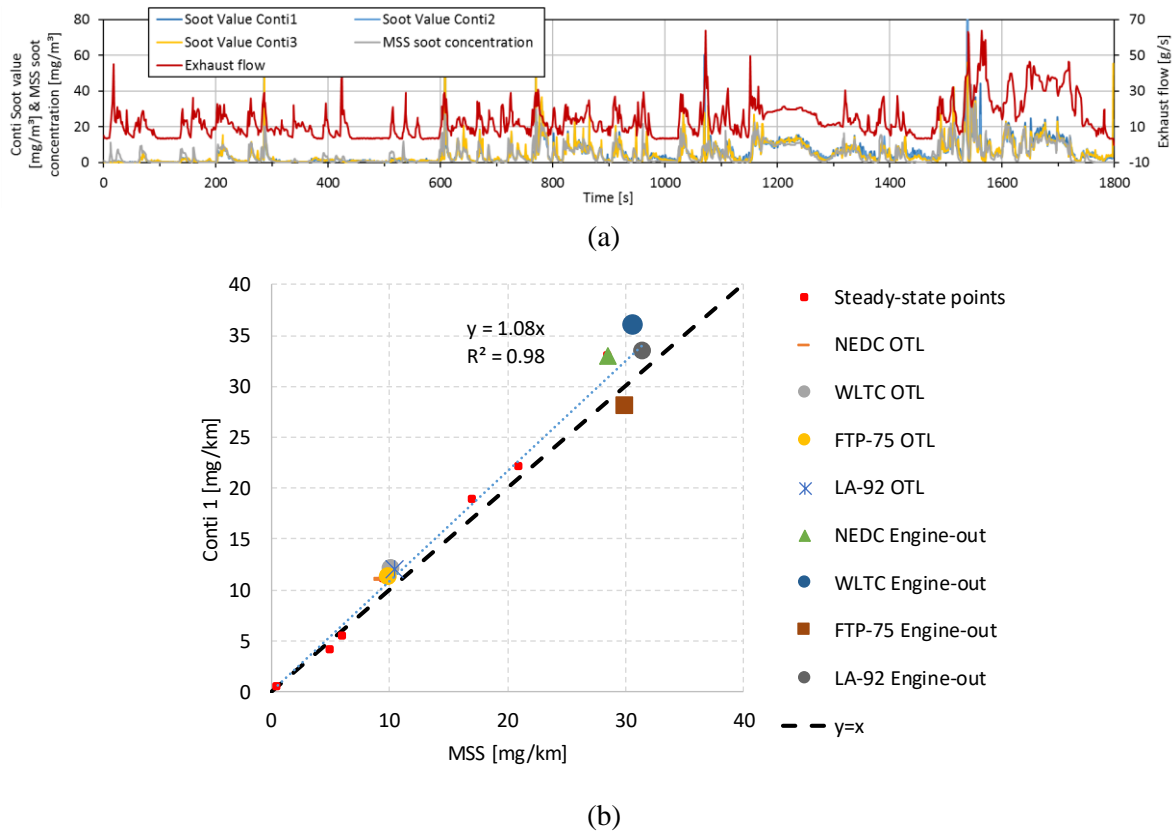


Figure 99: Correlation of electrostatic sensors with MSS a) example of WLTC b) steady-state and transient cycles (all measurements)

5.5. Summary and conclusions

The future OBD requirements and solution for PN/PM emission monitoring were the topic of this chapter. The main points of this investigation can be summarised as follows:

- Advanced PNPM sensor will be employed to future OBD systems. Both legislation and market needs drive this demand.
- Electric charge based and optical sensors are the available solutions which are in the market or close to it.
- An electrostatic sensor was tested as an alternative solution to the resistive soot sensor. Its performance is close to the reference MSS device.

- The main drawbacks of this sensor are the running-in time that is needed to build the first dendrites and the effect of the exhaust flow, which is currently further investigated.
- The advanced sensors as part of the future OBD will provide a continuous and more accurate estimation of the PN/PM emissions during the lifetime of a vehicle.
- Electrostatic sensors are readily available as an alternative to resistive sensors.

6. Summary, conclusions and future research

6.1. Summary and conclusions

This thesis focused on developing a method using a resistive soot sensor for detecting malfunction of the system before the PM emissions exceed the OBD threshold. The core of the study is the OBD Model that was developed using the commercial software MATLAB Simulink®. This model consists of the signal of the soot sensor (sensor box), the OBD algorithms which execute the final DPF diagnosis and three sub-models: soot, DPF and sensor sub-models (Figure 100).

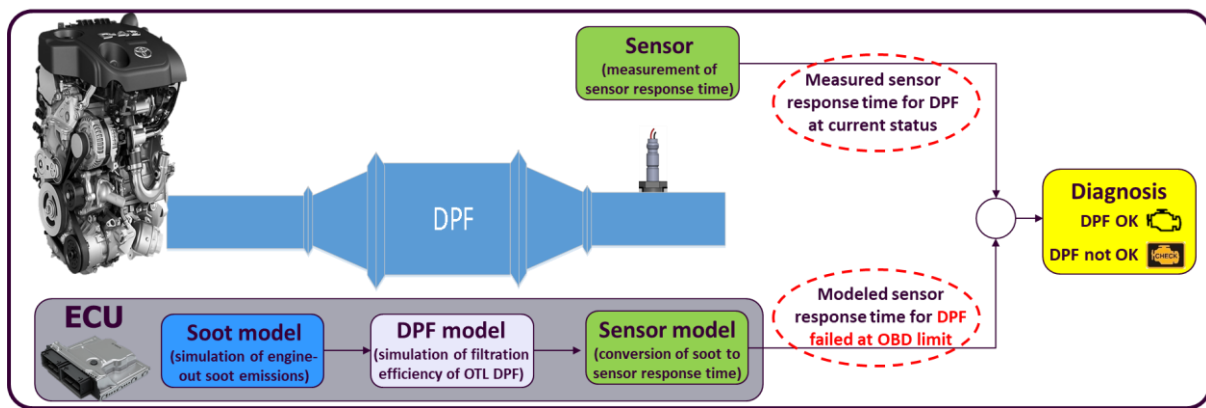


Figure 100: Overview of the OBD model developed in Matlab Simulink®

The concept is to check if due to a DPF failure, the actual PM emissions of the vehicle are higher than the OTL. The regulations require this check to be performed for the evaluation of the effectiveness of the DPF over a legislative driving cycle (NEDC in this study). Emissions higher than 12 mg/km over NEDC should turn the MIL on.

The diagnosis is achieved by comparing the actual sensor response time reported by a sensor during an NEDC (1st branch in Figure 100) with the simulated response time when the PM emissions are at the OTL (2nd branch):

- Higher measured response time means lower than the OTL emissions (DPF OK)
- Lower measured response time indicates higher than the OTL emissions (DPF not OK)

The developed map-based soot model can accurately predict the engine-out soot emissions using a base steady-state map (error: 25%) and a transient correction to compromise mainly for the airflow delays. An additional correction due to lower EGR amounts on transient operation compared to the steady-state map, further improves the accuracy and the error is reduced to 2% for the reference NEDC. The DPF model is commonly a constant filtration efficiency for the threshold DPF. For the

reference NEDC, this concludes to an error of 9% compared to the measured data. Nevertheless, the development of an advanced model can reduce the error to 5%. This model is able to predict the effect of the exhaust flow and adjust the filtration efficiency for clean and loaded DPFs. The sensor model for the prediction of the response time of the sensor over the threshold emissions can be successfully implemented using a statistical transfer function. The yielded error is 7%. The advanced physical model does not significantly improve the accuracy except the real driving conditions, but it is advantageous for the understanding of the comprehension of the operating principle of the sensor and the analysis of the parameters that affect its operation. The algorithm is an index which, by utilising rejection criteria can further improve the accuracy of the final diagnosis.

The overall error of the diagnosis for the NEDC was calculated at 19% (28% for the base models). This error will be further increased for real-driving conditions, and thus, it is crucial to improve the accuracy starting from the sensor itself. The validation of the OBD model in various transient profiles revealed that the sensor is able to distinguish between a TA approval DPF (4.5 mg/km) and an OTL DPF (12 mg/km). To eliminate the risk of the final diagnosis, the threshold is set below the OTL; for our application, it was calibrated at 9.7 mg/km. These results indicate that the diagnosis with a resistive soot sensor is accurate, and the focus for improved accuracy should be on the implementation of an advanced soot model and an improved sensor. For the soot model, the solution is available, and it was presented in detail.

The next section focused on the improvement of the sensor, along with the investigation of the limitations of the sensor model. The need for these improvements induced by the issues that arise during the first installation of the sensor in a commercial vehicle. Starting from relatively simple issues, the incomplete regeneration due to supply voltage below 9V can be resolved by slightly increasing the regeneration target temperature. The re-design of the sensor tip was also necessary to make sensor insensible to mounting orientation and protect the element from excessive water droplet impingement. Towards the better protection of the sensor during cold start, the dew point strategy was analysed. One significant concern was the sensor cross sensitivities to gaseous and solid compounds of the exhaust. High sulphur-content of the fuel and high exhaust concentration of methane, carbon monoxide and hydrogen, do not create any temporary or remaining effect on sensors. On the other hand, urea, ammonia and ash in high amounts can create deviations from the normal behaviour of the sensor. Solutions such as further improvement of the tip design and software solutions for repelling the contaminants can reduce the adverse effects. Finally, inconsistencies on predicted sensor response time due to extreme driving conditions can be successfully reduced by the measurement of more levels for the input parameters during the development of the transfer function.

The last chapter of the thesis is looking in the future of the OBD systems. The recent developments in the field for all regions have demonstrated the significant potential benefits of advanced

OBD on vehicular emission monitoring. EU can lead by adopting, combining and developing advanced methods for tracking, reporting and processing OBD-based emission data.

The tracking can be partially performed with the available on-board sensors and devices, but advanced sensors are needed for more comprehensive monitoring. As an example, monitoring of NO_x emissions can be sufficiently and accurately performed by current on-board NO_x sensors but for particulate matter emission monitoring the current resistive sensors are efficient only for diesel engines, and therefore, new sensors must be developed for GPF monitoring or more accurate diesel monitoring. Finally, an electrostatic sensor can be a reliable alternative to the resistive sensor as validated by several driving cycles that were measured and presented in the last section.

6.2. Future research

The current study presented and optimised an approach for the DPF diagnosis using the Stoneridge resistive soot sensor. The scope was limited in terms of the hardware to be used due to the need for development and optimisation of the specific sensor for diesel applications. Our initial tests on the GDI engine and the (limited) available publications, suggests the weaknesses of this technology to detect lower mass emission levels or complete a diagnosis during a legislative driving cycle. It is recommended that further research be undertaken towards the accomplishment of the ultimate environmental target, which is the effective monitoring of PN/PM emissions during the lifetime of all vehicles. The last chapter discussed the future needs and possible solutions for PN/PM monitoring, but it would be interesting to develop the necessary models and the diagnostic schemes using the advanced PN/PM sensors. The following paragraphs suggest some future research activity in this direction. The proposed working approach is summarised in Figure 101.

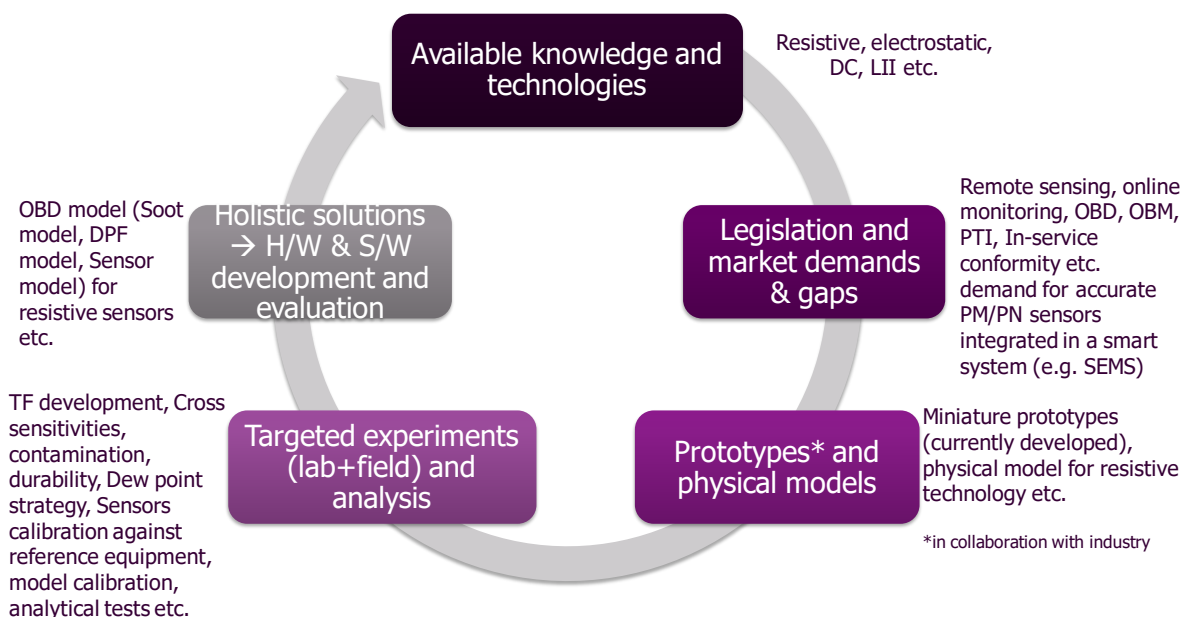


Figure 101: Schematic of the future approach

Starting from the currently used resistive technology, specific tasks are recommended to make the diagnosis more robust, less prone to sensor failures and less vulnerable to exhaust contaminants:

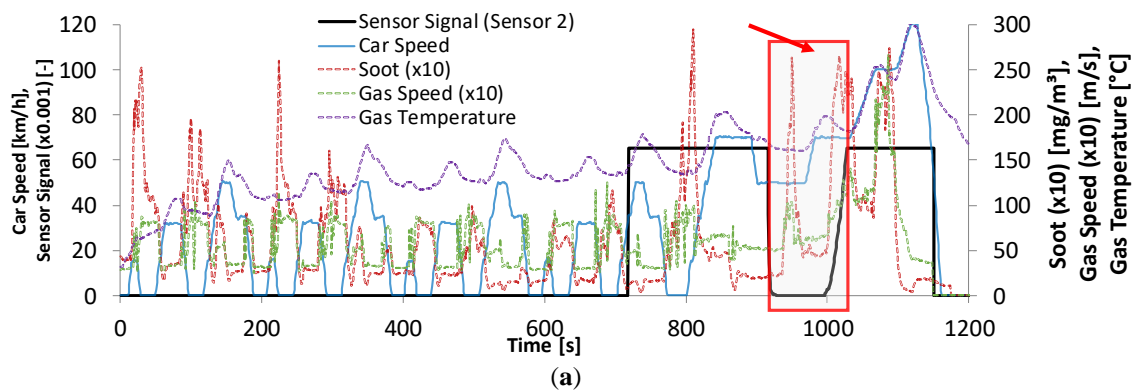
- **Investigation of the thermal shock of Platinum layer and Alumina substrate:** Ceramics have excellent strength, electrical resistivity wear-resistance and are chemically inert to very high temperatures. Ceramic brittleness opens the possibility of failure due to thermal shock. Thermal shock due to stresses from transient thermal gradients can occur between surface and interior. Ceramics are stronger in compression than in tension, so failure due to thermal shock is more likely due to rapid cooling.
- **New test protocol and measurements for the sodium effect and the advanced protection from contaminants:** Recent tests on brand new vehicles, revealed some durability issues mainly related to sodium contamination. The target is to develop protection mechanisms (e.g. P3 protection software) or implement hardware features (e.g. new tip design) to prevent contamination not only during sensing mode but also during standby or preheating mode which proved to be a significant fraction of the sensor operation during real driving.
- **Validation of the advanced Exothermia/Axisuite DPF model:** The validation of the DPF model was not possible due to an issue during the corresponding test campaign. Thus, it is suggested to repeat the validation measurements and evaluate the performance of the advanced model.
- **An alternative methodology for soot model:** Another possible future alternative for sensor model optimisation is the calibration of the model based on several data and machine learning techniques for real driving operation of the vehicle. Also, the utilisation of additional input parameters could enhance accuracy without the need for extensive calibration effort. An example of this scheme is the signal of low-cost cylinder pressure sensors (Hidria, 2011), which are currently investigated in our laboratory.

Regarding the broader target for future sensors, a natural progression of this work and a proposal for future research is to analyse and perform measurements with the presented sensors and technologies to create reliable conclusions for the readiness level and the necessary improvements needed for OBD applications. Also, as general recommendations in the topic, the investigation of the overall approach for future OBD is of high interest. What is currently missing is the effective reporting and processing of emission-related data. Wired access to OBD data during the periodic technical inspection and the MIL should be enhanced with remote access and data sharing. Cloud and server services, modelling and machine learning for vehicle status browsing should also be considered. These are highly demanding tasks, but the target can be to find the weak points and investigate for reliable and robust solutions.

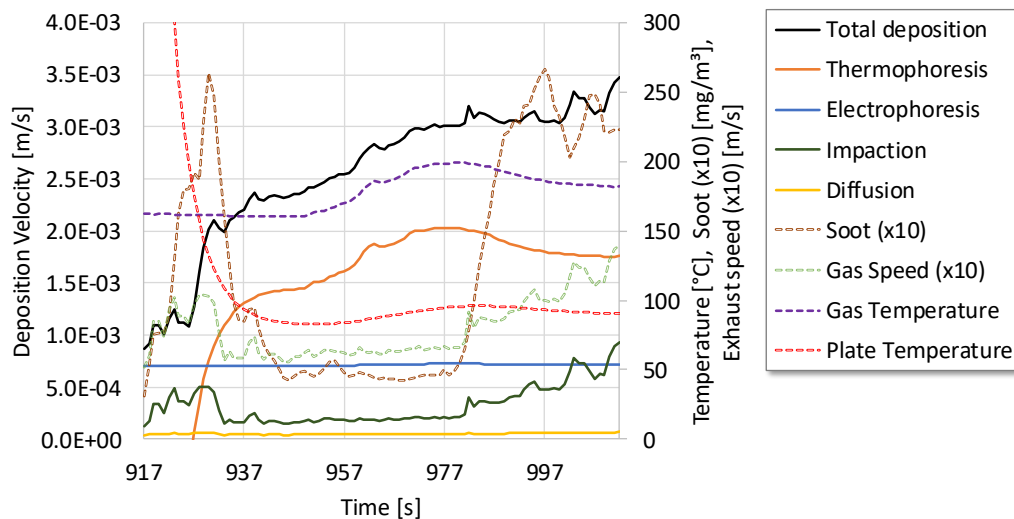
Finally, data security and anti-tampering techniques should be accounted in all steps, including the CAN messages for sensor's communication with the ECU, the transmitted data to the cloud and the overall vehicle connectivity.

Appendixes

Appendix A

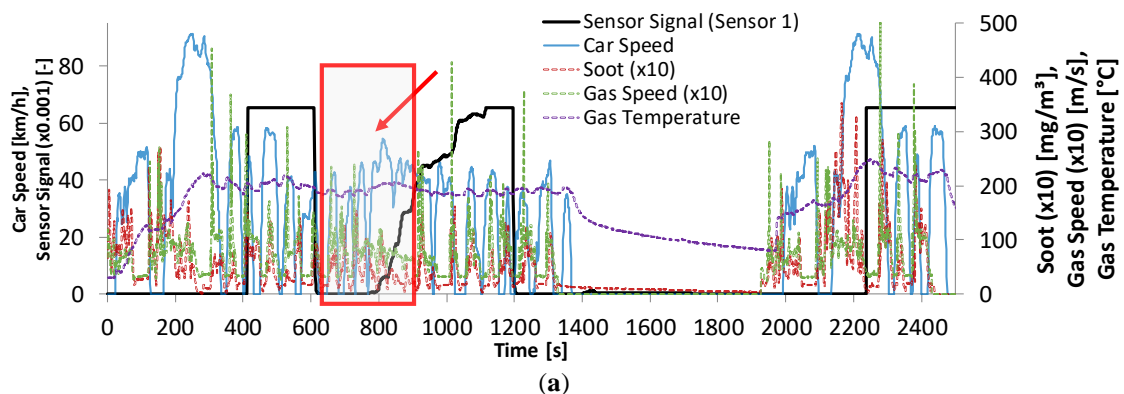


NEDC (Sensor 2, Region #2) Deposition Velocities



(b)

Figure A1. (a) First (valid) loading of the Sensor 1 (partial view) during the NEDC (cold) (Engine emission: 17.1 mg/km). (b) Deposition velocities at the specified time interval



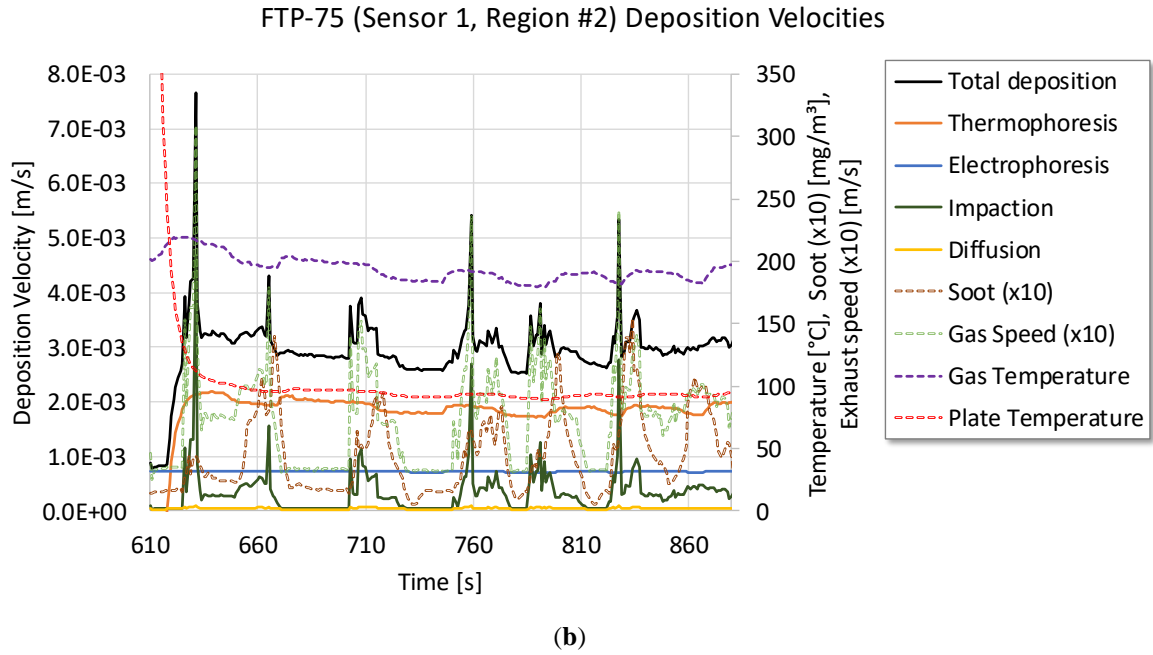


Figure A2. (a) First (valid) loading of the Sensor 1 (partial view) during the FTP 75 (cold) (DPF emission: 14.3 mg/km). (b) Deposition velocities at the specified time interval

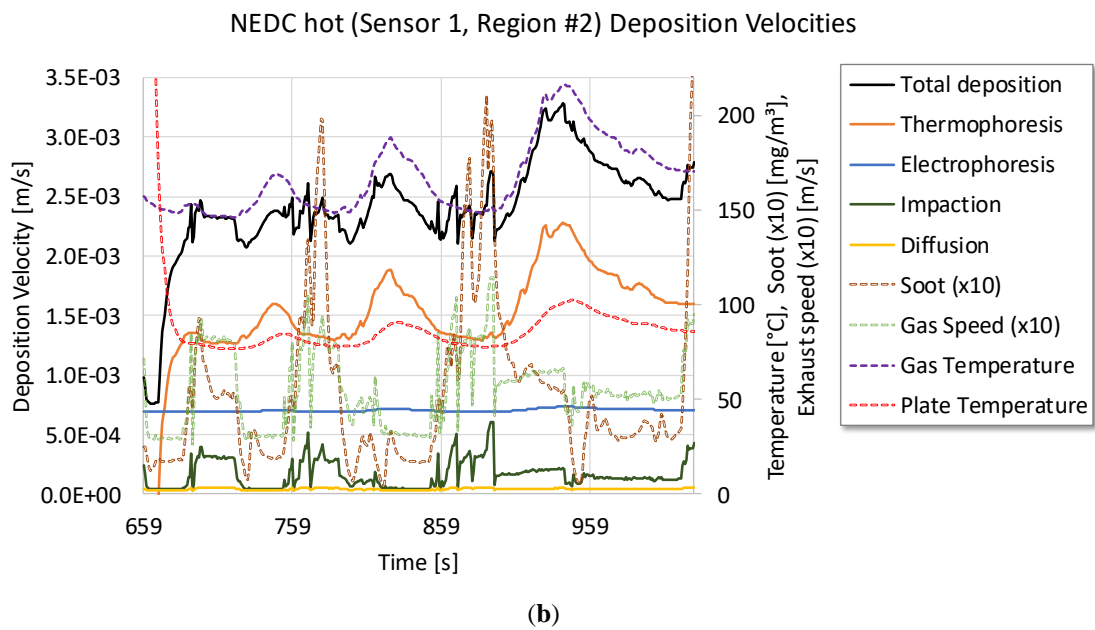
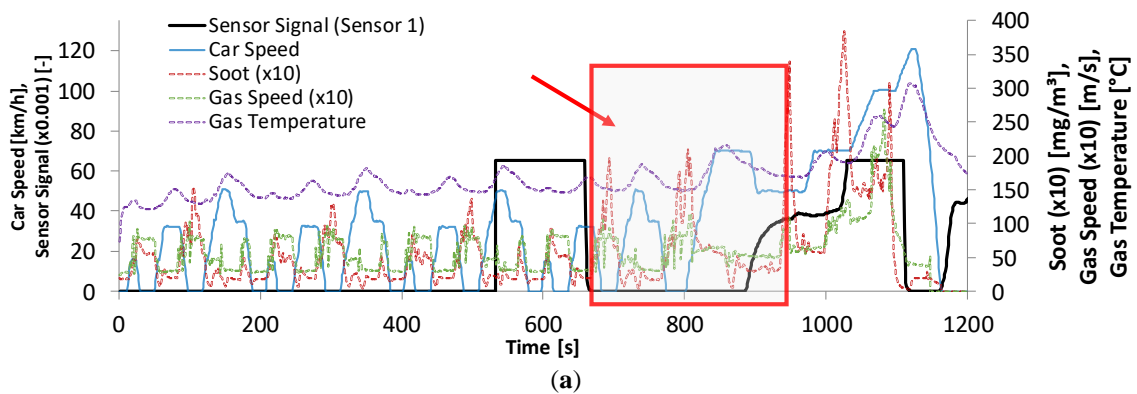


Figure A3. (a) First (valid) loading of the Sensor 1 (partial view) during the hot NEDC (Engine emission: 17.1 mg/km). (b) Deposition velocities at the specified time interval

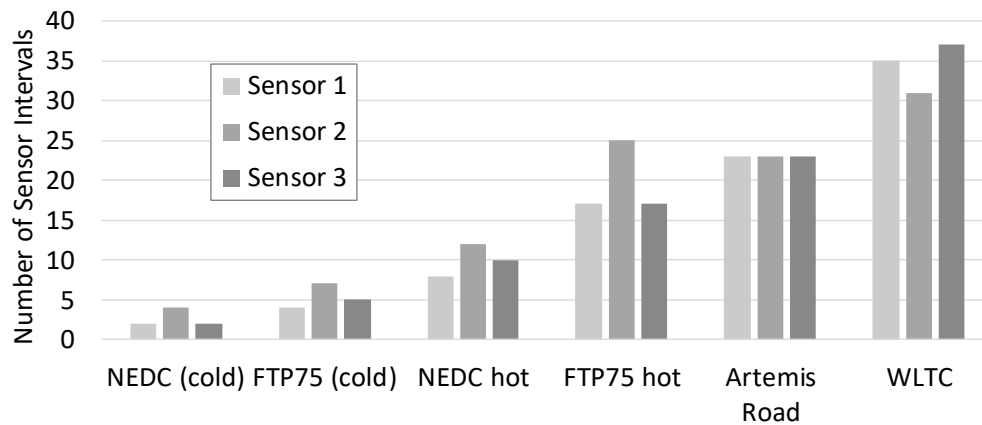


Figure A4. Comparison of the total number of sensor intervals per driving cycle and sensor

Appendix B

For the measurement of the particle size during transient operation, an Engine Exhaust Particle Sizer Spectrometer (EEPS, TSI 3090) was used which can measure the particle size distributions from 5.6 to 560 nm. The secondary outlet of a Particle Counter (APC, AVL 489) was used to condition and dilute the sample before the EEPS. Due to the volatile particle remover of the APC, only the solid particles were measured from the EEPS. The characteristics of the vehicle are depicted in Table A1, the driving cycle was the type approval World Harmonized Light Duty Test Cycle (WLTC), the fuel was market diesel, and the lube oil was according to manufacturer's specifications.

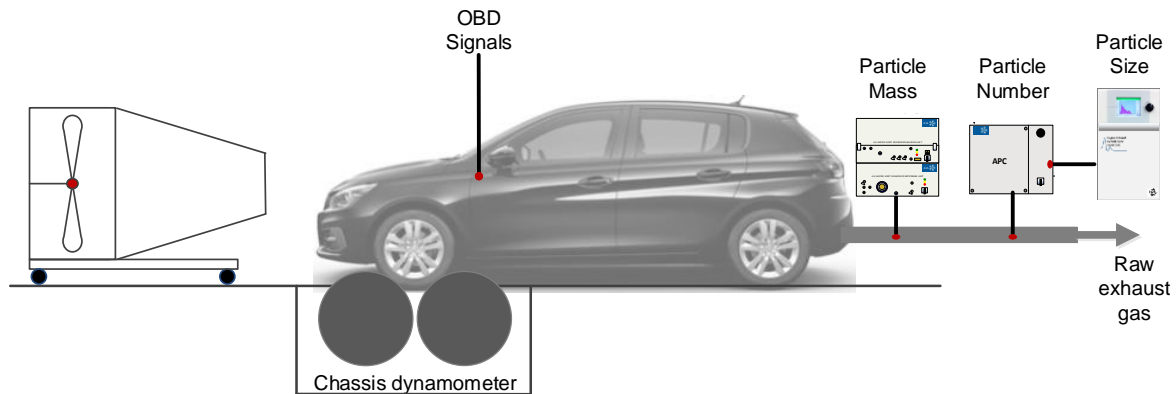


Figure A5. Experimental setup for the measurement of particle size distribution on WLTC

Table A1: Vehicle used for the size distribution WLTC test.

Feature	Value
Vehicle	Peugeot 308 1.6 HDi
Fuel	Diesel
Displacement [cc]	1560
Fuel injection system	Common Rail, DI

Max Power [kW/rpm]	88/3500
Max Torque [Nm/rpm]	300/1750
Cylinders	4
Gearbox	6-speed
Emission standards	Euro 6b

The results for the Geometric Mean Diameter (GMD) are illustrated in Figure A6. The profile of the GMD validates that during transient operation, the particle size can vary significantly from 23nm (cut-off size of our instrument) to 100 nm.

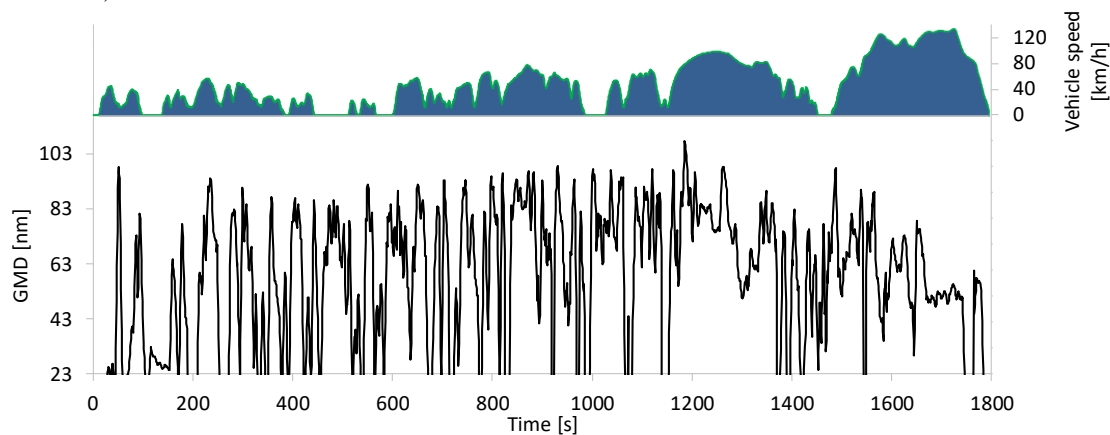


Figure A6. Size distribution and vehicle speed profile on WLTC

Appendix C

A few preliminary measurements on a GDI engine were performed aiming to draw some conclusion about the ability of the sensors to operate on low mass concentration, high temperature and lack of oxygen which are the main differentiating parameters compared to a diesel application. Also, gasoline engines are used for hybrid vehicles where the challenge is the extended engine-off conditions. This investigation was out of the scope of this study and is not further discussed.

The measurement campaign was performed on a Toyota GDI/PFI engine (Watanabe et al., 2014). This engine uses both direct and port fuel injection to efficiently control the PM/PN emissions under all driving conditions (Figure A7). The exhaust aftertreatment comprises only a three-way catalyst. For the current study, the sensors were measured on the steady-state and transient operation (WLTC) with either mixed injection (the strategy is decided by the ECU) or only GDI operation to increase PM/PN emissions.

Figure A8 shows the PM and PN emissions during a cold WLTC. Most of the emitted mass and number is observed during the cold operation of the engine. For the protection of the sensor though during the cold operation, the sensor (in order to protect the element from failures) should not be triggered to the necessary regeneration before the start of the accumulation period. Also, gasoline engines utilise stoichiometric combustion which significantly increases the water fraction in the exhaust gas compared to lean diesel operation. Therefore, the sensor may start its operation after this high-emission area if a similar to diesel applications dew point strategy is used. To overcome this issue, a

more aggressive dew point strategy was decided for these tests and sensors were triggered to their initial regeneration when the temperature reaches 100°C. No failures were observed in these measurements, but additional tests are needed to confirm the durability of the sensor. Finally, to allow for complete sensor regenerations during rich or stoichiometric engine operation, pressurised air was mixed with the exhaust gas before the resistive sensors to increase the available oxygen for soot oxidation.

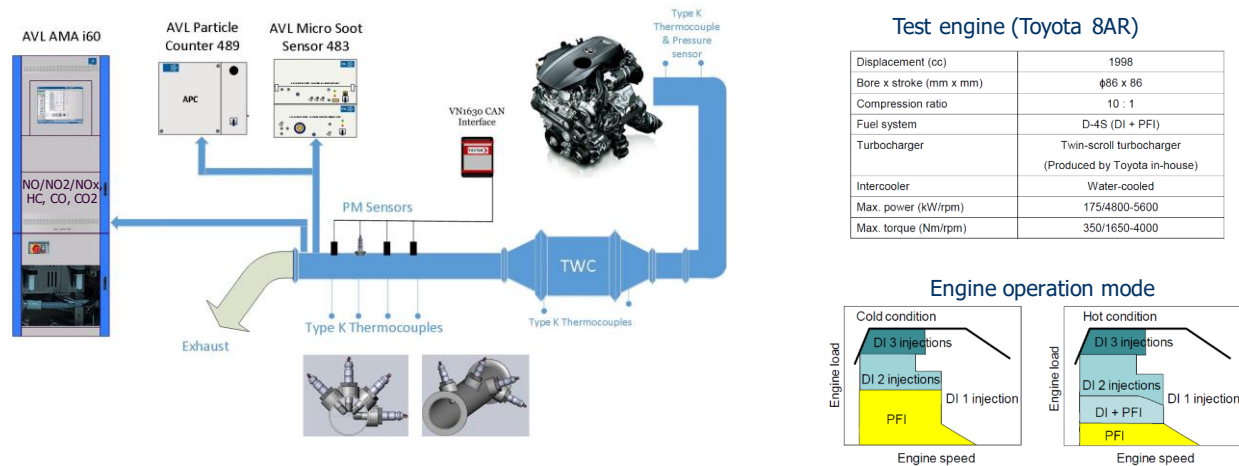


Figure A7: Gasoline engine and exhaust setup

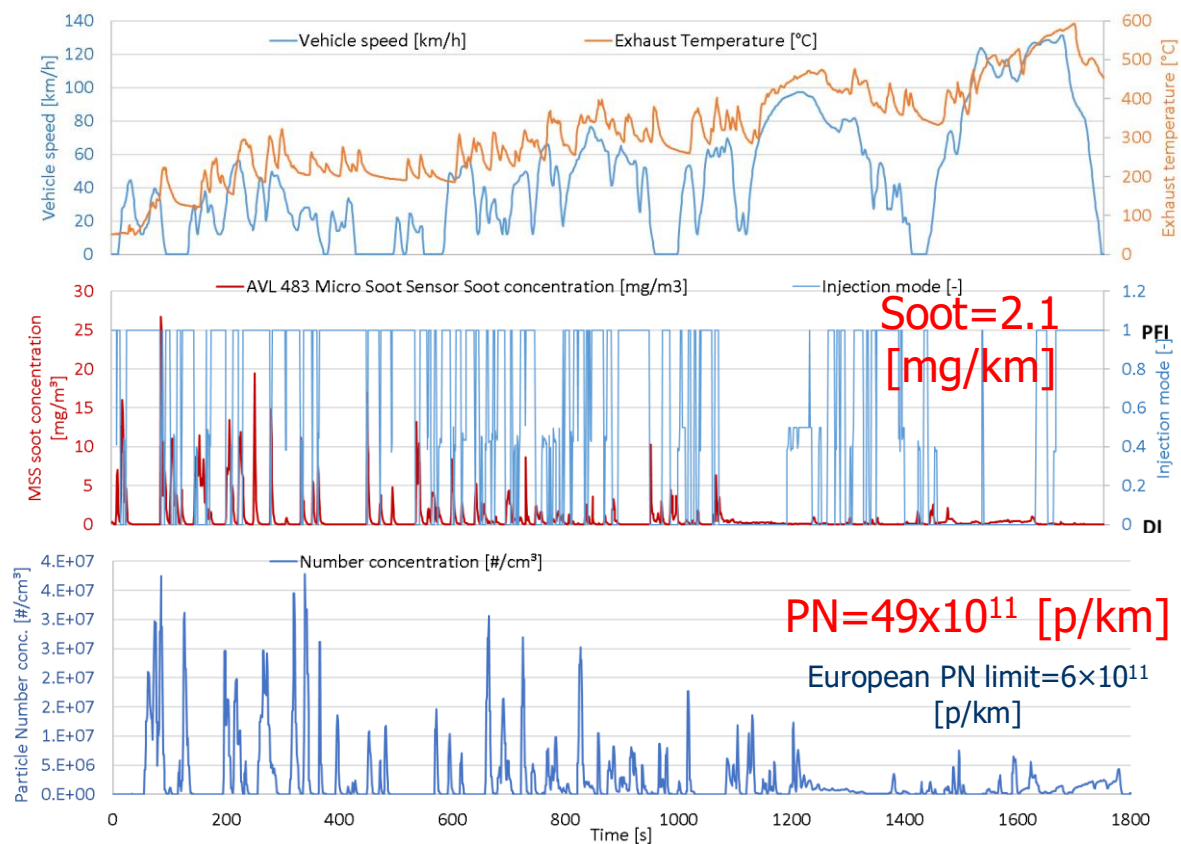
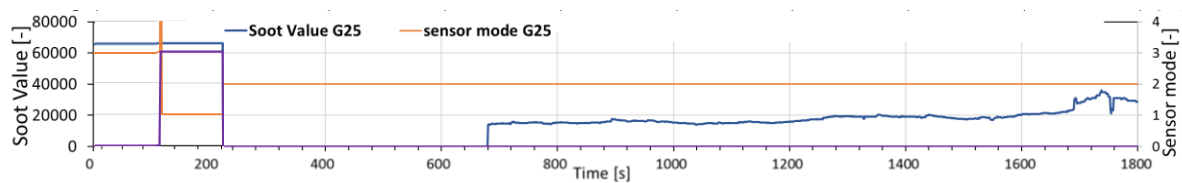


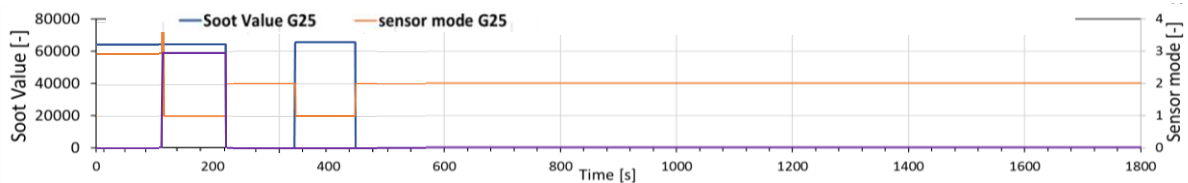
Figure A8: WLTC cold cycle on Toyota engine with PM and PN measurements.

The performance of the resistive sensors is presented in Figure A9. The sensor fails to complete a full accumulation period. Also, repetitions of the same cycle showed the low repeatability of the sensor during these conditions, which in some case did not respond at all during the cycle.

Therefore, the low mass emissions were a challenge for the construction of the soot bridges on the sensing element. To enhance the soot deposition, electrophoresis was increased to maximum technically allowed voltage for these parts, which is 25% higher than the nominal value of the standard diesel parts. Similarly, the regeneration threshold was increased to reduce the sensor response duration (3x higher). The results for the WLTC with the improved sensor settings are presented in Figure A9b. The sensor indeed became faster and completed a full accumulation period in the cold phase of the cycle. Nevertheless, there was no soot accumulation on the rest of the cycle. The issue was again that this behaviour was not consistent between repetitions of the same pattern.



(a)



(b)

Figure A9: Performance of the resistive sensor over WLTC (cold-start) a) default sensor settings b) enhanced electrophoresis and increased regeneration threshold

Based on these data for the performance of the resistive sensor on a GDI engine, it is evident that the current settings of the resistive sensor are not sufficient for operation on GDI vehicles and additional effort is needed to improve the accuracy and repeatability of the sensor.

Appendix D

Matlab/Simulink model

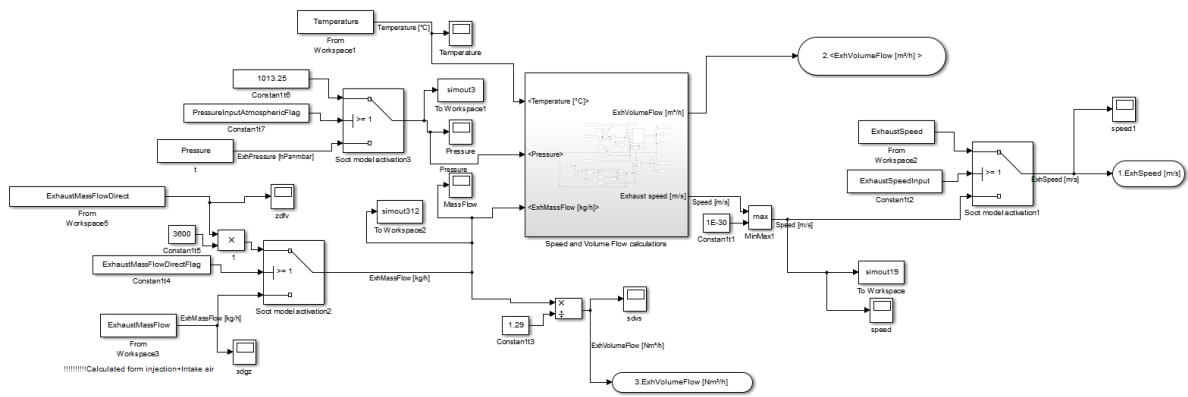


Figure A12: Calculation of the exhaust velocity as input in the Transfer Function

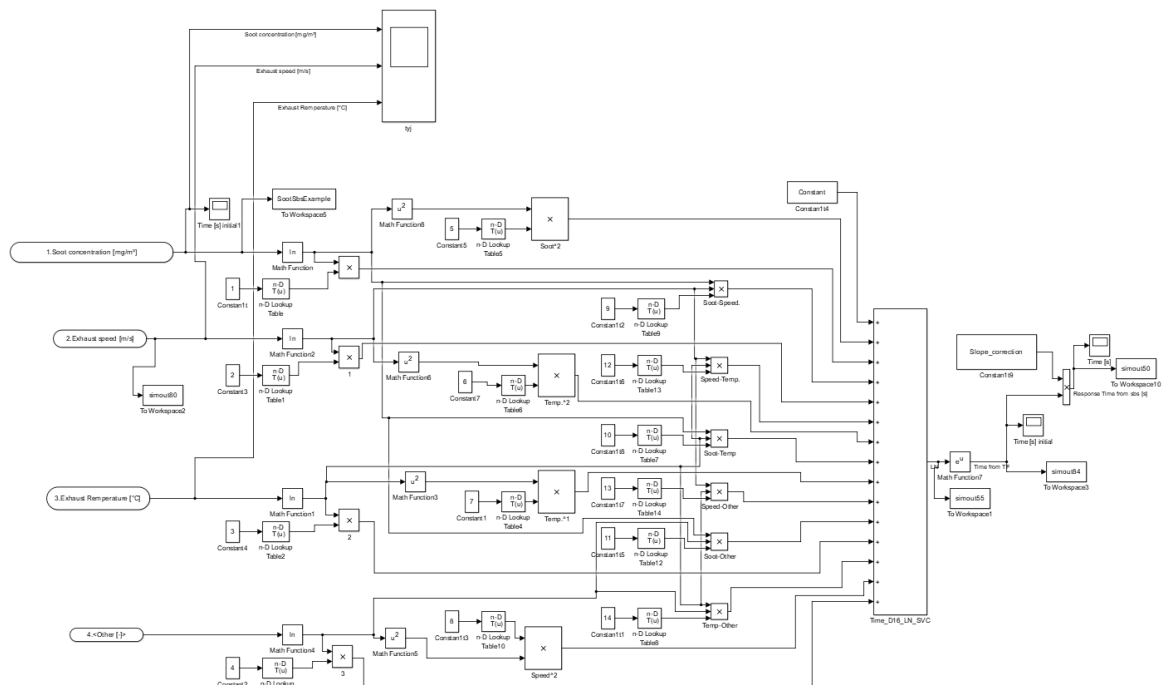


Figure A13: Implementation of the Transfer Function

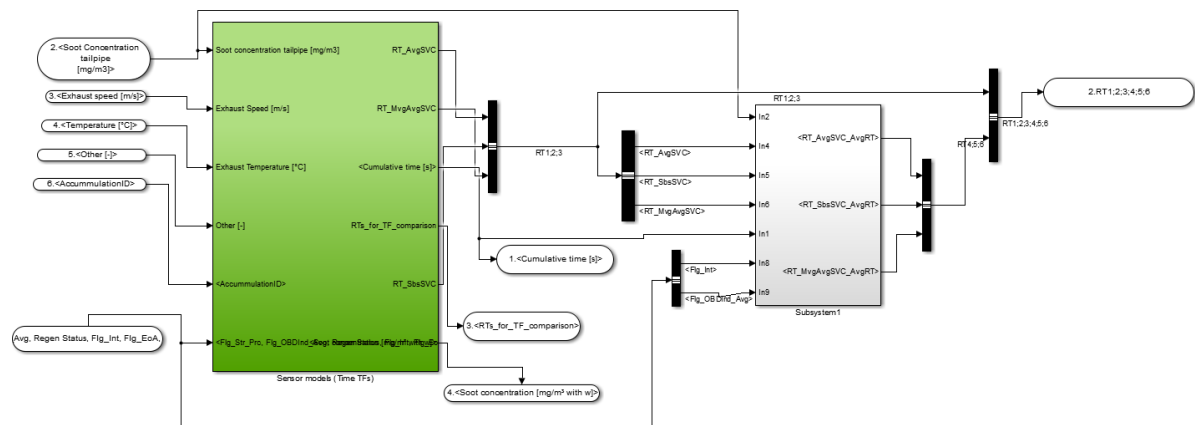


Figure A14: Various approaches that were tested for the calculation of the sensor response time

List of Abbreviations

Abbreviation	Description
ACEA	Association de Constructeurs Européens d'Automobiles (European Automobile Manufacturers Association)
APC	AVL Particle Counter
A/F	Air-to-Fuel ratio
CARB,	California Air Resources Board
CEL	Check-Engine Light
CO	Carbon Monoxide
CPC	Condensation particle Counter
CPM	Contamination prevention Mode
CVS	Constant Volume Sampling
DI	Direct Injection
DOC	Diesel Oxidation Catalyst
DoE	Design of Experiment
DPF	Diesel Particulate Filter
DTC	Diagnostic Trouble Code
EC	Elemental Carbon
ECE	Economic Commission for Europe
ECM	Electronic Control Module
ECU	Electronic Control Unit
EDS	Energy Dispersive Spectroscopy
EEA	European Environment Agency
EEPS	Engine Exhaust Particle Sizer
EGR	Exhaust Gas Recirculation
EPA	Environmental Protection Agency

EU	European Union
EUDC	Extra Urban Driving Cycle
FTP-75	Federal Test Procedure
GDI	Gasoline Direct Injection
GMD	Geometric Mean Diameter
GPF	Gasoline Particulate Filter
GPS	Global Positioning System
HC	Hydrocarbon
HD	Heavy-Duty (vehicles)
HV	Hybrid Vehicles
LD	Light-Duty (vehicles)
LNT	Lean NO _x Trap
MAF	Mass Air Flow
MIL	Malfunction Indicator Light
NEDC	New European Driving Cycle
NO _x	Nitrogen Oxides (Nitric Oxides and Nitrogen Dioxides)
OBD	On-Board Diagnostics
OBFCM	On-Board Fuel Consumption Monitoring
OBM	On-Board Monitoring
OEM	Original Equipment Manufacturer
PAH	Polycyclic Aromatic Hydrocarbons
PEMS	Portable Emissions Measurement System
PFI	Port Fuel Injection
PI	Positive Ignition
PM	Particulate Mass
PM _{2.5}	Fine Particulate Matter Mass (sub-2.5µm)
PMP	Particle Measurement Programme

PN	Particle Number
R ²	Correlation Coefficient
RDE	Real Driving Emissions
SCR	Selective Catalytic Reduction
SCU	Sensor Control Unit
SEM	Scanning Electron Microscopy
SET	Supplemental Emissions Test
SMPS	Scanning Mobility Particle Sizer Spectrometer
SOF	Soluble Organic Fraction
THC	Total Hydrocarbons
TWC	Three Way Catalyst
VPR	Volatile Particle Remover
UNECE	United Nations Economic Commission for Europe
WHO	World Health Organization
WLTC	Worldwide harmonized Light-duty Test Cycle
WLTP	Worldwide harmonized Light-duty Test Procedures

References

- ACEA, 2019. Access to Euro 6 RDE Data, Available online,. URL <https://www.acea.be/publications/article/access-to-euro-6-rde-monitoring-data> (accessed 4.8.19).
- ACEA, 2018. Cooperative, Connected and Automated Mobility, in: PZPM Conference, 26 February 2018 Warsaw, Poland.
- Adlouni, M., 2011. Modeling of soot emission for heavy-duty diesel engines in transient operation, PhD Thesis. Lund University.
- AECC, 2018. Modern, Real-Driving Emissions (RDE) - compliant cars : Key to improving urban air quality, in: Polis Conference, 22 November 2018, Manchester, UK.
- Allmendinger, K., Henderson, B., Steppan, J., Lourdhusamy, A., Wang, V., Fitzpatrick, J., Maricq, M., Kubinski Ford Motor Company, D., 2013. Comparison of Experimental and First Principles Modeling Results for the PMTrac ® Electrostatic Soot Sensor, in: UC Riverside Portable Emissions Measurement Systems Conference & Workshop, April 11-12, 2013, California, USA.
- Amanatidis, S., Maricq, M.M., Ntziachristos, L., Samaras, Z., 2016. Measuring number, mass, and size of exhaust particles with diffusion chargers: The dual Pegasor Particle Sensor. *J. Aerosol Sci.* 92, 1–15. <https://doi.org/10.1016/j.jaerosci.2015.10.005>
- Amanatidis, S., Ntziachristos, L., Giechaskiel, B., Bergmann, A., Samaras, Z., 2014. Impact of selective catalytic reduction on exhaust particle formation over excess ammonia events. *Environ. Sci. Technol.* 48, 11527–11534. <https://doi.org/10.1021/es502895v>
- AVL, 2017. AVL Powertrain Engineering Techday # 4 Gasoline Particle Filter Development and Calibration AVL Experience on GPF system.
- AVL, 2011. Avl Micro Soot Sensor, Application Paper.
- Bardasz, E.A., Cowling, S. V., Panesar, A., Durham, J., Tadrous, T.N., 2010. Effects of Lubricant Derived Chemistries on Performance of the Catalyzed Diesel Particulate Filters. *SAE Tech. Pap. Ser. 1*. <https://doi.org/10.4271/2005-01-2168>
- Barro, C., Obrecht, P., Boulouchos, K., 2015. Development and validation of a virtual soot sensor: Part 2: Transient engine operation. *Int. J. Engine Res.* 16, 127–136. <https://doi.org/10.1177/1468087414533786>

-
- Bartscherer, P., Moos, R., 2013. Improvement of the sensitivity of a conductometric soot sensor by adding a conductive cover layer. *J. Sensors Sens. Syst.* 2, 95–102. <https://doi.org/10.5194/jsss-2-95-2013>
- Basu, S., Henrichsen, M., Tandon, P., He, S., Heibel, A., 2013. Filtration Efficiency and Pressure Drop Performance of Ceramic Partial Wall Flow Diesel Particulate Filters. *SAE Int. J. Fuels Lubr.* 6, 877–893. <https://doi.org/10.4271/2013-01-9072>
- Benajes, J., Luján, J.M., Bermúdez, V., Serrano, J.R., 2002. Modelling of turbocharged diesel engines in transient operation. Part 1: Insight into the relevant physical phenomena. *Proc. Inst. Mech. Eng. Part D J. Automob. Eng.* 216, 431–441. <https://doi.org/10.1243/0954407021529237>
- Berger, J., Strohmaier, R., Heimann, D., Breuer, N., Wirth, R., Reinhart, K.-F., Schmidt, R., Bauer, W., Baldenhofer, K.-A., Kamp Bernard, Grau, T., 2009. BOSCH Patent: Sensor for detecting particles.
- Besch, M.C., 2016. In-line, Real-time Particulate Matter Sensors for OBD and Exhaust After-treatment System Control Applications, PhD Thesis. West Virginia University.
- Bilby, D., Kubinski, D., Maricq, M., 2016. Investigating the operating principle of the Emisense PMTrac sensor, in: 2016 PEMS Workshop, March 17th-18th, CE-CERT, California, USA.
- Brunel, O., Duault, F., Lavy, J., Creff, Y., Youssef, B., Duault, F., Youssef, B., Creff, Y., Lavy, J., Creff, Y., Youssef, B., Duault, F., Youssef, B., Creff, Y., 2013. Smart Soot Sensor for Particulate Filter OBD. *SAE Int. J. Passeng. Cars - Electron. Electr. Syst.* 6, 307–327. <https://doi.org/10.4271/2013-01-1334>
- Burtscher, H., 2005. Physical characterization of particulate emissions from diesel engines: a review. *J. Aerosol Sci.* 36, 896–932. <https://doi.org/10.1016/j.jaerosci.2004.12.001>
- CARB, 2018. Public hearing to consider proposed revisions to on-board diagnostic system requirements, including the introduction of real emissions assessment logging (real), for heavy-duty engines, passenger cars, light-duty trucks, and medium-duty vehicles and engine. California Environmental Protection Agency, California Air Resources Board.
- Chilumukuru, K., Gupta, A., Ruth, M., Cunningham, M., Kothandaraman, G., Cumararatunge, L., Hess, H., 2017. Aftertreatment Architecture and Control Methodologies for Future Light Duty Diesel Emission Regulations. *SAE Int. J. Engines* 10, 1580–1587. <https://doi.org/10.4271/2017-01-0911>
- Ciardelli, C., Nova, I., Tronconi, E., Chatterjee, D., Bandl-Konrad, B., Weibel, M., Krutzsch, B., 2007. Reactivity of NO/NO₂-NH₃ SCR system for diesel exhaust aftertreatment: Identification of the reaction network as a function of temperature and NO₂ feed content. *Appl. Catal. B Environ.* 70, 80–90. <https://doi.org/10.1016/j.apcatb.2005.10.041>

-
- Continental Automotive GmbH, 2019. Continental Automotive - Sensors, Available online,. Continental. URL <https://www.continental-automotive.com/en-gl/Off-Highway/Agriculture/Powertrain/Exhaust-Management-After-treatment/Sensors/Electrostatic-Particulate-Matter-Sensor> (accessed 2.26.19).
- Dec, J.E., 1997. A Conceptual Model of DI Diesel Combustion Based on Laser-Sheet Imaging. <https://doi.org/10.4271/970873>
- Delfino, R.J., Sioutas, C., Malik, S., 2005. Potential role of ultrafine particles in associations between airborne particle mass and cardiovascular health. *Environ. Health Perspect.* 113, 934–946. <https://doi.org/10.1289/ehp.7938>
- Delphi, 2018. Delphi-Emissions for pass car and light duty 2018-2019.
- Demuyne, J., Favre, C., Bosteels, D., Hamje, H., Andersson, J., 2018. Real-World Emissions Measurements of a Gasoline Direct Injection Vehicle without and with a Gasoline Particulate Filter Experimental Set-Up. <https://doi.org/10.4271/2017-01-0985>. Copyright
- Denis, M.S., Lindner, J., 2005. Review of Light-Duty Diesel and Heavy-Duty Diesel Gasoline Inspection Programs. *J. Air Waste Manag. Assoc.* 55, 1876–1884. <https://doi.org/10.1080/10473289.2005.10464773>
- Dhal, G.C., Dey, S., Mohan, D., Prasad, R., 2018. Simultaneous abatement of diesel soot and NOx emissions by effective catalysts at low temperature: An overview. *Catal. Rev. - Sci. Eng.* 60, 437–496. <https://doi.org/10.1080/01614940.2018.1457831>
- DieselNet. Diesel Engine Lubrication., Available online, 2019. URL <https://www.dieselnets.com/tech/lube.php> (accessed 5.28.19).
- DieselNet. Exhaust Particulate Matter., Available online, 2019. URL <https://www.dieselnets.com/tech/dpm.php> (accessed 5.28.19).
- DieselNet. Soot (PM) Sensors., Available online, 2019. URL https://www.dieselnets.com/tech/sensors_soot.php (accessed 5.28.19).
- DiGiulio, C.D., Pihl, J.A., Choi, J.-S., II, J.E.P., Lanc, M.J., Toops, T.J., Amiridis, M.D., 2013. NH₃ formation over a lean NOX trap (LNT) system: Effects of lean/rich cycle timing and temperature. *Appl. Catal. B Environ.* 147, 698–710. <https://doi.org/10.1016/j.apcatb.2013.09.012>
- Doebelin, E., 1990. *Measurement Systems: Applications and Design*, p.68-69.
- Dwyer, H., Ayala, A., Zhang, S., Collins, J., Huai, T., Herner, J., Chau, W., 2010. Emissions from a diesel car during regeneration of an active diesel particulate filter. *J. Aerosol Sci.* 41, 541–552.

<https://doi.org/10.1016/j.jaerosci.2010.04.001>

- Eastwood, P., 2008. Particulate Emissions from Vehicles, p42-48. SAE International, John Wiley & Sons, Ltd.
- Elser, M., El-Haddad, I., Maasikmets, M., Bozzetti, C., Wolf, R., Ciarelli, G., Slowik, J.G., Richter, R., Teinmaa, E., Hüglin, C., Baltensperger, U., Prévôt, A.S.H., 2018. High contributions of vehicular emissions to ammonia in three European cities derived from mobile measurements. *Atmos. Environ.* 175, 210–220. <https://doi.org/10.1016/j.atmosenv.2017.11.030>
- ETAS, 2019. ETAS - ES592 – Interface Module - ES59x – Universal Interface Modules - Bus Interface Modules, Available online,. URL <https://www.etas.com/en/products/es592.php> (accessed 7.10.19).
- ETAS, 2011. ELIS4: Software for liquid sensor, User guidw.
- EU, 2018a. Framework Contract for Studies and Technical Assistance in the Field of Emissions-No 688/PP/2018/FC. Off. J. Eur. Union.
- EU, 2018b. Commission Regulation (EU) 2018/1832. Off. J. Eur. Union.
- EU, 2017. Commission regulation (EU) 2017/1154. Off. J. Eur. Union.
- EU, 2016. Commission regulation (EU) 2016/646. Off. J. Eur. Union.
- EU, 2009a. Regulation (EC) No 595/2009. Off. J. Eur. Union 2008, 1–13.
- EU, 2009b. Directive 2009/28/EC. Off. J. Eur. Union.
- European Commission, 2018. Horizon 2020 Smart green and Integrated transport.
- European Environment Agency, 2019. Air pollution harms human health and the environment. <https://doi.org/10.1021/ac50165a001>
- European Environmental Agency (EEA), 2018. Air quality in Europe — 2018 report, Report. <https://doi.org/10.2800/62459>
- Fenn, M.E., Bytnerowicz, A., Schilling, S.L., Vallano, D.M., Zavaleta, E.S., Weiss, S.B., Morozumi, C., Geiser, L.H., Hanks, K., 2018. On-road emissions of ammonia: An underappreciated source of atmospheric nitrogen deposition. *Sci. Total Environ.* 625, 909–919. <https://doi.org/10.1016/j.scitotenv.2017.12.313>
- Feulner, M., Hagen, G., Müller, A., Schott, A., Zöllner, C., Brüggemann, D., Moos, R., 2015. Conductometric sensor for soot mass flow detection in exhausts of internal combustion engines.

- Finch, S., Hnilicka, B., Sindano, H., 2010. Euro 6 Light-duty vehicle OBD project: Evaluation and assessment of proposed EOBD emission thresholds.
- Fiorani, P., Gambarotta, A., Lucchetti, G., Ausiello, F.P., De Cesare, M., Serra, G., 2008. A detailed Mean Value Model of the exhaust system of an automotive Diesel engine. SAE Tech. Pap. 2008-28-00, 1–11. <https://doi.org/10.4271/2009-24-0131>
- Fitzpatrick, J., Henderson, B., Woo, L., 2018. Application of PMTrac ® Sensors for Low-cost PM Threshold Testing, in: UC Riverside PEMS 2018 International Conference & Workshop March 22, 2018, California, USA.
- Fragkiadoulakis, P., 2016. Model development and simulation of a prototype resistive soot sensor for OBD implementation, PhD Thesis. Aristotle University of Thessaloniki.
- Fragkiadoulakis, P., Geivanidis, S., Samaras, Z., 2018. Modeling a resistive soot sensor by particle deposition mechanisms. J. Aerosol Sci. 123, 76–90. <https://doi.org/10.1016/J.JAEROSCI.2018.06.005>
- Frenklach, M., Clary, D.W., Gardiner, W.C., Stein, S.E., 1985. Detailed kinetic modeling of soot formation in shock-tube pyrolysis of acetylene. Symp. Combust. 20, 887–901. [https://doi.org/10.1016/S0082-0784\(85\)80578-6](https://doi.org/10.1016/S0082-0784(85)80578-6)
- Frenklach, M., Wang, H., 1991. Detailed modeling of soot particle nucleation and growth. Symp. Combust. 23, 1559–1566. [https://doi.org/10.1016/S0082-0784\(06\)80426-1](https://doi.org/10.1016/S0082-0784(06)80426-1)
- Future Market Insights, 2019. Diesel Particulate Filter Market: Global Industry Analysis 2012 – 2016 and Opportunity Assessment; 2017 – 2027,.
- Galusková, D., Šajgalík, P., Galusek, D., Hnatko, M., 2009. Corrosion of Alumina Ceramics in an Aqueous Solution of Sodium Chloride. Key Eng. Mater. 409, 283–286. <https://doi.org/10.4028/www.scientific.net/kem.409.283>
- Giechaskiel, B., Maricq, M., Ntziachristos, L., Dardiotis, C., Wang, X., Axmann, H., Bergmann, A., Schindler, W., 2014. Review of motor vehicle particulate emissions sampling and measurement: From smoke and filter mass to particle number. J. Aerosol Sci. 67, 48–86. <https://doi.org/10.1016/J.JAEROSCI.2013.09.003>
- Givens, W.A., Buck, W.H., Jackson, A., Kaldor, A., Hertzberg, A., Moehrmann, W., Mueller-Lunz, S., Pelz, N., Wenninger, G., 2003. Lube Formulation Effects on Transfer of Elements to Exhaust After-Treatment System Components. SAE Tech. Pap. Ser. 1. <https://doi.org/10.4271/2003-01->

- Gkantonas, S., 2016. Exhaust gas flow analysis for model development of a prototype resistive soot sensor for OBD implementation, Diploma Thesis.
- Grob, B., Schmid, J., Ivleva, N.P., Niessner, R., 2012. Conductivity for Soot Sensing: Possibilities and Limitations. *Anal. Chem.* 84, 3586–3592. <https://doi.org/10.1021/ac203152z>
- Grondin, D., 2018. Didier Grondin. Développement d'un capteur de suies pour application automobile - Etude des paramètres clés affectant sa réponse. Autre. Université de Lyon, 2017. Français. <NNT : 2017LY- SEM012>. <tel-01823856> HAL.
- Grondin, D., Breuil, P., Viricelle, J.P., Vernoux, P., 2019. Modeling of the signal of a resistive soot sensor, influence of the soot nature and of the polarization voltage. *Sensors Actuators B. Chem.* <https://doi.org/DOI: 10.1016/j.snb.2019.126820>
- Grondin, D., Breuil, P., Viricelle, J.P., Vernoux, P., 2015. Development of a particulate matter sensor for diesel engine. *Procedia Eng.* 120, 1237–1240. <https://doi.org/10.1016/j.proeng.2015.08.838>
- Grondin, D., Westermann, A., Breuil, P., Viricelle, J.P.P., Vernoux, P., 2016. Influence of key parameters on the response of a resistive soot sensor. *Sensors Actuators B Chem.* 236, 1036–1043. <https://doi.org/10.1016/j.snb.2016.05.049>
- Grose, M., Sakurai, H., Savstrom, J., Stolzenburg, M.R., Watts, W.F., Morgan, C.G., Murray, I.P., Twigg, M. V., Kittelson, D.B., McMurry, P.H., Watts, W.F., Morgan, C.G., Murray, I.P., Twigg, M. V., Kittelson, D.B., McMurry, P.H., 2006. Chemical and physical properties of ultrafine diesel exhaust particles sampled downstream of a catalytic trap. *Environ. Sci. Technol.* 40, 5502–5507. <https://doi.org/10.1021/es052267+>
- Hagen, G., Feistkorn, C., Wiegärtner, S., Heinrich, A., Brüggemann, D., Moos, R., 2010. Conductometric soot sensor for automotive exhausts: Initial studies. *Sensors* 10, 1589–1598. <https://doi.org/10.3390/s100301589>
- Hagen, G., Feulner, M., Werner, R., Schubert, M., Müller, A., Rieß, G., Brüggemann, D., Moos, R., 2016. Capacitive soot sensor for diesel exhausts. *Sensors Actuators B. Chem.* 236, 1020–1027. <https://doi.org/10.1016/j.snb.2016.05.006>
- Hagen, G., Müller, A., Feulner, M., Schott, A., Zöllner, C., Brüggemann, D., Moos, R., 2014. Determination of the soot mass by conductometric soot sensors. *Procedia Eng.* 87, 244–247. <https://doi.org/10.1016/j.proeng.2014.11.646>
- Hagen, G., Spannbauer, C., Feulner, M., Kita, J., Müller, A., Moos, R., 2018. Conductometric soot

-
- sensors: Internally caused thermophoresis as an important undesired side effect. *Sensors* (Switzerland) 18. <https://doi.org/10.3390/s18103531>
- Haralampous, O., Kontzias, T., 2014. Approximate pressure drop and filtration efficiency expressions for semi-open wall-flow channels. *Can. J. Chem. Eng.* 92, 1517–1525. <https://doi.org/10.1002/cjce.21982>
- Haralampous, O.A., Mastellos, D., 2015. A multi-channel mathematical model for partially failed diesel particulate filters. 8th GRACM Int. Congr. Comput. Mech. 12 July - 15 July 2015, Volos, Greece.
- Harris, S.J., Maricq, M.M., 2001. Signature size distributions for diesel and gasoline engine exhaust particulate matter. *J. Aerosol Sci.* 32, 749–764. [https://doi.org/10.1016/S0021-8502\(00\)00111-7](https://doi.org/10.1016/S0021-8502(00)00111-7)
- Hedayat, K., Hart, J., Matson, E., Wilson, M., Poirier, N., 2017. Stoneridge patent for soot sensor. [https://doi.org/10.1016/j.\(73\)](https://doi.org/10.1016/j.(73))
- Hedayat, K., Hart, J., Matson, E., Wilson, M., Poirier, N., 2012. Stoneridge patent for soot sensor.
- HEI, H.E.I., 2013. Understanding the Health Effects of Ambient Ultrafine Particles. *Heal. Eff. Inst.* <https://doi.org/10.1177/0333102414566196>
- HEI, H.E.I., IHME, H.M. and E., 2018. a Special Report on Global Exposure To Air Pollution and Its Disease Burden.
- Herman, A., Wu, M.-C., Cabush, D., Shost, M., 2010. Model Based Control of SCR Dosing and OBD Strategies with Feedback from NH₃ Sensors. *SAE Int. J. Fuels Lubr.* 2, 375–385. <https://doi.org/10.4271/2009-01-0911>
- Heywood, J.B., 1989. Internal combustion engines fundamentals. McGraw-Hill. <https://doi.org/10987654>
- Hidria, 2011. Glow plug breakthrough. *Engine Technol. Int.*
- Hill, L., Clairotte, M., Astorga, C., Nakatani, S., Hibel, F., Ewers, J., Meyer, D., Suarez-Bertoa, R., Zardini, A.A., Lilova, V., 2015. Intercomparison of real-time tailpipe ammonia measurements from vehicles tested over the new world-harmonized light-duty vehicle test cycle (WLTC). *Environ. Sci. Pollut. Res.* 22, 7450–7460. <https://doi.org/10.1007/s11356-015-4267-3>
- Hinds, W.C., 1999. *Aerosol Technology: Properties, Behavior, and Measurement of Airborne Particles*, 2nd ed. ed. Wiley, New York, USA.
- Hiroyasu, 1983. Soot model. Konno, T. “Physical Chem. Chang. Med. Mix. with Adsorbents Solid State. IV. Study Reduced-pressure Mix. Pract. Use Amorph. Mix. Flufenamic Acid.” *Chem.*

-
- Pharm. Bull. 38, no. 7 2 117, 415–434. <https://doi.org/10.1248/cpb.37.3229>
- Honeywell Laboratories Plymouth, 2010. Demonstration of Particulate Matter (PM) Sensor in post-DPF Environment Innovative Clean Air Technologies (ICAT) 2008 Grant Program.
- Hong, S., Wooldridge, M.S., Im, H.G., Assanis, D.N., Pitsch, H., 2005. Development and application of a comprehensive soot model for 3D CFD reacting flow studies in a diesel engine. *Combust. Flame* 143, 11–26. <https://doi.org/10.1016/j.combustflame.2005.04.007>
- Husted, H., Roth, G., Nelson, S., Hocken, L., Fulks, G., Racine, D., 2012. Sensing of Particulate Matter for On-Board Diagnosis of Particulate Filters. *SAE Int. J. Engines* 5, 2012-01–0372. <https://doi.org/10.4271/2012-01-0372>
- Jessen, H., Willimowski, M., Meier, F., 2018. Bosch Solutions for Gasoline Particulate Filter monitoring Bosch Solutions for GPF monitoring Gasoline Particulate Filter OBD requirements and configurations Pressure based monitoring Hose line monitoring, in: SAE International, OBD Symposium, 5-7 March 2018, Barcelona, Spain.
- Johansson, P., 2008. Oil-related Particle Emissions from Diesel Engines, Licentiate Thesis. KTH University.
- Johnson, K., Boriboonsomsin, K., Barth, M., 2018. Dynamic Energy and Emissions Management (DEEM). PEMS Work. 2018, March 22, 2018, Univ. Calif. -Riverside, California, USA.
- Kadijk, G., Ligterink, N., Mensch, P. van, Smokers, R., Cuelenaere, R., Ligterink, N., 2016. NO_x EMISSIONS OF DIESEL CARS In the lab and on the road. TNO Innov. life Eur. Parliam. EMIS Comm. 21. <https://doi.org/10.13140/RG.2.2.30386.61126>
- Kadijk, G., Mayer, A., 2017. White paper NPTI – the New Periodic Technical Inspection emission test procedure for vehicles with emission control systems .
- Kamimoto, T., 2017. A review of soot sensors considered for on-board diagnostics application. *Int. J. Engine Res.* 18, 631–641. <https://doi.org/10.1177/1468087416678499>
- Karagulian, F., Belis, C.A., Dora, C.F.C., Prüss-Ustün, A.M., Bonjour, S., Adair-Rohani, H., Amann, M., 2015. Contributions to cities' ambient particulate matter (PM): A systematic review of local source contributions at global level. *Atmos. Environ.* 120, 475–483. <https://doi.org/10.1016/j.atmosenv.2015.08.087>
- Karamitros, D., 2016. Operation of Diesel Particulate Filters with Simultaneous Selective Catalytic Reduction of NO_x, PhD Thesis. Aristotle University.
- Khalek, I., Premnath, V., 2013. Particle Sensor Performance & Durability for OBD Applications &

-
- Beyond, in: CE-CERT Workshop, April 11, 2013, California, USA.
- Kirchen, P., 2008. Steady-state and transient diesel soot emissions development of a mean value soot model and exhaust-stream and in-cylinder measurements, PhD Thesis. ETH Univeristy.
- Kittelson, D.B., 1998. Engines and nanoparticles: A review. *J. Aerosol Sci.* 38, 197–204. [https://doi.org/10.1016/S0021-8502\(97\)10037-4](https://doi.org/10.1016/S0021-8502(97)10037-4)
- Kittelson, D.B., Pui, D.Y.H., Moon, K.C., 1986. Electrostatic Collection of Diesel Particles. SAE Tech. Pap. Ser. 1. <https://doi.org/10.4271/860009>
- Koebel, M., Madaia, G., 2002. Selective catalytic reduction of NO and NO₂ at low temperatures. *Catal. Today* 73, 239–247.
- Kontses, A., 2019. Methods and techniques for the assessment of vehicular exhaust particulate emissions using alternative fuels and advanced emission control systems, PhD Thesis. Aristotle University of Thessaloniki.
- Kumar, P., Morawska, L., Birmili, W., Paasonen, P., Hu, M., Kulmala, M., Harrison, R.M., Norford, L., Britter, R., 2014. Ultrafine particles in cities. *Environ. Int.* 66, 1–10. <https://doi.org/10.1016/j.envint.2014.01.013>
- Lee, Chunhwan, Oh, K., Kim, D., Lee, Chunbeom, 2010. A Characteristics of Particle Number Distribution for the Urea Solution Injection to Urea SCR System of Commercial Diesel Engine for an Emission Regulation. SAE Tech. Pap. Ser. 1. <https://doi.org/10.4271/2007-01-3455>
- Lei, H.J., Wang, H.L., Liu, B., Wang, C.A., 2016. Quantitative law of diffusion induced fracture. *Acta Mech. Sin. Xuebao* 32, 611–632. <https://doi.org/10.1007/s10409-015-0545-z>
- Liati, A., Schreiber, D., Dimopoulos Eggenschwiler, P., Arroyo Rojas Dasilva, Y., 2013. Metal particle emissions in the exhaust stream of diesel engines: An electron microscope study. *Environ. Sci. Technol.* 47, 14495–14501. <https://doi.org/10.1021/es403121y>
- Linke, J., Konrad, D., Gmbh, B.E., 2016. Concept for Diesel Particulate Filter monitoring based on BOSCH Particulate Matter Sensor (PMS), in: Internationales Stuttgarter Symposium, Stuttgart, Germany. <https://doi.org/10.1007/978-3-658-16988-6>
- Malik, A., Abdulhamid, H., Pagels, J., Rissler, J., Lindskog, M., Nilsson, P., Bjorklund, R., Jozsa, P., Visser, J., Spetz, A., Sanati, M., 2011. A potential soot mass determination method from resistivity measurement of thermophoretically deposited soot. *Aerosol Sci. Technol.* 45, 284–294. <https://doi.org/10.1080/02786826.2010.533214>
- Maricq, M.M., 2008. Bipolar diffusion charging of soot aggregates. *Aerosol Sci. Technol.* 42, 247–254.

<https://doi.org/10.1080/02786820801958775>

- Maricq, M.M., 2006. On the electrical charge of motor vehicle exhaust particles. *J. Aerosol Sci.* 37, 858–874. <https://doi.org/10.1016/j.jaerosci.2005.08.003>
- Maricq, M.M., Bilby, D., 2018. The impact of voltage and flow on the electrostatic soot sensor and the implications for its use as a diesel particulate filter monitor. *J. Aerosol Sci.* 124, 41–53. <https://doi.org/10.1016/j.jaerosci.2018.07.002>
- Maricq, M.M., Xu, N., 2004. The effective density and fractal dimension of soot particles from premixed flames and motor vehicle exhaust. *J. Aerosol Sci.* 35, 1251–1274. <https://doi.org/10.1016/j.jaerosci.2004.05.002>
- Meyer, N.K., Ristovski, Z.D., 2007. Ternary Nucleation as a Mechanism for the Production of Diesel Nanoparticles: Experimental Analysis of the Volatile and Hygroscopic Properties of Diesel Exhaust Using the Volatilization and Humidification Tandem Differential Mobility Analyzer. *Environ. Sci. Technol.* 41, 7309–7314. <https://doi.org/10.1021/es062574v>
- Mosbach, S., Celnik, M.S., Raj, A., Kraft, M., Zhang, H.R., Kubo, S., Kim, K.O., S.Mosbach, S., Celnik, M.S., Raj, A., Kraft, M., Zhang, H.R., Kubo, S., Kim, K.O., 2009. Towards a detailed soot model for internal combustion engines. *Combust. Flame* 156, 1156–1165. <https://doi.org/10.1016/j.combustflame.2009.01.003>
- Moser, M., Dietrich, M., Walte, S., 2019. Radio Frequency Antenna for Direct Load Measurement and OBD for EAT Components, in: SAE On-Board Diagnostics Symposium Europe, March, 2019, Stuttgart, Germany.
- Muñoz, X., Barreiro, E., Bustamante, V., Lopez-Campos, J.L., González-Barcala, F.J., Cruz, M.J., 2019. Diesel exhausts particles: Their role in increasing the incidence of asthma. Reviewing the evidence of a causal link. *Sci. Total Environ.* 652, 1129–1138. <https://doi.org/10.1016/j.scitotenv.2018.10.188>
- Neumann, E., Eckardt, D., Stölting, E., Gratzke, R., 2012. Efficient soot raw emission modelling for Diesel engine control units, in: 9th Symposium Automotive Powertrain Control Systems, Sept 20th 2012.
- NGK/NTK, 2019. Development of Oxygen Sensors, Available online,. URL <https://www.ngkntk.co.jp/english/special/story/story07.html> (accessed 7.19.19).
- Ntziachristos, L., 2017. Latest EU Regulatory Developments on Euro Standards and Measurement Requirements, EMISIA Workshop, Zurich, 2017-11-17.

-
- Ntziachristos, L., Amanatidis, S., Samaras, Z., Janka, K., Tikkanen, J., 2013. Application of the Pegasor Particle Sensor for the Measurement of Mass and Particle Number Emissions. *SAE Int. J. Fuels Lubr.* 6, 2013-01–1561. <https://doi.org/10.4271/2013-01-1561>
- Ntziachristos, L., Fragkiadoulakis, P., Samaras, Z., Janka, K., Tikkanen, J., 2011. Exhaust Particle Sensor for OBD Application. *SAE Int.* 1. <https://doi.org/10.4271/2011-01-0626>
- Ntziachristos, L., Papadimitriou, G., Triantafyllopoulos, G., Lupiáñez-villanueva, F., Marek, E., Veltri, G., Tornese, P., Borken-kleefeld, J., Franco, V., Mock, P., 2016. Preparation of the legal and technical background for a voluntary EU standard for low emitting combustion engine driven cars (EULES) Final Report.
- Ntziachristos, L., Tzamkiozis, T., Tikkanen, J., 2009. A New Sensor for On-Board Diagnosis of Particle Filter Operation - First Results and Development Potential, in: FAD Conference, Dresden, Germany.
- Ochs, T., Schittenhelm, H., Genssle, A., Kamp, B., 2010. Particulate Matter Sensor for On Board Diagnostics (OBD) of Diesel Particulate Filters (DPF). *SAE Int. J. Fuels Lubr.* 3, 61–69. <https://doi.org/10.4271/2010-01-0307>
- Pandis, S.N., Cruz, C.N., 1997. A study of the ability of pure secondary organic aerosol to act as cloud condensation nuclei. *Atmos. Environ.* 31, 2205–2214.
- Papitha, R., Suresh, M., Das, D., Johnson, R., 2013. Effect of micro-cracking on the thermal conductivity and thermal expansion of tialite (Al₂TiO₅) ceramics. *Process. Appl. Ceram.* 7, 143–146. <https://doi.org/10.2298/pac1303143p>
- Reynaud, A., Leblanc, M., Zinola, S., Breuil, P., Viricelle, J.-P., 2019. Responses of a Resistive Soot Sensor to Different Mono-Disperse Soot Aerosols. *Sensors* 19, 705. <https://doi.org/10.3390/s19030705>
- RICARDO, 2018. Expectations for Actual Euro 6 Vehicle Emissions.
- Riehle, C., Wadenpohl, C., 1995. Electrically stimulated agglomeration at an earthed surface 119–126.
- Robinson, M.A., Backhaus, J., Foley, R., Liu, Z.G., 2016. The Effect of Diesel Exhaust Fluid Dosing on Tailpipe Particle Number Emissions. *SAE Tech. Pap. Ser.* 1. <https://doi.org/10.4271/2016-01-0995>
- Rostedt, A., Marjamäki, M., Yli-Ojanperä, J., Keskinen, J., Janka, K., Niemelä, V., Ukkonen, A., 2009. Non-collecting electrical sensor for particle concentration measurement. *Aerosol Air Qual. Res.* 9, 470–477. <https://doi.org/10.4209/aaqr.2009.03.0023>

-
- Rostedt, A., Ntziachristos, L.D., Simonen, P., Rönkkö, T., Samaras, Z.C., Hillamo, R., Janka, K., Keskinen, J., 2017. A New Miniaturized Sensor for Ultra-Fast On-Board Soot Concentration Measurements. *SAE Int. J. Engines* 10, 2017-01–1008. <https://doi.org/10.4271/2017-01-1008>
- Rückerl, R., Schneider, A., Breitner, S., Cyrys, J., Peters, A., 2011. Health effects of particulate air pollution: A review of epidemiological evidence. *Inhal. Toxicol.* 23, 555–592. <https://doi.org/10.3109/08958378.2011.593587>
- Samaras, Z., Geivanidis, S., Vermeulen, R., Vonk, W., Noble, A., Andersson, J., Sindano, H., 2014a. Technical feasibility of different regulatory OBD threshold limits (OTL) for Euro 6 (LD) vehicles.
- Samaras, Z., Geivanidis, S., Vonk, W., Andersson, J., Sindano, H., Hausberger, S., Perujo, A., 2013. Testing of soot sensors for DPF failure monitoring, in: 17th ETH-Conference on Combustion Generated Nanoparticles, 23rd-26th June 2013, ETH, Zurich, Switzerland.
- Samaras, Z., Geivanidis, S., Vonk, W., Andersson, J., Sindano, H., Hausberger, S., Stadlhofer, W., Perujo, A., Carriero, M., 2014b. Evaluation of soot sensors for DPF failure monitoring, in: FISITA 2014 World Automotive Congress, Maastricht, Netherlands.
- Sappok, A., Bromberg, L., Parks, J.E., Prikhodko, V., 2010. Loading and Regeneration Analysis of a Diesel Particulate Filter with a Radio Frequency-Based Sensor. *SAE Int.* <https://doi.org/10.4271/2010-01-2126>
- Sappok, A.G., Wong, V.W., 2007. Detailed Chemical and Physical Characterization of Ash Species in Diesel Exhaust Entering Aftertreatment Systems. *SAE Tech. Pap. Ser. 1*, 776–790. <https://doi.org/10.4271/2007-01-0318>
- Schmid, J., Grob, B., Niessner, R., Ivleva, N.P., 2011. Multiwavelength raman microspectroscopy for rapid prediction of soot oxidation reactivity. *Anal. Chem.* 83, 1173–1179. <https://doi.org/10.1021/ac102939w>
- Schwelberger, M., Mamakos, A., Fierz, M., Giechaskiel, B., 2019. Experimental Assessment of an Electrofilter and a Tandem Positive-Negative Corona Charger for the Measurement of Charged Nanoparticles formed in Selective Catalytic Reduction Systems. *Appl. Sci.* 9, 1051. <https://doi.org/10.3390/app9061051>
- Sioutas, C., Delfino, R.J., Singh, M., 2005. Exposure assessment for atmospheric Ultrafine Particles (UFPs) and implications in epidemiologic research. *Environ. Health Perspect.* 113, 947–955. <https://doi.org/10.1289/ehp.7939>
- Soysal, U., Géhin, E., Algré, E., Berthelot, B., Da, G., Robine, E., 2017. Aerosol mass concentration measurements: Recent advancements of real-time nano/micro systems. *J. Aerosol Sci.* 114, 42–54.

- Steppan, J., Henderson, B., Lourduhasamy, A., Wang, V., Fitzpatrick, J., Allmendinger, K., 2014. Characterization of an In Situ Electrostatic Soot Sensor with Laboratory Measurement Instruments, in: UC Riverside Portable Emissions Measurement Systems Conference & Workshop, April 3-4, 2014, California, USA.
- Suarez-Bertoa, R., Mendoza-Villafuerte, P., Bonnel, P., Lilova, V., Hill, L., Perujo, A., Astorga, C., 2016. On-road measurement of NH₃ and N₂O emissions from a Euro V heavy-duty vehicle. *Atmos. Environ.* 139, 167–175. <https://doi.org/10.1016/j.atmosenv.2016.04.035>
- Suarez-Bertoa, R., Mendoza-Villafuerte, P., Riccobono, F., Vojtisek, M., Pechout, M., Perujo, A., Astorga, C., 2017. On-road measurement of NH₃ emissions from gasoline and diesel passenger cars during real world driving conditions. *Atmos. Environ.* 166, 488–497. <https://doi.org/10.1016/j.atmosenv.2017.07.056>
- Suresh, A., Khan, A., Johnson, J.H., 2000. An Experimental and Modeling Study of Cordierite Traps - Pressure Drop and Permeability of Clean and Particulate Loaded Traps. SAE Tech. Pap. Ser. 1. <https://doi.org/10.4271/2000-01-0476>
- Surve, P.R., 2008. Diesel Particulate Filter Diagnostics Using Correlation and Spectral Analysis, Master thesis. Purdue University.
- Sydbom, A., Blomberg, A., Parnia, S., Stenfors, N., Sandström, T., Dahlén, S.E., 2001. Health effects of diesel exhaust emissions. *Eur. Respir. J.* 17, 733–46.
- Takeuchi, Y., Hirano, S., Kanauchi, M., Ohkubo, H., Nakazato, M., Sutherland, M., Van Dam, W.T.Y.H.S.K.M.O.H.N.M.S.M., 2003. The impact of diesel engine lubricants on deposit formation in diesel particulate filters. SAE Int. 1. <https://doi.org/10.4271/2003-01-1870>
- Tan, P., Li, Y., Shen, H., 2017. Effect of lubricant sulfur on the morphology and elemental composition of diesel exhaust particles. *J. Environ. Sci. (China)* 55, 354–362. <https://doi.org/10.1016/j.jes.2017.01.014>
- Tan, P.Q., Wang, D.Y., 2018. Effects of Sulfur Content and Ash Content in Lubricating Oil on the Aggregate Morphology and Nanostructure of Diesel Particulate Matter. *Energy and Fuels* 32, 713–724. <https://doi.org/10.1021/acs.energyfuels.7b03017>
- Teike, G., Dietzel, M., Michaelis, B., Schomburg, H., Sommerfeld, M., 2012. Multiscale Lattice-Boltzmann approach for electrophoretic particle deposition. *Aerosol Sci. Technol.* 46, 451–464. <https://doi.org/10.1080/02786826.2011.634451>

-
- Tiefenbach, 2018. BOSCH patent: Method for controlling the function of a sensor for detecting particles.
- TNO, 2018. HORIBA and TNO Bundle Forces to Promote Smart Emission Measurement System (SEMS) | TNO, Available online,. URL <https://www.tno.nl/en/about-tno/news/2018/6/horiba-and-tno-bundle-forces-to-promote-smart-emission-measurement-system-sems/> (accessed 2.25.19).
- Tornehed, P., Olofsson, U., 2011. Advanced Petroleum Based Fuels–Diesel Emission Control (APBF–DEC), Lubricants Project, phase 1 Final Report, August 2003, Sponsored by The U.S. Department of Energy, American Chemistry Council, American Petroleum Institute, California Air Resources Board. Proc. Inst. Mech. Eng. Part D J. Automob. Eng. 225, 1055–1066. <https://doi.org/10.1177/0954407011402754>
- Triantafyllopoulos, G.K., 2018. Assessment of technologies to reduce fuel consumption and pollutant emissions of modern passenger cars in real - world driving conditions, PhD Thesis. Aristotle University of Thessaloniki.
- TRUE, 2018. Determination of real-world emissions from passenger vehicles using remote sensing data.
- Umicore, 2018. Light Duty Diesel: Diesel Exhaust Aftertreatment Systems for Efficient Reduction of NO_x, CO, HC and Particulate Emissions, Available online,. URL <https://ac.umicore.com/en/applications/light-duty-diesel/> (accessed 3.30.19).
- UNECE, 2017. Addendum 82: Regulation No. 83. Int. Transp. Comm.
- UNECE, 2015. UNECE Addendum 82: Regulation No. 83 (R083r5).
- US Department of Energy, 2007. Advanced Petroleum Based Fuels–Diesel Emission Control (APBF–DEC).
- US EPA, O., 2019. Climate Change Indicators: Climate Forcing, Available online,. URL <https://www.epa.gov/climate-indicators/climate-change-indicators-climate-forcing> (accessed 7.1.19).
- Vouitsis, E., Ntziachristos, L., Pistikopoulos, P., Samaras, Z., Chrysikou, L., Samara, C., Papadimitriou, C., Samaras, P., Sakellaropoulos, G., 2009. An investigation on the physical, chemical and ecotoxicological characteristics of particulate matter emitted from light-duty vehicles. Environ. Pollut. 157, 2320–2327. <https://doi.org/10.1016/j.envpol.2009.03.028>
- Vouitsis, E., Ntziachristos, L., Samaras, Z., Chrysikou, L., Samara, C., Miltsios, G., 2011. Effect of Lube Oil on the Physicochemical Characteristics of Particulate Matter Emitted from a Euro 4 Light Duty Diesel Vehicle. SAE Tech. Pap. Ser. 1. <https://doi.org/10.4271/2007-24-0110>
- Wallin, L., 2014. Investigation of urea deposit formation in vehicles with Selective Catalytic Reduction

system, Master Thesis. Chalmers University.

- Wang, D.Y., Yao, S., Shost, M., Yoo, J.-H., Cabush, D., Racine, D., Cloudt, R., Willems, F., 2010. Ammonia Sensor for Closed-Loop SCR Control. *SAE Int. J. Passeng. Cars - Electron. Electr. Syst.* 1, 323–333. <https://doi.org/10.4271/2008-01-0919>
- Watanabe, I., Kawai, T., Yonezawa, K., Ogawa, T., 2014. The New Toyota 2.0-Liter Inline 4-Cylinder ESTEC D-4ST Engine - Turbocharged Direct Injection Gasoline Engine -.
- Weigl, M., Roduner, C., Lauer, T., 2012. Partikelfilter-Onboard-Diagnose mittels eines Soot-Sensors nach Partikelfilter by Means of a Soot-Sensor Downstream 62–69.
- WHO, 2018. Mortality from Ambient Air Pollution (Accessed 07.30.19), Available online,.
- Wikipedia, 2019. Portable Emissions Measurement System (Accessed 07.23.19), Available online,.
- World Health Organization, 2006. WHO Air quality guidelines for particulate matter, ozone, nitrogen dioxide and sulfur dioxide: Global update 2005. Geneva. 1–21. [https://doi.org/10.1016/0004-6981\(88\)90109-6](https://doi.org/10.1016/0004-6981(88)90109-6)
- Wu, Y., 2019. 20 Years of Vehicle Emission Control in China : A Review and Outlook, in: TAP 2019, Thessaloniki, Greece.
- Zhang, X., Tennison, P., Ruona, W., 2010. 3D Numerical Study of Pressure Loss Characteristics and Filtration Efficiency through a Frontal Unplugged DPF. *SAE Int. J. Fuels Lubr.* 3, 177–193. <https://doi.org/10.4271/2010-01-0538>
- Zhang, Z., Del Re, L., Fuehrapter, R., 2017. Fast Hybrid Sensor for Soot of Production CI Engines. *SAE Tech. Pap.* 2017-Sept. <https://doi.org/10.4271/2017-24-0137>
- Zhang, Z., Fuehrapter, R., Waschl, H., Del Re, L., 2016. Calibration and Performance of a Novel In-situ Soot Sensor for Production Engines. *Procedia Eng.* 168, 43–46. <https://doi.org/10.1016/j.proeng.2016.11.135>
- Zhang, Z., Stadlbauer, S., Viskup, R., Re, L., Bergmann, A., Reinisch, T., Viskup, S.S.R., Re, R.F.L. del, 2014. Fast measurement of soot by in-situ LII on a production engine. *Proc. ASME 2014 Intern. Combust. Engine Div. Fall Tech. Conf.* 1–8. <https://doi.org/10.1115/ICEF2014-5555>

List of Figures

Figure 1: Radiative forcing caused by human activities and the results on climate cooling or warming (US EPA, 2019).....	17
Figure 2. Size distribution of particles from combustion (“DieselNet. Exhaust Particulate Matter.,” 2019).....	19
Figure 3: Particle composition. The focus of this study is on the carbonaceous part or soot, being usually the higher fraction of diesel particulates.	19
Figure 4. (a) Cracks on DPF substrate (LAT) (b) Melted DPF (LAT) (c) Partial unplugged DPF (LAT) (d) DPF removal (google image).....	22
Figure 5: Malfunction indicator lamps (MIL)	23
Figure 6. EU OBD legislation (a) First and second preconditioning cycles (b) Emission tests cycle (Example of NEDC).....	26
Figure 7. US OBD legislation (a) First and second preconditioning cycles (the second or even more preconditioning cycles can be applied upon request from the manufacturer) (b) Emission tests cycle	26
Figure 8: Delta pressure for two damaged and an intact (standard) DPFs (Daimler - ACEA OBD Seminar, January 23, 2008).....	27
Figure 9: Approach for the development of the OBD model for the DPF. The design and the realisation are the two distinct levels for the final implementation.	28
Figure 10: a) ECM with sensor tip b) sensor element (enlarged) c) operating principle and d) response time of the Stoneridge resistive soot sensor.	35
Figure 11. Overview of the OBD model developed in Matlab/Simulink®	38
Figure 12. Example of OBD index and sensor signal across a transient operation for (a) an above the OTL DPF where both sensor accumulation periods result in a correct diagnosis of DPF not OK (b) a below the OTL DPF where both sensor accumulation periods result in the correct diagnosis of a DPF OK.	41
Figure 13. Definition of threshold OBD Index, and type I and II errors as derived from the measurements of an OTL and a TA DPF. The target is to find a compromise between low Type I and Type II errors.	42
Figure 14: Exhaust setup for (a) Toyota engine for transient measurements (b) Toyota and Daimler engines for steady-state measurements	45
Figure 15. Schematic of the exhaust set-up for in-laboratory and on-road measurements of a) Honda Accord vehicle b) Peugeot 308 vehicle c) vehicle #3.	46
Figure 16: Differences between the rear and front plug removal technique (Haralampous and Kontzias, 2014) on a) axial and wall velocities and resulting soot cake pattern b) filtration efficiency and pressure drop.....	48

Figure 17: (a) Correlation between filtration efficiency and percentage of removed plugs (example for the removal of outlet plugs only) (b) Example of DPF removed plugs (c) Through holes in a DPF for failure simulation (d) Bypass of the DPF for controlling filtration efficiency	49
Figure 18: a) drop to idle technique for DPF cracking b) cracks on DPF (tomography)	49
Figure 19: (a) Pegasor Particle Sensor operating principle (b) Measuring unit	51
Figure 20: (a) Inlet gas heater's control unit (b) inlet heated pipeline (Honda Accord on-road measurements) (c) Power supply for every AC (d) air pressure regulator	51
Figure 21: Real driving one route a) Urban part b) Extra-urban and highway part	53
Figure 22: a) Real driving #2 and 3 route (RDE-compliant route and RDE-dynamic) consisted of urban, rural and motorway parts (Triantafyllopoulos, 2018) b) torque and engine speed points for RDE-compliant and dynamic routes (Kontses, 2019) c) comparison of vehicle speed and altitude for RDE-compliant and RDE-dynamic routes (Kontses, 2019).....	54
Figure 23: a) SEM equipment b) example of a resistive sensor after exposure to ash particles	55
Figure 24: Overview of the OBD model. Focus on the soot model	57
Figure 25: Equivalence ratio versus temperature region of diesel soot precursor formation (Dhal et al., 2018).....	58
Figure 26: Classification of soot models. The green boxes are referring to the current analysis, which aims in developing an empirical, grey-box, micro parameter-dependent model for transient correction supplementary to a black box statistical model.....	60
Figure 27: Step variation of MAF and recording of the resulting increase in soot concentration.....	63
Figure 28. (a) Overview of the VeLoDyn model for simulation of engine-out soot emissions (b) Soot map used for calculation of engine-out soot emissions in every time step according to engine speed and torque which are provided by the vehicle's ECU.....	64
Figure 29: Soot concentration for steady-state operation (base soot map, C_{0N}, T). The red marks are the measured points (12 levels of torque, nine levels engine of speed).	65
Figure 30: Steady-state maps (Z_0, kN, T) of (a) MAF (b) rail pressure (c) injection timing.	66
Figure 31: Partial derivative maps ($\partial C_0, k\partial Z kN, T$) for (a) MAF (b) rail pressure (c) injection timing	67
Figure 32: (a) Vehicle speed profile for NEDC cycle (b) Second-by-second soot concentration from the model (using only the base soot map) and the measurement (c) Cumulative soot concentration from the model (using only the base soot map) and the measurement.	68
Figure 33: Soot estimation from the base soot map and the transient correction (a) Second-by-second soot concentration from the model and the measurement (b) Cumulative soot concentration from the model and the measurement.	69
Figure 34: Correlation of EGR deviation with soot deviation.....	69
Figure 35: Steady-state maps for (a) EGR rate (b) partial derivative for EGR	70

Figure 36: Final soot estimation from the base soot map, the transient correction and the EGR adjustment (a) Second-by-second soot concentration from model and measurement (b) Cumulative soot concentration from model and measurement.	71
Figure 37: (a) Vehicle speed profile for WLTC cycle (b) Second-by-second soot concentration from model and measurement (c) Cumulative soot concentration from model and measurement.....	72
Figure 38: Overview of the OBD model. Focus on the DPF model	72
Figure 39: OTL DPF for the Toyota engine for the development of the DPF models. 219 plugs were symmetrically removed from the rear face of the filter a) 2D drawing b) photo after plug removal	75
Figure 40. Simulation of a partial unplugged DPF (Axisuite)	76
Figure 41: Evolution of the filtration efficiency and the pressure drop for a clean DPF during steady-state operation	77
Figure 42: Exhaust mass flow profile and evolution of the DPF load for a clean DPF during an NEDC	77
Figure 43: Constant filtration efficiency based on the 2 nd NEDC for the OTL DPF. The 1 st cycle is a preconditioning to avoid the depth filtration of the DPF. The cumulative values are calculated separately for each cycle.	78
Figure 44: Evolution of filtration efficiency during 13 NEDCs.....	78
Figure 45: a) Effect of exhaust volume on filtration efficiency b) effect of DPF load on filtration efficiency c) 2D map for the filtration efficiency as a function of exhaust volume flow and DPF load.....	79
Figure 46: Clean pressure drop tests for a) full DPF b) partially unplugged OTL DPF	80
Figure 47: Filtration efficiency tests for a) full DPF b) partially unplugged OTL DPF	81
Figure 48: Soot loading tests for a) full DPF b) partial unplugged OTL DPF	82
Figure 49: Filtration efficiency a) during 13 consecutive NEDCs b)focus on the second NEDC which is the reference cycle after the preconditioning c) focus at the end of the preconditioning cycle (are with low filtration efficiency).....	84
Figure 50: Overview of the OBD model. Focus on the sensor model.....	85
Figure 51. Example of performance of the statistical model over different levels of soot, velocity and temperature. (a) Sensor response time at 220°C for three exhaust gas velocity levels (b) Example of sensor response time at exhaust speed of 24 m/s for three exhaust gas temperature levels	88
Figure 52. Performance of the empirical function compared to measured data.....	90
Figure 53. Physical model (a and b) and statistical model (c and d) for all sensors (steady-state tests). Calibrated results (b and d) with the use of the SF shows good performance of both models with a slight advantage of the statistical model.	92
Figure 54. (a) Basic parameters of a WLTC measurement with high PM emissions (DPF emission: 13.1 mg/km). The sensor signal is described by the soot value (no physical meaning of the numbers). Part of the first (valid) loading of the Sensor 1 (highlighted area) is selected to analyse the deposition mechanisms. (b) Deposition velocities at the specified time interval	94

Figure 55. Satisfactory performance of the SF-corrected models for Sensors1-3 on all driving cycles (a) Physical model (b) Statistical model.	95
Figure 56. (a) Example of 600 seconds of on-road tests with urban and extra-urban driving. Zoom-in a sample loading of the P1 sensor during the urban route with Above OTL DPF, (b) Deposition velocities for the specified time interval.	96
Figure 57. Performance of the SF-corrected models for sensors P1 and P2 (on-road tests). The physical model outmatches the statistical model (a) Physical model and (b) Statistical model.	97
Figure 58: Overview of the OBD model. Focus on the sensor response time	98
Figure 59: 3 different resistive sensors. (a) Stoneridge resistive sensor (b) Resistive sensor b (c) Resistive sensor c	100
Figure 60: Soot accumulation and construction of dendrites for (a1,2) Stoneridge sensor (b1,2) Resistive b (c1,2) Resistive c.	101
Figure 61. Measured compared to modelled response times in steady-state points, depicted as (a) x=y diagram (b) relative error. The maximum error is 25%.	102
Figure 62: Overview of the OBD model. Focus on OBD algorithms	102
Figure 63: Engine and exhaust parameters during an example cold start NEDC. The temperature remains below the dew point (90°C) for more than the half duration of the cycle. The engine mode (0 or 4) indicates the normal or rich operation of the engine for NO _x release and conversion into N ₂ , respectively.	105
Figure 64: (a) Definition of threshold Index (b) Calibration of the threshold filtration efficiency to adjust the threshold Index to 1.	106
Figure 65: Real driving cycle with a TA DPF and two wrong diagnoses (false passes).	107
Figure 66: Example of debouncing strategies for DPF diagnosis over an FTP-75 driving cycle	108
Figure 67: a) OBD Indexes without rejection criteria b), c) with rejection criteria	110
Figure 68: Soot, velocity and temperature for RDE-compliant (colour-filled boxes) and dynamic routes (no-fill boxes)	114
Figure 69: a) Performance of the TF on DoE steady-state points b) Pareto charts for the contribution of each term of the TF. Soot is the most significant input parameter.	115
Figure 70: TF performance on RDE-compliant and RDE-Dynamic routes	116
Figure 71: TF performance on RDE-compliant and RDE-Dynamic routes with improved TF	117
Figure 72: Regeneration duration for two sensors. Low voltage increases the regeneration time	118
Figure 73: SEM images after 90 s of regeneration a) 12 V power supply; clean sensor b) 9 V power supply; sensor with soot deposits	119
Figure 74: a) Side view of the latest tip design, b) installation in the exhaust line and definition of orientation c) bottom view with orientation positions	120
Figure 75: Effect of orientation on 5 Gen1 sensors a) high exhaust velocity b) low exhaust velocity	120

Figure 76: a) CFD analysis for the effect of sensor orientation b) Experimental results for the same sensor orientations. Sensor response times are independent of the orientation.....	121
Figure 77: Example of start-stop operation during a WLTC cycle for a Euro 6 diesel vehicle a) driving profile b) start-stop during cold cycle c) start-stop during hot cycle.....	124
Figure 78: a) temperature profiles during cold start operation b) sensor signal.....	126
Figure 79: Experimental setup for gaseous exposure (H ₂ , CO, CH ₄). Example of a) H ₂ , b) CO and c) CH ₄ exposure.....	132
Figure 80: Experimental setup for AdBlue and Na exposure.....	133
Figure 81: a) Urea deposits during the AdBlue test b) effect of Urea injection on sensor response time	135
Figure 82: NH ₃ direct effect on sensor response time. All measurements are for a medium engine operating point of 5 mg/m ³ soot concentration, 15m/s exhaust velocity and 200°C exhaust temperature.	139
Figure 83: Evaluation of cumulative effect after 50 hours of NH ₃ exposure a) low-temperature exposure b) high-temperature exposure.....	140
Figure 84: Evaluation of cumulative effect after NH ₃ exposure (summary of all evaluation points) .	142
Figure 85: Transient pattern for ash exposure.....	145
Figure 86: Design of sensor tips used for the ash experiment a) single-tip b) alternative dual-tip c) dual-tip.....	146
Figure 87: a) Direct effect on the response time of ash exposure b) Cumulative effect after long evaluated every 18h of ash exposure	147
Figure 88: Accumulation pattern for a) soot particle b) ash particles. The higher conductivity of soot particles leads to the construction of dendrites between the electrodes instead of a particle layer on the element (Teike et al., 2012).....	148
Figure 89: Comparison of single and dual-tip sensors. a) ash layer onto the whole surface for single-tip sensor b) ash accumulated on the non-grounded electrode leaving enough space for soot dendrites .	149
Figure 90: a) Extensive ash contamination (whitish flakes) on the upper electrode due to electrophoresis for the dual-tip sensor with P1 software b) lower contamination for the dual-tip sensor with P2 software.	149
Figure 91: Exhaust aftertreatment of all vehicles. Particulate filters are the key-devices for the reduction of PN/PM emissions.....	151
Figure 92: Sensors as part of future online emission monitoring systems (ACEA, 2018; TNO, 2018; TRUE, 2018)	152
Figure 93: Optical sensors. LII sensors are still under development. AVL and BOSCH have presented prototypes for portable applications. 3DATX is commercially available and combines three low-cost sensors.	158

Figure 94: Electrical charge-based principle; electrostatic sensors. The University of Texas (Austin) started the development of an electrostatic sensor to make use of the amplified charge of particles in 1999 EmiSense presented the first prototype for OBD applications in 2010. Continental redesigned the electronics and introduced its sensor in 2015, but the development suspended and is currently available only for agriculture applications. CoorsTek acquired EmiSense technology (2013) and is the only supplier today for this technology. In parallel, Honeywell developed and presented a sensor which uses the natural charge directly, but the development suspended.	159
Figure 95: Electrical charge-based principle; Diffusion Charging. Dekati investigated the ionising technique by diffusion as a miniature device or sensor with ETaPS (Electrical Tail Pipe Sensor), which measures the escaping current. It was further refined and developed by Pegasor with the PPS (Pegasor Particle Sensor). Recently NGK/NTK presented a miniature PPS which is highly portable, cost-effective and integrated into the NGK/NTK compact emissions meter (NCEM) along with NO _x and lambda sensors. Rostedt et al., (2017) presented a miniaturised sensor for OBD applications, which is also a compact PPS in terms of operating principle and hardware components. Pegasor was acquired by CoorsTek in 2014. Testo has also developed a handheld nanoparticle counter based on the measurement of charge acquired by particles.	160
Figure 96: Electrostatic sensor a) sensor probe with the sensor control unit (SCU) b) details of sensor probe (Maricq and Bilby, 2018) c) forces on particles accumulated in one of the electrodes (Fitzpatrick et al., 2018).	163
Figure 97: Correlation of exhaust velocity with the signal correction factor	164
Figure 98: Running-in time for different driving cycles	165
Figure 99: Correlation of electrostatic sensors with MSS a) example of WLTC b) steady-state and transient cycles (all measurements)	166
Figure 100: Overview of the OBD model developed in Matlab Simulink®	169
Figure 101: Schematic of the future approach	172

List of Tables

Table 1: EU legislation limits for the first registration of vehicles (2014-2020)	24
Table 2: Main requirements of current legislation regarding the particulate filters	24
Table 3: Summary of the differences among the various sensor generations used for the study (HW: hardware, SW: software). Gen5 sensors were the most widely used in this thesis.	36
Table 4: Summary of the sensor generations used in this work	37
Table 5: Engines used for the measurements	43
Table 6: Vehicles used for the measurements	44
Table 7: Overview of engine and vehicle used for every section of the study	47
Table 8: Legislative cycles and real-driving routes for the tested vehicles and engine (c: cold, h: hot)	53
Table 9: Comparison of RDE-compliant and RDE-dynamic routes along with the legislation limits..	55
Table 10: Operating point levels for the development of the soot model. For the partial derivative values of the influencing parameters, the development was based on fewer levels compared to the base map to reduce the calibration effort (green font).....	62
Table 11: Step changes for the influencing parameters.....	62
Table 12. Errors of soot models	71
Table 13. Errors of DPF models.....	84
Table 14: Particle deposition mechanisms in a resistive soot sensor	86
Table 15. Steady-state levels for the tested sensors (Sensors1-3).	89
Table 16. Steady-state levels for the validation of the statistical model	90
Table 17. Comparison of R^2 , RMSE and SF between the physical and the statistical model (steady-state tests).	92
Table 18. Comparison of R^2 , RMSE and SF between the physical and the statistical model (driving cycles tests).	95
Table 19. Comparison of R^2 , RMSE and SF between the physical and the statistical model (on-road tests).	97
Table 20. Sensor model variables and associated errors	97
Table 21. Steady-state levels for the tested sensors (Sensors 1-3).	102
Table 22. OBD model variables and associated errors.....	103
Table 23: Number of accumulation periods, corresponding emissions and false events for the calibration of the Threshold filtration efficiency (final calibration).....	106
Table 24. Steady-state levels for the development of the new Transfer Function.	114
Table 25: Steady-state points and voltage levels for the investigation of voltage effect on sensor regeneration	117

Table 26: Correlation of exhaust, wall and sensor temperatures with the dew point temperature.....	127
Table 27: Cross sensitivities, the way they were investigated and the tested levels. (RT: response time). NH ₃ and ash are examined separately.	129
Table 28: Steady-state engine operation at three soot concentration levels.	131
Table 29: Commonly found contaminants in the diesel exhaust and their effect (direct or remaining) on the resistive sensors.	134
Table 30: Overview of methods for PN/PM estimation	157
Table 31: Summary table of PN/PM sensors for future applications	162

